The Thesis Committee for Julia Nicole Roberts
Certifies that this is the approved version of the following thesis:

Direct In-Situ Evaluation of Liquefaction Susceptibility

APPROVED BY
SUPERVISING COMMITTEE:

Supervisor:

Kenneth H. Stokoe, II

Brady R. Cox

Direct In-Situ Evaluation of Liquefaction Susceptibility

by

Julia Nicole Roberts, B.S.C.E.

Thesis

Presented to the Faculty of the Graduate School of

The University of Texas at Austin

in Partial Fulfillment

of the Requirements

for the Degree of

Master of Science in Engineering

The University of Texas at Austin

May 2014

Dedication

To the reader

Acknowledgements

The work completed in this thesis could not have been done without the help of many individuals over the past three years. First and foremost, I wish to thank Dr. Kenneth H. Stokoe, II, for his guidance as my research advisor and for answering my endless stream of questions regarding soil dynamics. I am also deeply grateful for the invaluable guidance from Dr. Brady R. Cox regarding the work done on this thesis as well as other research projects. I look forward to working together with both Dr. Stokoe and Dr. Cox for several more years in pursuit of the PhD.

I also extend my deepest gratitude to the NEES@UTexas team Cecil Hoffpauir, Dr. Farn-Yun Menq, Robert Kent, and Andrew Valentine, without whom none of this research would be possible, nor would it be nearly as much fun. I extend an additional thanks to my classmate and partner in crime out in the field, Sungmoon Hwang, for great times on past projects, and hopefully many more in the future.

Thank you to Dr. Gilbert, Dr. Rathje, Dr. Zornberg, and Dr. El Mohtar from whom I have taken courses or interacted with over the past few years, for creating an excellent community of learning and research in our geotechnical engineering program here at The University of Texas at Austin.

To those who first inspired me to go into geotechnical engineering, I extend a special acknowledgement to Dr. Lucy Jen and Dr. John Germaine at the Massachusetts Institute of Technology. Thank you for teaching me that “it is what it is” when it comes to soil, for introducing me to the excitement of research, and for overconsolidating me for the rest of my life.

To my friends here in Austin and scattered around the world, I am most appreciative of all the good times, the support, and the invaluable life advice I can always count on.

To my family, I am grateful for your continued support over the course of my life and my studies. The greatest gift of all has been access to an education that has repeatedly taught me the love of learning along with the freedom to make my own mistakes. You each, in your own way, inspire me everyday to work harder and to be smarter in hopes of making tomorrow better.

Abstract

Direct In-Situ Evaluation of Liquefaction Susceptibility

Julia Nicole Roberts, M.S.E.

The University of Texas at Austin, 2014

Supervisor: Kenneth H. Stokoe, II

Earthquake-induced soil liquefaction that occurs within the built environment is responsible for billions of dollars of damage to infrastructure and loss of economic productivity. There is an acute need to accurately predict the risk of soil liquefaction as well as to quantify the effectiveness of soil improvement techniques that are meant to decrease the risk of soil liquefaction. Current methods indirectly measure the risk of soil liquefaction by empirically correlating certain soil characteristics to known instances of surficial evidence of soil liquefaction, but these methods tend to overpredict the risk in sands with silts, to poorly predict instances of soil liquefaction without surface manifestations, and fail to adequately quantify the effectiveness of soil improvement techniques.

Direct in-situ evaluation of liquefaction susceptibility was performed at a single site at the Wildlife Liquefaction Array (WLA) in Imperial Valley, California, in March 2012. The project included a CPT sounding, crosshole testing, and liquefaction testing. The

liquefaction testing involved the measurement of water pressure and ground particle motion under earthquake-simulating cyclic loading conditions. The objective of this testing technique is to observe the relationship between shear strain in the soil and the resulting generation of excess pore water pressure. This fundamental relationship dictates whether or not a soil will liquefy during an earthquake event.

The direct in-situ evaluation of liquefaction susceptibility approach provides a more accurate and comprehensive analysis of the risks of soil liquefaction. It also has the ability to test large-scale soil improvements in-situ, providing researchers an accurate representation of how the improved soil will perform during a real earthquake event. The most important results in this thesis include the identification of the cyclic threshold strain around 0.02% for the WLA sand, which is very similar to results achieved by other researchers (Vucetic and Dobry, 1986, and Cox, 2006) and is a characteristic of liquefiable soils. Another key characteristic is the 440 to 480 ft/sec (134 to 146 m/s) shear wave velocity of the soil, which are well below the upper limit 656 ft/sec (200 m/s) and an indication that the soil is loose enough for soil liquefaction to occur. The third significant point is that the compression wave velocity of the sand is greater than 4,500 ft/sec (1,370 m/s), indicating that it is at least 99.9% saturated and capable of generating large pore water pressure due to cyclic loading. These three conditions (cyclic threshold strain, shear wave velocity, and compression wave velocity) are among the most important parameters for characterizing a soil liquefaction risk and must all be met in order for soil liquefaction to occur.

Table of Contents

List of Tables

List of Figures

Chapter 1 – Introduction

1.1 Introduction

During the 2010 Canterbury earthquake in New Zealand, almost two-thirds of all homes in the Christchurch area were damaged by soil liquefaction with the earthquake's total estimated cost to be $1.5 billion. Unfortunately, the amount of liquefaction caused by the subsequent 2011 Christchurch earthquake in the same area was orders of magnitude larger, as was the damage: 185 people died, 5,000 homes are marked for demolition, and costs are estimated to exceed $30 billion (McSaveney 2013). This grim scenario illustrates a lapse in the effective use and transfer of earthquake engineering knowledge to practical solutions, particularly since New Zealand's earthquake building codes are among the most advanced in the world. Of course, recent large earthquakes in places like Japan (2011 Tohoku) and Haiti (2010 Haiti) also caused widespread devastation, but those in the Christchurch area are particularly acute lessons in the potential for damage was caused by extensive soil liquefaction.

Soil liquefaction occurs in saturated granular soils with relatively high permeability such as sandy or gravelly soils. The phenomenon causes total loss of soil strength, resulting in landslides and foundation collapses. Mechanically, a rapid increase in ground water pressure from the shaking causes an upward pressure on the soil. Since granular soils derive their strength from the net vertical stress in the downward direction, an increase in water pressure immediately causes a decrease in soil strength. This loss in

strength is manifested in landslides and severe, uneven settlements that can cause the collapse of highways, bridges, and buildings.

Current methods for characterizing liquefaction potential include indirect methods and empirical correlations, which provide accurate results for clean, loose sands (Youd et al, 2001). Unfortunately, the majority of soil types involved in liquefaction include gravels, partially cemented soils, cobbles, tailings, silty sands, and even granular soils with a little plasticity. Currently, characterization of the liquefaction potential of these soils ranges from use of engineering judgment to inappropriate generalizations. Additionally, once liquefaction-susceptible soils are identified, remediation techniques promise to reduce the risk of liquefaction, but the ability for validation prior to an earthquake is essentially non-existent. With these challenges in mind, development of the direct test for in-situ evaluation of liquefaction characteristics represents a major breakthrough in liquefaction studies and will directly lead to significant gains in knowledge, developments of new models, and advances in remediation techniques.

1.2 PROJECT SCOPE

As noted in the previous paragraphs, there is a demonstrated need to identify soil deposits that are at risk for soil liquefaction prior to earthquakes that may trigger them to devastating effect. As such, the main objectives of this project were to continue the refinement of the direct, in-situ liquefaction testing technique and to successfully determine the liquefaction susceptibility of the in situ soil at the Wildlife Liquefaction Array in Imperial Valley, California.

The testing technique described in this thesis is actually a comprehensive study including the use of a seismic crosshole test and a staged liquefaction test. The staged liquefaction test simulates earthquake loading conditions directly in the in situ soil, which is instrumented with 3-D velocity transducers and a pore pressure transducer to capture the behavior that directly causes the triggering of soil liquefaction. The simulated earthquake loading conditions are achieved by shaking from a large vibroseis; each loading stage (repetition) consists of dynamic loading for any given number of cycles at a single force level that ranges from 3,000 lbs (13.3 kN) to 30,000 lbs (133 kN) over the course of the test.

Data collected from both tests includes soil particle motion recorded by 3-D velocity transducers (for both the crosshole test and the staged liquefaction test) and pore water pressure measurements recorded by a pore pressure transducer (for the staged liquefaction test). This data forms the foundation of the analysis, allowing the determination of P-wave and S-wave velocities in the in situ soil, the evaluation of shear strain induced in the soil by shaking during the staged liquefaction test, and the calculation of residual pore water pressure ratios.

Characterizing the increase in water pressure as a function of large cyclic shear strain is perhaps the most important accomplished goal as that relationship ultimately determines if a soil liquefies or not. This liquefaction test will fundamentally impact how liquefaction research is approached by enabling direct evaluation of liquefaction susceptibility and soil remediation performance in ways that other techniques cannot. Corollaries of this research include the ability to test soils that are impossible to

characterize using indirect methods and to evaluate remediation techniques prior to earthquakes for performance reliability

1.3 ORGANIZATION OF THESIS

This thesis is organized to provide the reader a comprehensive review of the completed research project. The following is a short synopsis of each of the remaining seven chapters and appendix.

In Chapter 2, a variety of publications are reviewed to provide background into the topics covered in this thesis. These publications cover the current state of liquefaction testing techniques, the previous generation of direct, in-situ liquefaction testing, past research at the Wildlife Liquefaction Array in Imperial Valley, California, methods for calculating in situ shear strain, and soil liquefaction research in the laboratory.

In Chapter 3, information regarding the field site and the field test equipment is presented. The field site description includes a review of its geology and earthquake history as well as some of the previous research studies that were performed there. The section on field-testing equipment describes the unique equipment used for the project and the fabrication of the 3-D velocity transducers.

In Chapter 4, the specifics of the liquefaction testing procedures are detailed. This first includes an overview of the instrumented array and the sensor installation process. Second, the details of performing the seismic crosshole test and staged liquefaction test are explained. Finally, the conclusion of the test is included for the details regarding the removal of sensors and cleanup of the site.

In Chapter 5, the results from the seismic crosshole test are presented. The first section explains the configuration of the instrumented array as it relates to the crosshole test. The results and discussion of the results from the crosshole test follow in the remaining portion of the chapter.

In Chapter 6, the data reduction procedures for evaluating shear strain and pore pressure are explained. These procedures detail the process of converting the data from raw voltage signals to signals in relevant engineering units and signal processing to remove noise and undesired frequencies for a variety of purposes. Additionally, the methods for calculating shear strain, obtaining average peak shear strain values, evaluating the degradation of shear wave velocity during pore pressure generation, and determining the residual excess pore water pressure ratio are each discussed in depth.

In Chapter 7, the results from the staged liquefaction test are presented and discussed. First, the performance of T-Rex is analyzed by looking at the baseplate displacement and force output as a function of frequency and the resulting shear strain. After understanding the performance of T-Rex, the soil response due to shaking is analyzed by looking primarily at the relationship between shear strain and the generation of excess pore water pressure.

In Chapter 8, the thesis is brought to a conclusion. The first section effectively reviews the content of the thesis and emphasizes some of the key findings along the way. Important conclusions ascertain through the results of testing are also summarized and briefly discussed. Finally, the chapter concludes by suggesting improvements to the testing technique for future projects.

Appendix A contains shear strain and pore pressure ratio time series from each of the loading stages (repetitions) from the staged liquefaction testing.

Chapter 2 – Literature Review

2.1 INTRODUCTION

The review of relevant research literature is important for establishing a baseline of knowledge from which new research can extend. In this chapter, five publications are summarized for the purpose of understanding the evolution of soil liquefaction testing techniques, the development of new analysis procedures, and the current state of soil liquefaction knowledge. Each publication was chosen for its particular expertise in different areas of soil liquefaction research, together providing a comprehensive review of the subject.

2.2 SUMMARY OF LIQUEFACTION FIELD-TESTING TECHNIQUES

In 2001, a summary report authored by twenty-one contributors laid out the known testing and analysis methods for predicting the earthquake-induced liquefaction susceptibility of in-situ soils (Youd et al, 2001). The authors are acknowledged leaders in the field of geotechnical earthquake engineering research and their collaboration on this publication stems from two workshops on the subject of evaluating the liquefaction resistance of soils. The objectives of the workshop and the report were to standardize some liquefaction testing and data analysis procedures as well as to reach a consensus on soil behavior models given the prior experience of each of the contributors. As such, this report is important because of its comprehensive look at the cutting edge soil liquefaction

research techniques available at the time, which are all precursors to the direct, in-situ soil liquefaction test described in this thesis.

At the time of the publication in 2001, there existed four field methods for evaluating the potential for earthquake-induced liquefaction in granular soils, all of which are indirect. The testing methods include the standard penetration test (SPT), the cone penetration test (CPT), the Becker penetration test (BPT), and shear wave velocity (V_s) measurements. The results from each method generally indicate the stiffness or strength of the soil, each of which certainly plays a role in determining the liquefaction-susceptibility of a soil but is not the only controlling factor. The models derived from the test-obtained data are verified by comparison against visually confirmed instances of soil liquefaction at specific sites for approximately magnitude 7.5 earthquakes, though scaling factors can be applied to adjust the models for earthquake magnitudes ranging from 5.5 to 8.5. A correction factor for earthquake magnitude is presented in Figure 1. The baseline of these soil liquefaction susceptibility models is also applicable only for clean sands (no fines content), but there exist corrections that can be applied for varying percentages of fines content.

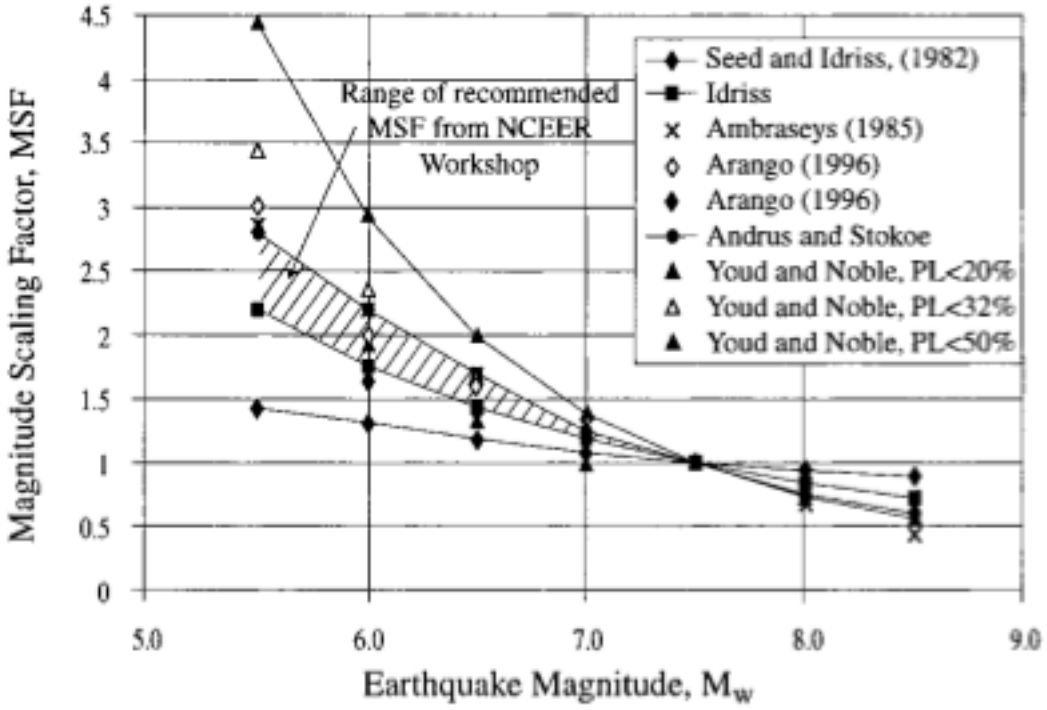

Figure 1. Magnitude Scaling Factors suggested by different researchers to adjust the soil liquefaction susceptibility models for earthquake magnitudes other than 7.5 (from Youd and Noble, 1997)

The first and most common method outlined in the report is the standard penetration test (SPT), which is preferred by many engineers because it is relatively quick, inexpensive, and the equipment is readily available. As a result, there is a large repository of SPT-collected data to reference. SPTs are good because not only are they indicative of strength of the soil through a blow count, but they also allow disturbed soil samples to be taken from depth for further analyses. Among the limitations of the test are: (1) the inability to test large grained materials such as gravels, (2) very localized large-strain deformations with loading conditions dissimilar to earthquake conditions, and (3) the lack of pore water pressure measurements. Figure 2 shows SPT Sand Based

Curves with supporting data for magnitude 7.5 earthquakes. The fines content in the sands for the SPT Sand Based Curves range from 0% to 35%. The corrected blow count, $(N_1)_{60}$, is normalized to a 1 ton/ft^2 (100 kPa) overburden pressure and a 60% hammer energy efficiency.

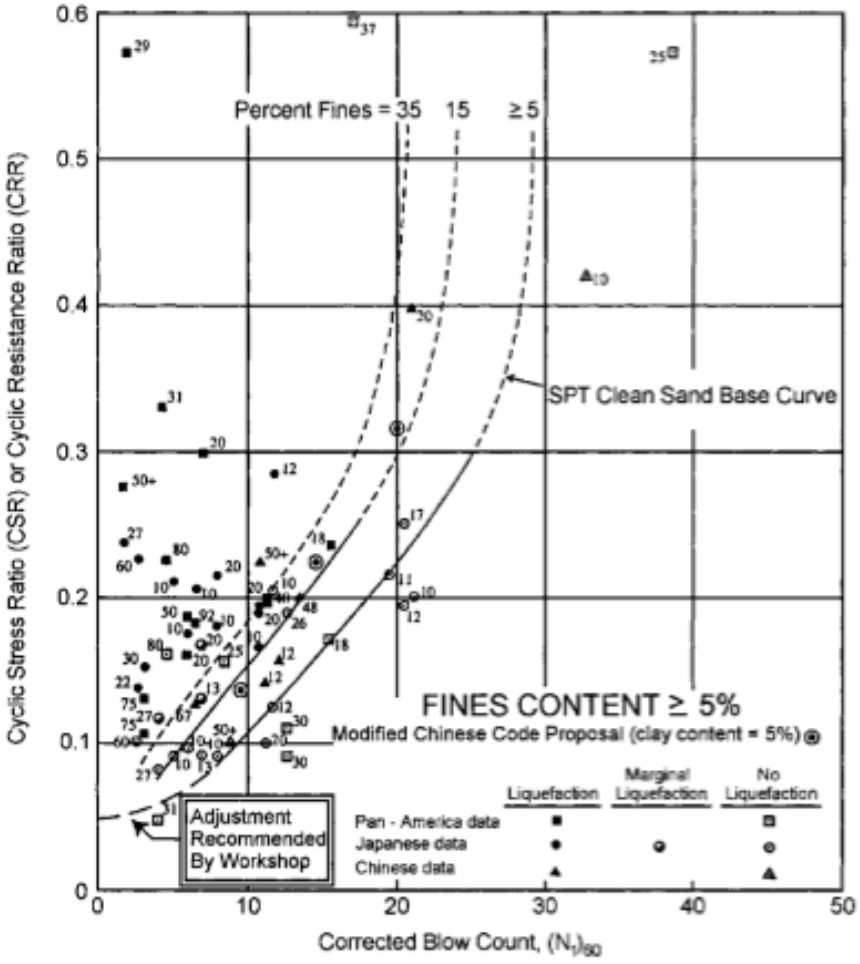

Figure 2. SPT Sand Base Curves for sands with fines contents ranging from 0% to 35%. These curves are applicable for 7.5 Magnitude earthquakes (from Seed et al, 1985).

The CPT is a more intricate testing technique than the SPT and it offers higher quality results. Unlike the SPT, the CPT is not operator dependent, meaning the results of the test should be the same regardless of the equipment and personnel used to obtain them. Additional advantages the CPT has over the SPT are: (1) the measurement of pore water pressure, (2) continuous measurements over a depth of interest, and (3) the estimation of fines content based on the ratio between the end bearing forces and side sleeve forces. Unlike the SPT, however, it cannot retrieve a soil sample from depth. As with the limitations of the SPT, the CPT cannot test gravels and its testing procedure relies on very localized large strain deformation with loading conditions dissimilar to earthquake conditions. Figure 3 presents the CPT Clean Sand Based Curve with supporting data for magnitude 7.5 earthquakes. The fines content for the sands in this model is less than 5%.

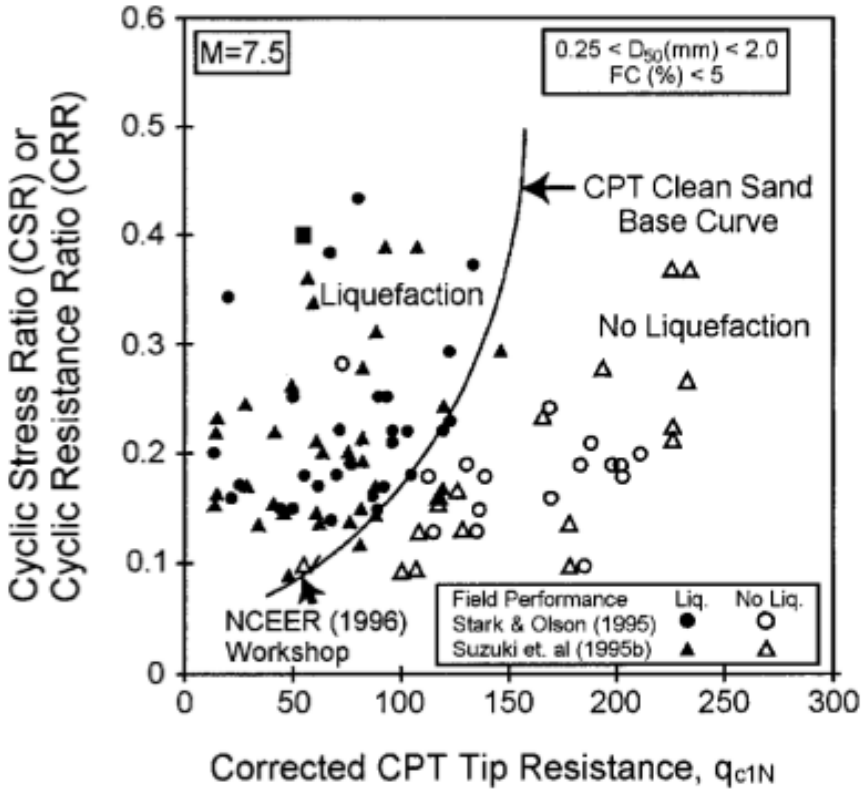

Figure 3. CPT Clean Sand Base Curve applicable for 7.5 magnitude earthquakes (from Robertson and Wride, 1998)

For gravel and cobbles that are not testable by the SPT and CPT, the BPT has been developed specifically for these hard to test soils. The application of the BPT for soil liquefaction susceptibility studies has been much more limited than that of SPT or CPT and as a result there is not much available data. At the time of the report's publication in 2001, results from BPTs were evaluated by converting the blow counts into equivalent SPT values and then commencing the evaluation of liquefaction susceptibility, which is not an ideal procedure because of the uncertainty inherent in adding a calculation based on equivalency. Other than its ability to test soils with gravels and

cobbles, this testing technique has not been able to contribute significantly to soil liquefaction research in general because it has not been utilized extensively and it also produces very localized large-strain deformations with loading conditions dissimilar to earthquake conditions.

The fourth testing method discussed in the report is the use of shear wave velocities. Shear wave velocities are a direct measure in the small-strain shear stiffness of soil and can be correlated to soil liquefaction susceptibility in the same way as the STP and CPT methods. In general, the database of measured in-situ soil shear wave velocities is not nearly as extensive as those of SPTs and CPTs, so the verification of liquefaction susceptibility models is less robust. Also, because shear wave velocities are measured at small strains, they still represent a correlation to liquefaction triggering since earthquakes that trigger liquefaction create strains several orders of magnitude larger. The advantages of using shear wave velocity testing techniques is that is can be employed in any soil type and that its measurement represents a soil property over a less localized region than SPTs and CPTs. Figure 4 presents the V_s Sand Based Curves with supporting data from assembled case histories. These curves are applicable for 7.5 magnitude earthquakes, but the note in the top left corner indicates scaling factors for other magnitudes. The fines contents in the sands for this model range from 0% to greater than 35%.

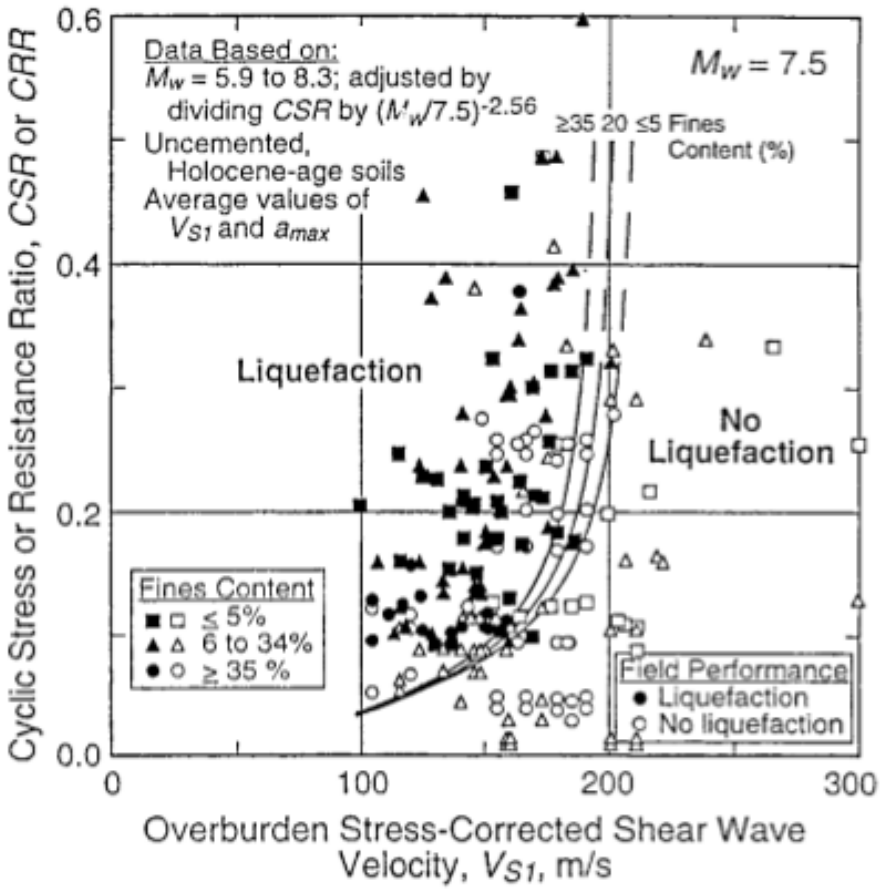

Figure 4. V_s Sand Based Curves for magnitude 7.5 earthquakes and fines contents ranging from 0% to greater than 35% (from Andrus and Stokoe, 2000).

At the time of the publication by Youd et al, 2001, these four testing methods represented the best techniques available to researchers to develop soil liquefaction susceptibility models based on data derived from in-situ field tests. While a lot of experience exists with SPTs and CPTs in particular, the overall ability of the models to predict earthquake-induced soil liquefaction was hampered by the indirectness of the testing methods. There is much more information in this report regarding the modification of liquefaction susceptibility models for different earthquake events and the

fines content of soils as well as the determination of the cyclic stress ratio and cyclic resistance ratio, but for the main points relevant to this thesis are contained in the discussion of testing methods. It is particularly relevant because the direct, in-situ liquefaction test described in this thesis was developed to overcome the limitations of the four previous testing techniques.

2.3 DIRECT IN SITU LIQUEFACTION TESTING

Direct in situ liquefaction testing was pioneered and continues to be developed at The University of Texas at Austin (Chang, 2002, and Cox, 2006). For his doctoral research, Dr. Cox advanced the capabilities of the soil liquefaction research by developing the second generation of the liquefaction test. Since the liquefaction test presented in this thesis is only a slight modification of Dr. Cox's version, Cox, 2006 provides invaluable information and guidance.

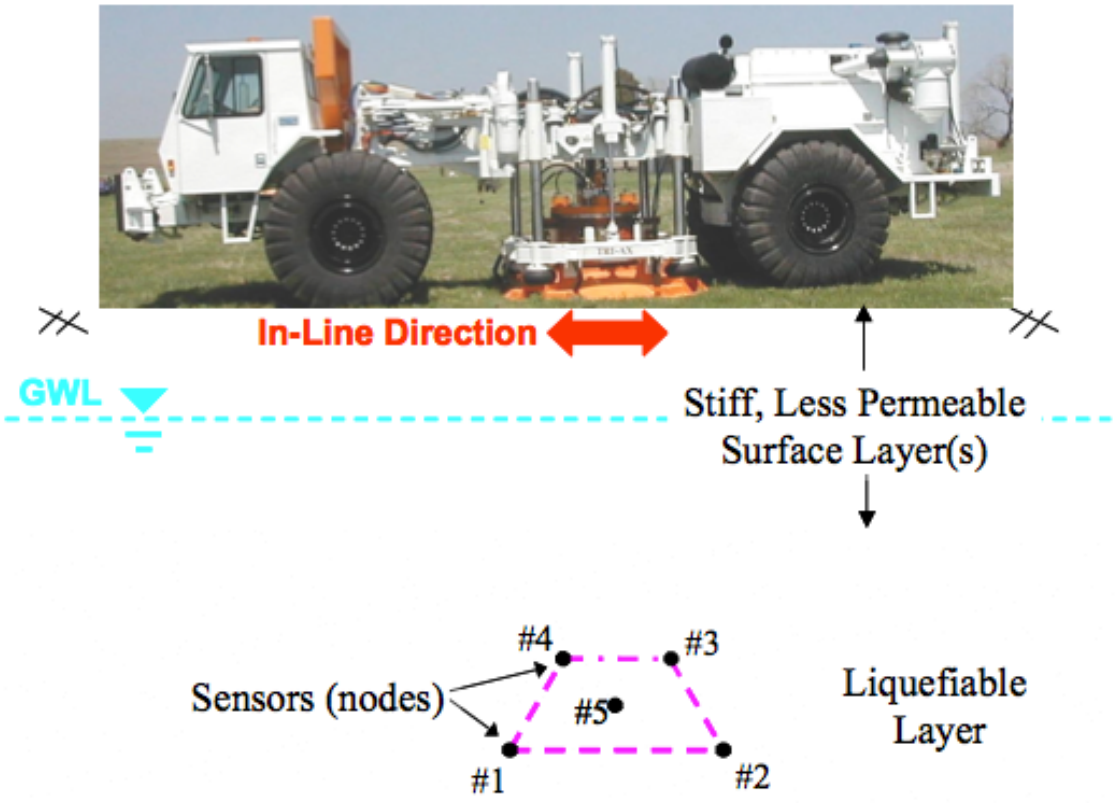

Figure 5. General test configuration for direct, in situ liquefaction testing performed by Cox, 2006 in Imperial Valley, California at the Wildlife Liquefaction Array (from Cox, 2006).

The liquefaction test is performed by shaking the ground surface with a large vibroseis in a staged loading sequence; the shaking at each loading stage (repetition) has a specific frequency, loading force, and number of cycles, all of which are meant to simulate downward propagating earthquake motions. The response of the in situ soil is simultaneously recorded by instruments embedded below the loading platen of the vibroseis. The test configuration in Figure 5 shows the relative location of the vibroseis to the five installed sensors. Sensors marked #1 through #4 are liquefaction sensors that

each contain a Micro-Electrical Mechanical Systems (MEMS) accelerometer and a miniature pore pressure transducer (see Figure 6). The sensor marker #5 in the center of the instrumented array is a pore pressure transducer that is larger and more stable than the mini pore pressure transducers in the liquefaction sensors (see Figure 7). The sensors were embedded in the same vertical plane at depths varying from approximately 10 to 12 ft (3 to 3.7 m) or 11 to 13 ft (3.4 to 4 m) below the ground surface, depending on the site.

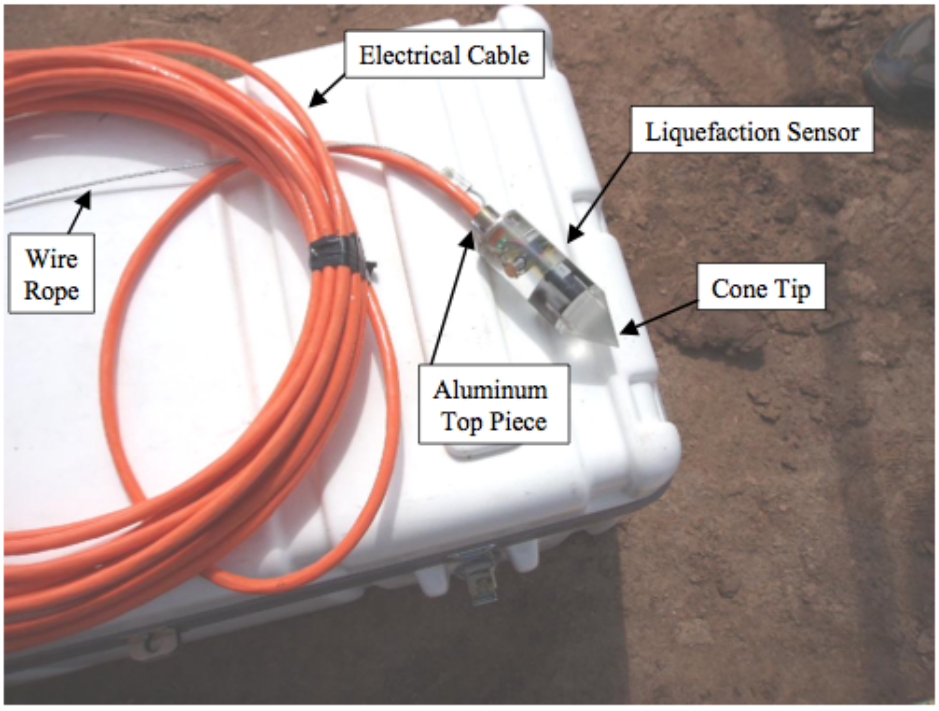

Figure 6. Liquefaction sensor used in liquefaction test by Cox, 2006. The liquefaction sensor includes a MEMS accelerometer and a miniature pore pressure transducer (from Cox, 2006).

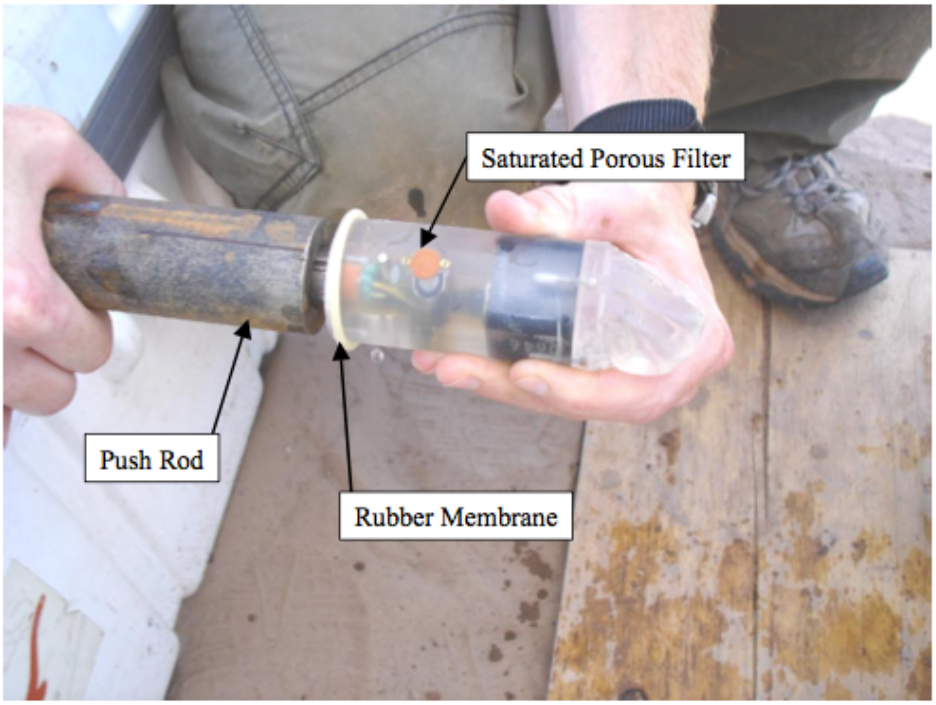

Figure 7. Pore pressure transducer used in liquefaction testing by Cox, 2006. The pore pressure transducer has been prepared for imminent installation (from Cox, 2006).

The actual field testing described in Cox, 2006, was performed at the Wildlife Liquefaction Array in Imperial Valley, California. The WLA is managed by the Network for Earthquake Engineering Simulation (NEES) Equipment Site at the University of California, Santa Barbara, NEES@UCSB. Three different locations at the WLA were tested. The general geology at the site includes approximately 8 ft (2.4 m) of clayey silt underlain by silty sand. Figure 8 shows a general soil profile for the WLA site with instrumentation installed soon after the 1981 Westmoreland Earthquake by USGS personnel.

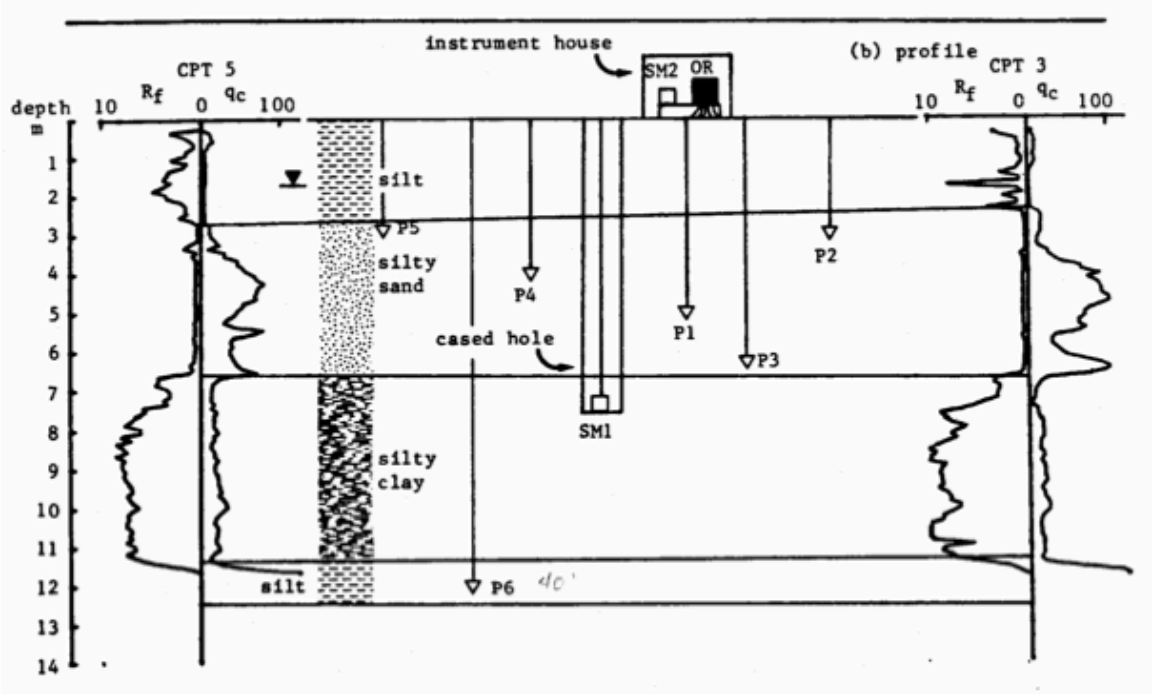

Figure 8. Cross section of the WLA site in Imperial Valley, California, showing representative soil geology near the site tested by Cox, 2006 (from Cox, 2006).

The 8-ft (2.4-m) top layer acts as a relatively impermeable cap over the liquefiable silty sand layer. The practical significance of this specific geology is that the silty sand layer can be repeatedly liquefied with little or no change in conditions at the top of the layer following soil liquefaction due to the re-sedimentation of the silty sand. The relatively impermeable cap prevents the pore water from seeping through it to reach the free ground surface, which prevents the upper portion of the liquefiable layer from becoming denser.

In addition to serving as a guideline for performing the test, Dr. Cox's dissertation also serves as the preeminent source of knowledge regarding the analysis of data derived

from a direct, in-situ soil liquefaction test. Among the objectives of the research was to evaluate shear strain in the soil during shaking and the build up of the residual excess pore water pressure. To this end, some of the results from the three locations at the WLA tested in Cox, 2006, are presented in terms of cyclic shear strain and pore water pressure ratio. The two plots in Figure 9 show example time records for the evaluated shear strain and the measure pore water pressure corresponding to a single loading stage (repetition) during liquefaction testing. The results in Figure 10 show the relationship between the pore pressure ratio and shear strain that was developed for the sand specimen at Site C (one of the three sites tested by Cox, 2006) of the WLA. These examples and their references are particularly important to understand because the evaluations performed in this thesis are based on those found in Cox, 2006.

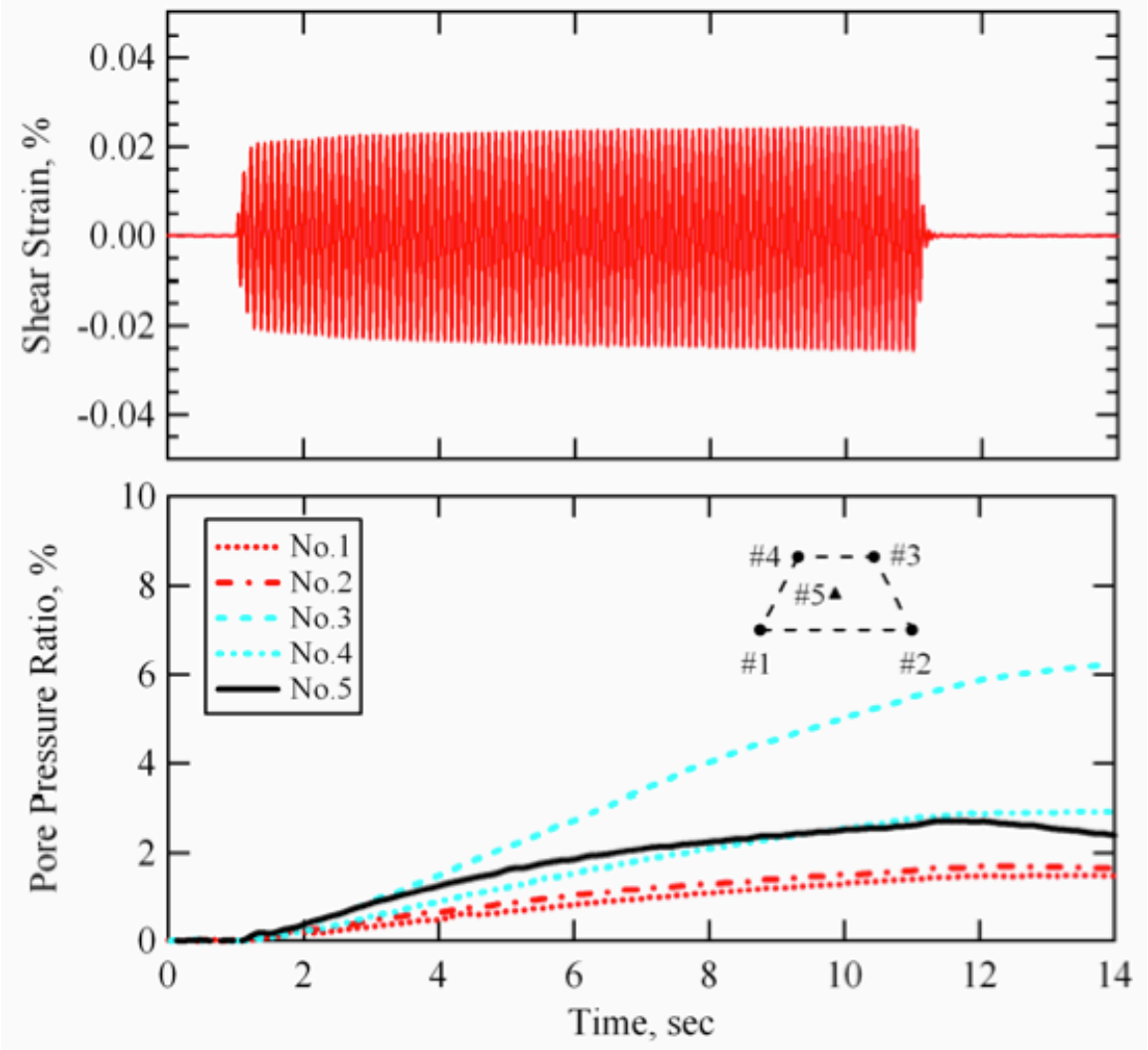

Figure 9. Evaluated shear strain and measured pore pressure ratio times series for a single loading stage during liquefaction testing by Cox, 2006 (from Cox, 2006).

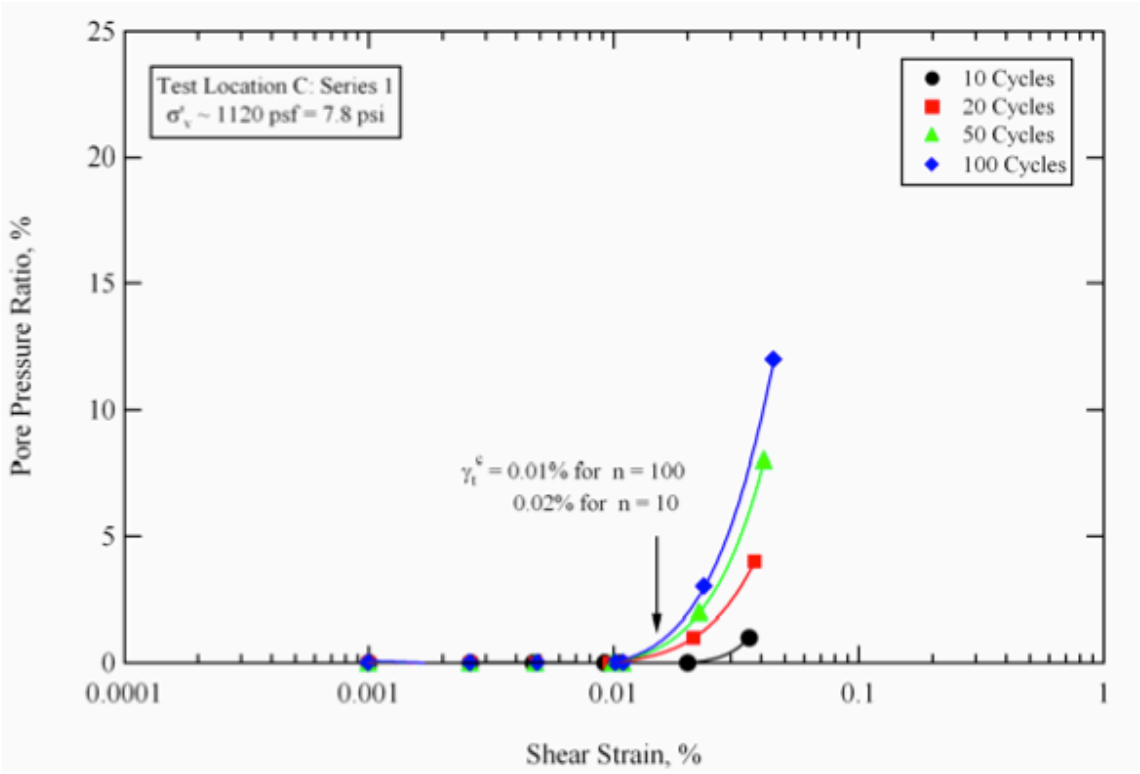

Figure 10. Pore pressure ratio versus shear strain for varying numbers of cycles. This data comes from liquefaction testing at Site C by Cox, 2006 (from Cox, 2006).

The work by Dr. Cox on in situ soil liquefaction testing has broken significant ground in the field of earthquake engineering, paving the way for a more comprehensive understanding of soil behavior in complex loading conditions. Some of his suggestions for future improvements in the testing technique are incorporated into the newest generation of liquefaction testing equipment, efficiently enabling the continued evolution of the technique.

2.4 LIQUEFACTION RESEARCH AT WILDLIFE LIQUEFACTION ARRAY

Early liquefaction research at the WLA in Imperial Valley provide a solid foundation for current projects. In Holzer and Youd, 2007, the authors take a second look at the data recorded during the 1987 Superstition Hills Earthquake. In the original equipment setup, six piezometers were permanently installed at depths varying between 2.9 and 6.6 meters (9.5 and 21.7 ft). Other instrumentation includes surface and downhole accelerometers to measure ground shaking. While the functionality of some of the piezometers has been questioned, there seems to be enough quality data to observe interesting trends in the soil behavior.

The earthquake of interest in this case, the 1987 Superstition Hills Earthquake, included a 6.6 magnitude mainshock preceded by a 6.2 magnitude foreshock. Soil liquefaction was observed only during the mainshock, as indicated by the formation of sand boils and soil cracks at the instrumented site. Further proof of soil liquefaction is offered by the significant increase in pore water pressure as recorded by several of the pore pressure transducers. Even discounting the quality of measurements from all of the pore pressure transducers, except one that was later accepted as fully functioning, the results indicate a pore pressure ratio of 100% was achieved as a result of the earthquake.

A closer look at the data provided by the single, functioning pore pressure transducer is warranted because of the interesting conclusions it suggests (see Figure 11). For this study, the pore pressure ratio is defined as the ratio between the recorded pore water pressure values and the value of pore water pressure at 97 seconds after ground

shaking commenced. The value of pore water pressure at this point seems to correspond to the maximum level of generated pore water pressure.

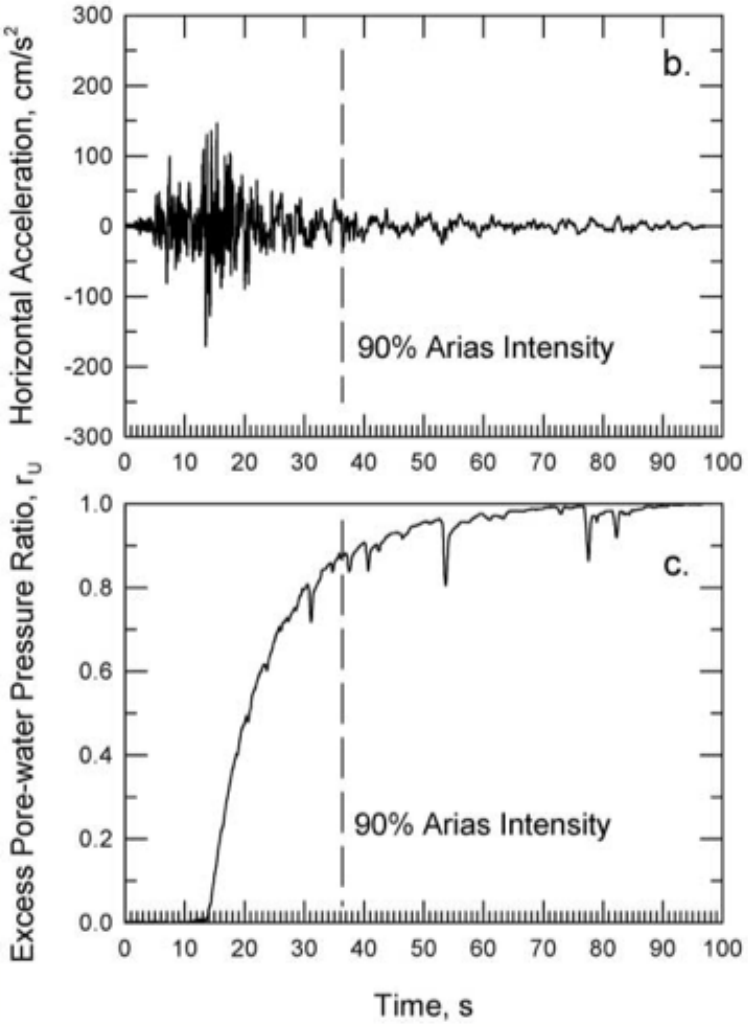

Figure 11. Recorded horizontal acceleration and excess pore water pressure ratio time series from the 1987 Superstition Hills Earthquake (from Holzer and Youd, 2007).

In looking at the pore water pressure records, it is interesting to note the behavior of the pore water pressure and how it increases with respect to the ground shaking. The

pore water pressure continues to increase even after much of the ground acceleration has ceased (as defined by 90% Arias Intensity and shown in Figure 11). The authors conclude that the presence of long period (~5.5 seconds) Love waves generating large cyclic strain (~1.5%) are responsible for the approximately 13% of the additional pore water pressure increase that continues after the high-frequency ground accelerations have passed. Critics of the research mostly discount the quality of data recorded by the pore pressure transducers, alleging they were likely not properly saturated immediately prior to capturing the data of interest. This phenomenon of continued generation of excess pore water pressure once strong ground motion shaking has ceased is not well explained and has not previously been given much merit. Until the phenomenon can be fully discounted or explained, it will continue to be a point of interest in soil liquefaction research.

2.5 METHODS OF CALCULATING IN SITU SHEAR STRAIN

Of particular interest during the literature review is to study different methods employed by researchers to calculate shear strain in the soil during direct, in-situ liquefaction testing with T-Rex. Generally speaking, there are two approaches to studying the triggering of liquefaction: the stress-based approach and the strain-based approach. The analysis of data collected during direct, in-situ liquefaction test is well suited to the strain-based approach, which is also the preferred approach. In the past decade, researchers have focused on several different methods for calculating shear strain from other directly measured quantities such as soil particle velocity or acceleration.

Types of calculations include two- or three-dimensional analyses for displacement-based and wave propagation-based methods.

Four methods of calculating in-situ soil strain are comprehensively described and compared in Rathje et al, 2004. The rise of in situ testing within earthquake engineering research has created a demand for more robust soil-strain evaluation techniques, and this paper evaluates the application of these techniques for soil. Studying strain in soil can be more complicated than in other materials because of the extreme inhomogeneity and nonlinearity found in soil on both the micro and macroscopic levels as well as the difficulty in accurately measuring particle motion. Soil with a high risk of liquefaction is also likely to experience significant losses in strength when large strains are generated, further complicating the pattern of response. It should be noted, however, that the triggering of liquefaction is a moderate strain phenomenon, often occurring around a shear strain value of 0.1%.

Keeping in mind the challenges regarding accurate evaluation of strain levels, the four methods present a robust effort to quantify strain. The range of strains analyzed represents both the small strain and larger strain components of soil strain behavior (0.0005% to 0.1%), which is important because soil response varies considerably within that range. The data for the strain evaluation comparisons were gleaned from an in-situ liquefaction experiment performed expressly for this purpose.

In the experiment, five sensors were embedded in a 4 ft by 4 ft by 4 ft (1.2 m by 1.2 m by 1.2 m) test pit while it was backfilled to create the reconstituted specimen; each

sensor was outfitted with two geophones (one oriented horizontally inline and one oriented vertically) and a pore pressure transducer. The sensors measured soil particle velocity and variations in pore water pressure within the soil during testing. The testing was performed by using a vertically vibrating vibroseis to cyclically load the test pit in a series of staged loadings. The vibroseis was horizontally offset from the test pit by 10.8 ft (3.3 meters) so that the main wave energy propagating through the test pit were Rayleigh waves. Figure 12 presents the general test configuration, showing the relative locations of the vibroseis, sensors, and test pit.

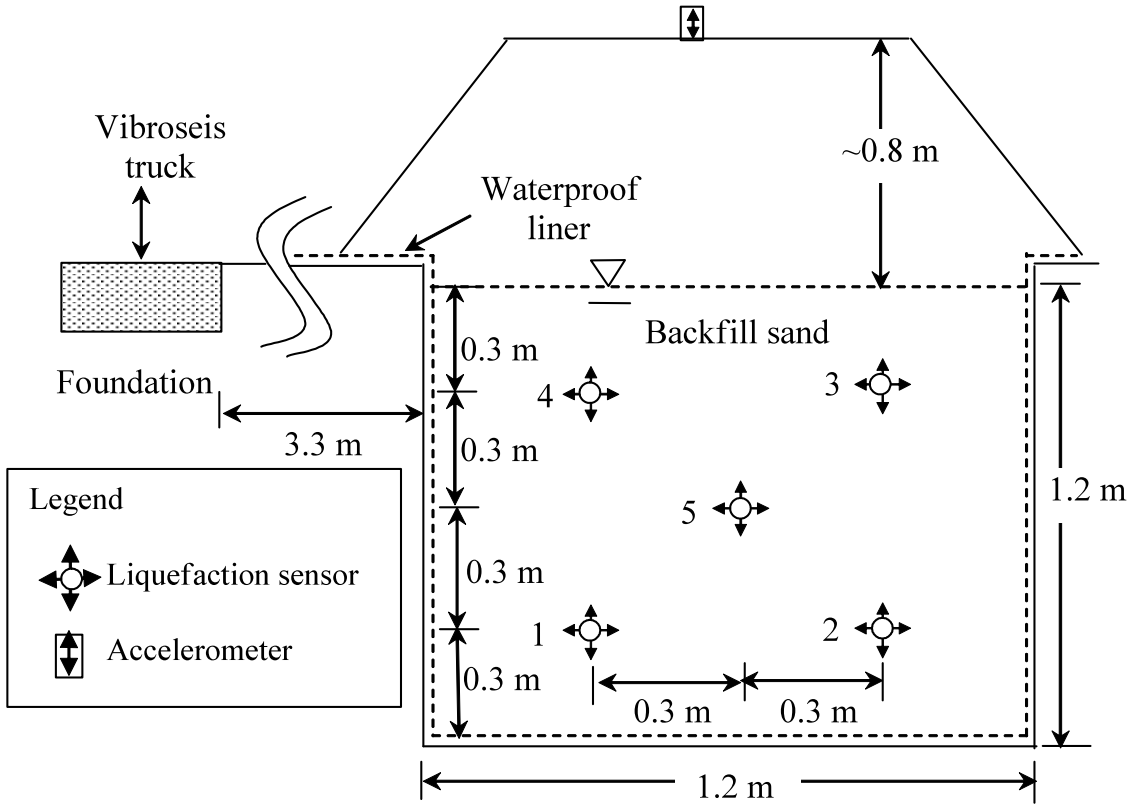

Figure 12. Schematic of test setup for the first generation direct, in-situ liquefaction evaluation test performed for the purpose of comparing shear strain evaluation methods in Rathje et al, 2004 (from Rathje et al, 2004)

The testing protocol involved staged testing at increasing levels of shaking force amplitude at a set frequency and number of cycles. The test began with the smallest shaking force amplitude and the amplitude level was gradually increased over the course of the test. The shaking was driven by a 20-Hz sinusoidal signal for 20 cycles. Thirty minutes of rest followed each loading stage at higher force levels to ensure total dissipation of excess pore pressure within the test setup prior to commencing the next repetition. The data recorded from this liquefaction test forms the data set from which the shear strain evaluation methods presented in the rest of the paper are based on.

2.5.1 Displacement-based strain

The experiment produced velocity recordings for soil particle motion at each of the five in-plane locations in the test setup. In the first strain calculation method, the displacement-based method, the velocity recordings were integrated once to obtain particle displacement data for each location. In this case, the four-node square formed by the position of the embedded sensors was selected to simplify the numerical analysis. The calculation of strain relies on the following basic definitions (Rathje et al, 2004):

$$\varepsilon_i = \frac{\partial u_i}{\partial x_i} \tag{2.1}$$

$$\gamma_{ij} = \frac{\partial u_i}{\partial x_j} + \frac{\partial u_j}{\partial x_i} \tag{2.2}$$

In this context, ε represents normal strain while γ represents shear strain. The partial derivatives are applied to u with respect to x where u is displacement and x the direction. The subscripts i and j represent the two out of three possible orthogonal dimensions that are used for calculating the two-dimensional strain. In the case of normal strain, the derivative of displacement with respect to direction is along the same axis. Shear strain, on the other hand, is the combination of partial derivatives of displacement along one axis with respect to direction along a perpendicular axis.

While more complex models exist, only two-dimensional shear strain is considered for this method of strain calculation. Using finite element analysis to evaluate shear strain, the displacement data from each node of the four-node isoparametric

element is converted from the local coordinate system to a global coordinate system. Partial differentiation of the displacements with respect to direction is then performed according to the above equation, yielding values for shear strain. This analysis provides values for strain at any location within the 4-node element based on the assumption that strain between those nodes varies linearly.

Conversion of displacement values from local coordinates to global coordinates (Rathje et al, 2004) gives:

$$u_x(x,z) = \frac{1}{4}\Big[u_{x1}(1-x/a)(1-z/b) + u_{x2}(1+x/a)(1-z/b) + \\ + u_{x3}(1+x/a)(1+z/b) + u_{x4}(1-x/a)(1+z/b)\Big] \tag{2.3}$$

$$u_z(x,z) = \frac{1}{4}\Big[u_{z1}(1-x/a)(1-z/b) + u_{z2}(1+x/a)(1-z/b) + \\ + u_{z3}(1+x/a)(1+z/b) + u_{z4}(1-x/a)(1+z/b)\Big] \tag{2.4}$$

Calculation of shear strain from displacement (Rathje et al, 2004):

$$\gamma_{xz}(x,z) = \frac{1}{4}\left[-\frac{u_{x1}}{b}(1-x/a) - \frac{u_{z1}}{a}(1-z/b) - \frac{u_{x2}}{b}(1+x/a) + \frac{u_{z2}}{a}(1-z/b) \right. \\ \left. + \frac{u_{x3}}{b}(1+x/a) + \frac{u_{z3}}{a}(1+z/b) + \frac{u_{x4}}{b}(1-x/a) - \frac{u_{z4}}{a}(1+z/b)\right] \tag{2.5}$$

2.5.2 Wave propagation-based strain: Plane shear waves

The first and simplest wave propagation-based strain calculation is referred to as plane shear wave, or PSW, analysis. This analysis is based on the assumption that the propagating stress wave is one-dimensional, meaning that it has a plane wave front moving along a single dimension. The following equation from Richart et al, 1970, is the foundation of wave propagation-based strain calculations, used with modifications depending on the particular wave field as:

$$Strain = \frac{-\dot{u}}{V} \tag{2.6}$$

where is peak particle velocity and V is wave propagation velocity. For the applications in this work, the strain is shear strain since shear waves are assumed (even though Rayleigh waves are the predominate waves generated by the vibroseis in Figure 12), though it can also be used to calculate normal strain. The . represents vertical particle velocity and are measured in the recorded velocity data from the experiment. Wave propagation velocity, V, includes a variety of values for wave propagation velocity depending on the wave field of interest and for the PSW method it is V_s.

Under the particular experiment setup covered in the paper, the one-dimensional stress wave is approximated as horizontally propagating, vertically polarized shear waves. In this scenario, the particle velocity from the vertically-oriented geophone ($\dot{u}_z$) and the shear wave velocity of a horizontally propagating, vertically polarized shear wave ($V_{S,hv}$) are of interest. The above general equation is modified to the following form:

$$\gamma_{xz} = \frac{-\dot{u}_z}{V_{S,hv}} \tag{2.7}$$

While simple to compute, the main concern with this method of strain calculation is the assumption that the wave field propagating through the area of interest is primarily a shear wave. Given the test setup shown in Figure 12, the wave field generated by the vibroseis is more likely to be dominated by Rayleigh waves because surface waves contain 68% of the energy generated from the source and they attenuate more slowly than body waves (Woods, 1968).

2.5.3 Wave propagation-based strain: Plane Rayleigh wave

Following a plane shear wave assumption, the next logical step is to consider a wave field dominated by Rayleigh waves. For an energy source at the surface of the earth, about two-thirds of the energy propagates horizontally away as Rayleigh waves while the remaining one-third is composed of body waves (Woods, 1968). Rayleigh waves are more complex than plane shear waves because particle motion occurs in both the vertical and horizontal directions. To incorporate the added complexity, an additional parameter is included in the calculation. This parameter, α_v, is the shear strain ratio. It is a function of depth relative to wavelength and Poisson's ratio, υ. An example is presented in Figure 13 for $\upsilon = 0.25$.

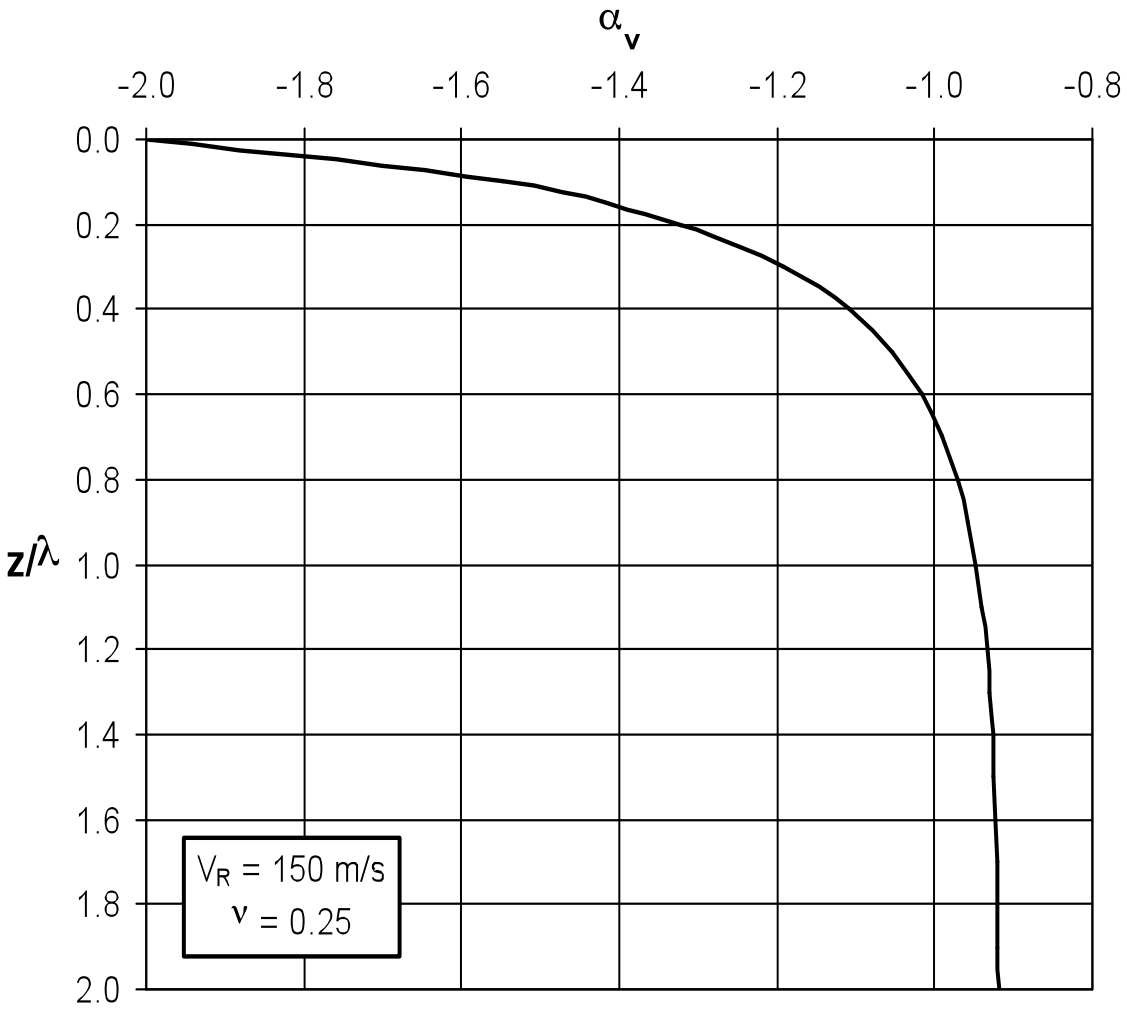

Figure 13. Variation of shear strain ratio (α_v) with depth (from Rathje et al 2004).

The general strain equation is modified for the plane Rayleigh wave (PRW) as:

$$\gamma_{xz} = \frac{\dot{u}_z}{V_R} \cdot \alpha_v \tag{2.8}$$

where shear strain is still represented by γ_{xz} and $\dot{u}_z$ remains vertical particle velocity. The wave propagation velocity is replaced by the Rayleigh wave velocity. The shear strain

ratio also appears in the equation to accommodate the more complex soil motion induced by Rayleigh waves.

Given the simplicity of the inputs, this strain calculation method is relatively easy to perform. In addition, it does not require much more effort than that of the PSW method, but provides a more accurate description of the motion in the soil due to propagating waves. Yet the assumption that only Rayleigh waves are responsible for the recorded ground motion is again too simplistic for the reality of the wave field generated in the test setup.

2.5.4 Wave propagation-based strain: Apparent wave

The fourth and final strain calculation method covered in Rathje et al, 2004 is referred to as apparent wave (AW) method. The AW method attempts to incorporate all wave motions present in the soil into a single analysis. The apparent wave is the combination of the body waves and Rayleigh waves generated from the vibroseis, with no attempt to isolate individual waveforms. The following equation is a form of the general strain equation modified for an AW analysis:

$$\gamma_{xz} = \frac{-\dot{u}_z}{V_{ah}} \tag{2.9}$$

where γ_{xz} is shear strain, $\dot{u}_z$ represents soil particle velocity in the vertical direction, and V_{ah} is the apparent wave velocity of the horizontally propagating wave front. Particularly during large strain shaking for long durations, the V_{ah} will to decrease over the duration

of the test if residual excess pore water pressure is generated; hence, it must be evaluated for degradation. This apparent velocity is determined by calculating the speed at which the wave front travels from one geophone to another geophone when the geophones are at the same depth and positioned parallel to the direction of wave propagation.

The AW method marks a third evolution of the wave propagation-based strain calculation methods. For the test case presented in Figure 12, this method is best suited to evaluate strain in the complex, vibroseis-generated wave field. It incorporates both body and Rayleigh wave fields into a single shear strain evaluation, an outcome that was not achieved by either the PSW or PRW methods.

2.5.5 Comparison of shear strain evaluation methods

In a comparison of each of the shear strain calculation methods, the point at the center of the sensor array was selected for evaluation. While the displacement-based shear strain calculation can be specified for any point within the four node finite element, the wave propagation-based methods produce results corresponding to the location of each sensor. Shear strain at the center of the array was achieved by averaging the shear strain time histories derived from each sensor.

The initial comparison showed that the shear strain values from the PSW and PRW methods consistently overestimated those of the displacement-based shear strain by 40% to 80% while the AW method yielded shear strain values similar to those of the displacement-based method. Further analysis between displacement-based shear strain and AW derived shear strain demonstrated that the two methods produced favorable

results but that AW tended to underestimate by 10% the level of shear strain in the soil for shear strains greater than 10^{-2} %. Figure 14 shows the results of the PSW, PRW, and AW shear strain evaluation methods compared against those from the DB shear strain evaluation method.

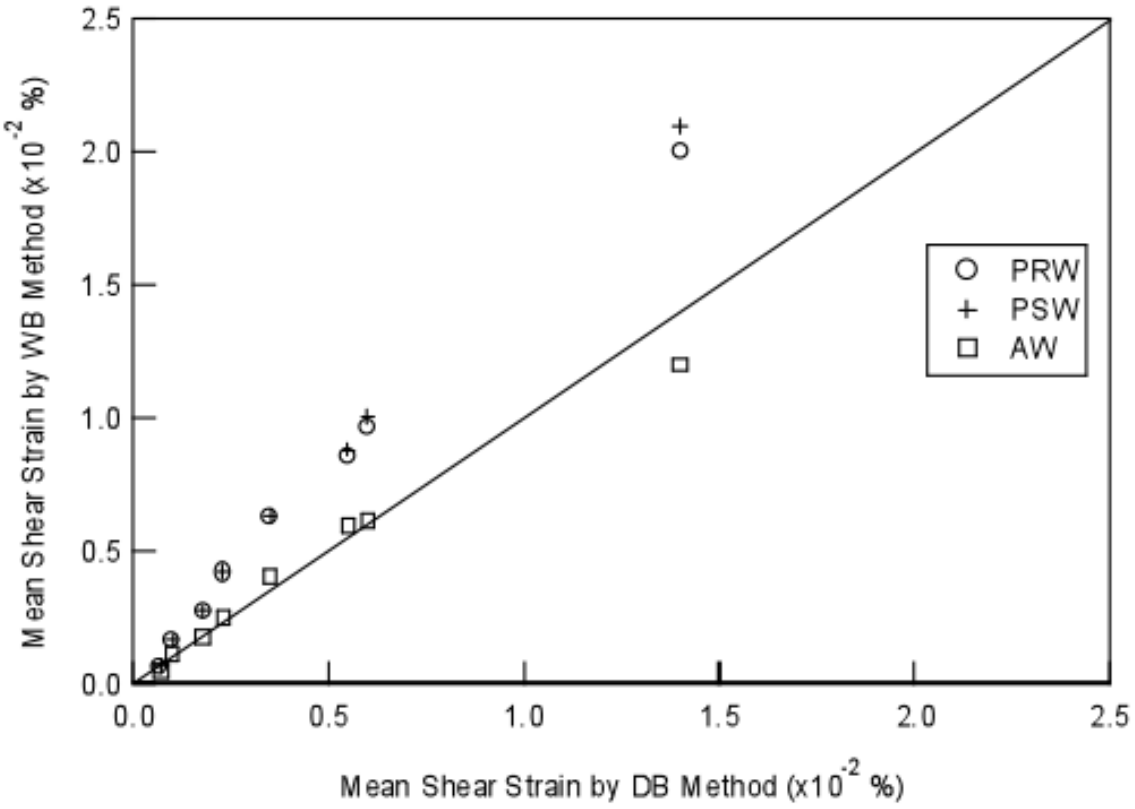

Figure 14. Comparison of Plane Shear Wave (PSW), Plane Rayleigh Wave (PRW), and Apparent Wave (AP) shear strain calculation methods against the Displacement Based (DB) method (from Rathje et al, 2004).

The limitations of AW lie in its reliance on soil particle motion in only the vertical direction while the displacement-based method is able to incorporate both horizontal and vertical particle motion. As discussed previously, the presence of

Rayleigh waves in the wave field indicates a small, yet noticeable, horizontal component to the wave propagation despite the strong vertical motion of the energy source. Additionally, the horizontal movement induced in the velocity sensors would distort the sensor-to-sensor wave velocity calculation, contributing to the error in shear strain evaluation.

Overall, both the AW method and the displacement-based method yielded satisfactory shear strain calculations; yet for the transient tests, the PSW method is a good approximation. The displacement-based method is considered to be more robust than that of the AW, but both should be valid for small strain deformations. It is expected that displacement-based shear strain calculations, however, is more accurate for more complicated loading conditions, like those found in large strain deformation tests, soil liquefaction tests, or tests employing non-sinusoidal loading cycles.

2.6 DOBRY ET AL, 1982 – LABORATORY SOIL LIQUEFACTION RESEARCH

Soil liquefaction research performed in the laboratory in the 1970s and 1980s established the baseline of knowledge that today's direct, in situ evaluation of soil liquefaction seeks to expand. In 1982, the "Prediction of Pore Water Pressure Buildup and Liquefaction of Sands During Earthquakes by the Cyclic Strain Method" was written by R. Dobry, R.S. Ladd, F.Y. Yokel, R.M. Chung, and D. Powell and is an excellent summary of the state of contemporary soil liquefaction research in the laboratory. Each author brings a different expertise to the publication and together they persuasively argue for a paradigm shift in how soil liquefaction research is approached.

The type liquefaction test overviewed in the publication is an undrained cyclic triaxial test performed in the laboratory with reconstituted sand samples. These tests were traditionally run as stress-controlled tests and it was believed that the relative density, D_r, of the soil was the controlling parameter regarding soil liquefaction susceptibility of a soil. In order to closely simulate in situ conditions, sand specimens would be compacted to the relative density of the in situ soil, which was determined from SPTs. The cycling stress (τ_c) for the test was a function of the horizontal peak acceleration at the ground surface (a_p), the acceleration of gravity (g), the total and effective overburden stresses at the depth of interest (σ_o and σ_o'), and the stress reduction factor as a function of depth (r_d):

$$\frac{\tau_c}{\sigma_o'} = 0.65 \frac{a_p}{g} \frac{\sigma_o}{\sigma_o'} r_d \qquad (2.10)$$

While the stress-based test was a reasonable approach for the time, the authors argue that the stress-based test is influenced by soil characteristics other than relative density such as soil fabric, overconsolidation ratio, prior seismic straining, and age effects. A strain-based approach, however, is less influenced by these factors because their effect is generally to either increase or decrease the shear strength of the soil, effects that are effectively captured by the measured shear modulus and intrinsically incorporated into the analysis. The strain-based approach relies less of relative density of the soil, which is difficult to accurately measure in the field, and relies more on the shear

modulus of the soil, which can be accurately measured in the field using small strain measurements.

One of the main goals of this research is to determine the cyclic threshold strain, γ_t, which is the strain at which residual excess pore pressure develops as a result of cyclic straining. This value also delimits the point at which densification of the soil begins, which is the behavioral tendency that induces the development of excess pore water pressure in undrained loading conditions because densification is prevented. The testing program reviewed in this publication involved 12 tests on normally consolidated, reconstituted Monterey No. 0 sand. A wide range of relative densities from 45% to 80% were used in the preparation of the specimen as well as confining pressures ranging from 533 psf (25.5 kPa) to 4,000 psf (190 kPa) for the test setup. During the test, the specimen were loaded at cyclic strains, γ_c, of $3x10^{-2}$ %, $1x10^{-1}$ %, and $3x10^{-1}$ %, all of which are above the cyclic threshold and intended to generate residual excess pore water pressure.

The data collected from this research enabled a number of analyses regarding the behavior of soil as it approaches liquefaction, but the most relevant topics for this thesis are the relationship between γ_c and residual excess pore water pressure as well as the degradation of the shear modulus. The results of the tests show good agreement for the range of relative densities tested and the confining pressures ranging from 533 psf (25.5 kPa) to 2,000 psf (95 kPa), indicating that variation in relative densities can be effectively captured in the strain-based approach and need not be considered the single controlling factor for liquefaction susceptibility of a soil. Figure 15 shows the degradation of shear

modulus with increasing number of cycles for a cyclic strain of 10^{-1} %, which larger than the strain threshold for this soil, for soils specimens of three different relative densities. Figure 16 shows the shear modulus degradation versus shear strain for a specimen with a relative density of 60% after both one cycle of loading and 30 cycles of loading. The final figure, Figure 17, shows the relationship between pore water pressure ratio and shear strain. In particular, it is from this figure that the threshold strain of 10^{-2}% can be identified because that it the point at which the pore water pressure ratio is greater than zero for shear strains greater than the threshold value.

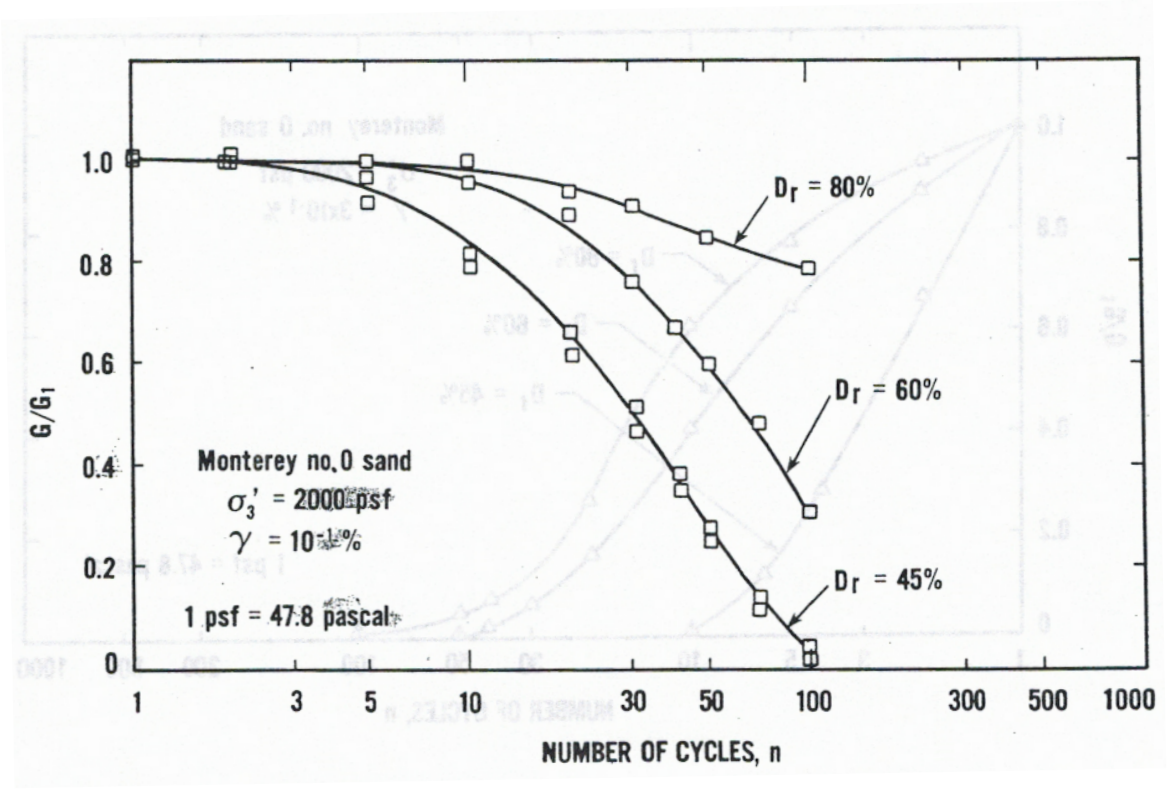

Figure 15. Degradation of shear modulus as number of loading cycles increases. The three lines represent specimen of Monterey No. 0 sand prepared at relative densities of 45%, 60%, and 80% (from Dobry et al, 1982).

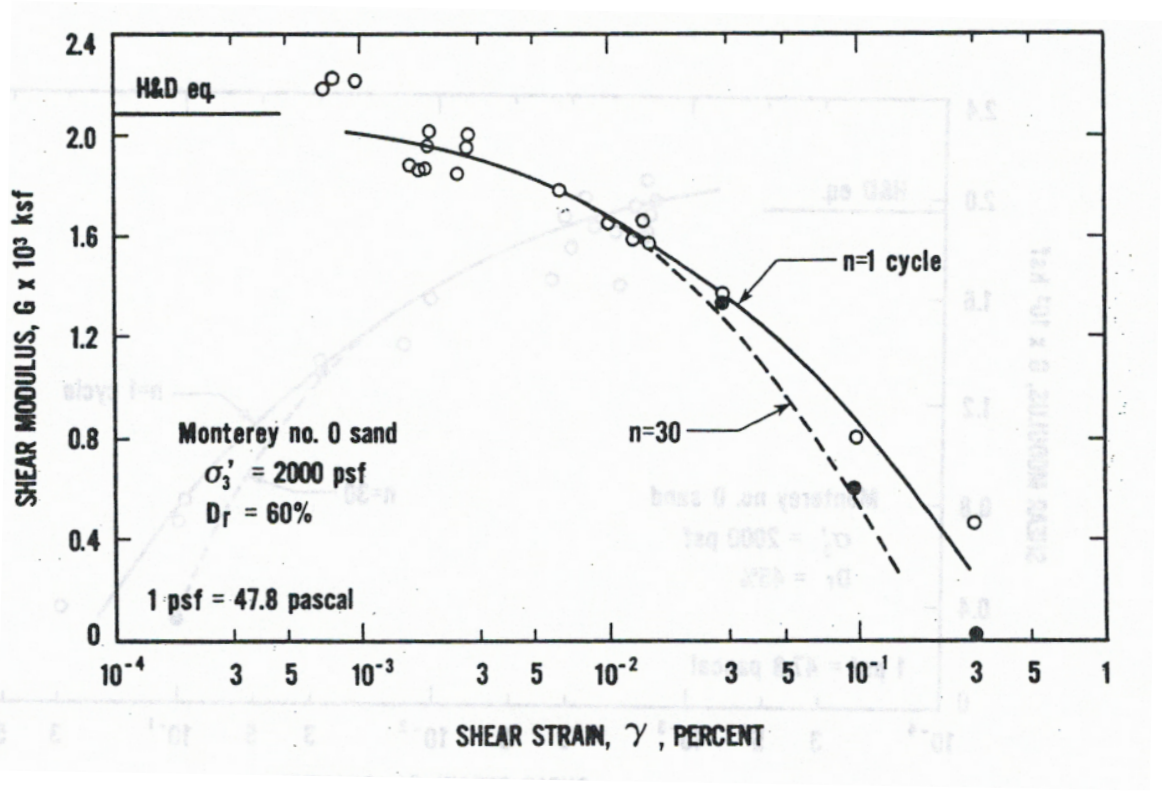

Figure 16. Degradation of shear modulus as shear strain increases. The solid black line represents soil behavior after one loading cycle while the dotted line corresponds to 30 loading cycles. The specimen shown is Monterey No. 0 sand compacted to 60% relative density (from Dobry et al, 1982).

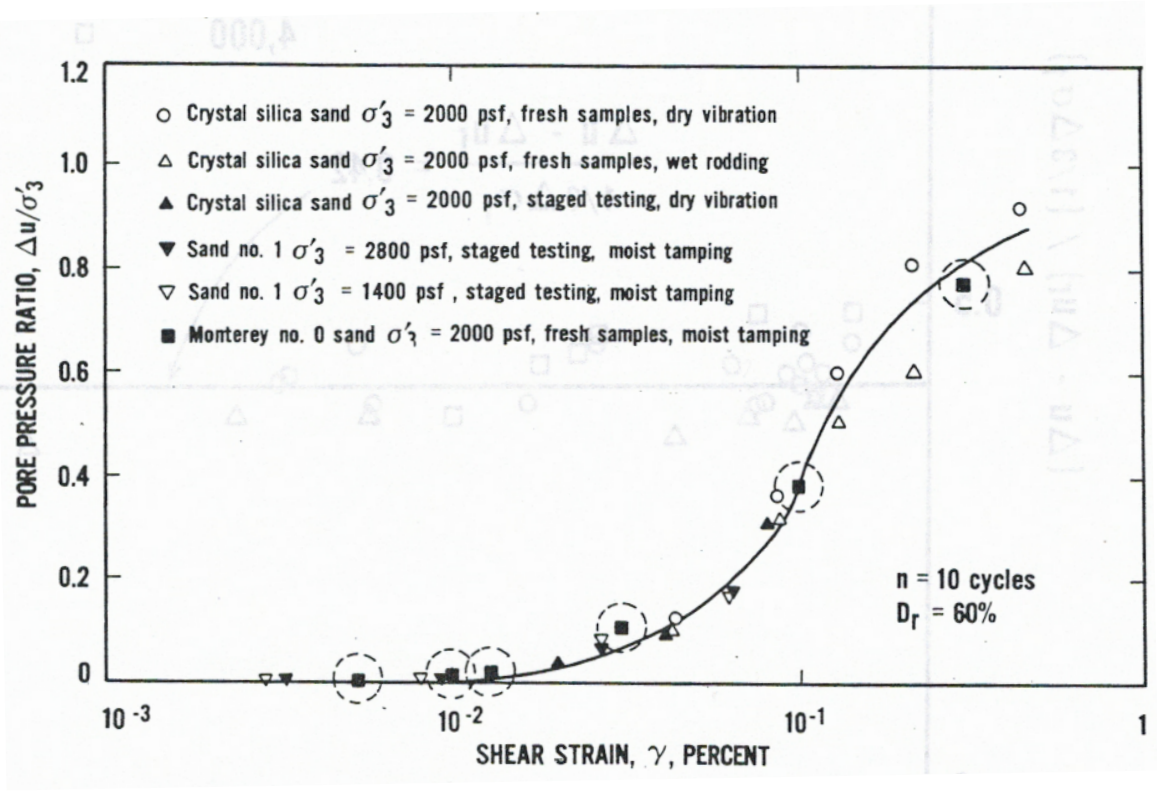

Figure 17. Pore pressure ratio versus shear strain after 10 loading cycles for the Monterey No. 0 sand specimen with a relative density of 60% (from Dobry et al, 1982).

The results and conclusions drawn from this publication are form an important foundation for the strain-based approached to soil liquefaction research. The research presented in this thesis also follows the strain-based approached in the analysis of the data and shows similar results regarding the relationship between pore water pressure ratio and shear strain, validating the effectiveness of the new direct, in situ testing technique.

2.7 SUMMARY

The publications reviewed in this chapter inform the basis of the research presented in the rest of the thesis. While not an exhaustive review of all soil liquefaction research, these publications have each been chosen for their unique contribution to the field and for the direct applicability to the research performed for this thesis. Youd et al, 2001, summarizes the contemporary state of field soil liquefaction research, detailing the strengths and weaknesses of a variety of techniques that preceded and were instrumental in influencing the direct, in-situ soil liquefaction test. Cox, 2006, is of particular interest because the soil liquefaction test developed is a direct progenitor of the soil liquefaction test presented in this thesis; the dissertation serves as a extensively documented guide for the implementation of the test as well as the analysis of the results. The publication from Holzer and Youd, 2007, presents data collected during an earthquake event at the original instrumented WLA, a project that precedes current research by almost three decades but is still relevant today as indicated by the authors' desire to revisit the topic with an updated discussion, indicating also that soil liquefaction research at the WLA is a worthwhile pursuit; results recorded from real earthquake events are important for purposes of comparison with the results collected from direct in-situ liquefaction testing. The paper by Rathje et al, 2004, presents and compares a variety of shear strain evaluation techniques for their application in direct in-situ soil liquefaction testing. The determination of shear strain is among the most crucial of calculations in the analysis because this is the parameter against which the development of pore water pressure is judged. Finally, Dobry et al, 1982, makes the case for a strain-based approach to soil

liquefaction research, arguing that the factors that influence the results of a stress-based approach such as relative density are less apparent in the strain-based approach and are not actually as important in determining the susceptibility of soils to liquefaction as initially thought. This research also establishes the cyclic threshold strain to be around 10^{-2} %, a value that continues to be valid and used as a benchmark today. Together, these publications provide excellent background for the research presented in the rest of these pages and serve as a reference for the evolution of soil liquefaction research in general.

Chapter 3 – Field Site and Test Equipment

3.1 Introduction

Liquefaction testing is an innovative technique that directly measures the liquefaction triggering potential of in situ soils by applying a range in shaking levels on the surface of a field site and recording the consequential pertinent soil behavior. The liquefaction testing technique described in this thesis is the third iteration of the technology, expanding on successful efforts of previous researchers as discussed earlier (Chang, 2002, and Cox, 2006). As a result, the foundation for the project is established and the selection of the test site and the design of the equipment are influenced by past projects. In this chapter, the site selection, geology and history of the site, and equipment utilized for the research project are discussed.

3.2 Field Site

The site selected for this project is the Wildlife Liquefaction Array (WLA) located in Imperial Valley, California. The WLA is managed by the Network for Earthquake Engineering Simulation (NEES) Equipment Site at the University of California, Santa Barbara, NEES@UCSB. This site is in an ideal location because soil liquefaction occurs there quite regularly. Medium sized earthquakes frequent the region as a result of its proximity to the southern end of the San Andreas Fault system. In the last 75 years, soil liquefaction has been triggered by six separate earthquakes in the region, so the risk of soil liquefaction is both well documented and high (NEES@UCSB, 2013). Additionally, UCSB maintains ground motion monitoring equipment at the site

and continuously records natural earthquakes. These events are easily compared to data collected during the liquefaction triggering testing conducted in this thesis. The WLA is also the site at which Dr. Brady Cox performed the second generation liquefaction testing, the details of which are expounded in his 2006 dissertation from The University of Texas at Austin (Cox, 2006).

The geology at the site provides a unique setting for studying soil liquefaction and refining the testing process. The soil profile, discussed in detail below, consists of approximately 8 ft (2.4 m) of low-permeability clay underlain by loose, saturated sand. The Alamo River flows adjacent to the site, ensuring the water table is generally located approximately 3 ft (0.9 m) below the ground surface. The presence of the overlying clay layer prevents the pore fluid, in this case water, from being expelled from the void space in the sand during seismic activity. Without adequate drainage for the sand layer, the upper portion of the sand layer does not densify but remains liquefiable after each earthquake. For this reason, it is possible to test repeatedly at the same site with little or no alteration to the ground properties, ensuring a stable control condition.

3.3 Site Geology and Earthquake History

While extensive analysis of the underlying geology was not performed for this research project, there exist several decades of records detailing the local geology from other projects. The WLA is located in the Salton Sink formation that includes Imperial Valley and the Salton Sea, an area that is approximately 85 miles (136 km) in length and a maximum of 30 miles (48 km) in width. The ground surface of the Salton Sink is

several hundred feet below sea level and is part of the same depression as the Gulf of California that lies to the south (USGS et al 1966) as shown in Figure 18.

Figure 18. Overview of the Salton Sink showing the Salton Sea, Imperial Valley, and the Gulf of California components. Picture from Google Maps, edited by author.

Much of the sediment found in the Salton Sink has been continuously deposited over the last 20 millions years in a process that began during the late Miocene epoch and is currently ongoing. As a result of this deposition, alluvial sand and silts as well as lacustrine silts and clays are found abundantly in this region. This region is additionally

characterized by the San Andreas right-lateral strike-slip fault system that terminates at the northwest corner of the Salton Sink formation. The faults associated with this system are active and have consistently produced medium sized earthquakes in this region that are responsible for many soil liquefaction events (USGS et al 1966).

An extensive local soil profile of the WLA was developed in April 2003 when the site was re-instrumented under the auspices of NEES by researchers Dr. Youd at Brigham Young University, Dr. Steidl at the University of California at Santa Barbara, and Dr. Nigbor at the University of Southern California. A representative soil profile, as seen in Figure 19, was determined from the results of 24 Cone Penetration Test (CPT) soundings. The top layer is 8 ft (2.4 m) in thickness and contains clays and silty clays. Additionally, the water table is consistently found in this top layer, approximately 3 ft (0.9 m) below the ground surface. The sandy layer below the clayey silt is roughly 15 ft (4.6 m) thick and is composed of silty sand, sandy silt, and sand, all soils with relatively high permeability. Based on permeability tests preformed by UCSB at the site, the values of permeability coefficients for this layer approximately range from 0.0002 cm/s to 0.002 cm/s (NEES@UCSB, 2013). The liquefiable layer is considered to range from 8.2 ft (2.5 m) to 22.3 ft (6.8 m), essentially encompassing the entire sand layer (Cox, 2006).

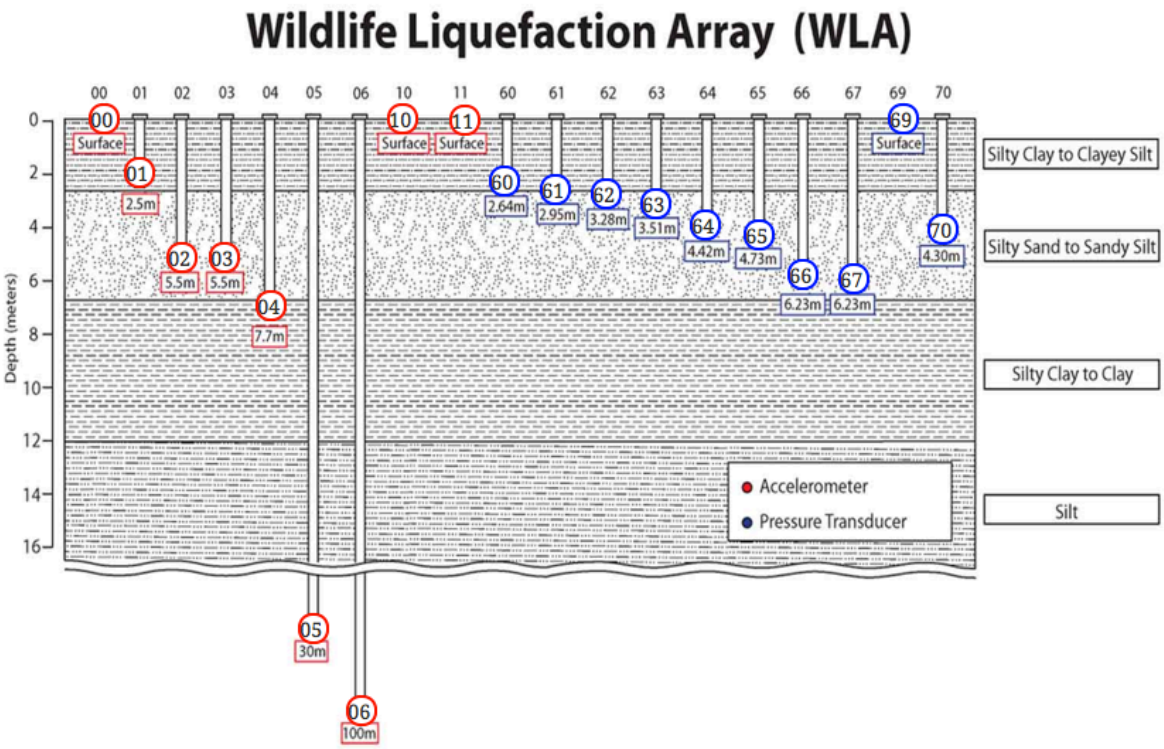

Figure 19. General cross-section of the Wildlife Liquefaction Array developed by NEES@UCSB for the re-instrumentation of the site. The accelerometers and pressure transducers in the figure are sensors continuously monitored by UCSB for seismic activity in the region (from NEES@UCSB, 2013).

In addition to characterizing the soil types present in the WLA, Dr. Youd and his team analyzed the WLA's susceptibility to soil liquefaction. Following the procedure published in Youd et al, 2001, the data from the CPT soundings was used to develop a soil liquefaction susceptibility profile for an earthquake event of magnitude 6.5 with peak ground accelerations in the range of 0.2 to 0.4 g. The results of the analysis shown in Figure 20 indicate the risk of soil liquefaction at this site is very high, a desirable attribute for the purpose of this research project.

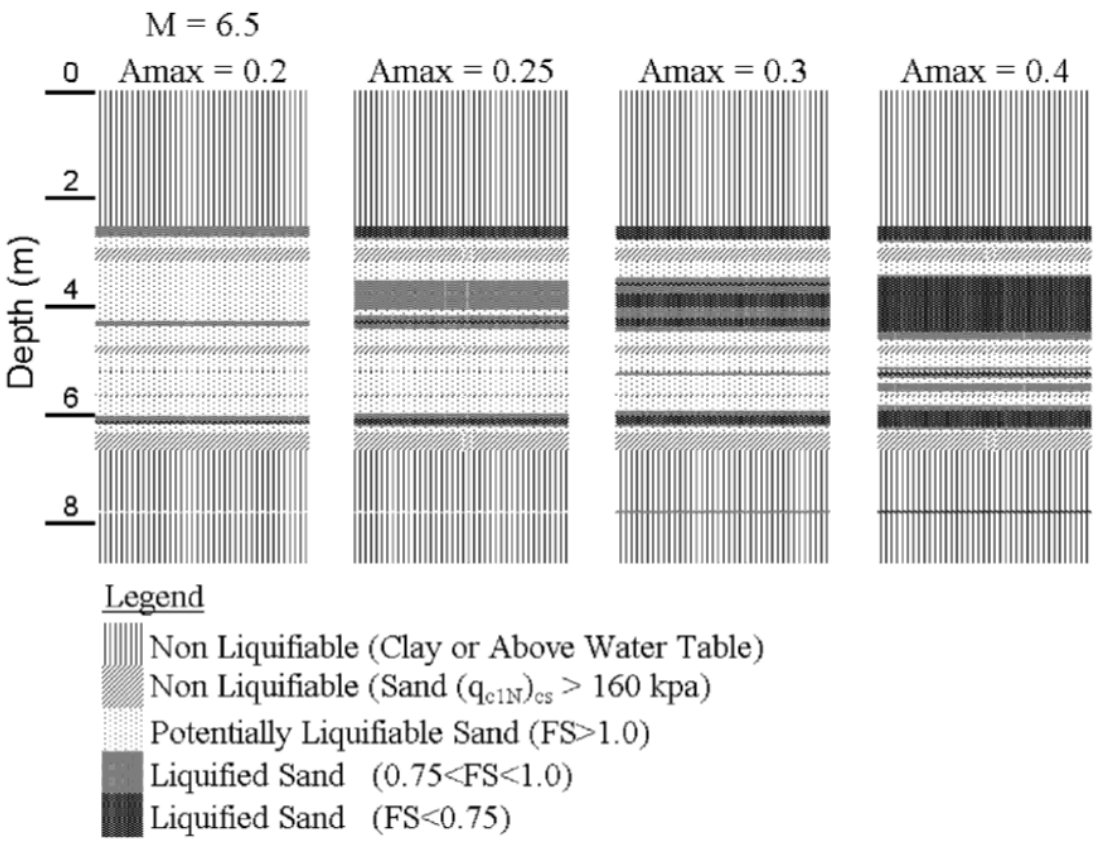

Figure 20. Predicted liquefaction resistance of local sediments for a magnitude 6.5 earthquake and various level of a_{max} (from Youd et al, 2004).

As discussed, the in situ soil conditions create an environment that is particularly prone to soil liquefaction. The final aspect contributing to the risk of soil liquefaction is the seismic activity in the region. In recent years, two earthquakes generated sand boils and soil liquefaction at the WLA site: (1) the 1981 Westmorland earthquake (magnitude 5.9) and (2) the 1987 Superstition Hills earthquake (magnitude 6.6) (Youd et al 2004). The epicenters of these earthquakes were within 25 miles (40 km) of the WLA site, as

shown in Figure 21. The San Andreas fault system continues to be active today and is predicted to generate more earthquakes in the future with similar characteristics.

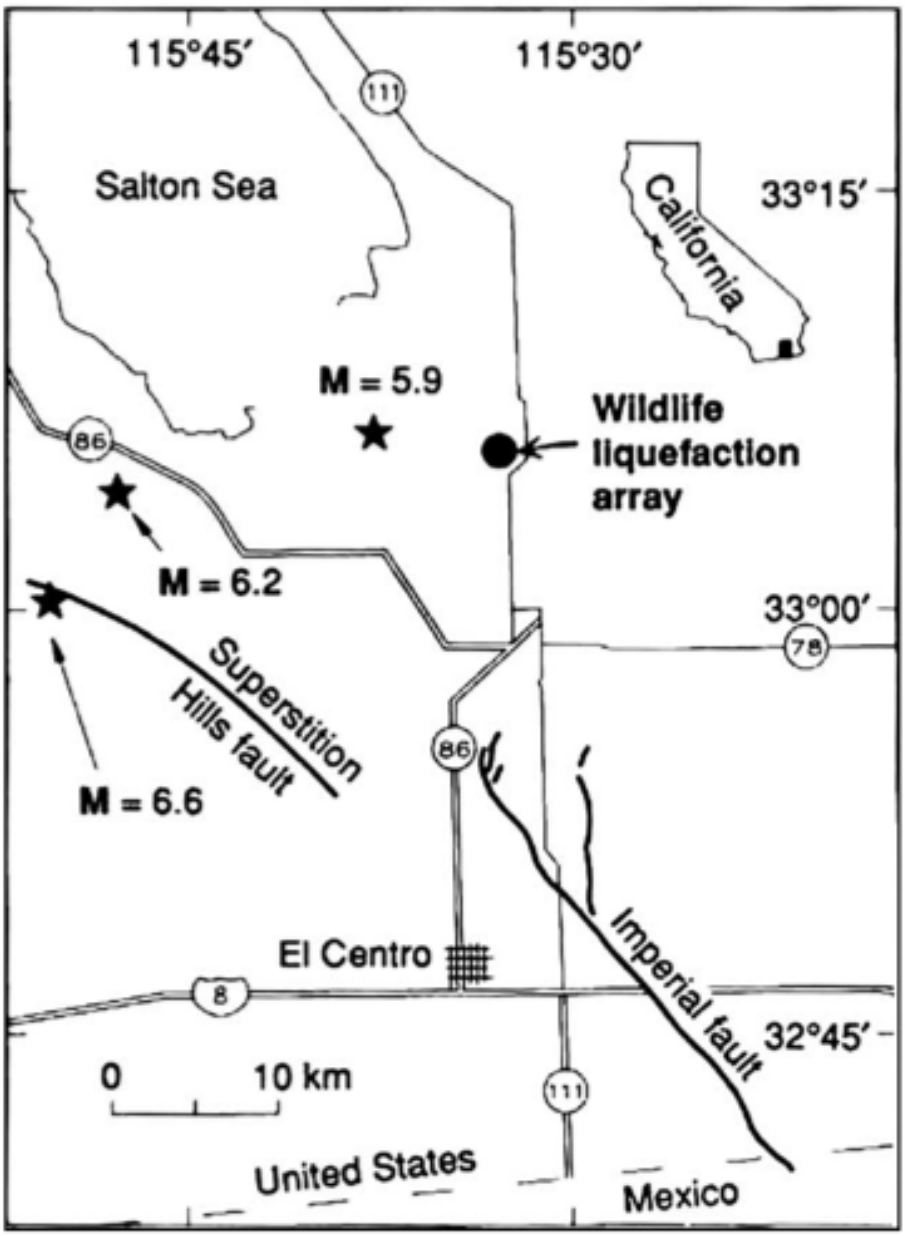

Figure 21. Overview of Imperial Valley region showing the Wildlife Liquefaction Array and epicenter locations of the 1981 Westmoreland earthquake (magnitude 5.9), 1987 Elmore Ranch earthquake (magnitude 6.2), and 1987 Superstition Hills earthquake (magnitude 6.6) (from Youd et al, 2004).

3.4 FIELD TESTING EQUIPMENT – T-REX

To create and monitor simulated earthquake motions for the in-situ liquefaction triggering tests, a large energy source and an embedded array of sensors are required. The energy source must be capable of outputting large horizontal, dynamic forces under controlled loading conditions. For this project, the energy source was the vibroseis known as T-Rex (shown in Figure 22) that is owned and operated by the NEES Equipment Site at The University of Texas at Austin (NEES@UTexas). This Equipment Site is operated with funding from the National Science Foundation's (NSF's) NEES research consortium. T-Rex is capable of horizontally shaking the ground with up to 30,000 pounds of force at frequencies ranging from 10 to 100 hertz.

Figure 22. Photograph of T-Rex in Imperial Valley at the Wildlife Liquefaction Array, ready for liquefaction testing. Participants from left to right: Paul Hegarty, Cecil Hoffpauir, Dr. Jamison Steidl, Dr. Kenneth Stokoe, II, Dr. Farn-Yuh Menq, Julia Roberts, and Robert Kent.

There are several features of T-Rex that make it well suited for this project. The base plate, which is located in the center of the vibroseis body, is the point of contact

between the machine and the ground and transmits the controlled shaking into the soil. The base plate is approximately 7.5 by 7.5 ft (2.3 by 2.3 m), enabling a large volume of soil directly below the plate to be uniformly loaded, as would be consistent with a natural earthquake; the assumption of a uniform loading condition is important and is supported by the motions measured in the ground. The large force output of T-Rex is also critical for the project. For liquefaction to be triggered in the sandy soil, the soil must experience large shear strain deformations during dynamic horizontal by T-Rex. For these reasons, T-Rex is an excellent energy source for simulating earthquake shaking on this project. Figure 23 shows the general configuration of the test setup with the location of the baseplate relative to the embedded monitoring equipment.

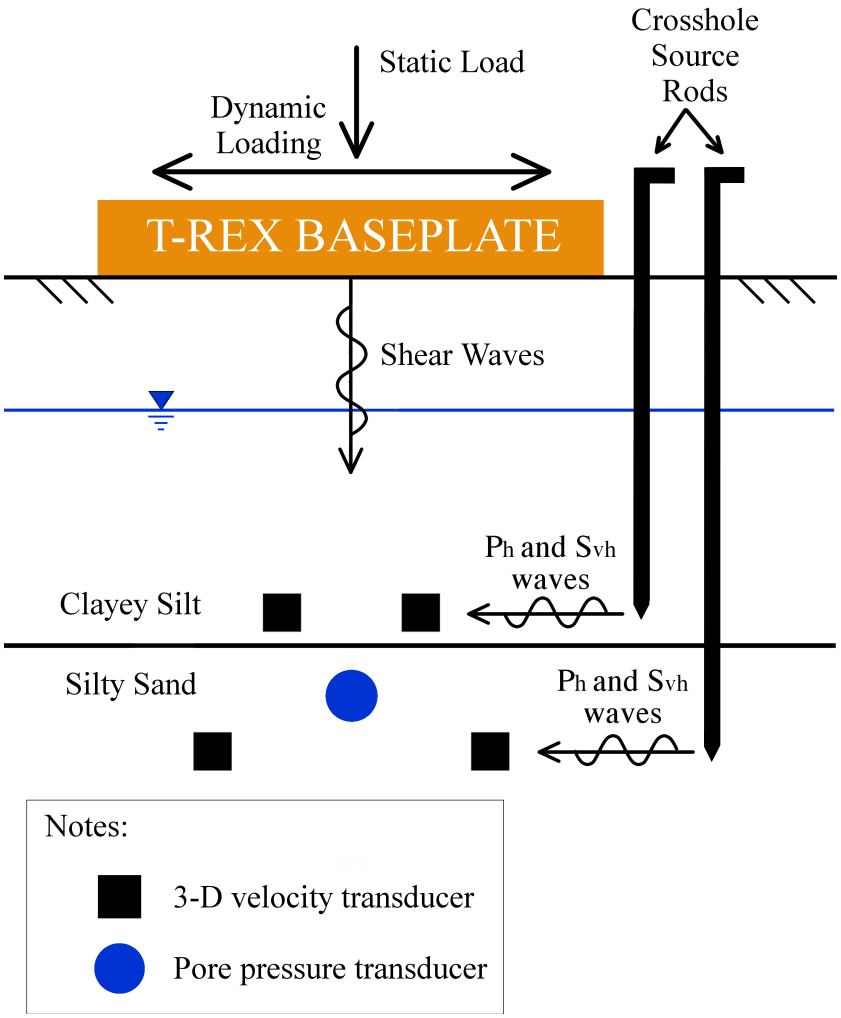

Figure 23. Drawing of the liquefaction test equipment configuration at the WLA.

3.5 EMBEDDED MONITORING EQUIPMENT

The uniqueness of liquefaction testing requires custom-built sensors that are tailored to the specific conditions of the test. In the test, the two most important parameters in the soil to measure are pore pressure generation at depth and ground motions at several locations above and below this depth. The data from these two parameters provide a detailed picture of soil behavior during earthquakes when combined

during the data analysis process. To that end, the sensors built for this project are specifically selected and designed to monitor the pore pressure of the ground water in the soil as well as the physical movement of the soil.

3.5.1 Pore pressure transducer

The pore pressure transducer to create the pore pressure sensor in this project is a Druck PDCR 1830-8388 Submersible Pressure Transducer. This pore pressure transducer weighs 3 pounds and measures 4 inches in length and 0.8 inches in diameter. The transducer is vented to the atmosphere, which helps prevent sensor drift and ensures accuracy in the results. It is rated to operate in conditions up to 10 psi and has a sensitivity of 0.98mV/V/psi. To protect the pore pressure transducer and to create a sensor that can be pushed into the ground, it is encased in a hard polycarbonate cylinder with a detachable cone tip. From this point forward, pore pressure transducer refers to the assembled unit that includes the polycarbonate casing with the encased pore pressure transducer.

To use the pore pressure transducer, the sensor must be saturated and prepared with a filter as discussed in Section 4.3.2. Before installation, the sensor is covered with a thin membrane intended to maintain saturation. This system just before pushing in shown in Figure 24.

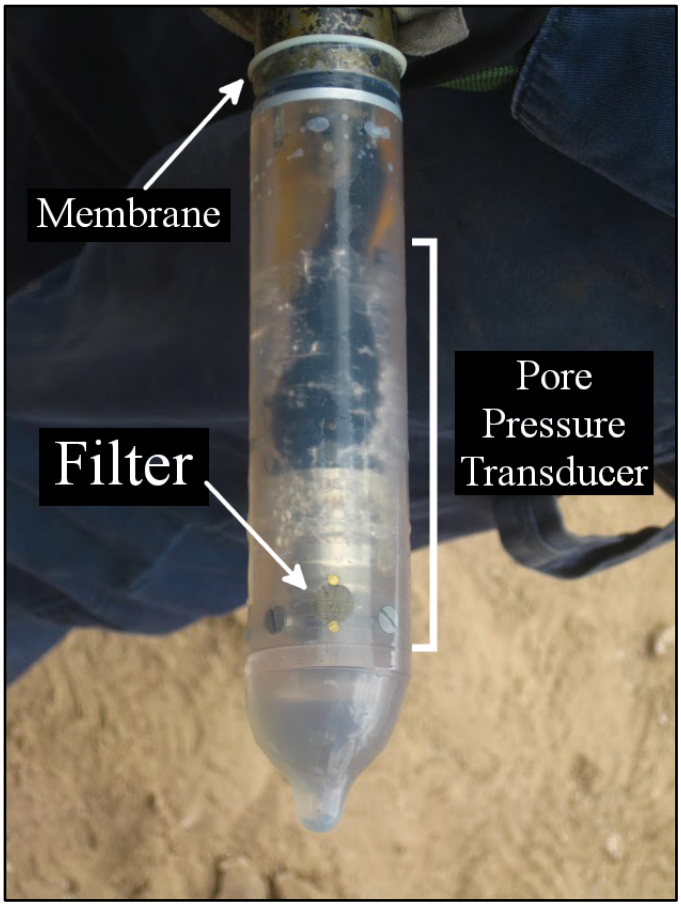

Figure 24. Components of assembled and saturated pore pressure transducer just before pushing into the ground.

3.5.2 Velocity transducers

The 3-D velocity transducers utilize geophones as the ground motion monitoring equipment. Geophones were selected to record the particle velocity at a point rather than accelerometers because of their robustness in the field and relatively low cost. The only perceived negative associated with choosing geophones over accelerometers, as done by Cox, 2006, is losing the ability to track the tilt and path of the sensors as they are pushed into the ground. This loss of accuracy is deemed insignificant based on Dr. Cox's

conclusion that the rods experienced minimal lateral movement during pushing when the test was performed under similar conditions at the same site (Cox 2006).

The number of geophones per sensor and the type of geophones selected were also carefully considered for this particular project. Three geophones per sensor are required in order to capture the full, three-dimensional motion of the sensor in the soil, which mirrors the motion of the soil itself at that particular location. Geo Space Corporation's 28-hertz resonant frequency geophones (GS-20DM 28-270) were selected for their size as well as their resonance frequency. Each geophone weighs 1.5 ounces (40 grams) and measures 1 in. (2.54 cm) in height and 0.875 in. (2.22 cm) in diameter. Their small size allows multiple geophones to be encased in a larger, protective casing and their resonant frequency ensures a range of frequencies from 10 hertz to 50 hertz is accurately recorded.

The geophones are encased in a custom designed hard polycarbonate cone-tipped cylinder. The cone tip, which facilitates pushing the 3-D velocity transducers into the soil, has an angle of 60° like a typical cone in the CPT. The diameter of the polycarbonate cylinder is 1.5 in. (3.8 cm) and the height, including the cone tip, is approximately 4.7 in. (11.9 cm). The placement of the geophones ensures they are aligned in orthogonal directions to one another (one in the vertical direction and two in the horizontal directions). Figure 25 shows a photograph of the 3-D velocity transducer and its associated components.

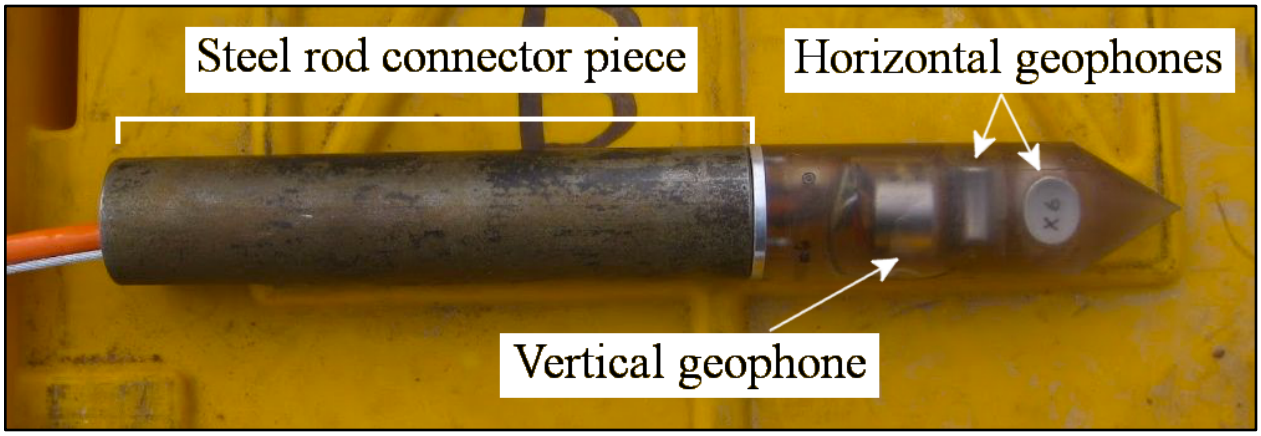

Figure 25. Components of assembled 3-D velocity transducer with attached steel rod connector piece.

In addition to housing the geophones and their respective electrical wires, the polycarbonate cylinder includes a steel pin inserted horizontally across the top of the cylinder. This pin anchors a steel wire that is used to pull (retrieve) the liquefaction sensor from the ground at the end of testing. The components of the velocity sensor inside the polycarbonate cylinder are secured with an epoxy that also fills the remaining voids in the sensor. Finally, the polycarbonate cylinder is sealed at the top with an aluminum cap that also serves to temporarily "attach" the velocity sensor to the steel rods used to push the sensor into the ground. The attachment of the sensor to the steel CPT push rods is simply a slip fitting with a key to allow the sensor to be oriented during pushing.

3.6 SUMMARY

For the liquefaction testing in this project, the geology of the site is just as important as the custom-made equipment. Since the objective of the research is to

characterize liquefiable soil, it is prudent to select a site that has a high risk of liquefaction because of its geology as well as because of the regional seismic activity. The selection of WLA fits these criteria and also has the added benefit that other research groups are also conducting experiments there, adding to the wealth of information obtained from these activities.

Given the unique nature of liquefaction testing, much of the equipment is also specialized. T-Rex is a one-of-a-kind energy source for simulating earthquakes and greatly expands the capabilities of liquefaction testing with its large force output and frequency range. The 3-D velocity transducer and pore pressure transducer used on the project are custom-built for their specific uses, ensuring high quality in data capture during the tests. Combined together, all of these aspects are important for preparing a successful project and were duly addressed prior to testing.

Chapter 4 – Liquefaction Testing Procedures at the Wildlife Liquefaction Array

4.1 INTRODUCTION

At the WLA site, liquefaction testing was performed approximately 130 ft (40 m) southwest of the Alamo River bank and a short distance from Rensselaer Polytechnic Institute's (RPI's) wireless shape-acceleration arrays (WSSA). In the photograph in Figure 26, the approximate locations of the sites of liquefaction testing and RPI's sensors are shown. Site preparation for liquefaction testing required a full day of labor to install the source rods for crosshole testing, the pore pressure transducer, and the 3-D velocity transducers. Instructions for sensor installation were provided by Professor Brady Cox via his personal notes, which are based on his doctoral research (Cox, 2006). In this chapter, the layout of the sensor array, sensor installation, testing procedures, sensor removal, and site cleanup are described.

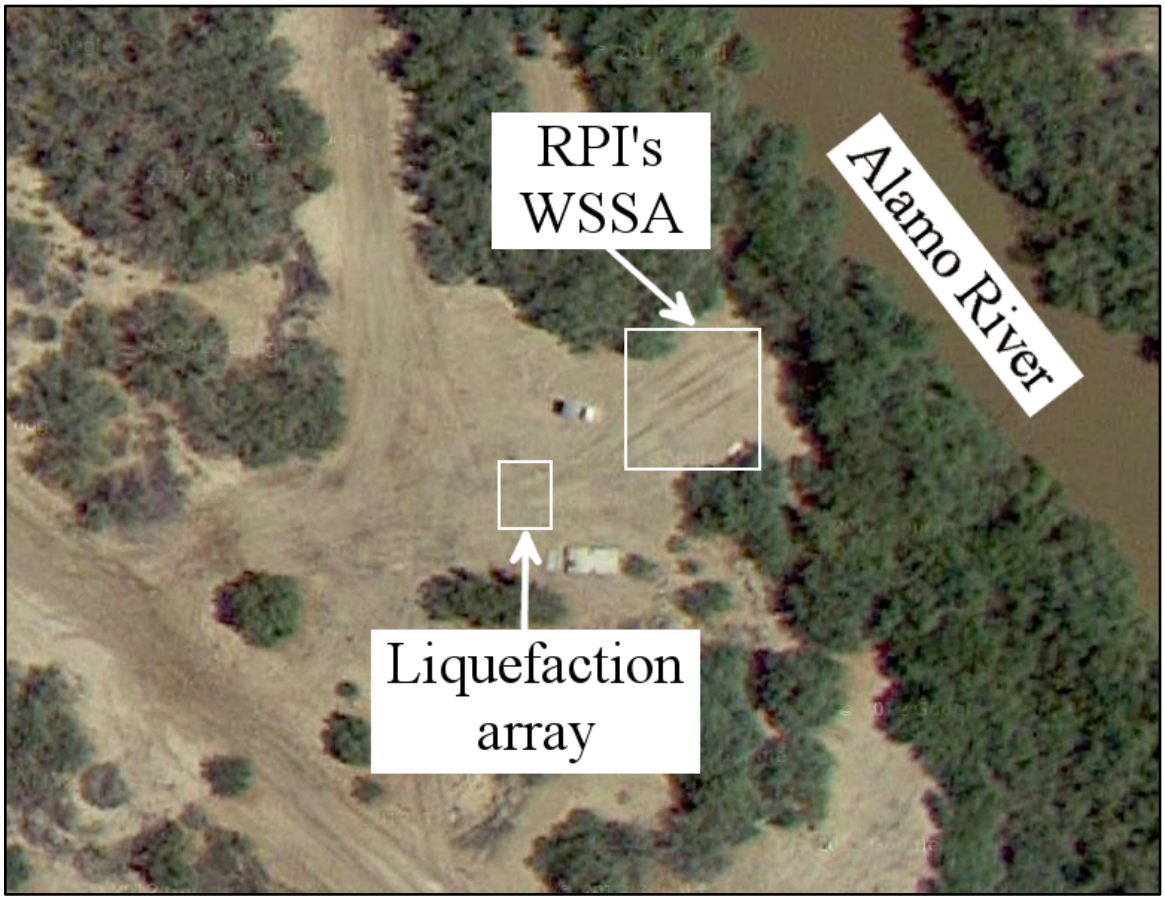

Figure 26. Photograph of test site showing the relative locations of the liquefaction array, RPI's WSSA, and the Alamo River. Picture from Google Maps, edited by author.

4.2 LIQUEFACTION SENSOR ARRAY

The configuration of the sensor array used in this research is shown in Figure 27. The array configuration and location were selected to optimize measurement of the loosest silty sand just below the low-permeability clayey silt "cap" at the WLA. The location of each 3-D velocity transducer marks the corner of a trapezoid. The interface between the clayey silt and sand layers intersects the trapezoid so that two velocity

sensors are in the clayey silt layer and two velocity sensors are in the sand layer; the pore pressure sensor is also located in the sand layer.

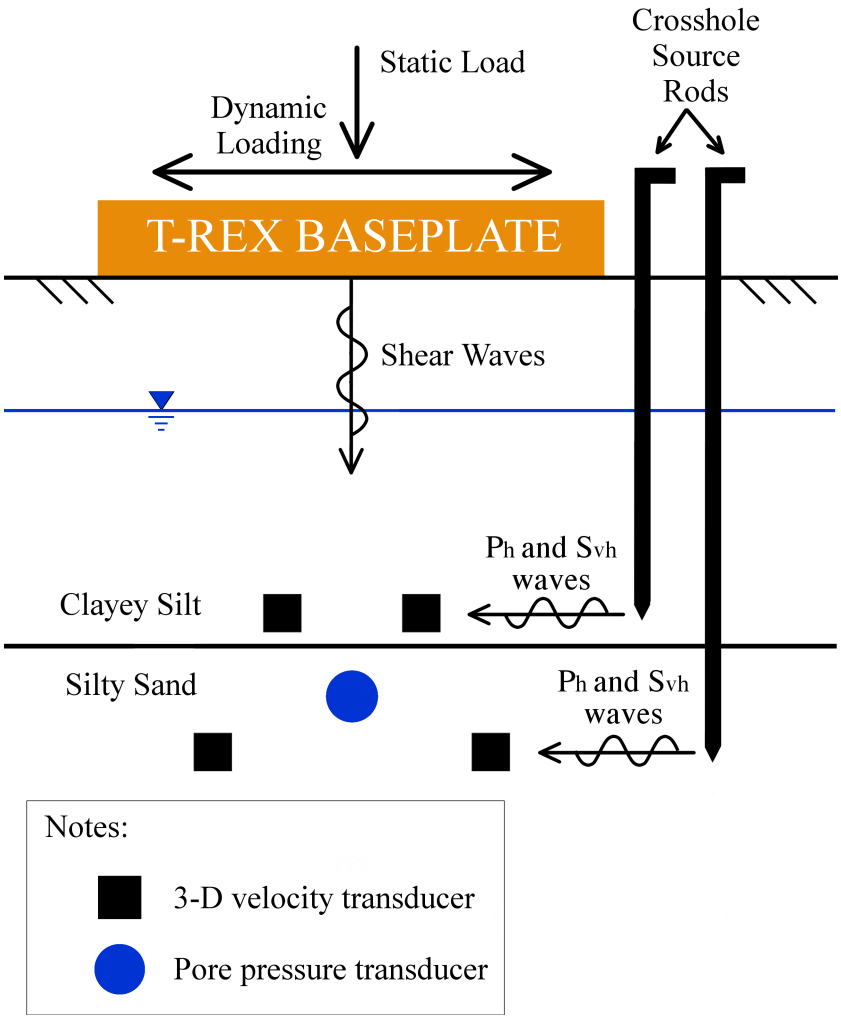

Figure 27. Drawing of the liquefaction test equipment configuration after installation is complete.

The objective of straddling the interface was to capture the behavior of the loose sand as close to the interface as possible. During an earthquake simulation using T-Rex, the pore pressure is greatest in the sand near the interface immediately below the center of T-Rex because the loosest sand is generally next to this interface and because the

water cannot flow through the clayey silt as quickly as it can through the sand. As a result, dissipation of pore pressure is slowest at the center of the sensor array, making it the likeliest location for soil liquefaction to occur.

The exact location of the interface was determined by performing a cone penetration test (CPT) prior to sensor installation. A ram mechanism for pushing rods into the ground is located on the back bumper of T-Rex and is utilized for CPT tests. The interface is located by monitoring both the end-bearing force on the cone tip and the side-shear force along the side of the cone that is just above the tip. Generally, the end-bearing force is greater in sand than in clay while the side friction force is, relative to the end-bearing force, greater in silt and clay than in sand. The results of the CPT test showed that the interface between the sand and clay layers is located approximately 8.7 ft (2.6 m) below the ground surface for that particular location. Based on the data from past projects at WLA, it is believed that the depth of the interface does not vary significantly over the localized testing area. In this project, the interface is assumed to be at a constant elevation.

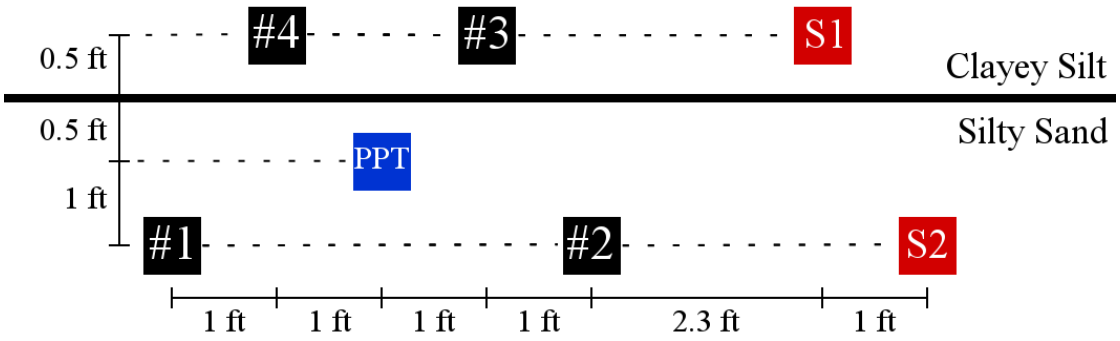

Figure 28. Schematic diagram of the sensor array used in liquefaction testing. The black squares with numbers represent each of the velocity sensors, the blue square labeled "PPT" represents the pore water pressure sensor, and the red squares with an "S" followed by a number represent the tips of the source rods used to perform crosshole testing at the top and bottom levels of the embedded array.

Given the desired characteristics of the sensor array discussed above and the known location of the interface between the clayey silt and sand layers, 3-D velocity transducers #1 and #2 are located 10.2 ft (3.1 m) below the ground surface in the sand layer while 3-D velocity transducers #3 and #4 are 8.2 ft (2.5 m) below the ground surface in the clayey silt layer. The pore pressure transducer is positioned in the sand layer at the center of the trapezoid at 9.2 ft (2.8 m) below the ground surface so that pore pressure measurements at that location can be matched with the strain estimates. The 3-D velocity transducers and pore pressure transducer are located in the same vertical plane with 1 ft (0.3 m) horizontal separation between each sensor location as shown in Figure 4.3. The two source rods used in crosshole seismic testing are also located in the same vertical plane at depths of 8.2 ft (2.5 m) and 10.2 ft (3.1 m) below the ground surface, matching the depths of the two rows velocity sensors, as can also be seen in Figure 28.

4.3 SENSOR INSTALLATION

The first step in sensor installation is digging a trench that is used to embed the electric cables and the portions of the steel rods that remain in the ground after pushing the sensors in place. The embedment is done to protect the electric cables and steel rods from the movement of the T-Rex shaking platen during testing. This trench is T-shaped as shown in Figure 29; the sensors are located in the horizontal portion of the trench while the electric cables are fed through the vertical stem of the "T" and daylight about 18 in. (46 cm) away from the edge of the loading platen. The trench is nominally 1 ft (0.3 m) deep, 1 ft (0.3 m) wide and of varying lengths to accommodate the sensor locations. After installation of the sensors is complete, the trench is backfilled with the originally excavated soil to cover the electric cables and tops of the steel push rods.

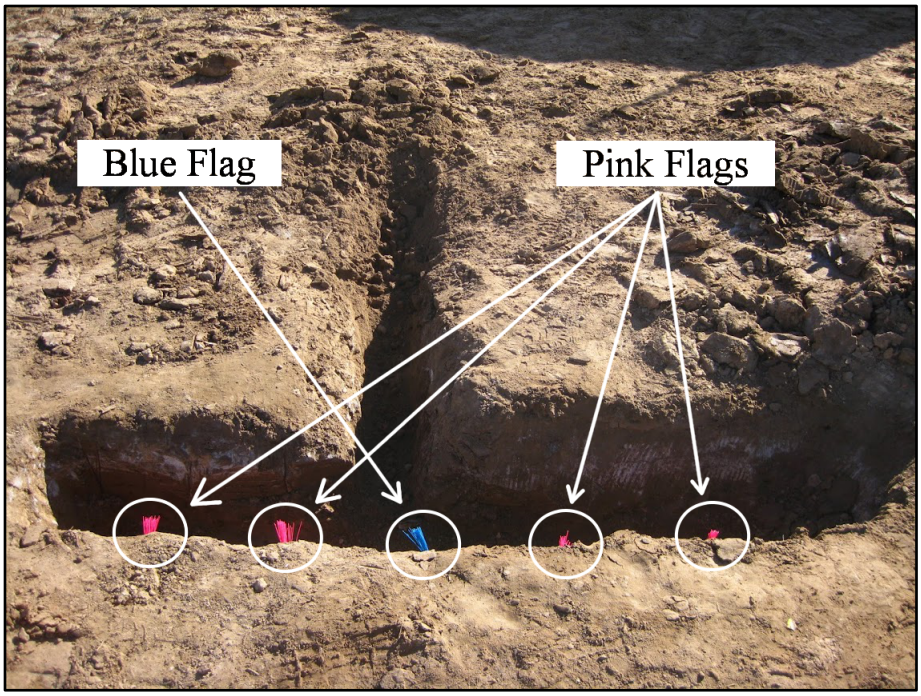

Figure 29. Photograph of the sensor trench prior to sensor installation. The pink flags mark the entry point for each of the 3-D velocity transducers and the blue flag marks the entry point of the rods used to push the pore pressure transducer. The trench extending backward in the photograph allows the electric cables to be drawn out from below T-Rex's base plate before they daylight and are connected to the analyzers.

4.3.1 Installation of seismic source rods

Once the trench is dug and the sensor locations are marked with survey flags, installation of seismic source rods and sensors follows. The back bumper of T-Rex is outfitted with a pushing/pulling mechanism (hydraulic cylinder) that is used to push steel rods into the soil and then retrieve the rods when testing is completed. Starting with the two seismic source rods, a series of hollow steel rods of varying lengths are connected and pushed into the ground to the finals depths of 8.2 ft (2.5 m) and 10.2 ft (3.1 m) below the ground surface. The outer diameter of the steel rods 1.5 in. (3.8 cm), the inner

diameter is 0.5 in. (1.3 cm), and the segment lengths range from 1 ft (0.3 m) to 4 ft (1.2 m). One end of the 4-ft (1.2-m) long rod is a steel cone that facilitates penetration into the ground, while the other end is threaded on the interior surface of the hollow rod. All of the other steel rod lengths are threaded on both ends, though one end is threaded on the exterior while the other end is threaded on the interior. This design allows the steel rods to be quickly and securely screwed together, resulting in a longer, continuous rod.

The process of installation begins by fastening the 4-ft (1.2-m) rod, which has a dummy cone tip end that disseminates energy into the surrounding area during seismic crosshole testing, to the pushing adaptor on the ram mechanism of T-Rex. The rod fits smoothly into the chamber of the pushing adaptor and contact is maintained between the two via the compressive force applied by the ram mechanism. The ram mechanism pushes the 4-ft (1.2-m) long rod into the ground until there is enough clearance to screw another segment of the steel rod to the already driven rod. This process is repeated until the source rod is driven to the appropriate depth. Additionally, the tops of the rods are exposed approximately 1 to 2 ft (0.3 to 0.6 m) above the ground surface and are topped with flat caps. The flat caps provide a target surface to strike the rod with a hammer during the crosshole testing (discussed in Section 4.4.1 and shown in Figure 33).

4.3.2 Pore pressure sensor preparation

Preparation of the pore pressure transducer is best commenced at least 6 hours prior to testing to ensure full saturation of the equipment. For this research project, preparation was started the day before sensor installation and continued for over 12

hours. The filters were prepared by being saturated in a laboratory flask filled with distilled water and boiled on a hot plate. The water was boiled for 4 to 6 hours to remove air, all the while making sure to maintain the water level in the flask. After boiling, the flask was cooled and capped with a rubber stopper until further use.

At all times, the pore pressure transducer and accompanying equipment were checked for air bubbles because contamination by air severely hampers the performance of the pore pressure sensors. A 5-gallon (19-liter) bucket filled with water was used as the assembly area (see Figure 30). Items submerged in the bucket includes the pore pressure transducer, filters, screw driver, and bubble probe. All items submerged in the bucket were checked multiple times for clinging air bubbles. While all items were under water, a filter was selected and inserted into the side of the pore pressure transducer. The filter acts as a permeable barrier between the diaphragm of the sensor and the soil; it allows water to flow freely through but protects the diaphragm from any potentially damaging interaction with the soil. The filter was secured by fastening two screws into the polycarbonate casing.

Figure 30. Preparing to submerge the pore pressure sensor in the 5-gallon water bucket. While difficult to see, filters and tools are at the bottom of the bucket, saturated and ready for sensor preparation.

Following installation of the filter, a latex membrane is removed from its packaging and then submerged in the bucket of water. After removing air bubbles, the membrane is unfurled over the entire pore pressure sensor to maintain the saturation of the sensor when it is removed from the water. At this point, the pore pressure sensor is set aside in the water bucket until it is pushed into the ground.

4.3.3 Installation of 3-D velocity transducers and pore pressure transducer

After the source rods were installed, the 3-D velocity transducers and pore pressure transducer were installed. Immediately prior to pushing the 3-D velocity transducers, a 1.75-in. (4.5-cm) diameter pilot rod was pushed to create pilot holes for each of the 3-D velocity transducers and the pore pressure transducer. The 1.75-in. (4.5-cm) pilot rod was pushed to a maximum depth of 4 ft (1.2 m) below the ground surface. In addition, a 1.5-in. (3.8-cm) diameter pilot rod was used to extend the pilot holes to depths ranging from 7.3 ft (2.2 m) to 8.3 ft (2.5 m) below the ground surface, depending on the ultimate depth of the sensor to be pushed through that hole. For the 3-D velocity transducers located in the clayey silt layer, the 1.5-in. (3.8-cm) diameter pilot rod reached a maximum depth of 7.3 ft (2.2 m) below the ground surface while for the 3-D velocity transducers located in the sand layer, the pilot reached a maximum depth of 7.8 ft (2.4 m) below the ground surface. In the case of the pore pressure transducer, the maximum depth of the pilot rod was 8.3 ft (2.5 m) below the ground surface. These pilot holes reduced the stress on the 3-D velocity transducers during pushing and allowed the integrity of the membrane that was used to isolate the pore pressure transducer from air until it was below the water table. The pilot holes did not extend to the final depth of the sensors so that the sensors were pushed through undisturbed soil for the last few feet, ensuring adequate coupling between the sensors and the soil.

In a procedure similar to installing the seismic source rods, the pushing mechanism on the back bumper of T-Rex is used to push the sensors into position. The sensors are connected to the steel rods by means of custom-made connectors. These

connectors are made of steel with an outer diameter of 1.5 in. (3.8 cm), an inner diameter of 0.75 in. (1.9 cm), and an approximate length of 6 in. (15.2 cm). One end of the connector piece has internal threading so it can be screwed into the steel pushing rods and the inside of the other end is smooth except for two lines of bead welding on opposite sides. The smooth end is where the top cap of the sensor is inserted into the rod and the bead welding fits into the grooves in the top cap (the top cap is shown in Figure 31). The fit between the bead welding and the grooves prevents rotation of the 3-D velocity transducers as they are pushed into the ground, which is important for maintaining the proper orientation of the embedded geophones (velocity transducers).

Figure 31. Photograph of the top caps prior to 3-D velocity transducer assembly. The two grooves on each top cap are directly opposite one another.

To begin installation the process, the electric cable and steel pullout wire for each sensor is first threaded through a connector piece so that the connector piece can be fastened to the top cap of the transducer. The electric cable and steel pullout wire must then be threaded through each segment of steel rod that will be used for pushing so that the cable has an unobstructed path on the inside of the steel rods to reach the surface. This process in an early stage is shown in Figure 32. The ram mechanism on T-Rex is then used to push the sensor, connector piece, and the first steel rod segment into the ground until there is enough clearance to add the next steel rod segment. Steel rod segments are added until the sensors reach their final depth and all of the sensors are installed.

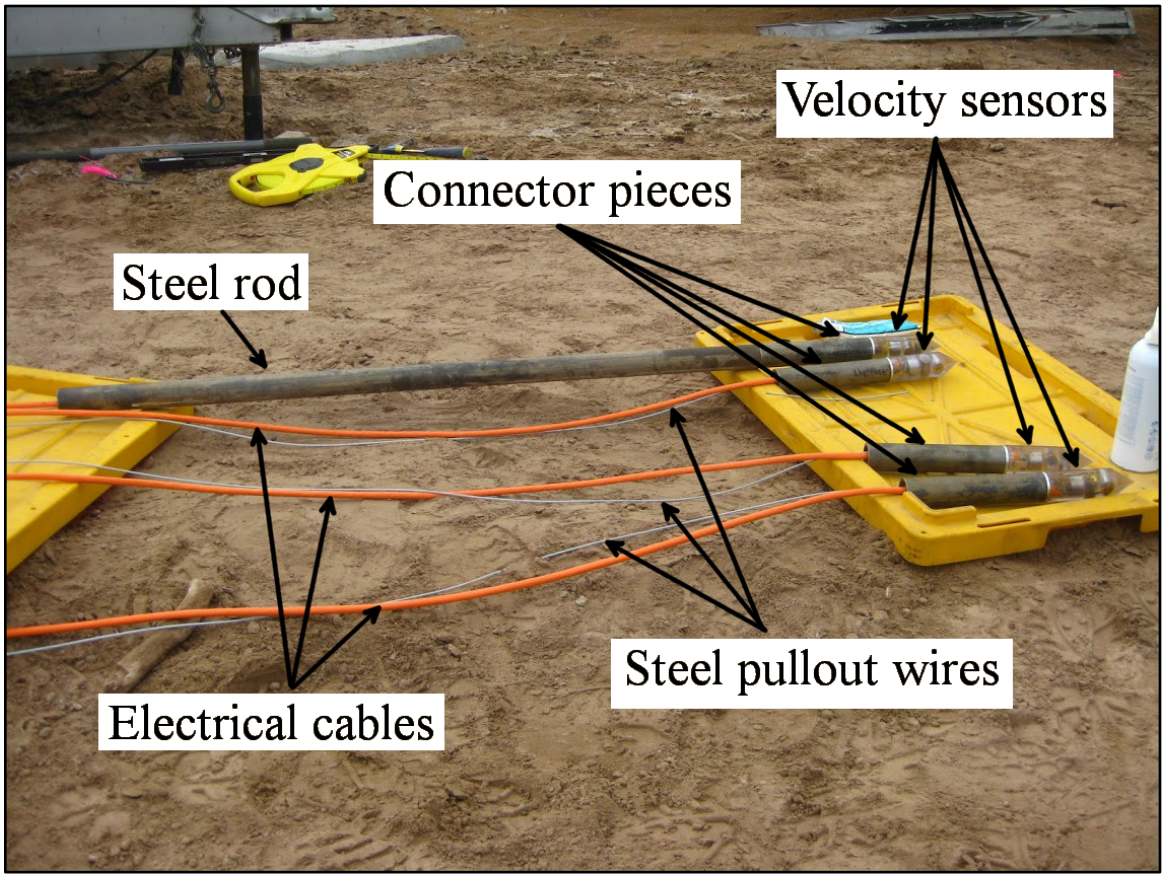

Figure 32. Photograph of 3-D velocity transducers being prepared for pushing. The 3-D velocity transducers, connector pieces, steel rods, electrical cables, and steel pullout wires are shown in the process of final assembly.

After the 3-D velocity transducers and pore pressure transducer have been pushed into position, they are fully disconnected from the steel rods used to push them into position. This step is important because it enables the sensors to uninhibitedly move due to the shaking of the surrounding soil, capturing the behavior of the soil without influencing it significantly. The connection between the aluminum top cap and the steel rod is loose enough to be easily pulled apart when the friction between the soil and sensor prevents movement of the transducer during retraction of the steel rods. In order to

isolate the sensors, the rods are retracted 3 in. (7.6 cm) after pushing the transducers to their final depths. It is important to verify that the electric cables do not move during rod retraction because electric cable movement indicates the sensor is still attached to the rod and is not staying in the intended measurement point.

4.4 TESTING PROCEDURES

Testing for this project began the day following site preparation and sensor installation and was primarily completed in a single day. The project encompassed two separate kinds of testing (crosshole testing and liquefaction testing), each with a number of repetitions and/or stages. The crosshole seismic tests provided information about the small-strain stiffnesses (compression and shear) of the soil both before and after the liquefaction testing. The goal of the staged liquefaction testing sequence was to gradually increase the strain level in the soil over several repetitions in order to observe how different strain levels affected the build up of pore water pressure. The parameters of the test were intended to simulate earthquake loading conditions that would be appropriate for the seismic risk of the region. In addition to recording data from the crosshole and liquefaction tests, the pore pressure was checked periodically to verify the stability of the system and to monitor the ground water conditions.

4.4.1 Crosshole seismic testing

Crosshole seismic testing was performed before liquefaction testing to provide baseline P-wave and S-wave velocities of the soil in both the clayey silt and sand layers. The crosshole testing performed after liquefaction testing sought to determine how much,

if any, permanent soil degradation occurred. For all crosshole tests, the base plate of T-Rex applied the same hold down force of 60,000 pounds (267 kN) as it did during the liquefaction testing to ensure consistent static, total stress levels in the soil. The hammer used to strike the top of the source rod as an energy source was outfitted with an accelerometer that triggered the recording equipment, allowing an accurate measurement of travel time between the source rod and the velocity transducers of both P and S waves. Figure 33 shows the crosshole test in progress, with the source rods and source hammer accelerometer indicated.

Figure 33. Photograph of crosshole test in progress. The source hammer is outfitted with an accelerometer and is being used to strike the top of source rod #1.

As discussed previously, the sensor array geometry is such that two 3-D velocity transducers are located 8.2 ft (2.5 m) below the ground surface and the other two are 10.2 ft (3.1 m) below the ground surface. The two source rods are aligned in the same plane as the 3-D velocity transducers, one at a depth of 8.2 ft (2.5 m) and the other at a depth of 10.2 ft (3.1 m). The result is that three sets of velocities can be determined from the set

up at each depth as follows: (1) the P- and S-wave velocities between the source rod and the first 3-D velocity transducer, (2) the P- and S-wave velocities between the source rod and the second 3-D velocity transducer, and (3) the P- and S-wave velocities between the first 3-D velocity transducer and the second 3-D velocity transducer. By measuring all three velocities at each depth, it is also possible to identify lateral variability in the soil at each depth.

The repetitions of the crosshole tests were the same for both the tests performed prior to liquefaction testing and those performed afterward. Each rod was struck once in two directions (upward vertical and downward vertical) for a total of eight repetitions. The direction of the hammer blow has the effect of polarizing the both the P and S wave, meaning the direction in which the soil compresses or shears is reversed. For the P wave time records, hits in the downward direction generated stronger wave signals, making it easier to identify the first arrival.

4.4.2 Liquefaction testing

Liquefaction testing was begun once the initial crosshole tests were completed. The shaking generated from T-Rex was directed horizontally, in-line with the longitudinal axis of the sensor array (see Figure 34). This orientation means the direction of shaking was parallel to the plane in which the sensors were positioned. This setup primarily generates vertically propagating shear waves through the region of interest, although it must be acknowledged that the wave field is more complex due to the limitations of T-Rex with regard to producing pure shear motion. The base plate of T-

Rex experiences a slight rocking motion when shaking horizontally, meaning that there is a minimal, but noticeable, vertical component in the ground motions measured with the 3-D velocity transducers in the array.

The frequencies utilized in the test would ideally fall within the range of typical earthquake shaking. Although the frequencies in liquefaction testing vary between 10 to 30 Hz, they fall within the earthquake range but within the upper frequencies in this range. The force output levels from T-Rex began at a low peak level of 3,000 lbs (13.3 kN) and then gradually increased over the course of testing to a maximum peak level of 30,000 lbs (133 kN). The number of loading cycles ranged from 10 to 50 in the early tests and then was increased to 100 to 500 at the maximum-force-output tests. By starting the tests at low force levels and small numbers of loading cycles, the small-strain behavior of the in situ soil was captured before the degradation created by larger strains occurred and liquefaction altered the soil characteristics. The repetitions performed at the beginning of the test generated dynamic pore pressure fluctuations, but no noticeable increase in the excess residual pore pressure.

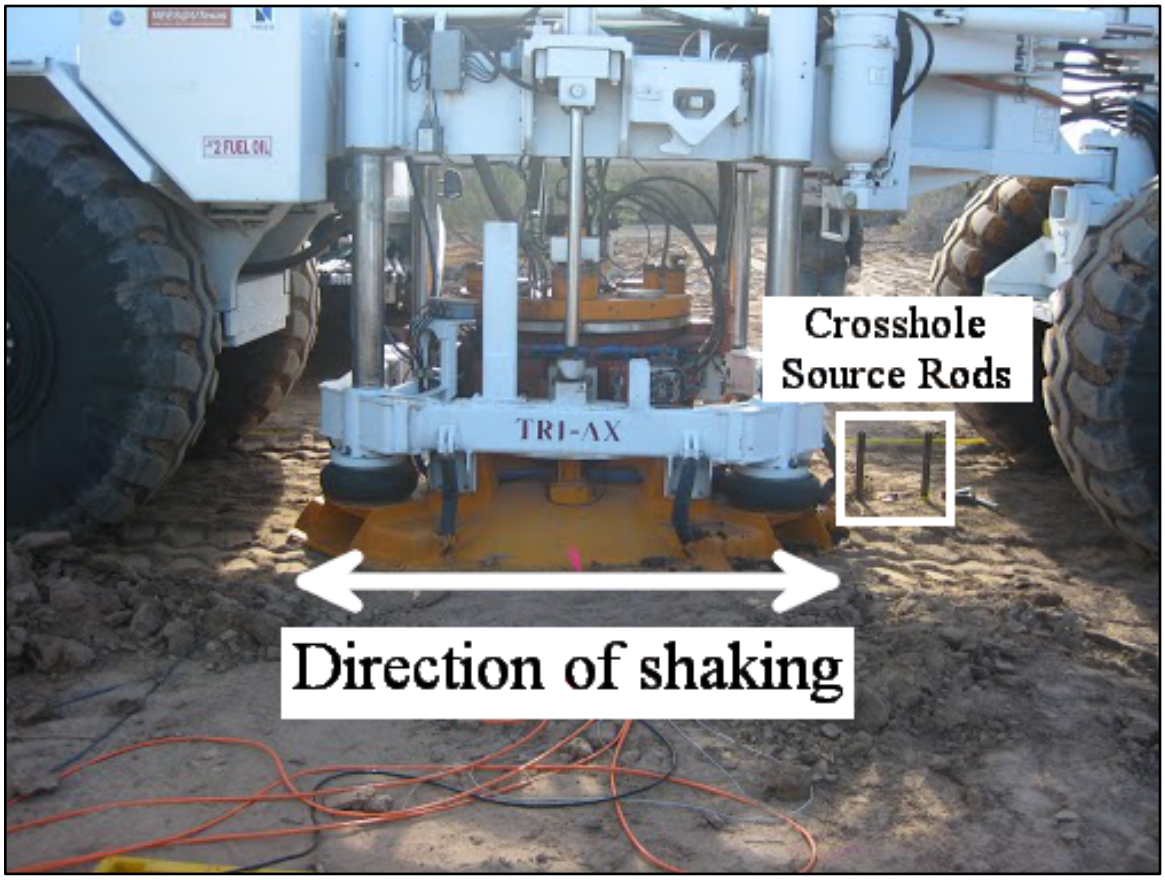

Figure 34. T-Rex in position over the liquefaction sensor array. The locations of the adjacent crosshole source rods are also shown. The direction of shaking is parallel to the axis of the truck and the vertical plane in which sensor array is embedded.

The duration of rest periods between repetitions (staged loading) was determined by the time required for the pore water pressure to dissipate as indicated by the pore pressure transducer that all excess pore pressure from the previous test had dissipated. By the end of testing, the wait between repetitions could be as long as 15 minutes to ensure pore pressure conditions had re-stabilized to the original conditions. Table 1

presents the staged sequence of liquefaction testing with the loading frequencies, number of cycles, force levels, and starting times listed.

Table 1. Sequence of repetitions in liquefaction testing at the WLA with force, frequency, and cycle setting and time at which each series was begun.

Trial #	Test Date	Starting Time	Frequency (Hz)	Cycles	Drive signal input (lbs)
1	3/19/12	12:58	20	50	3,000
2	3/19/12	13:04	25	50	3,000
3	3/19/12	13:07	30	50	3,000
4	3/19/12	13:08	30	20	3,000
5	3/19/12	13:10	15	20	3,000
6	3/19/12	13:10	12	20	3,000
7	3/19/12	13:11	10	20	3,000
8	3/19/12	13:12	30	50	3,000
9	3/19/12	13:14	10	10	3,000
10	3/19/12	13:15	10	20	6,000
11	3/19/12	13:33	30	20	6,000
12	3/19/12	14:13	30	10	6,000
13	3/19/12	14:15	30	10	7,500
14	3/19/12	14:17	30	10	9,000
15	3/19/12	14:19	30	10	10,500
16	3/19/12	14:25	30	10	12,000
17	3/19/12	14:29	30	20	9,000
18	3/19/12	14:32	30	20	12,000
19	3/19/12	14:34	30	20	13,980
20	3/19/12	14:39	30	20	16,020
21	3/19/12	14:45	30	20	18,000
24	3/19/12	15:07	20	20	22,020
25	3/19/12	15:15	20	50	24,000
26	3/19/12	15:22	20	100	27,000
27	3/19/12	15:43	20	100	30,000
28	3/19/12	15:52	10	100	30,000
29	3/19/12	16:07	20	300	30,000
30	3/19/12	16:20	20	500	30,000
31	3/19/12	16:35	10	300	30,000
32	3/20/12	9:55	20	300	30,000
33	3/20/12	10:13	10	300	30,000

4.5 SENSOR REMOVAL AND TEST SITE CLEANUP

Following completion of liquefaction testing, all equipment was removed from the site. The conclusion process included extraction of the sensors and retrieval of the source rods, all of which were recovered intact and redeployed in future projects. Once site cleanup was complete, there was no noticeable permanent deformation of the ground surface.

Before removing the sensors, T-Rex was relocated away from the sensors to allow easy access to the area. The original trench was re-dug to expose the tops of the steel rods that were used to push the velocity sensors into the ground. In addition, the electric cables leading from the sensors to the equipment trailer were also exposed. Care was taken in this work to avoid puncturing the electric cables so they would be in good condition for future testing. The steel rods were prepared for extraction by twisting off the steel caps that protected the rods during testing.

In a reversal of the process that pushed the steel rods into the ground, the hydraulic ram on the back of T-Rex was used to pull the rods out of the ground. For this procedure, a special pulling adaptor was added to the ram mechanism that was outfitted with external threads. These threads allowed the pulling connection to be screwed into the steel rods via the internal threads found at the ends of the rods, ensuring a strong connection between the two. The extraction process commenced by connecting the topmost steel rod to the pulling adaptor and using the ram to slowly pull the rods out of the ground. At the same time, the steel pullout wire connected to the embedded transducer is wrapped several times around a steel peg located on the side of the pulling

adaptor. The steel pullout wire is required for extraction of the transducers because the steel rods were disconnected from the transducers prior to the test. In this manner, both the steel rods and transducer are extracted simultaneously from the ground. Also, the procedure is paused while disconnecting the topmost segments of the steel rod as they clear the ground surface by twisting them off the steel rods that were still in the ground. As discussed previously, the steel rods used for driving the sensors into place are composed of shorter steel rod segments, each varying in length from 1 ft to 4 ft (0.3 to 1.2 m).

After removing the velocity sensors and pore pressure sensor from the ground, the source rods are extracted in a similar manner. The top cap on each of the source rods is removed to expose the internal threads on the steel rods, allowing the pullout connection to be attached. Because there are no separate sensors located below the source rods, the full procedure is restricted to simply pulling out the steel rod and dissembling the segments from one another as they reach the ground surface. Following the removal of the steel rods, velocity sensors, and pore pressure sensor, everything is washed with water to remove accumulated soil before being packed for transport.

4.6 SUMMARY

The overall scope of the project includes the site preparation and sensor installation, testing, and site cleanup. Each aspect is carefully choreographed prior to arriving on site to make sure no step is overlooked and that everything will be functional for the duration of the project. The instrumentation array was designed in geometry,

instrumentation, and location to best capture liquefaction triggering behavior. The preparation and installation of the transducers was a fairly involved process that was performed with care to ensure the reliability and precision of the systems were not compromised. The testing procedures outlined for both the crosshole seismic test and liquefaction test present a methodical approach to data collection that later facilitated data analysis. Finally, the careful extraction of sensors from the ground and reorganization of equipment was particularly important because the majority of the instrumentation are reusable and will be redeployed in future projects.

Chapter 5 – Crosshole seismic testing

5.1 INTRODUCTION

To comprehensively describe the response of the silty sand to large strain cyclic loading, it is important to also understand if and to what extent the sand skeleton has been affected by the cyclic loading. Seismic measurements are well suited to this type of evaluation, often referred to as evaluating small-strain behavior. Changes in the small-strain behavior of a given soil specimen can indicate an alteration in the soil structure that is caused by other phenomenon. As explained earlier in Chapter 2, the risk of liquefaction for in situ soils has also been predicted, in part, by small-strain characteristics; in other words, shear wave velocity measurements. Therefore, there is much to be learned about the in situ soil from small-strain measurements even if the triggering of soil liquefaction itself is a larger strain phenomenon; often at shear strains in the 0.1 to 0.3% range.

For this project at the WLA site, crosshole tests were performed immediately before and after the liquefaction test. The measured P-wave velocities verify that the sensor array was located within fully saturated soil, a condition normally assumed for soil liquefaction to occur. The initially measured S-wave velocities indicate the stiffness of the soil while the S-wave velocities measured after the liquefaction test permit evaluation of any permanent change of the soil skeleton due to test-induced soil liquefaction. The generally low S-wave velocities that were recorded in the sand layer are indicative of its loose structural state, a key characteristic for soil liquefaction.

5.2 CROSSHOLE TEST CONFIGURATION

The crosshole test performed as part of the soil liquefaction project utilized the installed 3-D velocity transducers used to evaluate shear strains during the liquefaction test and the addition of crosshole source rods. The schematic in Figure 35 shows how the crosshole test was performed using the same sensor array as for the liquefaction test. The depths of the two crosshole source rods correspond to the two depths of the 3-D velocity transducers (8.2 ft and 10.2 ft (2.5 and 3.1 m)) and are aligned in the same plane as the sensor array. This arrangement allows a single test repetition to provide wave velocities over direct travel paths in the clayey silt and sand between the following locations: (1) the source and first 3-D receiver, (2) the source and second 3-D receiver, and (3) the first receiver and the second receiver.

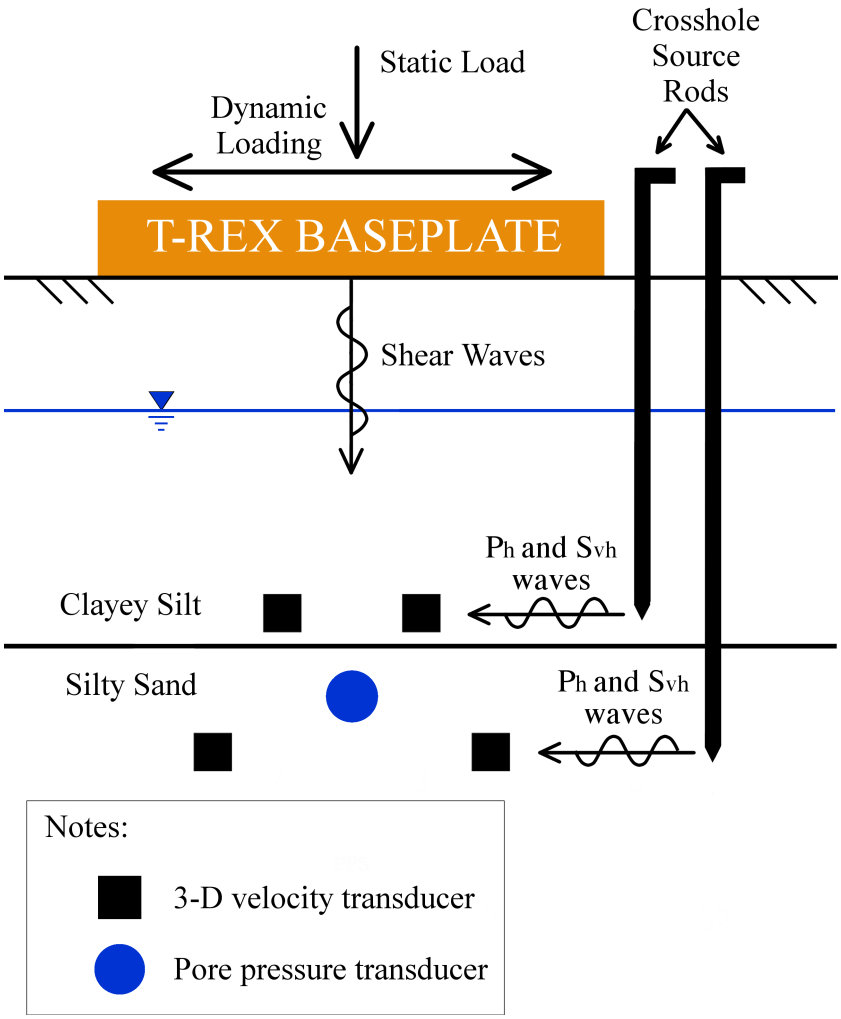

Figure 35. Configuration of the liquefaction equipment and crosshole seismic sources.

Each velocity sensor contains three, 1-D geophones orthogonally situated in an orientation that is optimal for both crosshole and liquefaction testing. The inline horizontal geophone is used to record the arrival of the P-wave because it is oriented in the direction of P-wave particle motion. The vertical geophone is used to record the arrival of the horizontally propagating, vertically polarized S-wave that is generated in

this crosshole setup, also because the vertical geophone is oriented in the direction of the S-wave particle motion.

The top caps screwed onto the top of the crosshole source rods are designed to provide a flat striking surface for a ball peen hammer striking in both the downward and upward directions (used in separate tests). The ability to hit in each direction allowed the shear wave to be polarized in each direction in separate tests, facilitating identification of its arrival in the recorded time series data. The ball peen hammer serves as the energy source for the crosshole test, initiating the propagation of an unconstrained compression wave down the length of the crosshole source rod, which then produces both P- and S-waves propagating horizontally away from the rod. As shown in Figure 36, the hammer head is instrumented with an accelerometer to capture the time at which the initial impact occurs, allowing that time to serve as a reference zero point for travel time measurements and the resulting wave velocity calculations. The time required for the energy to travel the length of the rod from the top cap to the cone tip is recorded (calibrated) in a controlled laboratory setting. This source-rod travel time is subtracted from the overall travel time to ensure only the velocity in the soil is being determined in the measurements.

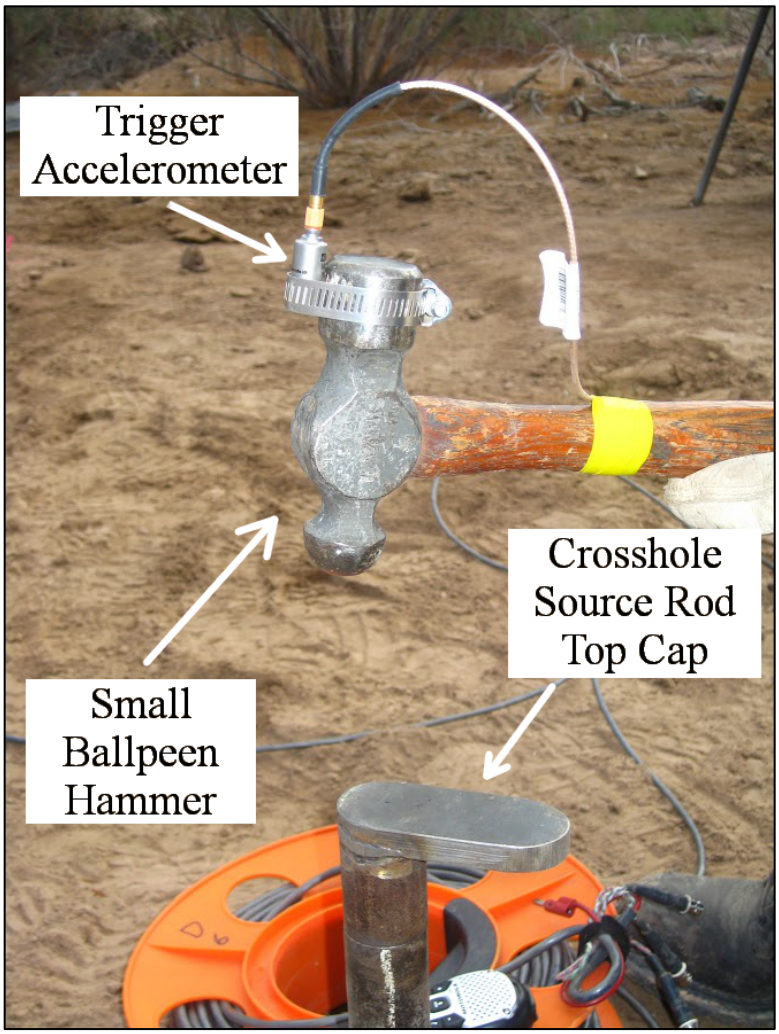

Figure 36. Small hammer with affixed trigger accelerometer that was used as the crosshole source.

5.3 CROSSHOLE TEST RESULTS

The crosshole test was performed both before and after liquefaction testing. The test involved striking the plate attached to the top of the source rods several times in the downward direction to collect one record. The procedure was repeated in the upward direction to collect a second travel-time record. An example time record that was used to identify P-wave arrival times at the two receivers at a depth of 10.2 ft (3.1 m) is shown in

Figure 37. An example of the same measurement, except for the S-wave, is presented in Figure 38. The arrivals of the P-wave and S-wave at each receiver were manually picked for use in the wave velocity calculations.

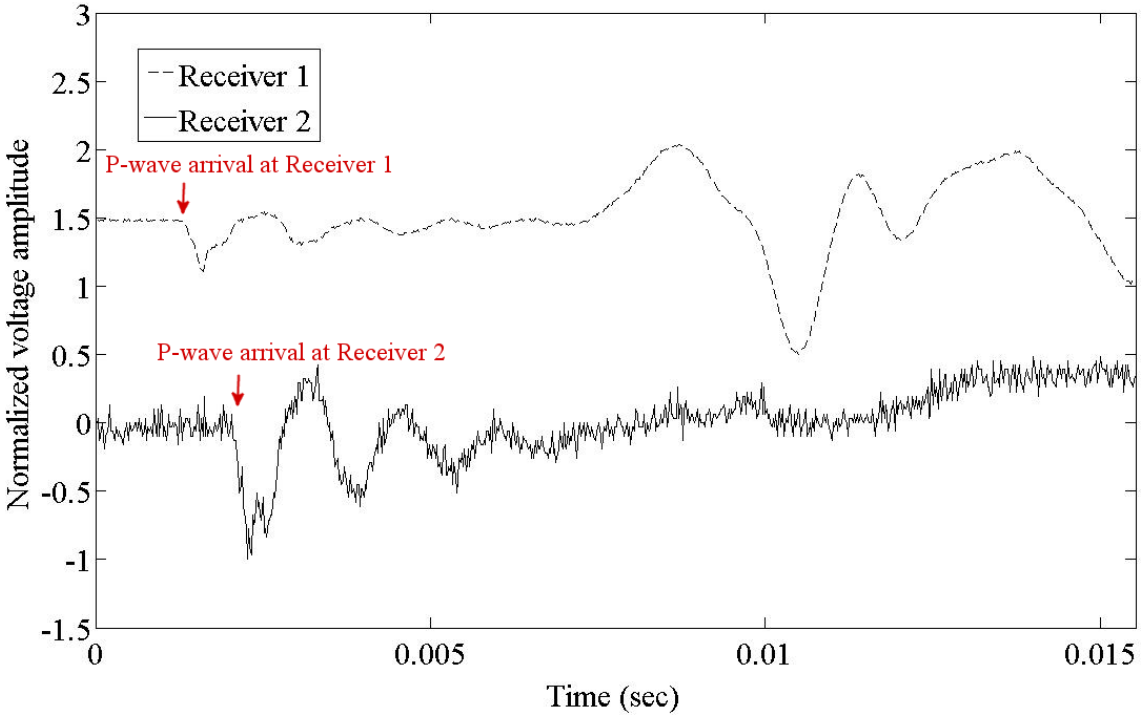

Figure 37. Example voltage time series for P-wave arrivals at Receivers 1 and 2 at a depth of 10.2 ft (3.1 m). The arrivals of the P-waves are identified by the red arrows. In this case, the time records correspond to a crosshole test performed in the sand layer before liquefaction testing.

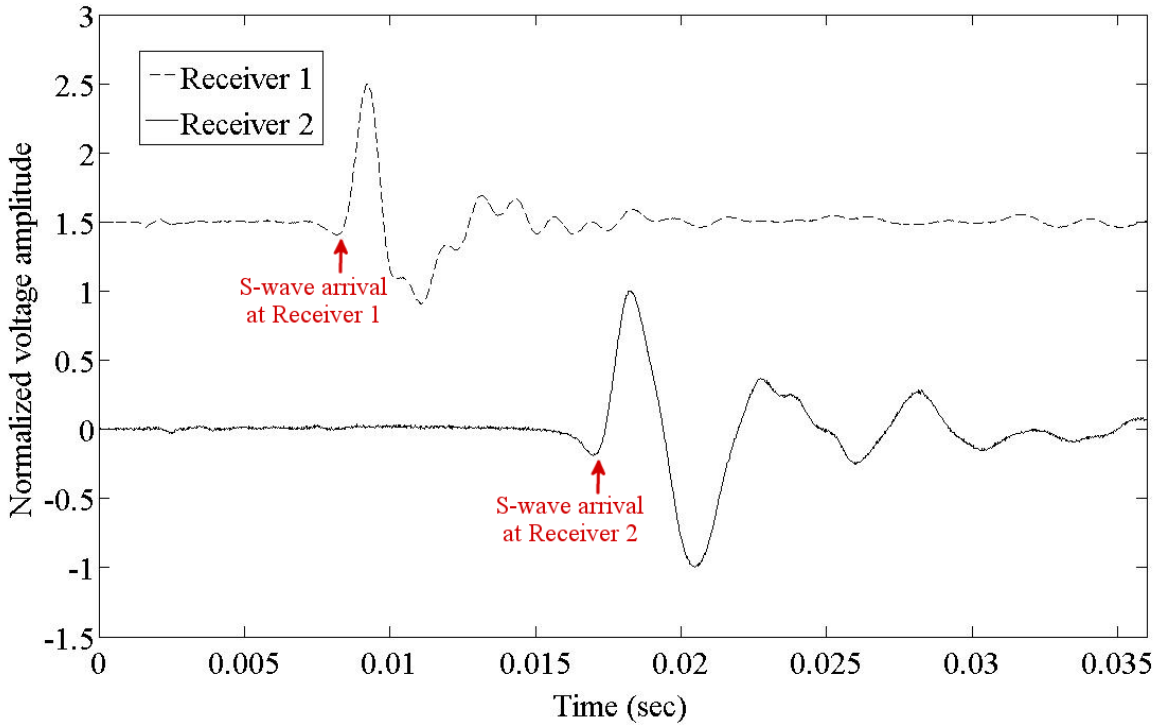

Figure 38. Example voltage time series for S-wave arrivals at Receivers 1 and 2 at a depth of 10.2 ft (3.1 m). The arrivals of the S-waves are identified by the red arrows. In this case, the time records correspond to a crosshole test performed in the sand layer after liquefaction testing.

The wave velocities are determined by dividing the nominal distance between the source/receiver or receiver/receiver pair by the recorded travel time. With the equipment deployed in the field, source rods were initially oriented vertically and then pushed. However, it was not possible to determine if the rods remained vertical during installation or if they drifted off path once they were below the ground surface. However, based on past liquefaction experiments at this site, it is believed that any rod tilting was negligible and that using the nominal horizontal distance between sensors provides adequate accuracy for these calculations.

The summary results presented in Table 2 show the P- and S-wave velocities for the clay and sand corresponding to crosshole tests performed before and after liquefaction testing. The reported values are determined by averaging the two calculated wave velocities resulting from the downward and upward hits.

Table 2. Summary of P- and S-wave velocities determined from crosshole testing.

		Source to Receiver 1		**Source to Receiver 2**		**Receiver 1 to Receiver 2**	
		P-wave velocity	S-wave velocity	P-wave velocity	S-wave velocity	P-wave velocity	S-wave velocity
Material		(ft/sec)	(ft/sec)	(ft/sec)	(ft/sec)	(ft/sec)	(ft/sec)
Before	Clay layer	4,508	367	4,170	343	4,022	305
After	Clay layer	4,527	383	4,347	352	4,657	310
Before	Sand layer	4,920	481	5,058	469	5,058	442
After	Sand layer	4,986	480	5,129	472	5,182	449

There are a number of interesting observations to be made from the results of the crosshole tests. First and foremost, it should be noted that the P-wave velocity measurements greater than 4,500 ft/sec (1,370 m/s) indicate the soil has a degree of saturation greater than 99.9% (Valle-Molina 2006). Full saturation of the soil (or $S_r >$ 99.8%) is an important condition for soil liquefaction to occur; the presence of even a tiny amount of air in the soil-water-air system during dynamic loading increases the compressibility tremendously, stunting the increase in water pressure that triggers soil liquefaction. At this time, there is no clear guideline of how close to 100% saturation a soil needs to be for liquefaction to occur, but greater than 99.8% is probably considered fully saturated for this purpose.

To quantify the permanent change in the soil structure resulting from liquefaction testing, the S-wave values derived from the crosshole tests before and after liquefaction testing can be compared. In this case, the S-wave velocities from before and after liquefaction testing are essentially identical. The velocities recorded across the three pairs of measurement distances (source to first receiver, source to second receiver, and first receiver to second receiver) vary no more than 7 ft/sec (2.1 m/s), which represents less than 2% variation in wave speed. This variation is less then the resolution of the measurements, which is within 4 to 5%. Therefore, this amount of variation is negligible in terms of structural changes to the soil skeleton, indicating there was essentially no permanent change of the soil skeleton as a result of test-induced soil liquefaction. Given the large number of repetitions performed over the course of liquefaction testing, it is important for the overall analysis that the same soil conditions are present at the beginning of each repetition. Thus, these before and after S-wave velocity measurements provide confidence that the initial soil conditions at the beginning of each repetition remained relatively constant over the duration of the test.

5.4 SUMMARY

The purpose of the crosshole seismic testing, with regard to the overall scope of liquefaction testing, was to provide additional insight into characteristics of the in situ soil. Crosshole testing was conducted around and through the liquefaction array at depths of 8.2 ft (2.5 m) and 10.2 ft (3.1 m) to capture the small strain behavior within both the clayey silt and sand layers. The results of the test showed that the sand was saturated, as

indicated by the P-wave velocity, and that there was no change in the soil skeleton due to shaking, as indicated by the before and after S-wave velocities. These two conclusions validate the assumption that initial conditions required for the liquefaction test were present at the time of testing.

Chapter 6 – Data Reduction Procedures for Shear Strain and Pore Pressure

6.1 INTRODUCTION

The data collected in the liquefaction test must be converted into meaningful units before it can be used in an analysis of the soil response during shaking. In this chapter, the methods used to reduce, convert, and derive data sets from the raw data are described. All data reduction in this thesis was performed in MATLAB.

Two kinds of raw data were collected during liquefaction testing: (1) ground particle motion and (2) pore water pressure. A number of important parameters are derived from these two data sets. The ground particle motion recordings by the four, 3-D velocity transducers permit particle velocity to be measured directly, from which 3-D displacements at each velocity transducer are calculated. Shear strains induced in the soil are then derived from the ground motion data. Another useful parameter derived from the 3-D velocity transducers is the shear wave velocity of plane shear waves that are horizontally polarized and vertically propagating through the instrumented array. Finally, the pore water pressures are measured by the pore pressure transducer located in the center of the embedded array, from which ratios of the pore water pressure to the initial vertical effective stress (r_u) are calculated, with the triggering of initial liquefaction occurring when r_u equals 1.0 (or 100%).

6.2 REDUCTION OF RAW DATA SIGNALS FROM THE 3-D VELOCITY TRANSDUCERS

The three, 1-D geophones in each 3-D velocity transducers directly measure particle velocity in three orthogonal directions. The output signal from each geophone is

recorded as a voltage time series, which is then converted to engineering units using a calibration curve. The geophones were calibrated in the laboratory prior to assembly in the 3-D velocity transducer to develop a calibration curve for each 1-D geophone. The calibration procedure used a downward, stepped-sine sweep from 200 Hz to 2 Hz in 1 Hz increments. An example calibration curve for one of the geophones from the project is presented in Figure 39.

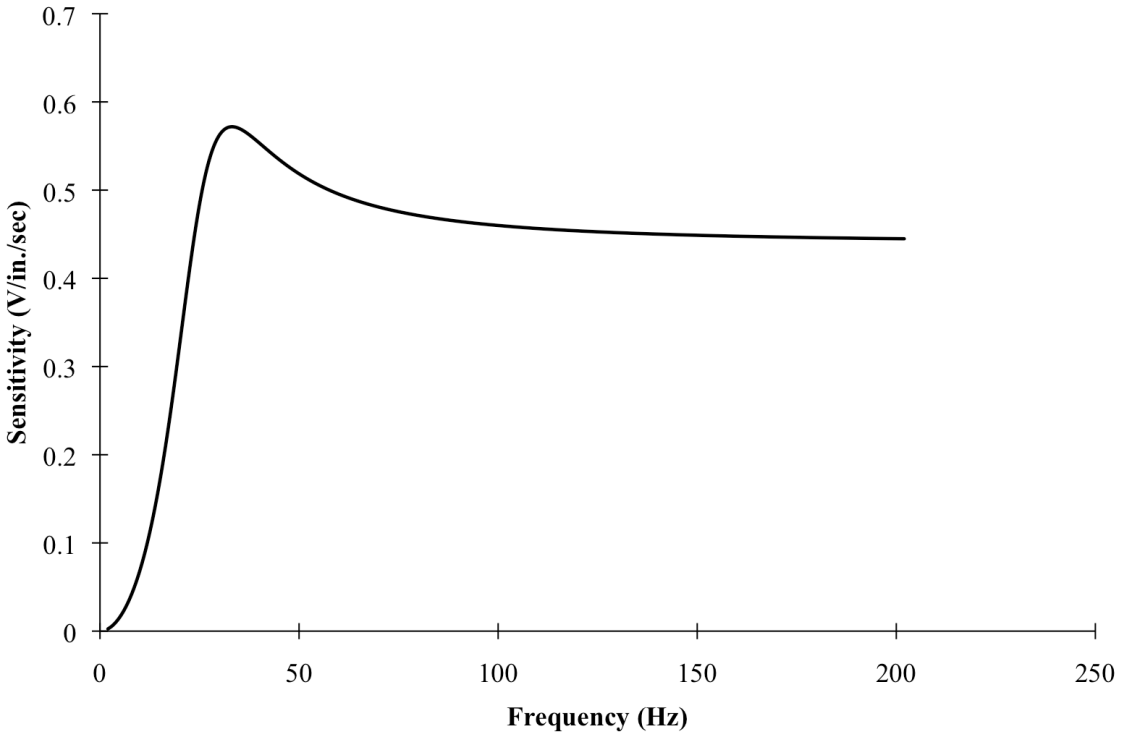

Figure 39. Example calibration curve for one, 24-Hz geophone placed in a 3-D velocity transducer.

The conversion from voltage to velocity units of inches per second is performed in the frequency domain. The Fourier transform of the voltage time series is calculated

and the magnitude of each frequency is scaled according to the calibration curve. Once properly scaled, an inverse Fourier transform converts the data back to the time domain and produces a velocity time series in units of inches per second.

At this point in the data reduction, the time series is also filtered to remove frequencies lower than three hertz. The filtering of low frequencies before integrating velocity to displacement is performed to avoid the appearance of permanent sensor displacement due to low-frequency noise in the data. The low-frequency "filtering" is accomplished with an acausal Butterworth filter. An example of the time series of raw voltage recorded in the field is shown in Figure 40. The converted signal to a particle velocity time series in units of inches per second is shown in Figure 41.

The displacement-time series is calculated from the particle velocity-time series by integration. For a discrete time series, integration is estimated by the trapezoid method where the velocities of two adjacent time steps are averaged and then multiplied by the length of the time step. An example displacement-time series shown in Figure 42 was calculated from the example particle velocity-time series shown in Figure 41.

The shear strain evaluation method employed in the analysis is the displacement-based method described in Rathje et al, 2004, and explained in detail in Section 2.5.1. While velocities in three dimensions were recorded during testing, only those in the vertical and inline horizontal directions were used to calculate shear strain. The finite-element analysis method utilizes the two-dimensional velocity measurements from each of the four nodes in the trapezoidal array. The example shear strain time series calculated

using eight, displacement-time series, encompassing all four nodes, is shown in Figure 43.

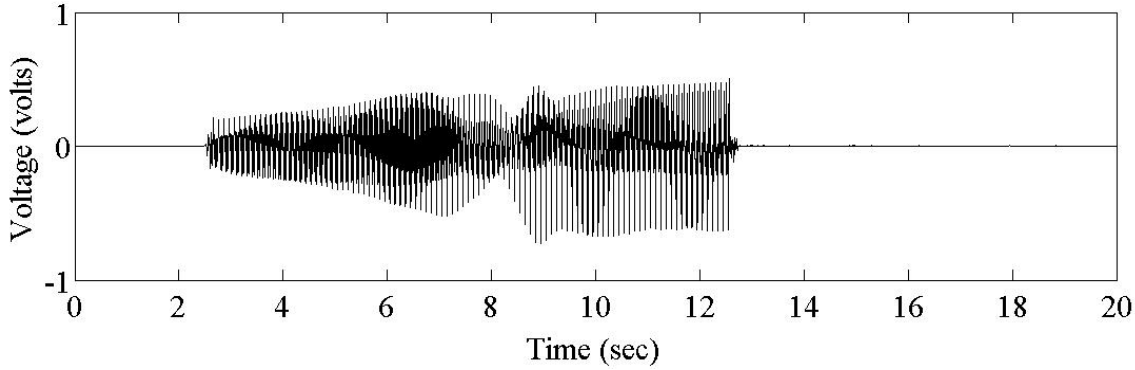

Figure 40. Example voltage time series from 1-D horizontal geophone in direction of shaking in Repetition 28 of the liquefaction test. This time record is the unprocessed signal recorded in the field.

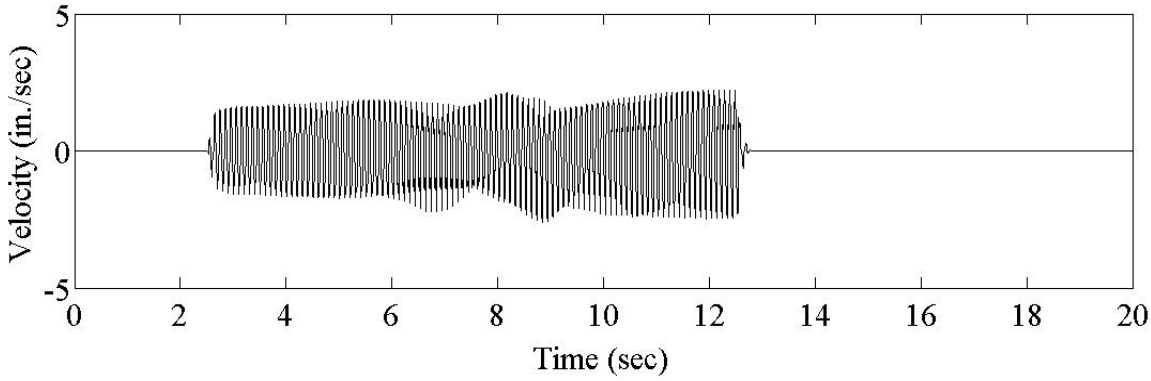

Figure 41. Example velocity-time series corresponding to Repetition 28. This time record was filtered to remove frequencies below 3 Hz and was converted from voltage to particle velocity by applying a frequency-dependent calibration factor.

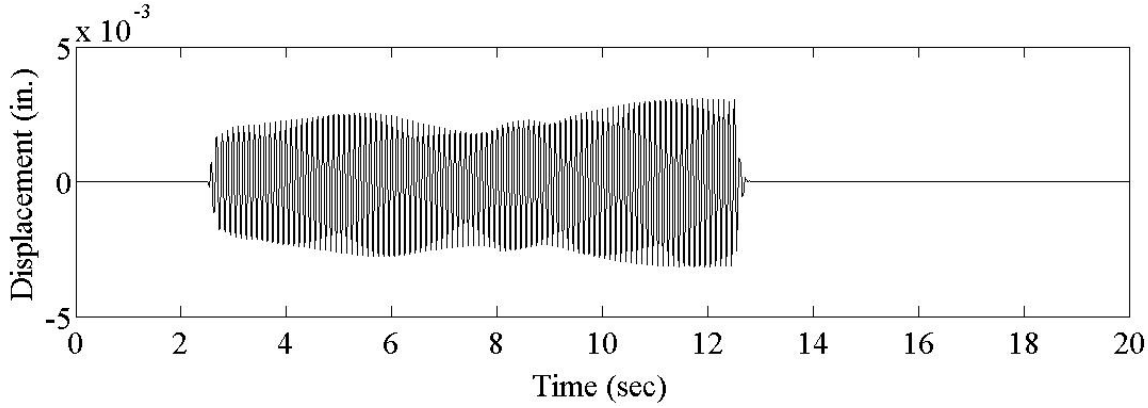

Figure 42. Example displacement-time series corresponding to Repetition 28. This time record was calculated from the particle velocity time series (Figure 6.3) by integration using the trapezoid method.

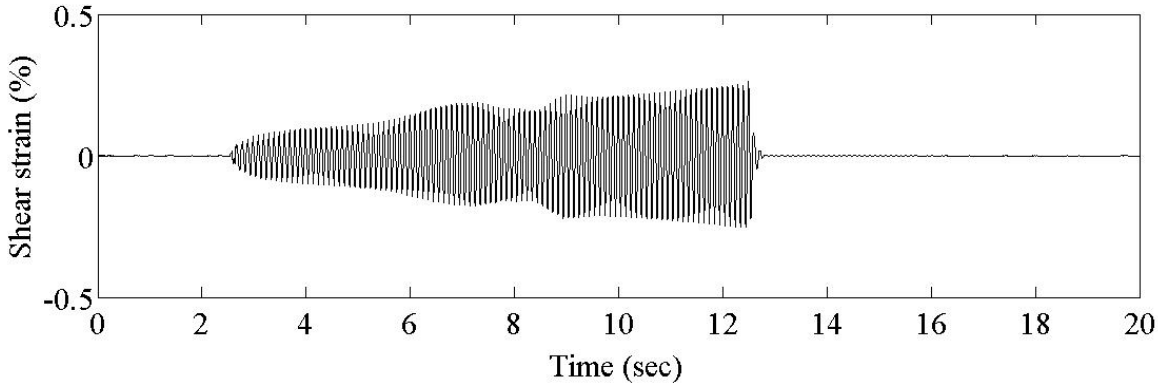

Figure 43. Example shear strain-time series corresponding to Repetition 28. This time record was calculated from the eight, particle displacement-time series evaluated at the four nodes (vertical and inline horizontal components at each node).

Calculation of shear strain from the particle velocity recordings marks the final step in data reduction from the full time series. As discussed, the geophones directly provide records of particle velocity (once the calibration factor is applied), from which the other parameters of displacement and shear strain can be evaluated. Additional

information can be obtained by analyzing each of these time series in more detail, with the process discussed in following sections.

6.3 CALCULATION OF PEAK AND AVERAGE SHEAR STRAIN AMPLITUDES

Calculation of shear strain within the instrumented array is one of the more critical aspects of the data analysis in liquefaction testing. The magnitude of shear strain induced over the course of staged loading is subject to variation depending on the number of cycles and loading force being applied. For example, for a large number of cycles and high loading forces, the amplitude of the shear strain signal may increase or decrease during the cyclic loading. On the other hand, for a low number of cycles and low loading forces, more consistently similar shear strain amplitudes during the loading period occur.. To capture the variation in shear strain magnitude over the course of each loading stage (repetition), peak shear strain values are averaged after 10, 20, 50, and 100 cycles when the total number of cycles permits.

Peak shear strain values are first calculated by identifying the portion of the time series in which shaking occurred and then separating each cycle for individual analysis. The maximum and minimum points in each cycle are found, which correspond to the positive and negative shear strain peaks achieved during that point in the time record. Since the distinction between a positive and a negative number is the direction in which the soil is straining, the absolute values of the positive and negative shear strain peaks are averaged to give a single peak value for the respective cycle. An example of how the

positive and negative peaks were successfully identified for Repetition 28 is shown in Figure 44.

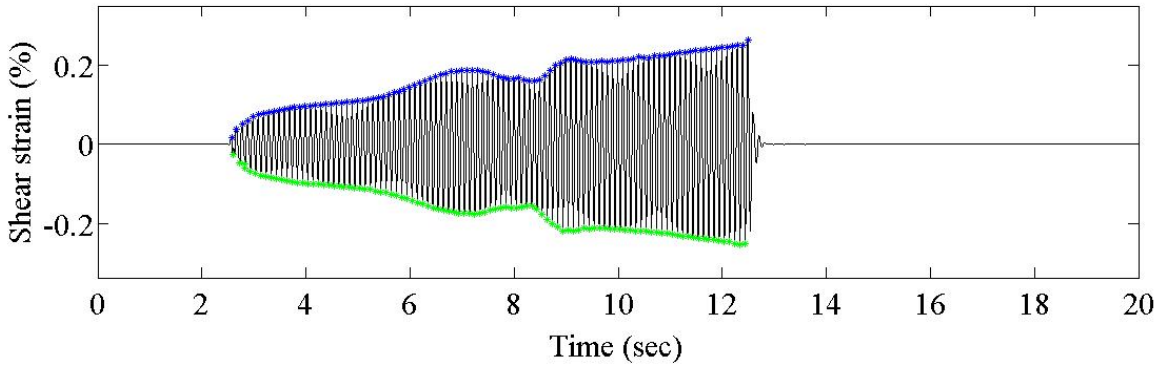

Figure 44. An example of the positive and negative peak values selected for the shear strain time series corresponding to Repetition 28 of liquefaction testing. The blue dots identify the positive peaks while the green dots identify the negative peaks, ensuring the peaks were accurately identified.

Once the peak shear strain values for each cycle are determined, it is a simple matter to find the average shear strain after 10, 20, 50, and 100 cycles. For this analysis, shear strain averages always begin from the first cycle rather than moving along the time record, though a moving average method may also be valid and should be considered in the future. These calculated averages are a way of summarizing the shear strain time history so that they can be more easily compared across repetitions as well as against the generation pore pressure.

6.4 Analysis of Shear Wave Velocity Degradation During Pore Pressure Generation

Shear wave velocity of soils is an important parameter used to monitor changes (in this case degradation) in the soil skeleton. A change in shear wave velocity during the

generation of positive pore water pressure indicates a soil skeleton that is softening from a decreasing effective stress as well as structural deformation, both of which occur at the largest cyclic loading stages as the soil approaches soil liquefaction. Calculation of the shear wave velocity of the soil skeleton during a loading stage is less precise than an individual downhole test at the same stress state. However, it is not possible during a loading stage to perform downhole testing during each cycle. Therefore, the cycle by cycle the results during each loading stage still provide insight into degradation of the sand as it approaches liquefaction.

The basic assumption is that the majority of energy generated by a horizontally shaking baseplate of T-Rex is vertically propagating shear waves with a reasonably plane wave front directly beneath the baseplate. Based on this assumption, the shear wave velocity corresponds to material located vertically beneath the baseplate, between the top 3-D velocity transducers in the clay layer and the bottom 3-D velocity transducers in the sand layer. Shear wave velocity values can be determined between pairs of 3-D velocity transducers in each layer, with the transducer in the adjacent layer on the same side of T-Rex's baseplate. Each receiver pair can be established and two shear wave velocity calculations can be made as illustrated in Figure 45.

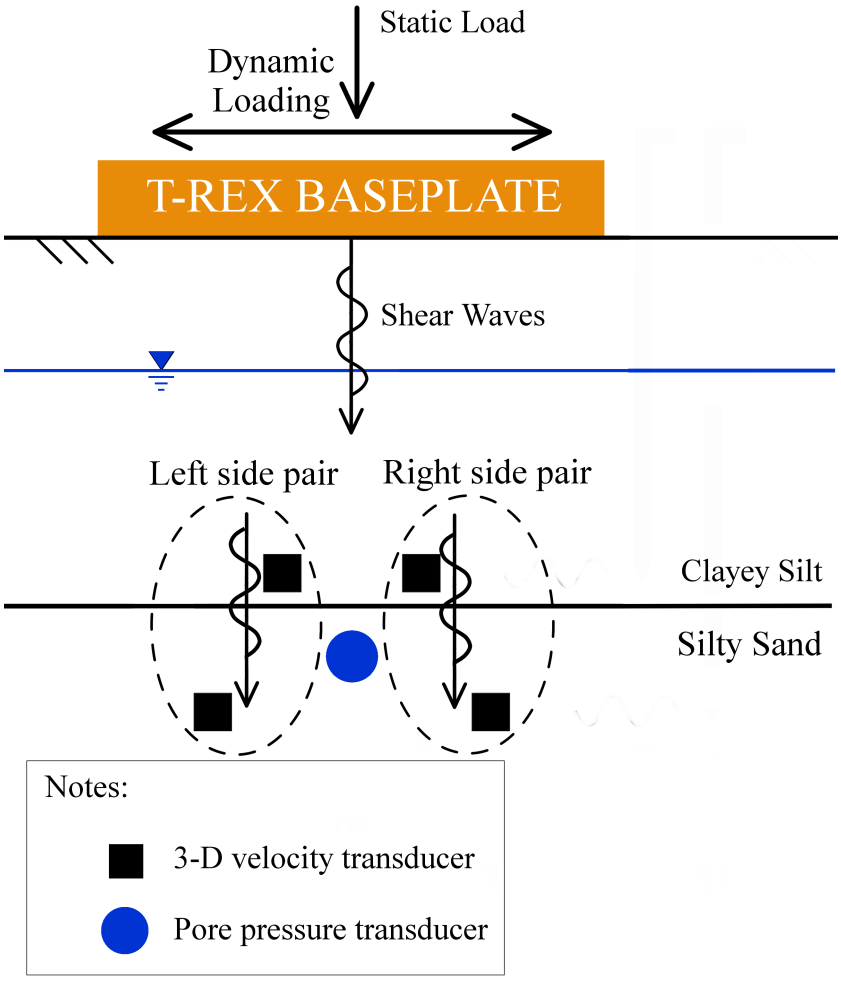

Figure 45. Pairs of 3-D velocity transducers used to calculate shear wave velocities during horizontal shaking. The two receivers on the left side form one pair and the two receivers on the right side form the other pair.

By looking at the velocity time records from the in-line horizontal geophones in each receiver pair, the travel time for the shear wave is determined by measuring the time delay between the waveform in the clayey silt layer geophone compared to that in the sand layer below, keeping in mind that at least 75% of the travel path is in the sand. The time delay between time records is determined identifying significant, similar features in

each waveform and matching them across records; in this case, the peaks of the cyclic shear strain were identified and matched. While less precise than using a simple transient record, this method allows a shear wave velocity to be calculated for each loading cycle rather than just a single value for the entire time series or several values for segments of the time series. This method works well for Repetitions 12 through 27 because the waveform remains relatively uniform through the loading cycle. Before Repetition 12, the recorded wave form is not strong enough to provide precise calculations of the shear wave velocity and beyond Repetition 27 the waveform is too nonlinear to be analyzed using this method and, at this time, has not been evaluated further. Figure 46 shows an example of the results from this shear wave velocity analysis for Repetition 26 (see Table 1 for summary of liquefaction testing loading stage information).

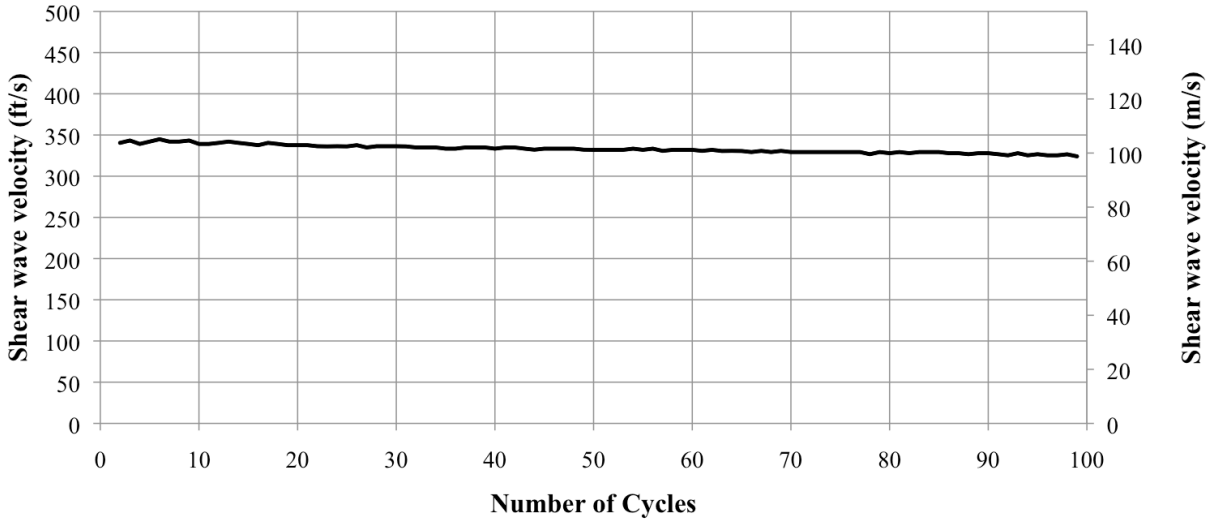

Figure 46. Example of the shear wave velocity trend versus number of cycles of loading for Repetition 26 of liquefaction testing over the course of 100 cycles

Cross-correlation was initially considered for this analysis but ultimately rejected in favor of the matching-peaks method; the nonlinearity in the time records made it inappropriate for the cross-correlation method to be used because it would average the time delays over portions of the time records. In the end, however, the results from this shear wave velocity analysis are not presented in this thesis. The main challenge with the analysis is that the sampling frequency used to collect data during shaking for this project was much to slow to accurately see any meaningful change in shear wave velocity during shaking. Future projects will address this issue by increasing the sampling frequency accordingly.

6.5 ANALYSIS OF PORE WATER PRESSURE DATA

The pore water pressure data come directly from the pore pressure transducer located in the center of the instrumented array. The recorded differential voltage is converted into units of pounds per square inch using the sensitivity factor of 0.98mV/V/psi, as discussed in Chapter 3. To study pore water pressure generation and the triggering of soil liquefaction, pore water pressures are best considered in terms of the pore water pressure ratio, r_u, which is equal to the change in pore water pressure (excess pore water pressure) divided by the initial vertical effective stress (σ_v'):

$$r_u = \frac{\Delta u}{\sigma_V'} \tag{6.11}$$

The value of r_u is individually calculated for each repetition using the static pore water pressure value recorded during the quiet period before shaking begins. This presumes

that the static pore water pressure at that time is indicative of the in situ conditions that are normally present; indeed, Figure 47 shows that the pore water pressure in the vicinity of the pore pressure transducer remains constant throughout the experiment except for some slightly elevated values for the last three repetitions.

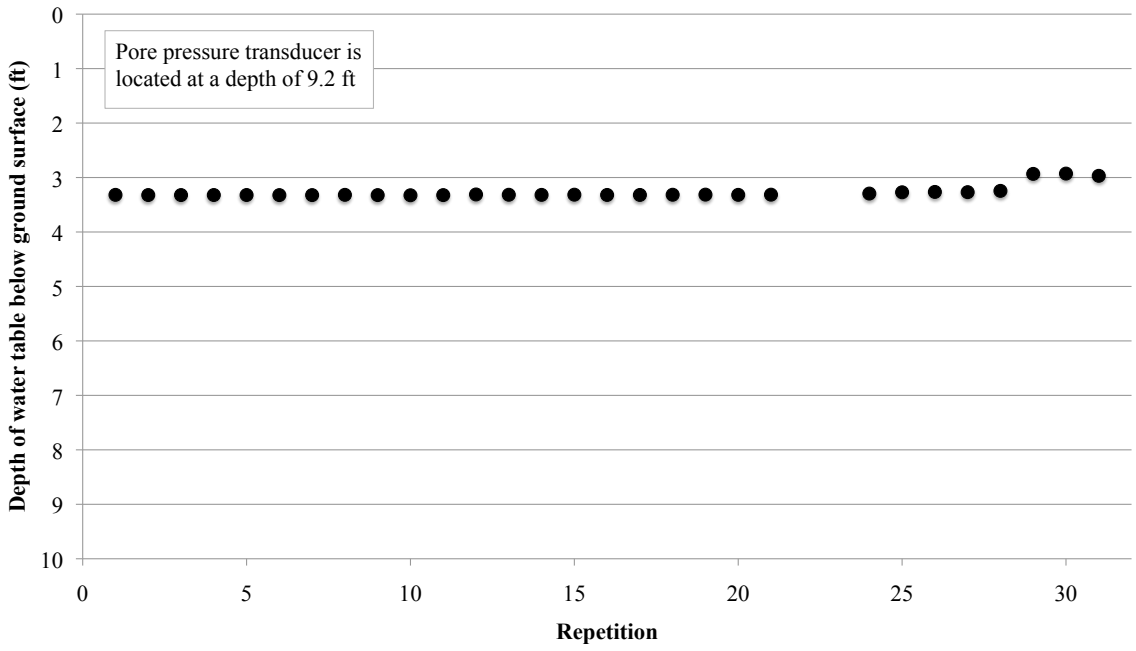

Figure 47. Depth of water table below the ground surface at the commencement of shaking for each repetition.

In a manner similar to the signal processing for the particle velocity time records, the data from the pore pressure transducers are processed to remove frequencies greater than 40 Hz. The objective of this filtering is to remove high-frequency noise from the signal and improve the signal-to-noise ratio. The high-frequency filtering is accomplished with an acausal Butterworth filter. Figure 49 presents an example of a pore

water pressure ratio time series that has been processed in the aforementioned manner from the unprocessed voltage time series shown in Figure 48.

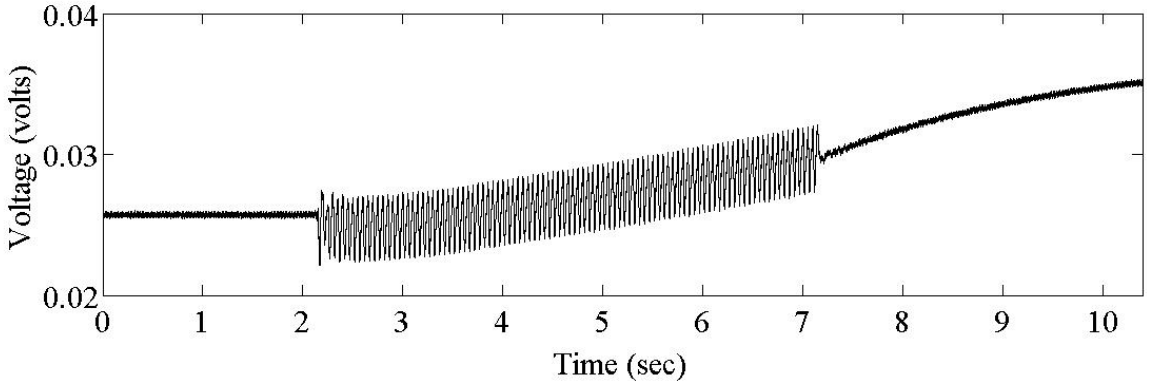

Figure 48. Example voltage time series from the pore pressure transducer. This time record is the unprocessed signal recorded in the field and corresponds to Repetition 26 of liquefaction testing.

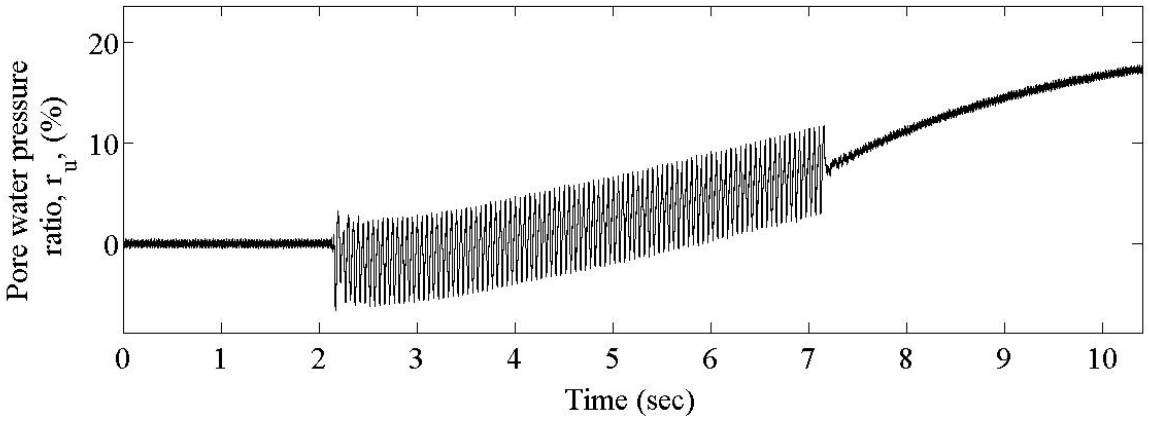

Figure 49. Example pore water pressure ratio time series corresponding to Repetition 26 of liquefaction testing.

Once a pore water pressure time series is processed, the next step is to determine the r_u value at the end of 10, 20, 50, and 100 cycles for comparison with the shear strain averages at those same number of cycles. In this case, the residual excess pore water

pressure is a better indicator of the excess pore water pressure at that point than the transient excess pore water pressure. The cutoff frequency used to filter out the transient excess pore water pressure is dependent on the shaking frequency, but is generally 10 to 20 Hz less than the shaking frequency when possible. This filtering is also accomplished with an acausal Butterworth filter, but this time as a low-pass filter. The r_u values at the end of 10, 20, 50, and 100 cycles are determined from this residual pore water pressure plot and then later matched with the corresponding peak shear strain average. Illustration of the use of a low-pass filter to separate the residual pore water pressure from the transient pore water pressure and the identification of the 10^{th}, 20^{th}, 50^{th}, and 100^{th} loading cycles is shown in Figure 50.

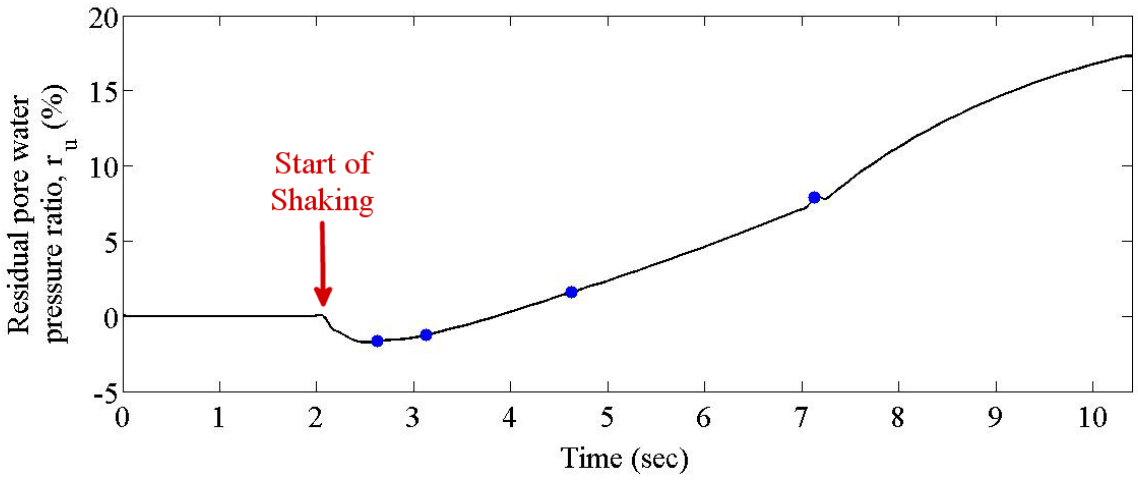

Figure 50. Example of residual pore water pressure ratio plot corresponding to Repetition 26 of liquefaction testing. The black line is the residual pore water pressure ratio and the four blue dots indicate the points at which the 10^{th}, 20^{th}, 50^{th}, and 100^{th} cycles occur.

6.6 SUMMARY

The 3-D velocity transducers and pore pressure transducers are the primary recording instruments in direct liquefaction testing in the field. The raw data from both types of transducers are enhanced by signal processing to remove frequencies outside the range of interest, making it easier to view and analyze the data. The information contained within the velocity time series can be used to determine shear strain at any point within the instrumented array as well as to calculate the shear wave velocity of horizontally polarized, vertically propagating, shear waves traveling through the instrumented array. The pore water pressure transducers are used to determine the elevation of static water table prior to shaking and to record both the residual and transient pore water pressures during shaking. Together, the 3-D velocity transducers and pore water pressure transducers capture the complex behavior of pore water pressure generation with number of cycles and shear strain amplitude that lead to the triggering of soil liquefaction, enabling a direct evaluation of the parameters that influence the liquefaction susceptibility of soil.

Chapter 7 – Analysis of T-Rex Performance and Soil Response During Cyclic Loading

7.1 INTRODUCTION

The main objective of direct field liquefaction testing is to characterize the liquefaction susceptibility of soil in situ. The response of the soil during testing, however, is affected by complex relationships between the performance of T-Rex, the response of the soil system, and possible drainage during cycling. To better understand the response of the soil to cyclic loading, the performance of T-Rex in terms of force output, frequency dependence, and baseplate displacement and its effect on soil response is investigated in these field tests.

Once the performance of T-Rex is better understood, the response of the soil during cyclic loading can be studied in detail. Of great importance in soil liquefaction susceptibility studies is the amount of residual excess pore water pressure developed for given levels of shear strain during cyclic loading. To this end, relationships between pore water pressure generation, cyclic shear strain, γ, and number of loading cycles, N, are evaluated. These relationships are presented in terms of r_u versus γ plots for selected values of N. These plots also aid in the identification of the cyclic threshold strain, γ_t^c, for the material, a parameter that indicates the minimum shear strain at which the generation of residual excess pore water pressure begins to occur.

7.2 PERFORMANCE OF T-REX DURING HORIZONTAL, CYCLIC LOADING

T-Rex is a complex, electro-mechanical nonlinear machine that is capable of generating very large vibrational output forces in both the vertical and horizontal directions, as discussed in Section 3.4. Shaking in the horizontal mode (direction) is of particular interest for this project since the objective is to generate shear strains in the soil column below the baseplate. The amount of shear strain induced in the soil by T-Rex, however, is not just a function of the force output but also a function of the displacement of the baseplate which is impacted by the shaking frequency.

As a first order approximation, the force output of T-Rex is considered to be constant regardless of frequency for frequencies between 5 and 180 Hz, as shown in Figure 51. Because of the large drop-off in force output for frequencies below 5 Hz, the minimum shaking frequency used in the study is 10 Hz. The maximum frequency used in the study is 30 Hz, which is well below the maximum frequency beyond which force output drops off exponentially.

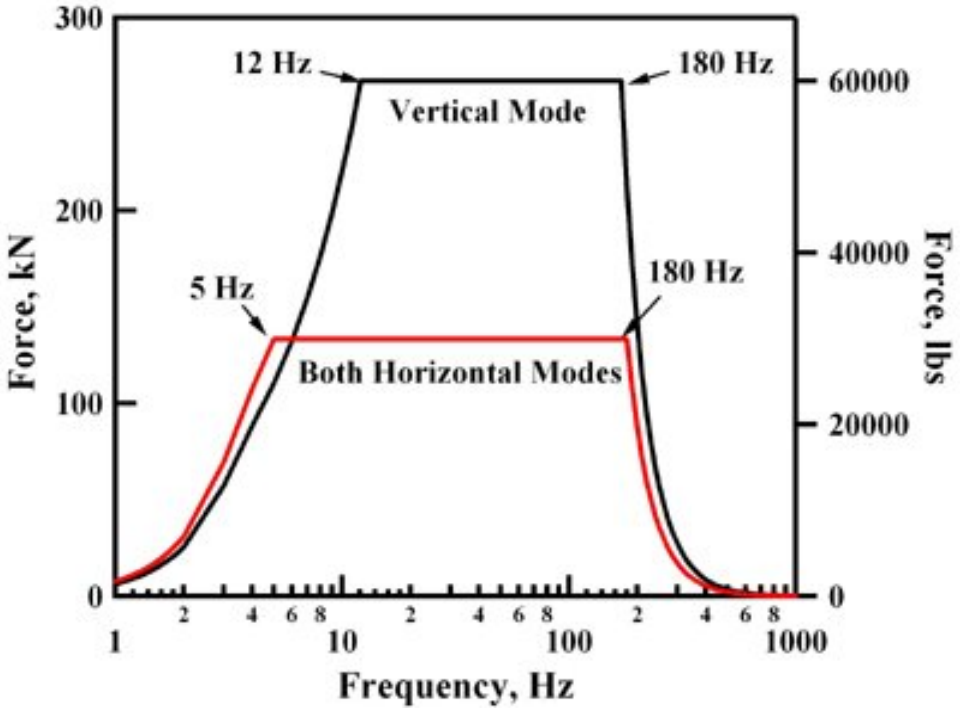

Figure 51. Theoretical force output of T-Rex shaking a rigid halfspace as a function of frequency for shaking in the vertical and horizontal modes (directions).

The difficulty in assuming a constant force output regardless of frequency is that the operator can only control the voltage of the drive signal that is sent to T-Rex. The theoretical drive force can be converted to engineering units from voltage using Equation 7.12:

$$F = \frac{XV}{5V} \times 30{,}000lb \tag{7.12}$$

where X is the drive voltage and 5V is the maximum allowable drive voltage that will generate a 30,000 lbs (133 kN) output force on a rigid half-space. Due to non-linearities in the internal electrical and mechanical systems of T-Rex, there is not a linear relationship between the voltage chosen for the drive signal and the voltage resulting

from the vibe output signal, which is a calculated estimate of the true force imparted by the baseplate. The vibe output signal is calculated by summing the dynamic force of the baseplate and the reaction mass, as determined by Equation 7.13:

$$F_{output} = m_{RM} \times a_{RM} + m_{BP} \times a_{BP} \tag{7.13}$$

where m_{RM} is the mass of the reaction mass, a_{RM} is the recorded acceleration of the reaction mass during shaking, m_{BP} is the mass of the baseplate, and a_{BP} is the recorded acceleration of the baseplate during shaking (Menq et al., 2008).

The relationship shown in Figure 52 compares the estimated output force from T-Rex against the inputted drive signal representing the desired output force. This plot can also be considered the relationship between observed force output (T-Rex force output) and theoretical force output (Drive signal). If the relationship between force output and drive signal was linear and one-to-one, the data points would fall along the 45° line drawn through the graph. For force levels lower than 15,000 lbs, there is good agreement between the drive signal and the force output, though there is a slight bias for the vibe output to be lower than the drive signal. As soon as the drive signal force exceeds 15,000 lbs, the force output of T-Rex at the WLA site flattens out and essentially becomes independent of the drive signal. While this behavior is concerning, it is difficult to know if the force output experiences saturation and ceases to increase. To add to the complexity of the problem, it is seen that for several shaking trials corresponding to the 30,000-lbs drive signal, there is significant scatter in the output forces level of T-Rex that range from 12,000 to 22,200 lbs.

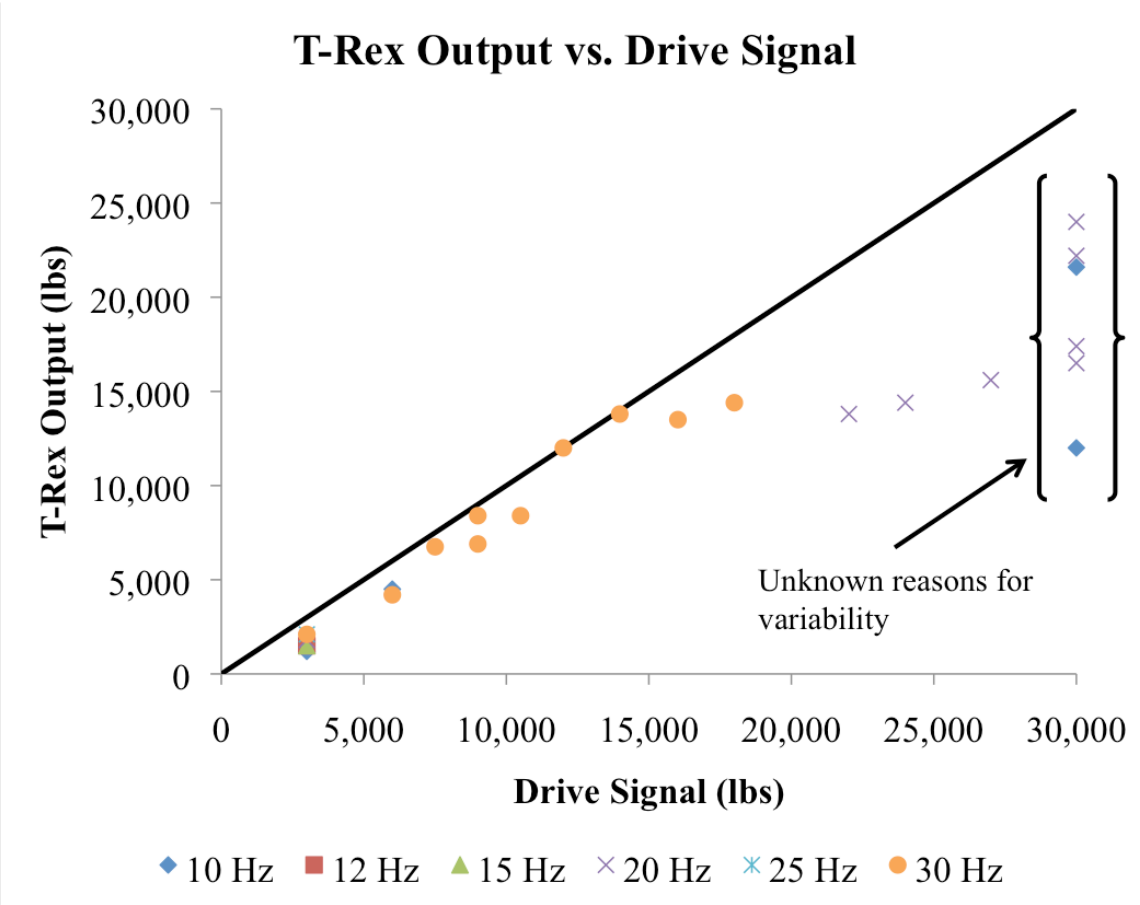

Figure 52. T-Rex output force versus the drive signal for T-Rex for all 31 shaking trials at WLA.

In addition to the non-linear relationship between the drive signal input and force output, the shaking force generated by T-Rex is also slightly frequency dependent. For the lowest force levels of shaking, it is observed that the force output consistently increases with increasing frequency. The results in Figure 53 show the first six shaking trials performed in the experiment, all of which had a 0.5 V drive signal (equivalent to a 3000-lbs shaking level on a rigid half-space). The shaking frequencies ranged from 10 to 30 Hz and the force output ranged from 1,200 to 2,100 lbs. Unfortunately, this is the only

drive signal level that can be analyzed at multiple frequencies due to limitations in the data set. While the relationship between vibe output force and shaking frequency is clear for this low drive signal level, it is also known that T-Rex does not operate well at these low forces. It is unclear what the frequency dependence of the system would be at larger forcing values.

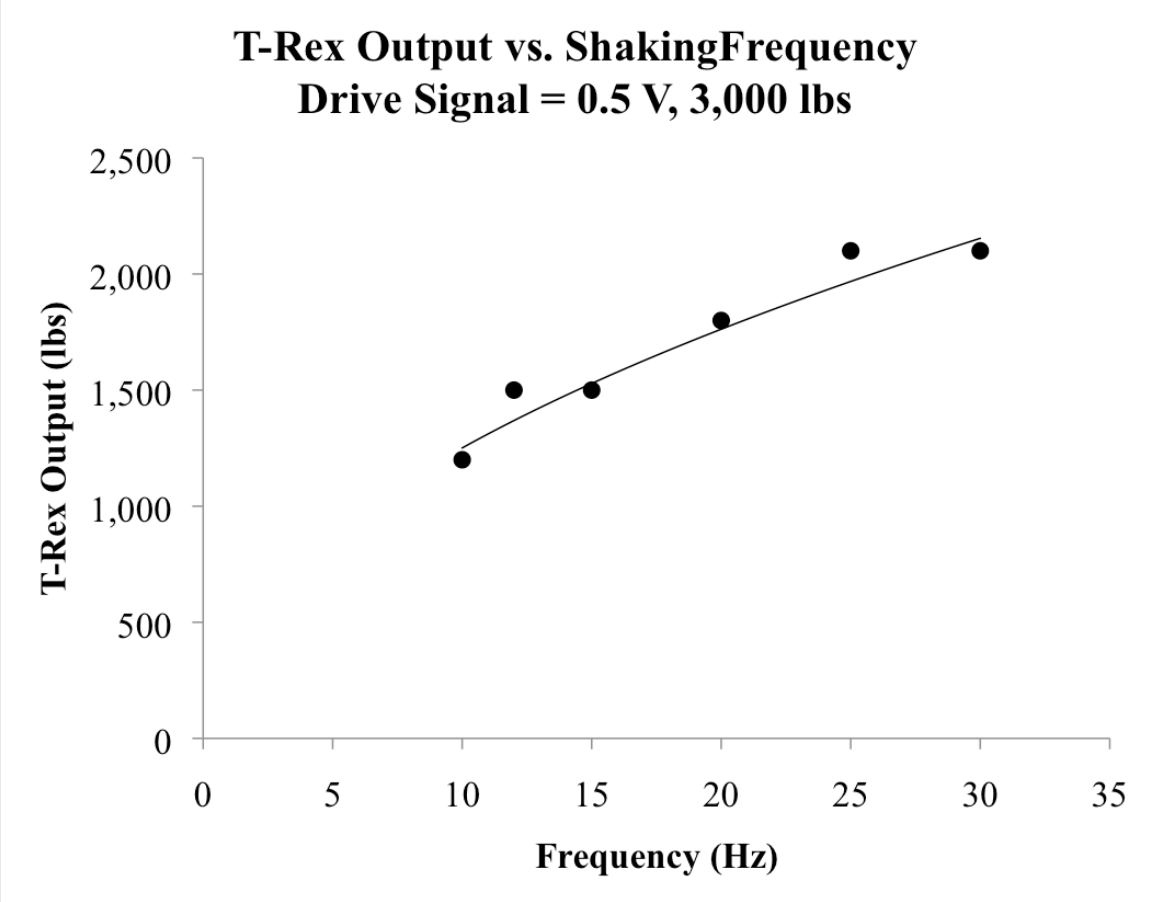

Figure 53. Output force level versus cyclic frequency for the first 6 shaking trials, all with a 0.5-V (3,000-lbs) drive signal.

Another angle from which to approach the dynamics of T-Rex shaking is to look at the displacement of the baseplate as a function of frequency and force output. The displacement of the baseplate is an important parameter because it is the surface deformation in the soil that will propagate with depth and is the source of induced shear strain. The baseplate displacement is calculated by twice integrating the acceleration time record from an accelerometer affixed to the baseplate. In Figure 54, the baseplate displacement and shaking frequency are reported for the first six shaking trials, all of which had the same 0.5-V (3,000-lbs) drive signal. As expected, there is a clear trend of displacement decreasing as frequency increases. It is interesting, however, that the largest baseplate displacement at 10 Hz also corresponds to the lowest vibe force output as shown in Figure 53. Again, due to limitations in the data set, this analysis could not be performed at forces beyond the lowest level.

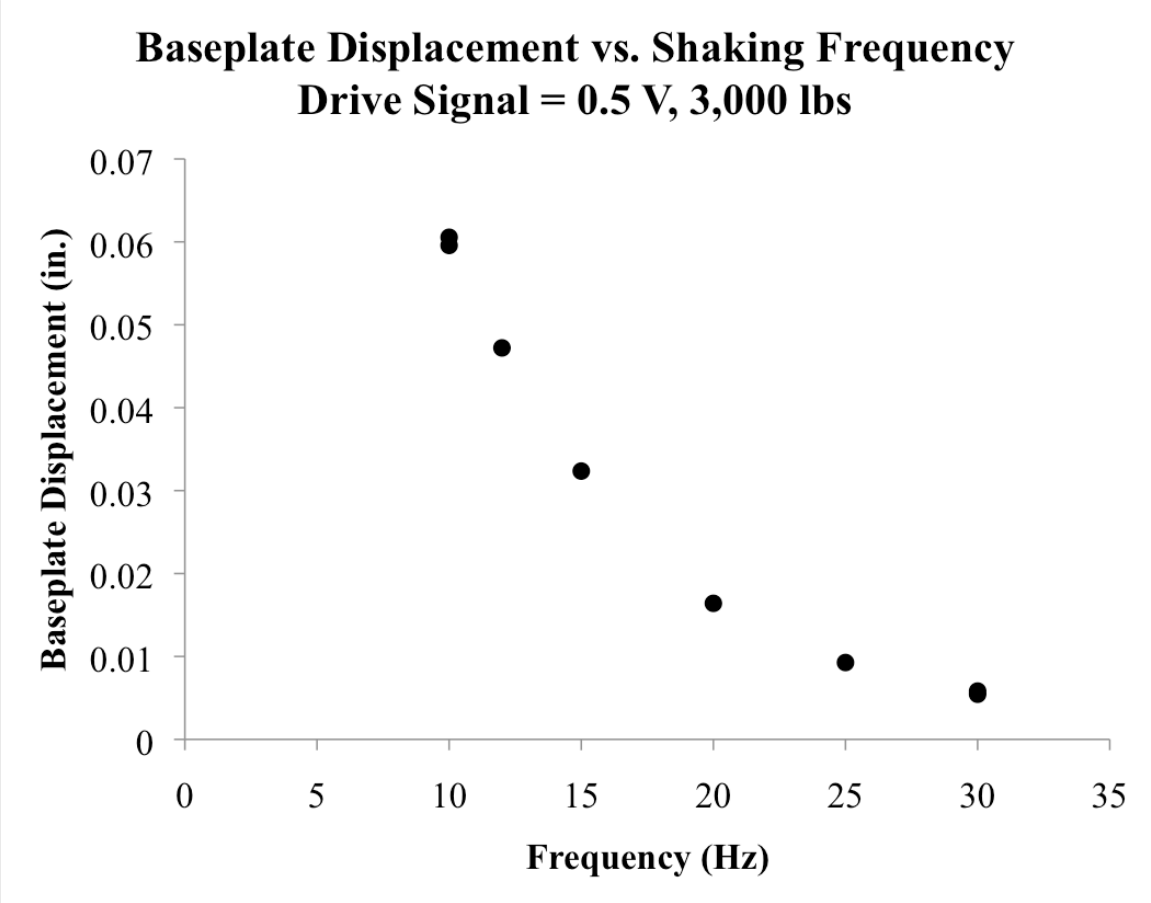

Figure 54 Baseplate displacement versus cyclic frequency for the first 6 shaking trials, all with a 0.5-V (3,000-lbs) drive signal.

It is important to understand the performance of T-Rex in horizontal shaking so that a comprehensive set of strain levels can be generated in the soil to later permit an understanding the response of the soil due to this shaking. As discussed above, T-Rex is a complex machine with nonlinear outputs that vary, at the very least, as a function of drive signal level and the excitation frequency. In addition, the soil itself has an effect on the shaking of the baseplate due to soil/structure interaction. The stiffness and response of the soil will have an effect on how much force and displacement the baseplate can impart,

which are parameters that will change over the course of the experiment with increasing force levels. Understanding the performance of T-Rex under varying of conditions needs to be pursued in greater detail in future projects.

7.3 ANALYSIS OF SHEAR STRAINS AND PORE WATER PRESSURES GENERATED DURING SHAKING

7.3.1 Frequency dependence of shear strain

Based on the results shown and discussed in Section 7.2, it is apparent that the shaking frequency is a factor that affects the level of shaking created by the baseplate as well as the response of the soil. The stiffness and natural frequency of the soil will also affect the response motion of the baseplate during shaking, making isolation of each system during shaking very difficult if not impossible. However, an analysis of the shear strain as a function of frequency while attempting to hold other variables constant offers some insight into the behavior of the overall system.

Given the instrumentation available during testing, the best parameter to represent the dynamic response of the soil is the estimated shear strain. As a reminder, the shear strain is calculated from time records of particle velocity captured by eight individual vertical and horizontal geophones located at four discrete points in the soil. Therefore, the shear strain is an estimation of the deformation in the soil at a single point due to soil motion throughout the area within the sensor array. A summary of results for each shaking trial is reported in Table 3 and includes the test date, shaking frequency, number of loading cycles, the drive signal input, the force output, T-Rex's baseplate displacement, and the calculated shear strain at a depth of 9.2 ft (2.8 m).

Table 3. Summary of shaking trials with corresponding test data, shaking frequency, number of loading cycles, drive signal input, force output, T-Rex baseplate displacement, and estimated shear strain at 9.2 ft (2.8 m) below the ground surface at the WLA site.

Trial #	Test Date	Frequency	Cycles	Drive signal input	T-Rex force output	Baseplate displacement	Shear strain
		(Hz)		(lbs)	(lbs)	(in.)	(%)
1	3/19/12	20	50	3,000	1,800	0.016	0.0008
2	3/19/12	25	50	3,000	2,100	0.009	0.0007
3	3/19/12	30	50	3,000	2,100	0.006	0.0006
4	3/19/12	30	20	3,000	2,100	0.005	0.0006
5	3/19/12	15	20	3,000	1,500	0.032	0.0010
6	3/19/12	12	20	3,000	1,500	0.047	0.0009
7	3/19/12	10	20	3,000	1,200	0.060	0.0008
8	3/19/12	30	50	3,000	2,100	0.006	0.0006
9	3/19/12	10	10	3,000	1,200	0.061	0.0008
10	3/19/12	10	20	6,000	4,500	0.181	0.0033
11	3/19/12	30	20	6,000	4,200	0.014	0.0017
12	3/19/12	30	10	6,000	4,200	0.006	0.0018
13	3/19/12	30	10	7,500	6,750	0.007	0.0024
14	3/19/12	30	10	9,000	6,900	0.024	0.0033
15	3/19/12	30	10	10,500	8,400	0.027	0.0043
16	3/19/12	30	10	12,000	12,000	0.015	0.0054
17	3/19/12	30	20	9,000	8,400	N/A	0.0035
18	3/19/12	30	20	12,000	12,000	0.015	0.0056
19	3/19/12	30	20	13,980	13,800	N/A	0.0070
20	3/19/12	30	20	16,020	13,500	0.037	0.0082
21	3/19/12	30	20	18,000	14,400	0.044	0.0092
24	3/19/12	20	20	22,020	13,800	N/A	0.0200
25	3/19/12	20	50	24,000	14,400	0.166	0.0232
26	3/19/12	20	100	27,000	15,600	0.181	0.0278
27	3/19/12	20	100	30,000	22,200	0.194	0.0303
28	3/19/12	10	100	30,000	12,000	0.848	0.0875
29	3/19/12	20	300	30,000	16,500	0.189	0.0505
30	3/19/12	20	500	30,000	17,400	0.191	0.0634
31	3/19/12	10	300	30,000	12,000	0.843	0.3221
32	3/20/12	20	300	30,000	24,000	0.133	0.0556
33	3/20/12	10	300	30,000	21,600	0.335	0.3474

To observe frequency dependence in the shear strain amplitude, it is helpful to view it in several different ways. In Figure 55, the data are grouped by shaking frequency and the vibe force output is plotted against estimated shear strain. The sequence of shaking trials that used a shaking frequency of 30 Hz show a fairly linear relationship between the increase in vibe force output and the logarithmic increase in shear strain. These 30-Hz shaking trials in general represent the intermediate levels of force loading in the experiment and do not exceed a 14,400-lbs force output. Higher force levels were used in later shaking trials with 10- and 20-Hz shaking frequencies and are not directly comparable to the results from the 30 Hz shaking trial frequencies. With the few data points shown for 10- and 20-Hz shaking frequencies at high vibe force output levels, it appears that for a given vibe force output, the 10-Hz shaking frequency can induce larger shear strains in the soil than the 20-Hz shaking frequency. Another way of considering the relationship is to say as shaking frequency increases, the vibe force output required to achieve a given shear strain also increases. Unfortunately, given the limitations of the data set, this hint of a relationship is only applicable for 10- and 20-Hz shaking frequencies and for vibe force output levels greater than 12,000 lbs. Fortunately, there will be another opportunity to improve this relationship at the WLA site in the summer of 2014, when another set of tests are planned. This summer 2014 project will feature a more extensive embedded sensor array with two or three times as many sensors installed in the ground.

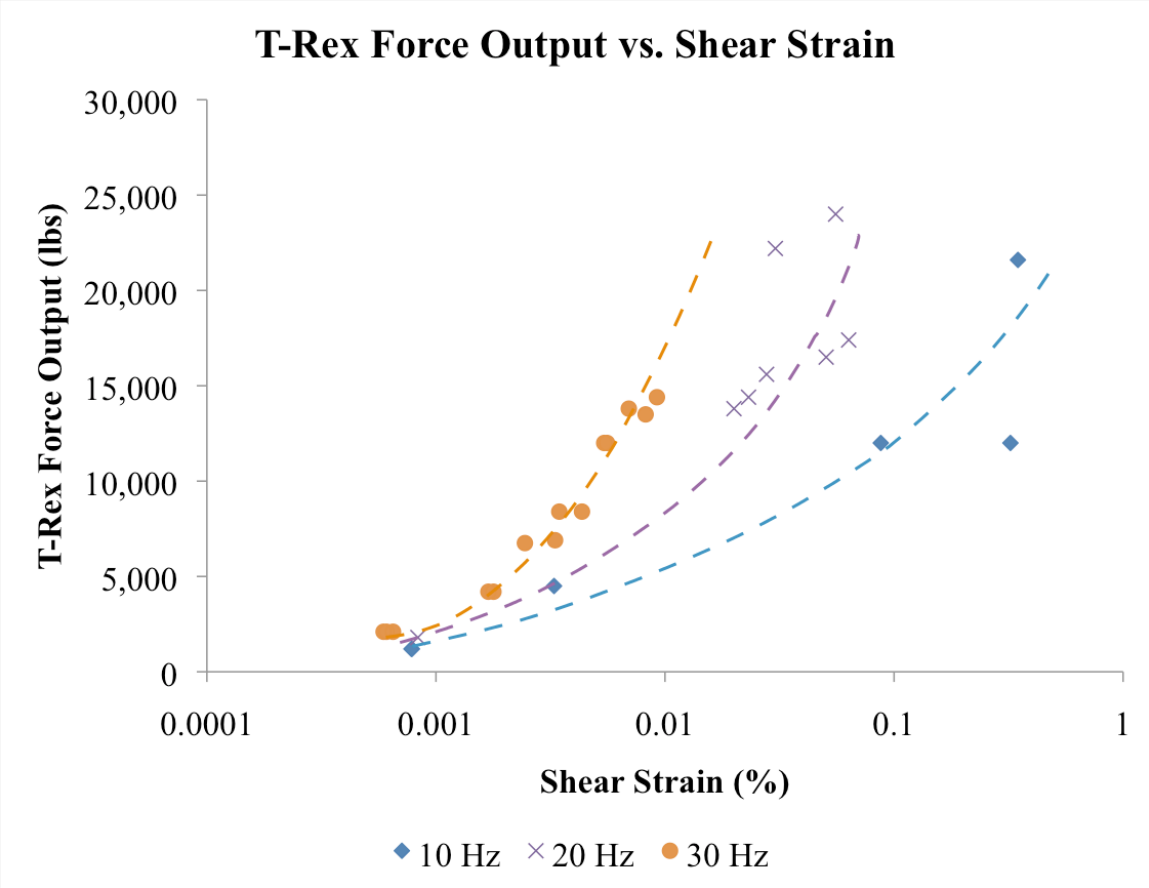

Figure 55 Vibe force output versus shear strain at N = 20 for each of the 31 shaking trials to observe the frequency-dependence of the system.

As seen in the data set summarized by Table 3, there are few sets of shaking trials for which the shaking frequency is varied and the drive signal input is held constant. The best exception to this limitation is the collection of the first nine shaking trials in which the frequency ranged from 10 to 30 Hz and the drive signal input was held constant at 3,000 lbs. Figure 56 presents the results from these nine shaking trials, plotting vibe force output against shear strain. It is interesting to see that despite some minor variation, shear strain at that drive signal force level is nearly independent of vibe force output. Vibe

force output, however, is once again shown to be a function of shaking frequency. For these low drive signal inputs, vibe force output consistently increases with increasing shaking frequency.

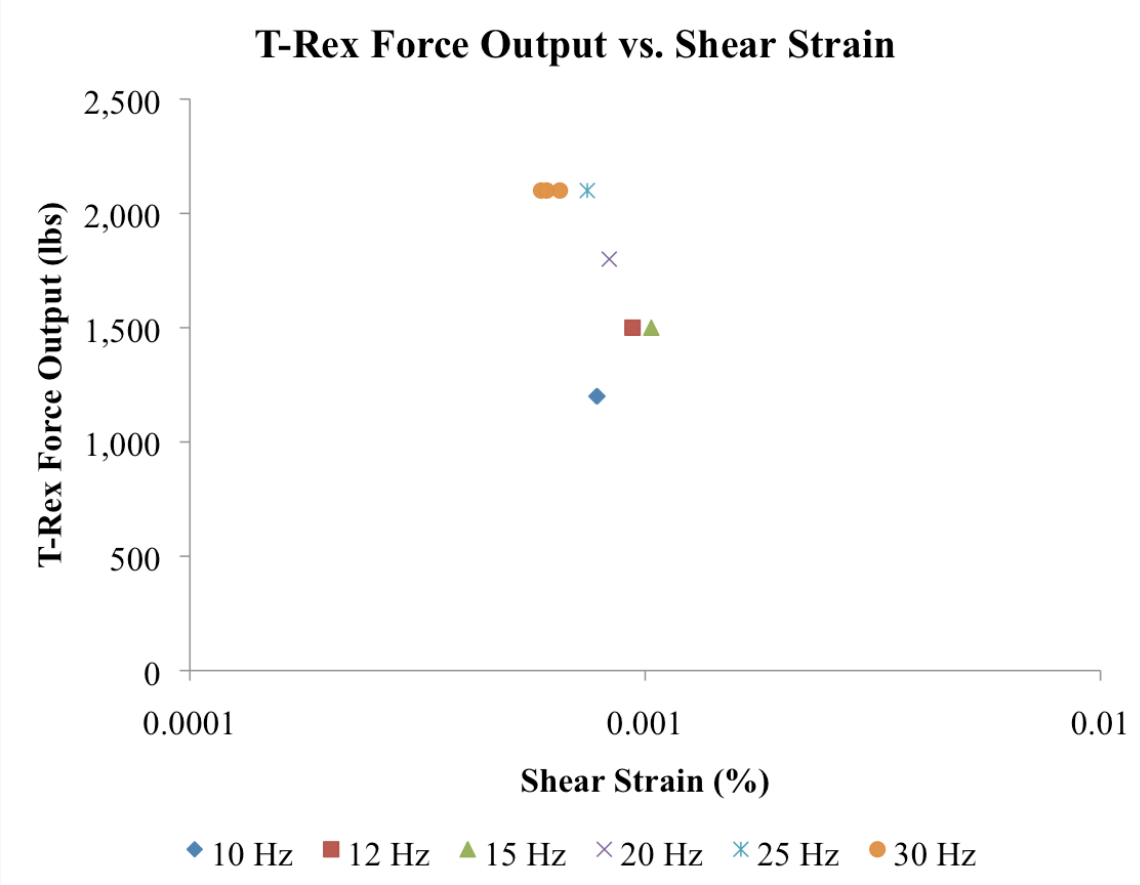

Figure 56. Focused view of vibe force output versus shear strain for the first 9 shaking trials for which the drive signal input is 0.5 V (3,000 lbs).

Another perspective from which to consider the frequency dependency of shear strain is to consider it as a function of T-Rex's baseplate displacement. The effect of shaking frequency at a constant force level on baseplate displacement is shown to be inversely proportional in Figure 54. This effect is the opposite of the directly proportional

effect frequency has on vibe force output. The general trend in Figure 57 shows that shear strain in the soil increases as baseplate displacement increases. By focusing on the largest shaking levels at 10 and 20 Hz, some preliminary conclusions can be drawn. For a given baseplate displacement, the shear strain tends be greater for greater shaking frequencies. Another way of stating the relationship is an increase in shaking frequency requires greater baseplate displacement to achieve a given shear strain level. Again, this observed relationship is only applicable for 10 and 20 Hz shaking frequencies at very high levels of vibe force output levels. Limitations in the current data set make it difficult to confidently make claims about the frequency dependence of shear strains over large ranges of values. This relationship will be studied in greater detail at WLA in the summer of 2014.

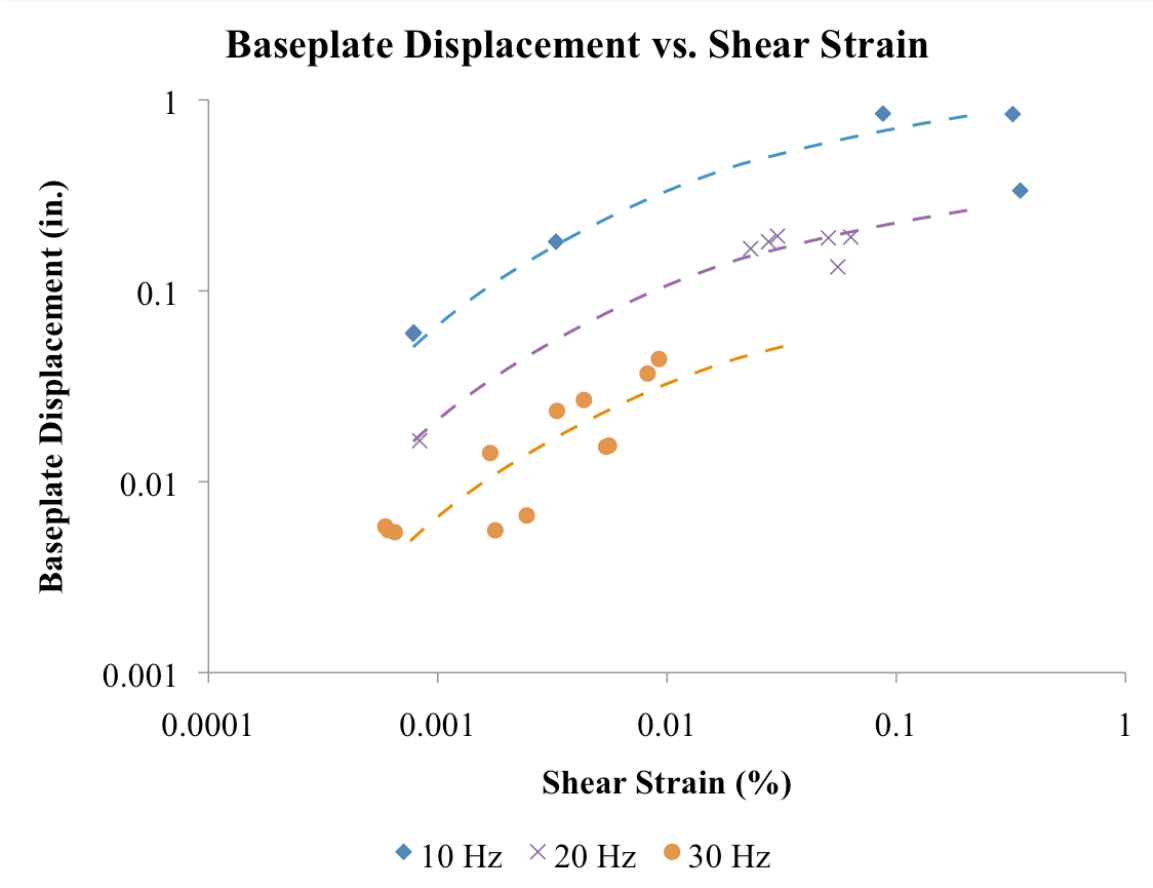

Figure 57 Baseplate displacement versus shear strain for each of the 31 shaking trials to observe the frequency-dependence of the system.

In another figure similar to Figure 56 that looks at only the first nine shaking trials for vibe force output and shear strain, Figure 58 presents those nine trials by looking at the baseplate displacement versus shear strain. As before, for a very low 3,000 lbs drive signal input, the shear strain is shown to be fairly independent of both baseplate displacement and shaking frequency. Just as vibe force output was declared to be frequency-dependent as that low force level, baseplate displacement is similarly affected. The difference, however, is that baseplate displacement increases as shaking frequency

decreases, which is the opposite relationship between vibe force output and shaking frequency. These results are consistent with the observations seen previously in Section 7.2.

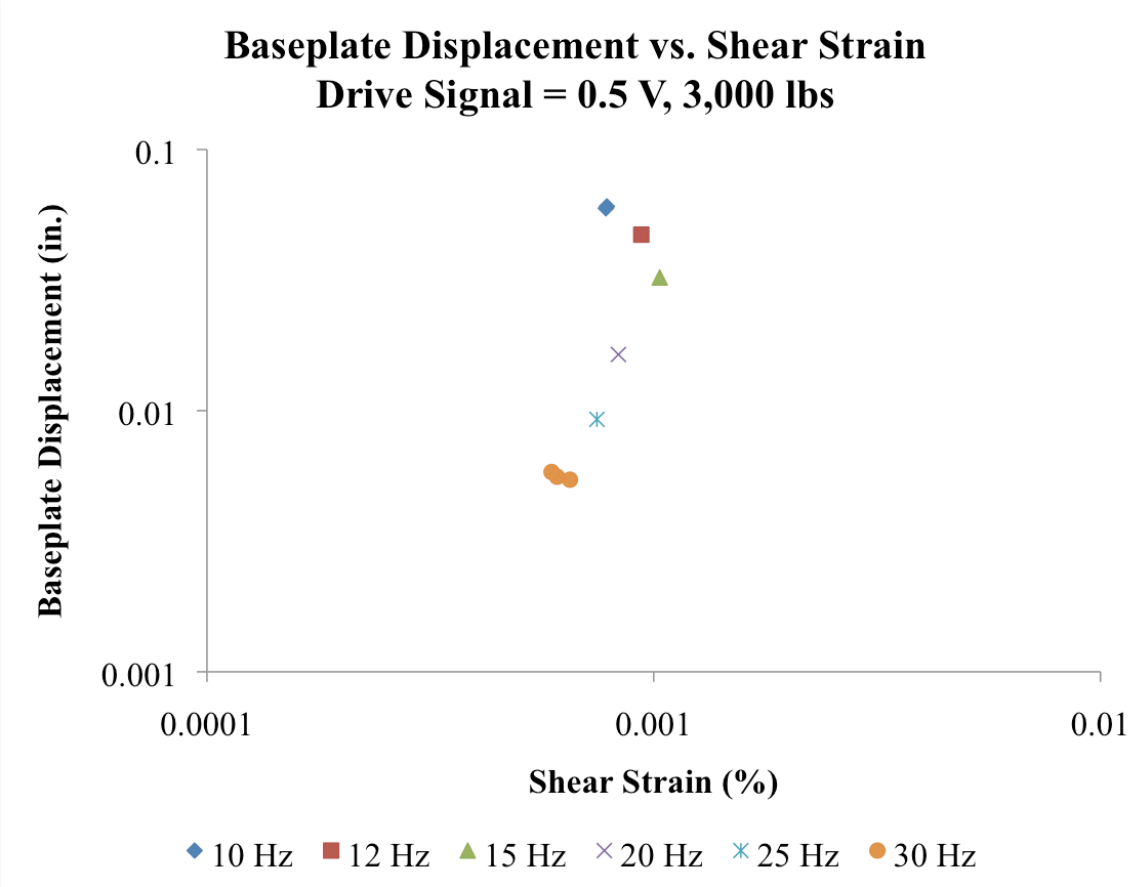

Figure 58 Focused view of baseplate displacement versus shear strain for the first 9 shaking trials for which the drive signal input is 3,000 lbs.

Despite the large variations in vibe force output over the entire set of 31 shaking trials, there were a few instances in which the same vibe force output was achieved for more than one shaking frequency. The rare cases provide an opportunity to see directly how shaking frequency affects shear strain and these results are presented in Figure 59. A

review of the plotted data appears to lack any definitive relationship between shaking frequency and shear strain for given levels of vibe force output. However, based on previous discussion in Section 7.2, it is known that T-Rex does not operate well at low force shaking levels and that there is marginal improvement in performance as shaking frequency increases at those levels. This known poor performance at low shaking levels helps explain the apparent random scatter of frequency-dependence in shear strain for the vibe force outputs of 1,500 and 2,100 lbs. Force outputs of 12,000, 13,800, and 14,400 lbs, however, show a clear inverse relationship between shear strain and frequency. There is confidence that T-Rex is operating well at these force levels and shaking frequencies, so the observed relationship is considered reasonable.

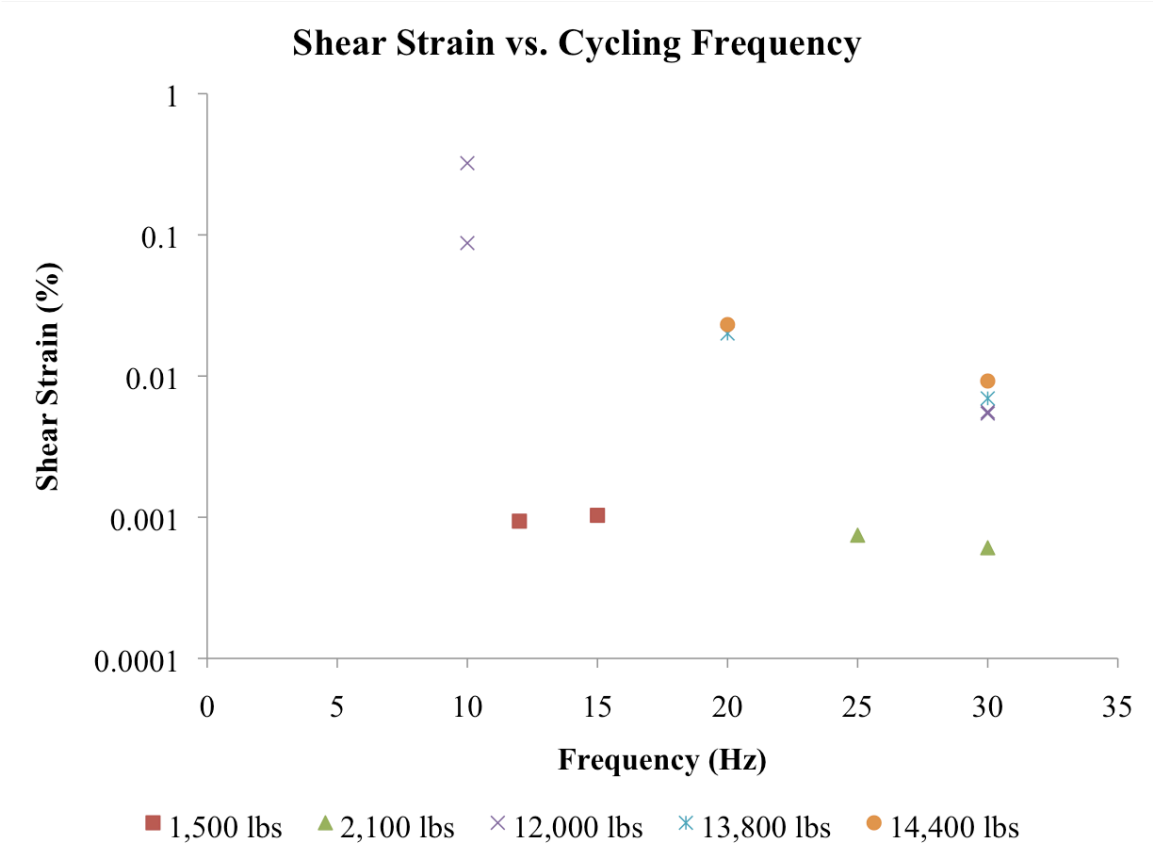

Figure 59 Shear strain versus frequency for a select number of shaking trials in which the vibe force output was approximately equal for multiple frequencies.

Determining the frequency-dependence of shear strain is a difficult task for many reasons. Firstly, it is impossible to decouple the response of the soil (shear strain) from the performance of T-Rex in terms of both baseplate displacement and vibe force output, all three of which have been shown to be frequency dependent. Secondly, this particular data set makes it difficult to perform an in-depth analysis of frequency dependence because there are very few instances in which testing variables were held constant while frequency was varied. While frequency-dependence cannot be fully comprehended at this time, this is an important analysis to be performed at WLA in the summer of 2014.

7.3 RELATIONSHIPS BETWEEN SHEAR STRAIN AND THE GENERATION OF EXCESS PORE WATER PRESSURE

The most informative relationship regarding the liquefaction susceptibility of a soil is the generation of excess pore water pressure as a function of shear strain, γ, at a given number of cycles. A plot showing this relationship incorporates the results from each staged loading in the experiment, clearly showing the cyclic threshold strain for the instrumented soil element. Beyond the cyclic threshold strain, the plots show how many cycles of a given shear strain are required to trigger initial liquefaction, corresponding to r_u equal to 100%.

As described in Section 4.4, the full shaking experiment involved 33 trials over two days. The data acquisition system was improperly initiated during two shaking trials (Trials 22 and 23) and those trials are not included in the analysis. In addition, the two trials performed on the second day (Trials 32 and 33) are not included because elapsed time between the trials performed on different days is much greater than average and may affect the results of the test. The remaining 29 trials provide an in-depth view of the soil response in the linear range up to the non-linear (inelastic) range. The residual pore water pressure ratio and shear strain results are presented in Table 4 and Table 5.

For the first nine shaking trials, the shear strain does not exceed 0.001% and there is no observed residual excess pore water pressure (The complete set of records are plotted in Appendix A). In trials 10 through 21, the shear strain ranges from 0.0017% to 0.0092%, the pore water pressure ratio ranges from 0 to 1.4% in no consistent pattern,

there is no increase in excess pore water pressure after shaking stops, and the total number of cycles in each trial varies from 10 to 20. Since the cyclic threshold is estimated to be around 0.01% to 0.02% for the liquefiable layer at WLA based on the work by Cox (2006) and Vucetic and Dobry (1982), it is moderately surprising to see these very small residual excess pore water pressures. However, their existence is not troubling nor does it affect the rest of the analysis because the magnitude is very small and the trend is inconsistent with shear strain. Because the pore pressure transducer is located at the sharp interface between the sand and clay layers, it is possible that the minor excess pore water pressure is due to higher straining at the interface that cannot be observed by the instrumentation array. If true, this localized straining can only produce small levels of excess pore water pressure and is not a concern for the triggering of soil liquefaction. Unfortunately, only small numbers of loading cycles were used in these shake trials (N = 10 and 20) and it is not clear how the pore water pressure would respond with greater loading cycles.

Beyond shaking trial 21, significant residual excess pore water pressures develop during shaking and, in some cases, increase after the end of shaking. For shake trials 24 through 31, the shear strain ranges from 0.02% to 0.3474% for N = 20 through 300. The build up of significant residual excess pore water pressure indicates that the cyclic threshold strain of the sand has been exceeded.

Table 4. Summary details for each shaking trial as well as the measured ru at the End of Loading (EOL), measured ru at the End of Recording (EOR), and the calculated shear strain averaged over the entire time record.

Trial #	Test Date	Frequency	Cycles	T-Rex force output	r_u EOL	r_u EOR	Time between EOL & EOR	Shear strain at EOL
		(Hz)		(lbs)	(%)	(%)	(sec)	(%)
1	3/19/12	20	50	1,800	0	0	0.0	0.0008
2	3/19/12	25	50	2,100	0	0	0.8	0.0007
3	3/19/12	30	50	2,100	0	0	2.0	0.0006
4	3/19/12	30	20	2,100	0	0	2.0	0.0006
5	3/19/12	15	20	1,500	0	0	1.5	0.0010
6	3/19/12	12	20	1,500	0	0	1.1	0.0009
7	3/19/12	10	20	1,200	0	0	0.7	0.0008
8	3/19/12	30	50	2,100	0	0	1.0	0.0006
9	3/19/12	10	10	1,200	0	0	1.5	0.0008
10	3/19/12	10	20	4,500	0.5	0.5	0.7	0.0033
11	3/19/12	30	20	4,200	0.1	0.1	0.7	0.0017
12	3/19/12	30	10	4,200	0	0	0.3	0.0018
13	3/19/12	30	10	6,750	0.4	0.4	0.3	0.0024
14	3/19/12	30	10	6,900	0.8	0.8	0.3	0.0033
15	3/19/12	30	10	8,400	1.1	1.1	0.3	0.0043
16	3/19/12	30	10	12,000	1.4	1.4	0.3	0.0054
17	3/19/12	30	20	8,400	0	0	0.0	0.0035
18	3/19/12	30	20	12,000	0.8	0.8	0.0	0.0056
19	3/19/12	30	20	13,800	1	1	0.0	0.0070
20	3/19/12	30	20	13,500	1	1	0.0	0.0082
21	3/19/12	30	20	14,400	1	1	0.0	0.0092
24	3/19/12	20	20	13,800	1.4	1.4	0.3	0.0200
25	3/19/12	20	50	14,400	2.8	8	1.5	0.0232
26	3/19/12	20	100	15,600	8	18	3.0	0.0278
27	3/19/12	20	100	22,200	8	15	2.0	0.0303
28	3/19/12	10	100	12,000	30	52	22.0	0.0875
29	3/19/12	20	300	16,500	54	62	7.0	0.0505
30	3/19/12	20	500	17,400	58	62	6.0	0.0634
31	3/19/12	10	300	12,000	70	78	6.0	0.3221

Table 5. Summary details of measured r_u and shear strain for each shaking trial after 10, 20, 50, 100, 200, 300, and 500 cycles, as applicable.

Trial #	N = 10, r_u	N = 10, γ	N = 20, r_u	N = 20, γ	N = 50, r_u	N = 50, γ	N = 100, r_u	N = 100, γ	N = 200, r_u	N = 200, γ	N = 300, r_u	N = 300, γ	N = 500, r_u	N = 500, γ
	(%)	(%)	(%)	(%)	(%)	(%)	(%)	(%)	(%)	(%)	(%)	(%)	(%)	(%)
1	0	0.0008	0	0.0009	0	0.0008	N/A	N/A	N/A	N/A	N/A	N/A	N/A	N/A
2	0	0.0008	0	0.0008	0	0.0007	N/A	N/A	N/A	N/A	N/A	N/A	N/A	N/A
3	0	0.0007	0	0.0007	0	0.0006	N/A	N/A	N/A	N/A	N/A	N/A	N/A	N/A
4	0	0.0007	0	0.0006	N/A	N/A	N/A	N/A	N/A	N/A	N/A	N/A	N/A	N/A
5	0	0.0010	0	0.0010	N/A	N/A	N/A	N/A	N/A	N/A	N/A	N/A	N/A	N/A
6	0	0.0010	0	0.0009	N/A	N/A	N/A	N/A	N/A	N/A	N/A	N/A	N/A	N/A
7	0	0.0008	0	0.0008	N/A	N/A	N/A	N/A	N/A	N/A	N/A	N/A	N/A	N/A
8	0	0.0006	0	0.0006	0	0.0006	N/A	N/A	N/A	N/A	N/A	N/A	N/A	N/A
9	0	0.0008	N/A	N/A	N/A	N/A	N/A	N/A	N/A	N/A	N/A	N/A	N/A	N/A
10	0.5	0.0032	0.5	0.0033	N/A	N/A	N/A	N/A	N/A	N/A	N/A	N/A	N/A	N/A
11	0.1	0.0017	0.1	0.0017	N/A	N/A	N/A	N/A	N/A	N/A	N/A	N/A	N/A	N/A
12	0	0.0018	N/A	N/A	N/A	N/A	N/A	N/A	N/A	N/A	N/A	N/A	N/A	N/A
13	0.4	0.0024	N/A	N/A	N/A	N/A	N/A	N/A	N/A	N/A	N/A	N/A	N/A	N/A
14	0.8	0.0033	N/A	N/A	N/A	N/A	N/A	N/A	N/A	N/A	N/A	N/A	N/A	N/A
15	1.1	0.0043	N/A	N/A	N/A	N/A	N/A	N/A	N/A	N/A	N/A	N/A	N/A	N/A
16	1.4	0.0054	N/A	N/A	N/A	N/A	N/A	N/A	N/A	N/A	N/A	N/A	N/A	N/A
17	0	0.0035	0	0.0035	N/A	N/A	N/A	N/A	N/A	N/A	N/A	N/A	N/A	N/A
18	0.6	0.0056	0.8	0.0056	N/A	N/A	N/A	N/A	N/A	N/A	N/A	N/A	N/A	N/A
19	0.8	0.0069	1	0.0070	N/A	N/A	N/A	N/A	N/A	N/A	N/A	N/A	N/A	N/A
20	0.8	0.0082	1	0.0082	N/A	N/A	N/A	N/A	N/A	N/A	N/A	N/A	N/A	N/A
21	0.8	0.0092	1	0.0092	N/A	N/A	N/A	N/A	N/A	N/A	N/A	N/A	N/A	N/A
24	0.0	0.0192	1.4	0.0200	N/A	N/A	N/A	N/A	N/A	N/A	N/A	N/A	N/A	N/A
25	-0.8	0.0210	-0.3	0.0219	2.8	0.0232	N/A	N/A	N/A	N/A	N/A	N/A	N/A	N/A
26	-1.7	0.0239	-1.3	0.0249	1.7	0.0263	-1.7	0.0278	N/A	N/A	N/A	N/A	N/A	N/A
27	-2.6	0.0264	-2.2	0.0277	0.9	0.0292	-2.6	0.0303	N/A	N/A	N/A	N/A	N/A	N/A
28	0.1	0.0314	1.6	0.0391	9.6	0.0605	-2.5	0.0875	N/A	N/A	N/A	N/A	N/A	N/A
29	-1.8	0.0435	1.9	0.0436	10.8	0.0455	22.6	0.0505	41	0.0553	54	0.0539	N/A	N/A
30	3.7	0.0870	5.6	0.0812	13.0	0.0707	23.3	0.0634	36.7	0.0552	44.23	0.0492	58	0.0434
31	-16.0	0.2918	-16.9	0.3155	-3.8	0.3346	17.2	0.3221	50.6	0.3149	70	0.3144	N/A	N/A

While all 29 shaking trials provide important insight into the behavior of the soil during cyclic loading, it is sufficient to select a few representative data points at given values of N to establish the relationship between shear strain and the development of excess pore water pressure. In Figure 60, eight representative shaking trials are shown. No shake trials beyond Trial 28 are included because the pore water pressure and shear strain time records indicate that the shaking in Trial 28 permanently affected the response of the soil for all remaining shaking trials, which is discussed later in this section. The results in Figure 60 show how shear strain and pore water pressure ratio develop as a function of loading cycles. It is evident that minor negative pore water pressures are only present at small numbers of loading cycles ($N < 50$). In addition, pore water pressure ratio and shear strain tend to increase as the number of loading cycles increase as well.

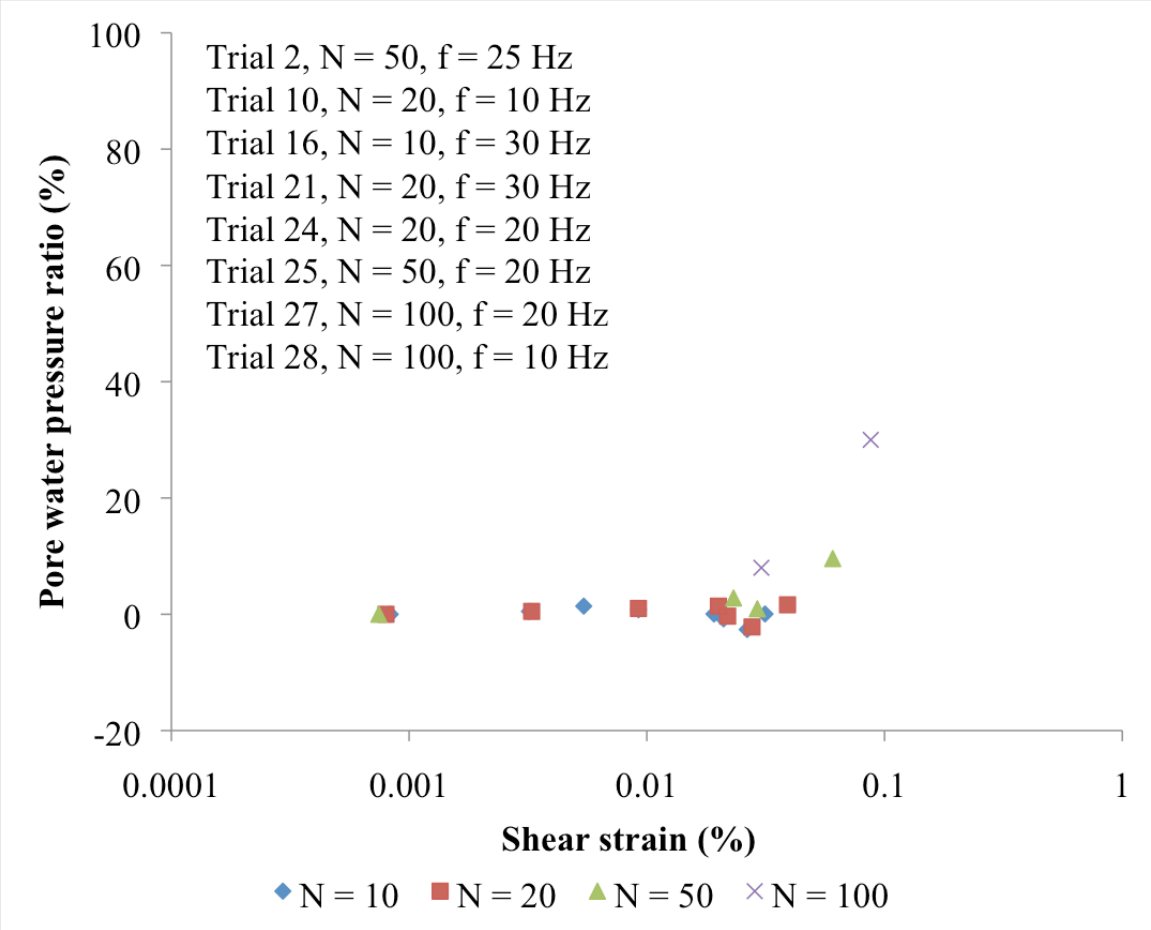

Figure 60. Pore water pressure ratio versus shear strain for eight representative shaking trials. Each data set shows the average shear strain and measure pore water ratio after N cycles. Given the varying number of cycles between each trial, only N = 10 includes all eight trials.

Figure 61 makes it possible to identify the cyclic threshold strain for this soil as between 0.02% and 0.0232%. for N = 50 to 100. In Trial 24, the shear strain is estimated to be 0.02% exactly and only 1.4% pore water pressure ratio is generated. In the next trial, the shear strain increases to 0.0232% and the pore water pressure ratio at the end of shaking is 2% and continues to increase to 8% before the time record is cut off. The

generation of residual excess pore water pressure is markedly different for shear strains 0.02% and lower than for shear strains 0.0232% and higher. While only 20 cycles are used in Trial 24 versus the 50 used in Trial 25, the lack of continued rise in excess pore water pressure after the end of shaking in Trial 24 indicates that the generation of pore water pressure is not a pervasive in the soil system as it is for Trial 25. It is acknowledged, however, that this is an imperfect analysis comparing shake trials with varying numbers of cycles.

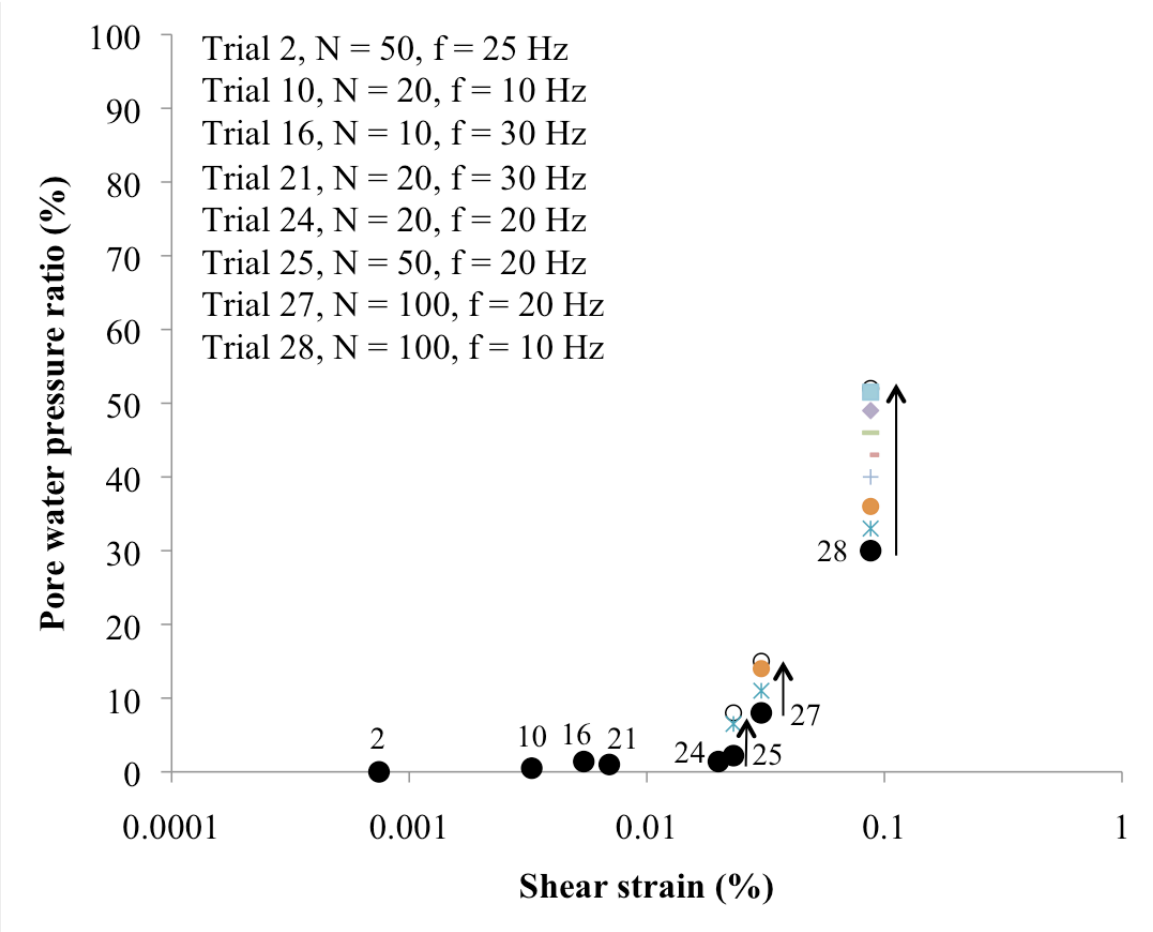

Figure 61. Pore water pressure ratio versus shear strain for eight representative shaking trials. The black dots show the pore water pressure ratio at End of Loading regardless of the total number of cycles applied; the additional data points indicate the increase in pore water pressure ratio in 1-second increments after the end of the shaking until the water pressure peaked or the record was terminated.

The observed results from this experiment match well with the field results from Cox, 2006, and the laboratory results from Vucetic and Dobry, 1986, for the same WLA sand. In Figure 62, the eight representative shaking trials from this project are plotted with the results from Cox, 2006, and Vucetic and Dobry, 1986. The boundaries set by Vucetic and Dobry, 1986, for 10 and 100 loading cycles capture many of the field results

produced by Cox, 2006, and by this project for number of loading cycles varying between 10 and 100.

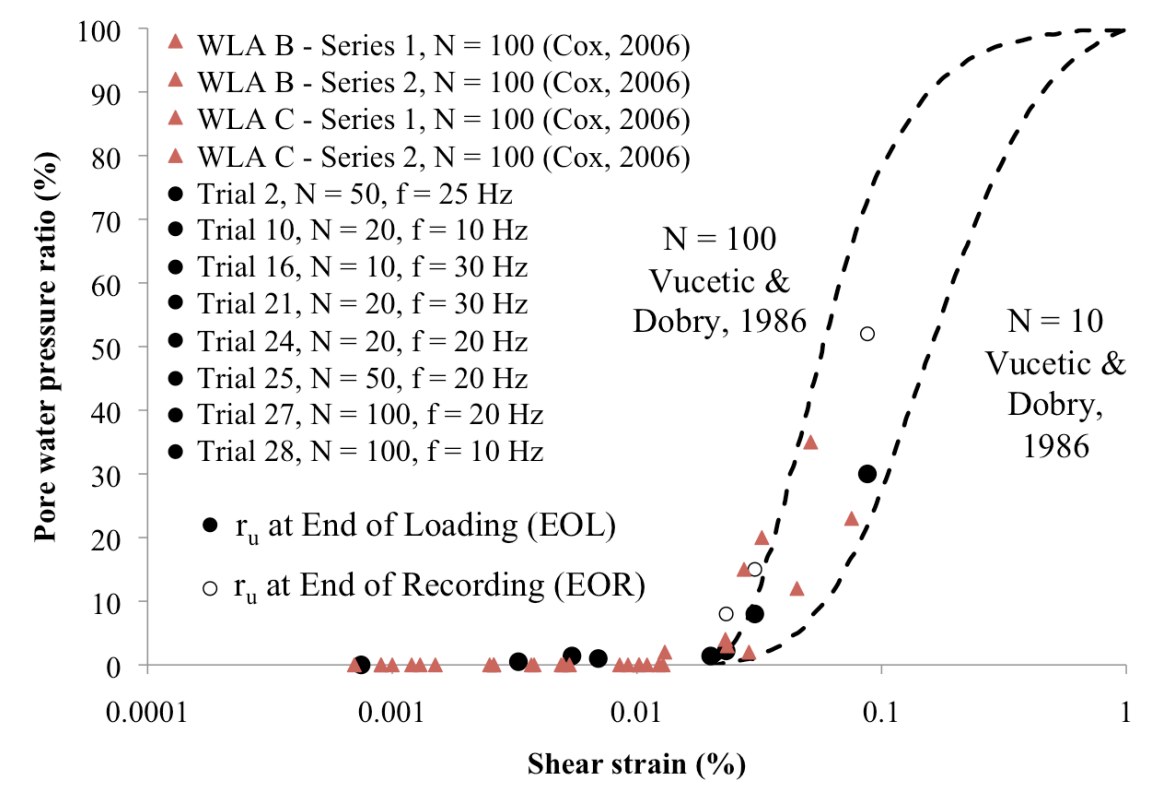

Figure 62. Pore water pressure ratio versus shear strain data from Figure 62 shown with field data from WLA B and WLA C (Cox, 2006) and laboratory data (Vucetic and Dobry, 1986).

While shaking Trials 28 through 31 exhibit distinctly non-uniform behavior in both the pore water pressure and shear strain time records, it is still informative to consider them. These results are shown in Figure 63 and in good agreement with the N = 10 and N = 100 relationships from Vucetic and Dobry, 1986. For these time records, the estimated of shear strain is less accurate because the displacement-based shear strain calculation assumes the excitation energy is a downward propagating planar wave. With

the large shaking forces seen in Trials 28 through 31, the soil response is very nonlinear and the correctness of the fundamental assumption and the accuracy of the shear strain at the center of the instrumentation array are more elusive. On the other hand, measurement of residual excess pore water pressure and calculation of pore water pressure ratio remains unchanged in terms of accuracy.

The results for Trials 25 through 31 that are presented in Figure 63 show the capability of the soil to generate very large residual excess pore water pressures and indicate a susceptibility to liquefy during a large earthquake. The pore water pressure ratios generated range from 2.8% (Trial 25) to 70% (Trial 31) at the End of Loading and range from 8% (Trial 25) to 78% (Trial 31) at the End of Recording. It is important to note that the excess pore water pressure water still increasing at the End of Loading as noted in Table 4. The continued rise in pore water pressure after the end of shaking also indicates that even larger pore water pressure ratios were generated during shaking in adjacent locations in the deposit. Due to the short recording times, unfortunately, most of the white circles correspond to the pore water pressure measured at the end of the time record rather than the maximum value, which would have peaked some time after the recording ended. These time records, and those for all shaking trials, can be found in Appendix A.

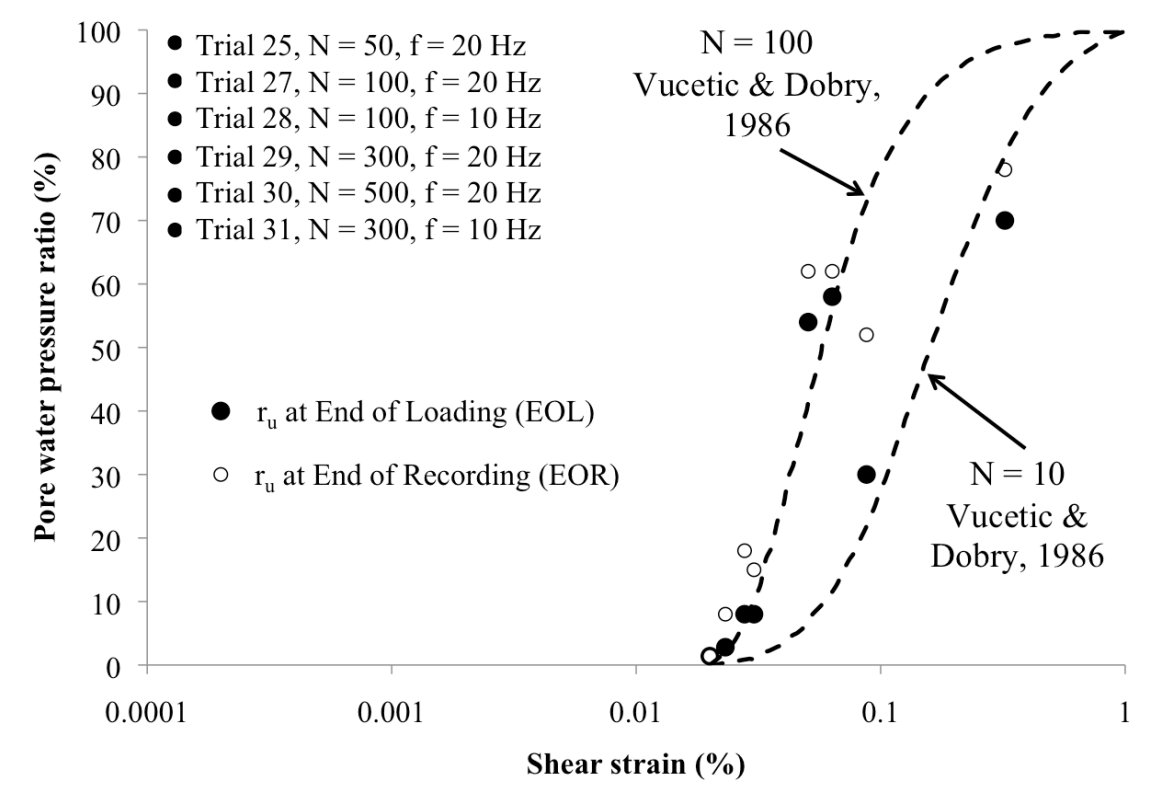

Figure 63. Pore water pressure ratio versus shear strain for the final six shaking trials. Solid black circles indicate the pore water pressure ratio at the End of Loading; white circles indicate the pore water pressure ratio at the End of Recording.

The generation of large, positive residual excess pore water pressures is the main focus of this liquefaction-triggering experiment. However, the generation of negative residual pore water pressure ratios is also important to fully understanding the complexity of the soil behavior. In this project, only minor negative pore water pressure ratios were observed (-0.88% to -2.6%) during shaking trials up through Trial 28 in which the cyclic strain threshold (0.02 to 0.0232%) was exceeded. The manner in which negative pore water pressure was generated is shown in Figure 64 for shaking Trial 27. The residual

pore water pressure ratio decreases to a minimum value of -2.6% after about 10 cycles and then increases yet continues to remain negative for the next 30 cycles of loading. Beyond this point, the pore water pressure continues increasing to a maximum value of 8% at the End of Loading and 15% at the End of Recording.

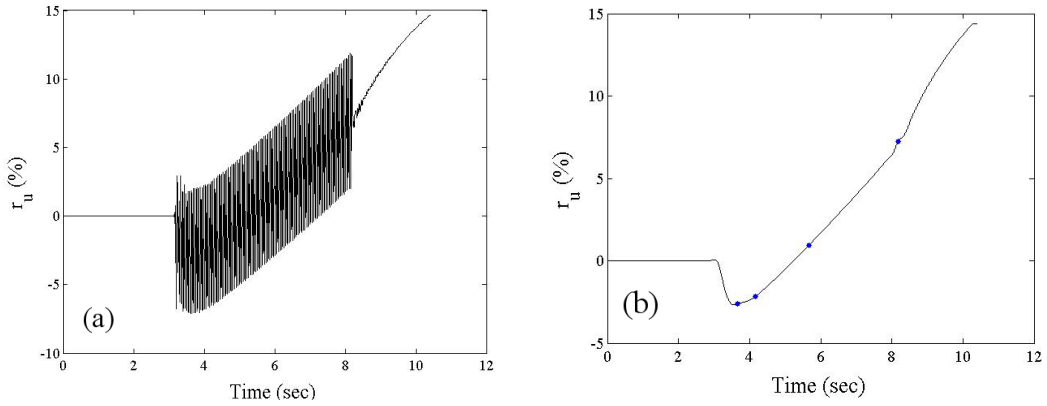

Figure 64. Time record of pore water pressure generation for Trial 27 (a) and time record of low-pass filtered excess residual pore water pressure ratio record for Trial 27 (b).

The -2.6% minimum residual pore water pressure ratio shown for Trial 27 is relatively small compared to the positive 8% and 15% eventually generated. For shaking trials beyond Trial 28, the generation of negative pore water pressure ratios is more significant and accompanied by very non-uniform water pressure and shear-strain time records, as discussed previously. For Trials 28 through 33, the minimum negative pore water pressure ratio ranges from 0% to -16.9%. The pore water pressure ratio time record for Trial 31 is shown in Figure 65 shows the generation of very large negative pore water pressures that reaches a minimum value of -16.9% after 20 loading cycles before increasing to 70% at the End of Loading and 78% at the End of Recording. The

inconsistent generation of negative pore water pressure ratios between shaking trials makes it difficult to identify any pattern or reason for the magnitude of the negative pore water pressure ratio. At this time the development of initial negative pore water pressures as a phenomenon is identified, but the reasons for this response need to be studied further.

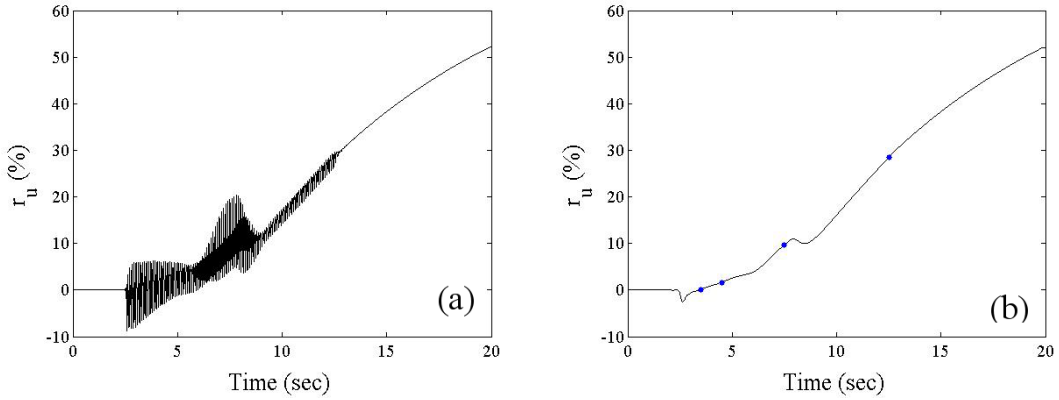

Figure 65. Pore water pressure ratio time record for Trial 31 (a) and low-pass filtered residual pore water pressure ratio time record for Trial 31 (b).

With the generation of significant negative pore water pressure ratios, another way to consider the pore water pressure generation potential of the soil is to consider the full range over which it varies rather just the maximum value. In Table 6, various values of pore water pressure ratios are summarized for each shaking trial: r_u min is the minimum residual pore water pressure ratio observed during shaking; r_u EOL is the value of r_u measured at the End of Loading; r_u EOR is the value of r_u measured at the End of Recording; (r_u EOL – r_u min) represents the range over which the pore water pressure

ratio changes during shaking; and (r_u EOR – r_u min) represents the range over which the pore water pressure ratio changes during the entire recording.

Table 6. Pore water pressure ratios measured at different points in the time record with estimated shear strain

Trial #	Cycles	r_u min	r_u EOL	r_u EOR	r_u EOL - r_u min	r_u EOR - r_u min	Time between EOL & EOR	Shear strain at EOL
		(%)	(%)	(%)			(sec)	(%)
1	50	0	0	0	0	0	0.0	0.0008
2	50	0	0	0	0	0	0.8	0.0007
3	50	0	0	0	0	0	2.0	0.0006
4	20	0	0	0	0	0	2.0	0.0006
5	20	0	0	0	0	0	1.5	0.0010
6	20	0	0	0	0	0	1.1	0.0009
7	20	0	0	0	0	0	0.7	0.0008
8	50	0	0	0	0	0	1.0	0.0006
9	10	0	0	0	0	0	1.5	0.0008
10	20	0	0.5	0.5	0.5	0.5	0.7	0.0033
11	20	0	0.1	0.1	0.1	0.1	0.7	0.0017
12	10	0	0	0	0	0	0.3	0.0018
13	10	0	0.4	0.4	0.4	0.4	0.3	0.0024
14	10	0	0.8	0.8	0.8	0.8	0.3	0.0033
15	10	0	1.1	1.1	1.1	1.1	0.3	0.0043
16	10	0	1.4	1.4	1.4	1.4	0.3	0.0054
17	20	0	0	0	0	0	0.0	0.0035
18	20	0	0.8	0.8	0.8	0.8	0.0	0.0056
19	20	0	1	1	1	1	0.0	0.0070
20	20	0	1	1	1	1	0.0	0.0082
21	20	0	1	1	1	1	0.0	0.0092
24	20	0	1.4	1.4	1.4	1.4	0.3	0.0200
25	50	-0.9	2.8	8	3.7	8.9	1.5	0.0232
26	100	-1.7	8	18	9.7	19.7	3.0	0.0278
27	100	-2.6	8	15	10.6	17.6	2.0	0.0303
28	100	-2.5	30	52	32.5	54.5	22.0	0.0875
29	300	-3	54	62	57	65	7.0	0.0505
30	500	0	58	62	58	62	6.0	0.0634
31	300	-16.9	70	78	86.9	94.9	6.0	0.3221

For shaking trials beyond the cyclic strain threshold, γ_t^c, Trials 25 through 31, the pore water pressure ratio range versus shear strain is shown in Figure 66. The comparison

of the field results from Trials 25 through 31 match well with the laboratory results reported by Vucetic and Dobry, 1986, for the zone represented by the N = 10 and N = 100 loading cycle relationships. From this perspective, it appears that the triggering of soil liquefaction due to T-Rex shaking is eminent, particularly in the case of Trial 31 where the pore water pressure ratio range is 94.9%.

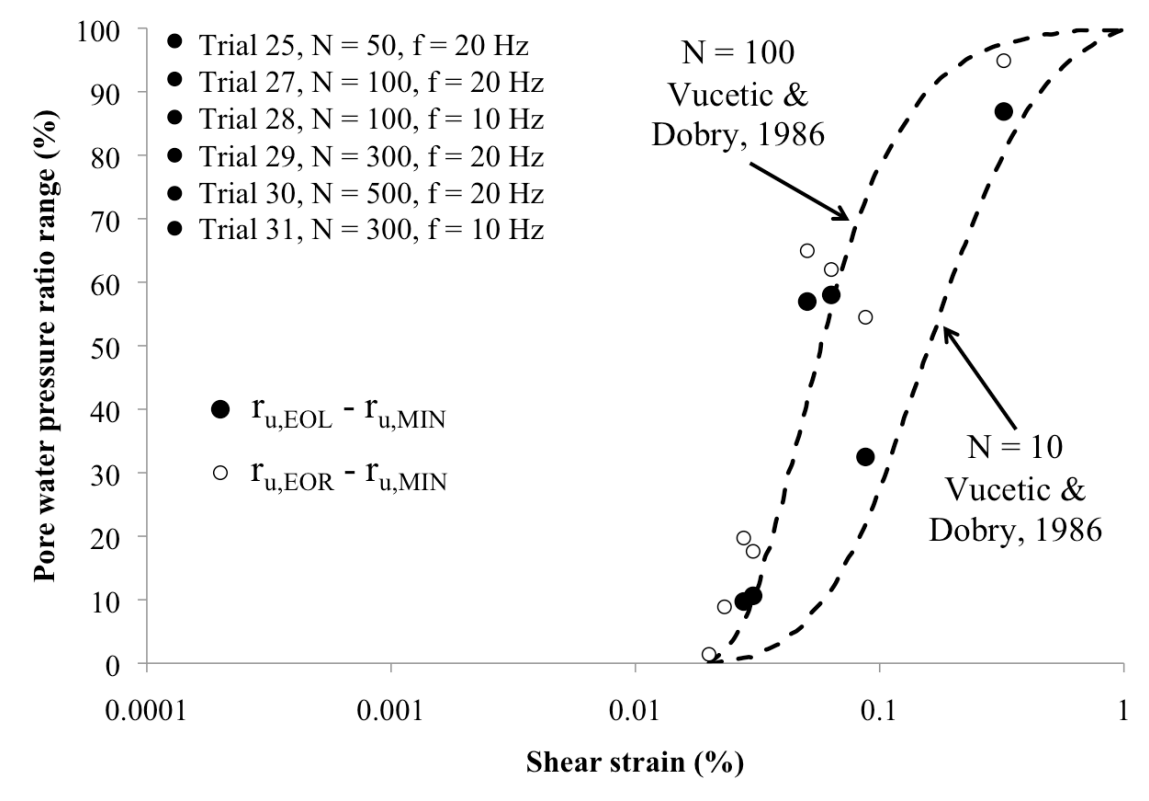

Figure 66. Pore water pressure ratio range versus shear strain for the final six shaking trials. Solid black circles indicate the adjusted pore water pressure ratio at the End of Loading; white circles indicate the adjusted pore water pressure ratio at the End of Recording.

7.4 SUMMARY

The proper analysis of soil liquefaction susceptibility requires understanding the influence of the excitation mechanism, T-Rex, on the soil response. It has been shown that the vibe force output, baseplate displacement, and shear strain soil response are all frequency-dependent with varying outcomes. The complete system is too complicated and inter-related, however, to completely isolate the frequency-dependent contribution of each component (vibe output force, baseplate displacement, and shear strain soil response). Instead, it must be accepted that the interaction between each component mutually affects the other components to create a system that exhibits overall frequency-dependence. This dependence can be studied in greater detail with careful variation of frequency for given drive signal inputs.

The relationship between pore water pressure ratios and shear strain is of utmost importance in predicting soil liquefaction triggering. Using time records in which both the pore water pressure and shear strain are relatively uniform in shape, the cyclic strain threshold is identified to be between 0.02% and 0.0232% and is consistent with findings from Cox, 2006, and Vucetic and Dobry, 1982. The maximum generated pore water pressure ratio recorded during testing is 86.9%, which is very close to the 100% required to trigger soil liquefaction. The generation of negative pore water pressure ratios raises a number of questions regarding its true cause and requires more investigation. The generation of negative pore water pressure ratios has the effect of increasing the range of pore water pressure ratios achieved during testing; the maximum observed pore water

pressure range is 94.9%. Even within the constraints for the present analysis, it is confidently predicted that the sandy layer below the clay cap will liquefy during a large earthquake.

Chapter 8 – Final Discussions

8.1 SUMMARY

The primary objective of the research project covered in this thesis was to continue developing the direct, in-situ liquefaction test that was first pioneered at The University of Texas at Austin (Chang, 2002, and Cox, 2006). The successful implementation of this liquefaction test has great potential to advance the state of knowledge in earthquake engineering. While the ultimate goal of the test is to determine the shear strain at which soil liquefaction is triggered, determining that single answer involves an extensive process of collecting and analyzing data.

While this testing technique is relatively new and represents a new approach to strain-based testing, it is preceded by several decades of influential soil liquefaction research. Chapter 2 reviewed a number of publications that are most relevant for understanding the evolution of testing techniques toward the direct, in-situ liquefaction test (Cox, 2006, Dobry et al, 1982, and Youd et al, 2001), the importance of the Wildlife Liquefaction Array (WLA) as a research site (Cox, 2006, and Holzer and Youd, 2007), and the nature of data analysis procedures employed (Cox, 2006, Rathje et al, 2004).

The information discussed in Chapter 3 provided background information regarding the field site itself as well as the equipment used in liquefaction testing. The Wildlife Liquefaction Array is a site well suited to liquefaction testing because of its proximity to the seismically active San Andreas Fault system and recorded instances of soil liquefaction from several earthquakes; indeed, for these reasons, the WLA has been the focus of many earthquake engineering research projects over the last 30 years (Bennet

et al, 1984, Bierschwale and Stokoe, 1984, Youd and Holzer, 1994, Youd et al, 2004, Youd and Holzer, 2007, Cox, 2006). In addition, much of the field equipment used to gather data is highly specialized, and in some cases custom built, because of the unique nature of this relatively new testing technique.

The complete implementation of the liquefaction test, as described in Chapter 4, is a complex process that involves site characterization, installation of a comprehensive instrumentation array, testing, and site cleanup. While previous research at the site provided a rough estimate of the depth from the ground surface to the interface between the clayey silt and sand layers, the results from a CPT sounding provided an accurate determination of this interface depth. Knowing the depth of the interface allowed the four, 3-D velocity transducers, one pore pressure transducer, and two crosshole source rods to be pushed to depths that would provide the most valuable information regarding soil behavior from the test. The preparation and installation of the equipment was a process orchestrated to ensure precision in the measurements and integrity of the recording system. Once ready, the executions of the seismic crosshole tests and liquefaction tests were designed and regimented to maximize the amount of meaningful results obtained from each test. Finally, the conclusion of the test involved carefully retrieving and disassembling the equipment so that it can be reused in future projects.

The results of the seismic crosshole tests are presented in Chapter 5 with some discussion. In the overall scope of the liquefaction test, the seismic crosshole tests seem rather simple, but they are important because they provide a preliminary characterization of the soil and confirms the presence of conditions required for liquefaction to occur

(loose, soft sand that is saturated). It was convenient that the configuration of the instrumented array allowed crosshole testing to be performed through and around the array, providing insights into the characteristics of the same soil that was also analyzed during the liquefaction test. The objective of the crosshole tests was to determine the P- and S-wave velocities in both the clayey silt layer and the upper portion of the sand layer. The P-wave velocities in both layers were high enough to indicate a degree of saturation greater than 99.9%, a condition under which soil liquefaction can occur. The comparison of the S-wave velocities from before and after the liquefaction testing verified that there was negligible change in the structural composition of the soil skeleton, implying that the soil conditions at the beginning of each liquefaction test loading stage (repetition) can be considered uniform.

The data reduction procedures for the liquefaction test are discussed in Chapter 6. The raw data recorded from the four, 3-D velocity transducers and one pore pressure transducer required signal processing to facilitate the analysis, notably by removing noise or other undesired frequencies that differ from the loading frequencies. The recordings from the four, 3-D velocity transducers were the main inputs into the shear strain calculations and the shear wave velocity degradation during pore pressure generation calculations. The recordings from the pore pressure transducer were the main input in calculating the pore water pressure ratio, r_u. The results obtained by the processes described in Chapter 6 present the data in a format suitable for further analysis.

In Chapter 7, results from the liquefaction testing are presented. First the performance of T-Rex is analyzed by considering the frequency dependence of force

output and baseplate displacement, as well as its effect on the shear strain induced in the soil. Despite the limited data set, a number of trends were observed and discussed, providing a basic understanding of the performance of T-Rex in the modes of operation used in liquefaction testing. In addition, the response of the soil to cyclic loading was studied by developing relationships between shear strain and the generation of excess pore water pressure as well as identifying the cyclic threshold strain, γ_t^c. The overall discussion of results provides insight into their meaning and drew comparisons to similar results obtained in Dobry et al, 1982, and Cox, 2006.

In the end, the attempt is made to provide a comprehensive overview of the direct, in-situ liquefaction test in the previous chapters. This overview is accomplished with a review of the state of knowledge leading up to present time, an introduction to the test site, field equipment, and testing procedures, and a presentation of the data analysis and results with discussions.

8.2 CONCLUSIONS

The success of the research project is enhanced by the quality of results obtained from testing. The comprehensiveness of the research project and agreement of results between and within testing techniques engender confidence in the overall process and its conclusions. As a result, the following major conclusions are made based on the results from the direct, in-situ liquefaction testing program performed at the WLA in March 2012.

1. The P-wave velocities in the sand and clayey silt determined from seismic crosshole testing was consistently found to be greater than 4,500 ft/sec (1,370 m/s). According to Valle-Molina, 2006, P-wave velocities greater than this value indicate a degree of saturation greater than 99.9% in the soil. This saturation level is an important condition for soil liquefaction to occur because even a tiny amount of air in the system will slow the increase in water pressure that triggers soil liquefaction.
2. The S-wave velocities in the sand and clayey silt indicated how soft the clayey silt and sand layers are. The average S-wave velocity in the clayey silt layer within 2 ft (0.6 m) above the sand layer was 343 ft/sec (105 m/s) and the average S-wave velocity in the sand layer was 466 ft/sec (142 m/s). The change in S-wave velocity in the sand from before and immediately after performing liquefaction testing varied by no more than 7 ft/sec (2.1 m/s). This change represents less than 2% variation in wave speed and is on the order of the resolution of the test itself. The result in effect means the S-wave velocity in the sand is unchanged by the build up of pore pressure and induced shear strain and that the conditions in the soil at the beginning of each loading stage (repetition) remained constant.
3. The static water pressure readings from the pore pressure transducer prior to the beginning of shaking showed a constant water pressure reading at the beginning of each loading stage (repetition). This water pressure indicated that the water table was located approximately 3.3 ft (1 m) below the ground surface, which was consistent with and confirmed by visual inspection of the adjacent river level. It

is important to have a consistent water pressure reading at the beginning of each loading stage (repetition) because it means that any and all residual excess pore pressure due to shaking during a prior loading stage (repetition) had been dissipated and "normal" soil conditions were re-established.

4. The cyclic threshold strain of the tested sand specimen at WLA was found to be in the range of 0.020% to 0.023% for 50 to 100 cycles of shaking. The value of the cyclic threshold strain was consistent among results from each of the loading stages (repetitions). For all loading stages in which the average shear strain did not exceed 0.02%, no residual excess pore water pressure was generated while loading stages whose values did exceed 0.023% did begin to generate residual excess pore water pressure. This value is very close to the cyclic threshold strains ranging from 0.012% to 0.027% reported in Cox, 2006, for a similar sand specimen also at the WLA. Dobry et al, 1982, also report a similar cyclic threshold strain of 0.01% for a clean sand tested in the laboratory using a cyclic triaxial test.
5. The use of staged loading for liquefaction testing allows a range of shear strains to be tested in the soil, starting with small shear strains at the early loading stages and increasing to moderate shear strains at the later loading stages. The values of shear strains achieved range from 0.0006% to 0.35%, a factor of almost 600 between the smallest and largest shear strains. The ability to achieve a wide range of shear strains with good resolution allows good definition of the relationship between residual excess pore water pressure and shear strain. The smallest shear

strains achieved are below the cyclic threshold strain and well within the linear range for the soil. The largest shear strains achieved are considered to be intermediate-level strains, those that are responsible for the triggering of liquefaction.

6. The excess pore water pressure generated during liquefaction testing was analyzed in terms of residual excess pore water pressure ratio, r_u, which equals the ratio between the change in pore water pressure and the initial vertical effective stress. The values of residual excess pore water pressure ratio measured over the course of the liquefaction test ranged from -17% to 78%. While soil liquefaction is considered to be triggered once the residual r_u reaches a value of 100%, the range of values achieved still provide meaningful insight into the potential of triggering liquefaction in this sand.

8.3 RECOMMENDATIONS AND FUTURE WORK

This research project was concluded with a reflection on its successes and limitations so as to improve the process for the future. While the success of the project was buoyed by the knowledge and experience base acquired from the previous two generations of the direct, in-situ liquefaction test (Chang, 2002, and Cox, 2006), there are always ways to refine and improve the testing process. In fact, in the time between the liquefaction testing in March 2012 and the writing of this thesis, the direct, in-situ liquefaction test has been performed dozens of times with significant updates. Therefore, the following list of recommendations for improving the testing technique and

suggestions for future work includes some items that have already been successfully incorporated into the procedure.

1. The installation of additional 3-D velocity transducers would allow the creation of more four-node elements for calculating shear strain. Calculating shear strains in multiple locations will provide greater insight into the motions induced in the soil during shaking.
2. Four-node elements formed by 3-D velocity sensors should be contained within a single material layer to avoid layer interfaces mid-element. While vertical motions are continuously propagated across the horizontal interface, horizontal motions can induce a discontinuity at the interface where the horizontal displacement in one layer does not match that in the other layer, causing the layers to slip against each other. The current finite element analysis shear strain calculation is not able to incorporate the presence of a layer interface in the element, so it is suggested that the inclusion of the interface simply be avoided in any future testing.
3. The installation of additional pore pressure transducers would allow greater resolution regarding the generation and dissipation of excess pore water pressure in the soil. In addition, increasing the number of locations where pore water pressure is measured permits r_u versus Υ relationships to be defined in more locations, providing a more complete analysis of the field specimen.
4. The steel connector rods used for connecting the transducers to the steel rods during installation should be redesigned to encourage easy disconnection of the

transducer at the desired depth. In their current form, the simple compression slip fit has very little clearance between the transducer cap and the connector rod, which can easily jam with fine soil particles during pushing.

5. Depending on the project, the number of geophones in each velocity transducer can be reduced from three to two. The current finite element analysis shear strain calculation method only uses two dimensions, so the data from the third dimension is of minor importance at this time. There are times, however, when the presence of the third dimension is useful. For instance, on can: (1) perform seismic crosshole tests using a single receiver and multiple sources from different angles, (2) perform liquefaction-test shaking along two different axes when orientation may need to be considered, and (3) confirm the inline horizontal geophone is parallel to the direction of shaking and was not rotated off axis during installation.
6. Redesign the tip of the pore pressure transducer so that there are two filters 180° from one another. The generation of negative residual excess pore water pressure during the incipient loading cycles was not well understood and mildly thought to be the result of the asymmetric tip design. The design of two holes creates symmetric access for the water to reach the pore pressure transducer's diaphragm. (Note: This redesign was used in the most recent implementation of liquefaction testing in Christchurch, New Zealand (2013); it appears that the generation of negative residual excess pore water pressure is not a manifestation from the equipment but rather a real phenomenon).

7. Capturing the cycle-by-cycle degradation of shear wave velocity due to the generation of residual excess pore water pressure from shaking during a loading stage would provide great insight into the gradual reduction in soil stiffness and strength. The resolution afforded by a cycle-by-cycle analysis is higher than can be achieved via cross-correlation. For this analysis to be effective, however, a much higher sampling frequency must be used to increase precision.
8. The incorporation of seismic downhole tests immediately before and after a loading stage (repetition) can further provide information regarding changes in the small-strain behavior of the soil. A downhole test performed before a liquefaction test loading stage would provide a baseline S-wave velocity, and subsequent downhole tests performed immediately after the shaking while the residual excess pore water pressures are still elevated would allow the change in S-wave velocity due to changes in the effective stress to be observed.
9. In another attempt to use seismic tests to capture small-strain behavior, the crosshole test can be modified so that it can be used during shaking in a liquefaction test loading stage. To do this, a sensor installed to any desired depth can be outfitted with a mechanism to emit a constant, single, high-frequency signal during shaking. The 3-D velocity transducers would capture the energy generated from both T-Rex and the seismic crosshole source. Being energies generated at very different frequencies, each one can theoretically be identified when the data is shown in the frequency domain, and filtering in the time domain

should allow the separation of the signals. In this way, a continuous crosshole test can be performed simultaneously with the liquefaction test shaking.

As a footnote to these recommendations, another liquefaction testing campaign is planned for June, 2014 (about 6 weeks from this writing). It is planned to try to implement Recommendations #2, #3, #4, #5, #6, #7, and #8 in this new work.

Appendix A

Appendix A contains the shear strain and pore water pressure ratio time histories for each of the staged loadings (repetitions) for which the data permitted analysis. Also included for reference is the table summarizing the time at which the loading stage began, the shaking force level, the shaking frequency, and the number of cycles.

Table 7. Sequence of repetitions in liquefaction testing at the WLA with corresponding force, frequency, number of cycles, and time at which each series was begun.

Trial #	Test Date	Starting Time	Frequency	Cycles	Drive signal input
			(Hz)		(lbs)
1	3/19/12	12:58	20	50	3,000
2	3/19/12	13:04	25	50	3,000
3	3/19/12	13:07	30	50	3,000
4	3/19/12	13:08	30	20	3,000
5	3/19/12	13:10	15	20	3,000
6	3/19/12	13:10	12	20	3,000
7	3/19/12	13:11	10	20	3,000
8	3/19/12	13:12	30	50	3,000
9	3/19/12	13:14	10	10	3,000
10	3/19/12	13:15	10	20	6,000
11	3/19/12	13:33	30	20	6,000
12	3/19/12	14:13	30	10	6,000
13	3/19/12	14:15	30	10	7,500
14	3/19/12	14:17	30	10	9,000
15	3/19/12	14:19	30	10	10,500
16	3/19/12	14:25	30	10	12,000
17	3/19/12	14:29	30	20	9,000
18	3/19/12	14:32	30	20	12,000
19	3/19/12	14:34	30	20	13,980
20	3/19/12	14:39	30	20	16,020
21	3/19/12	14:45	30	20	18,000
24	3/19/12	15:07	20	20	22,020
25	3/19/12	15:15	20	50	24,000
26	3/19/12	15:22	20	100	27,000
27	3/19/12	15:43	20	100	30,000
28	3/19/12	15:52	10	100	30,000
29	3/19/12	16:07	20	300	30,000
30	3/19/12	16:20	20	500	30,000
31	3/19/12	16:35	10	300	30,000
32	3/20/12	9:55	20	300	30,000
33	3/20/12	10:13	10	300	30,000

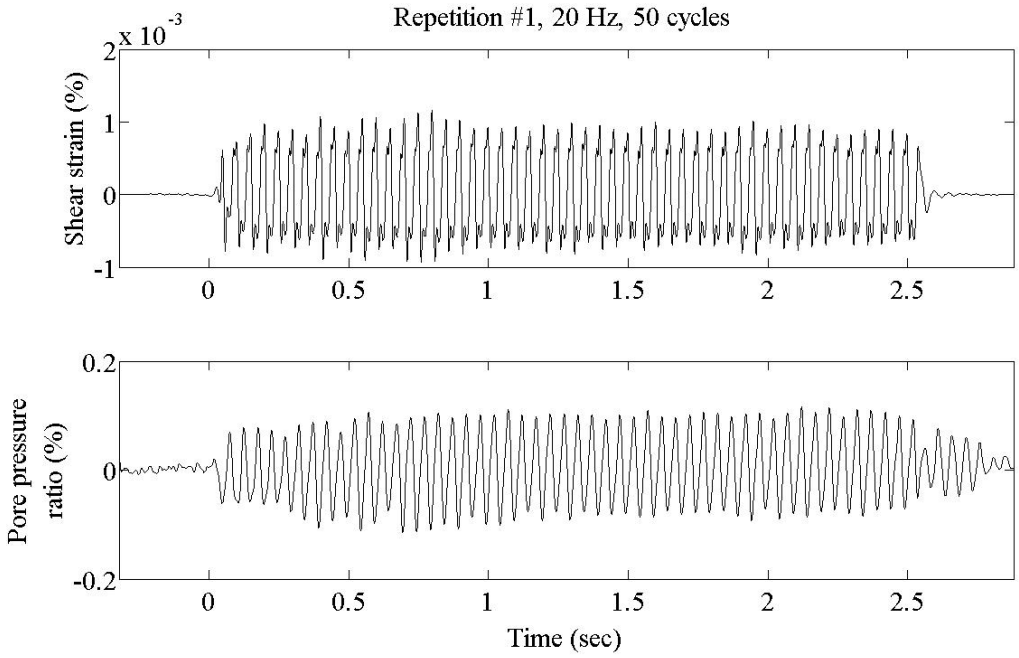

Figure 67. Shear strain and pore pressure ratio time series for Loading Stage (Repetition) #1.

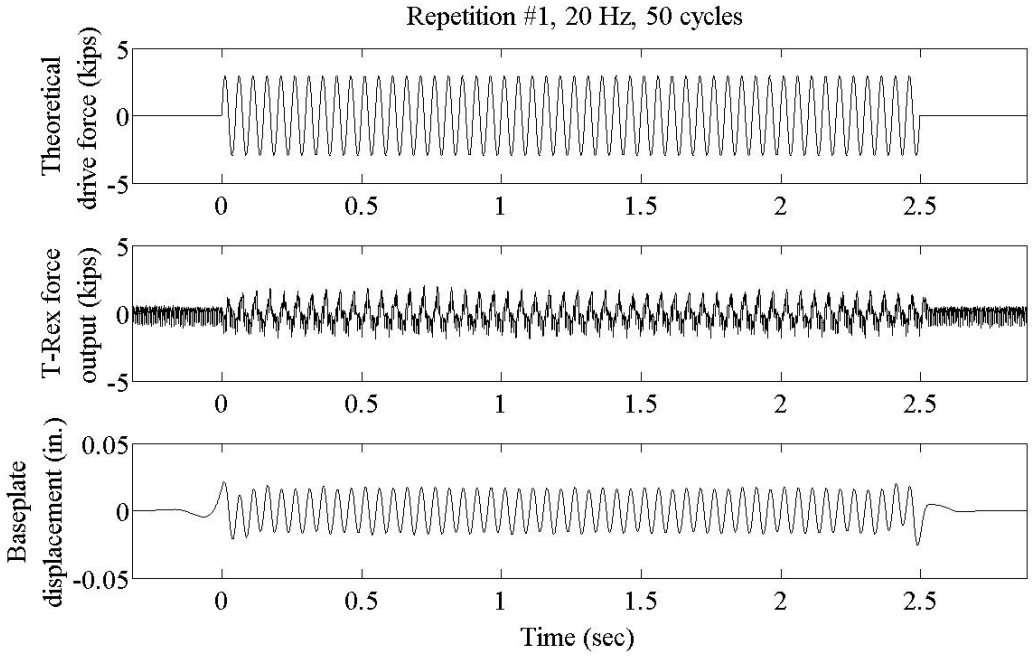

Figure 68. Theoretical drive force, T-Rex force output, and baseplate displacement for Loading Stage (Repetition) #1.

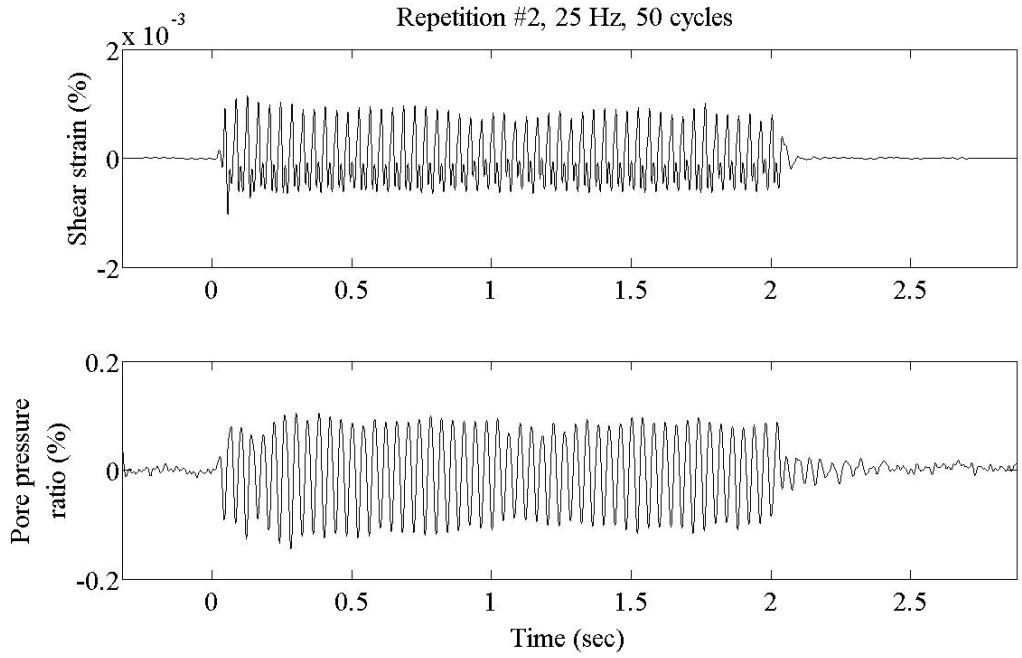

Figure 69. Shear strain and pore pressure ratio time series for Loading Stage (Repetition) #2.

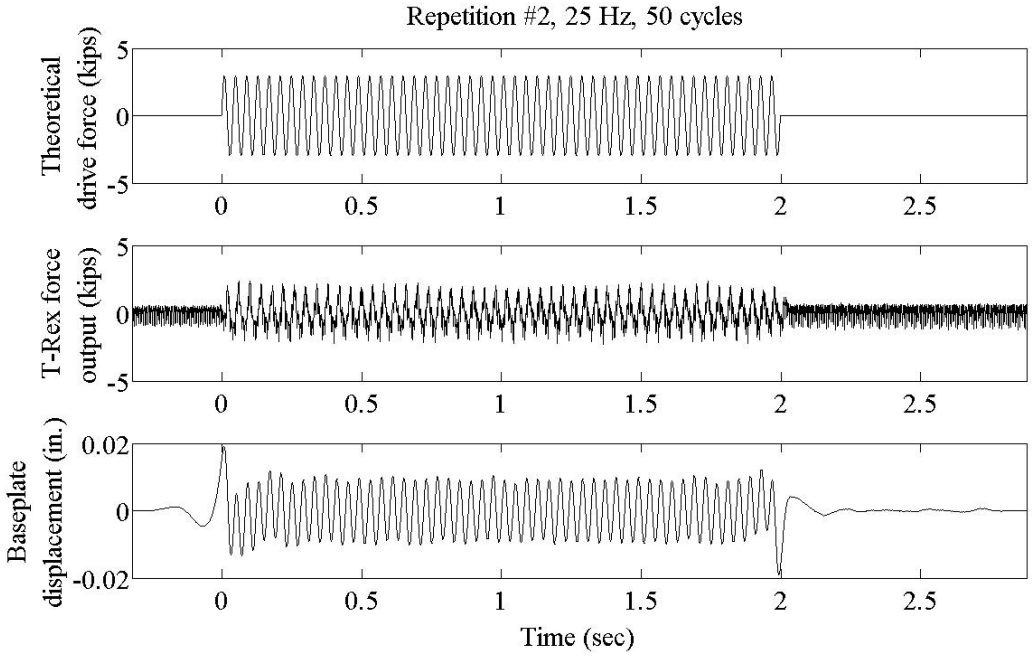

Figure 70. Theoretical drive force, T-Rex force output, and baseplate displacement for Loading Stage (Repetition) #2.

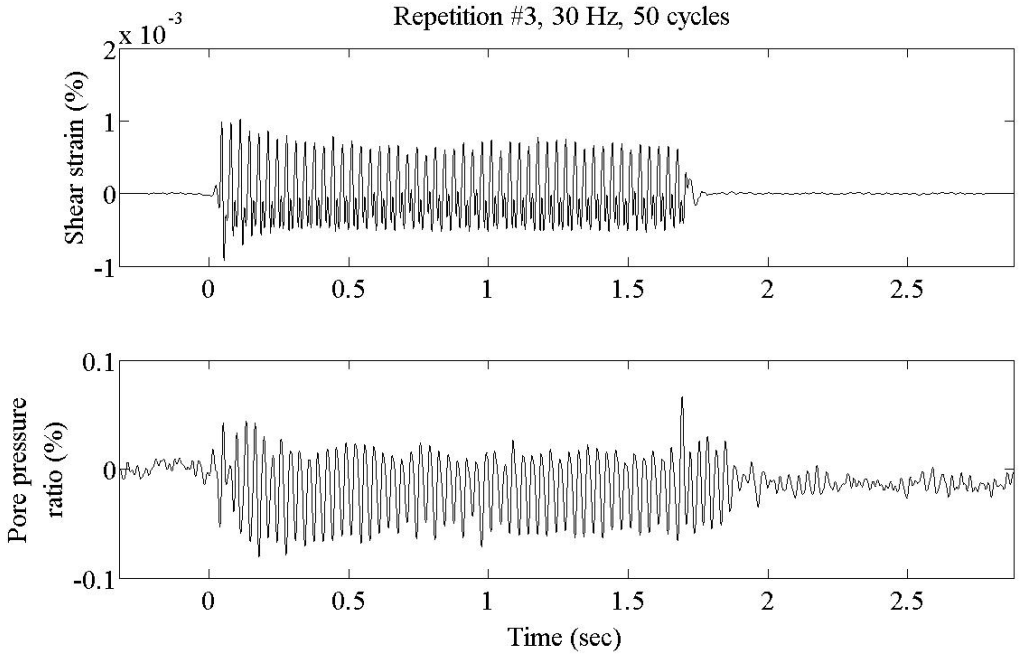

Figure 71. Shear strain and pore pressure ratio time series for Loading Stage (Repetition) #3.

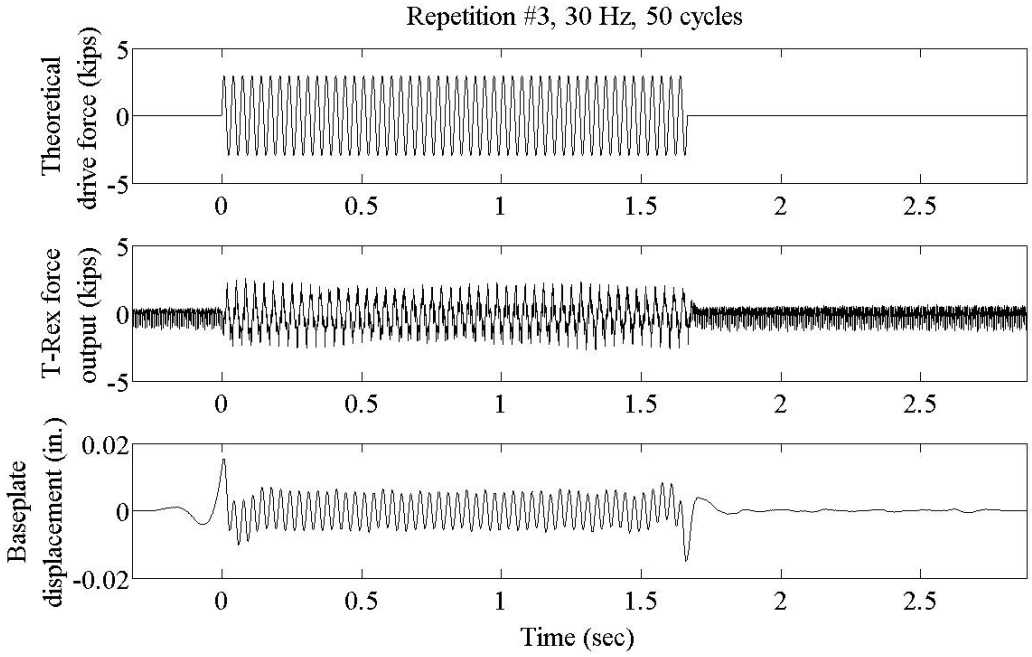

Figure 72. Theoretical drive force, T-Rex force output, and baseplate displacement for Loading Stage (Repetition) #3.

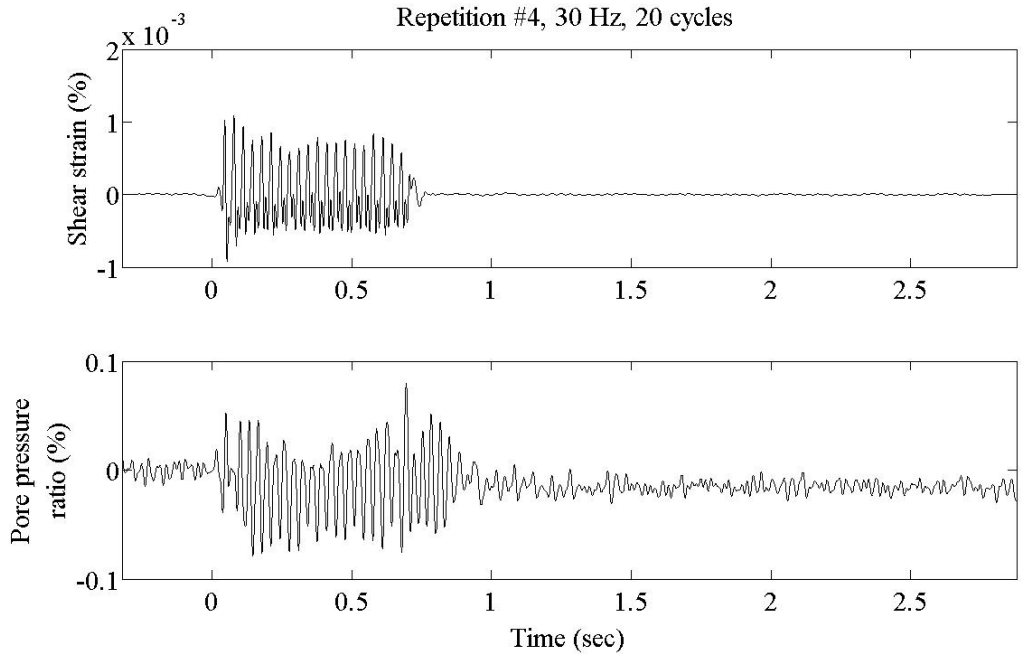

Figure 73. Shear strain and pore pressure ratio time series for Loading Stage (Repetition) #4.

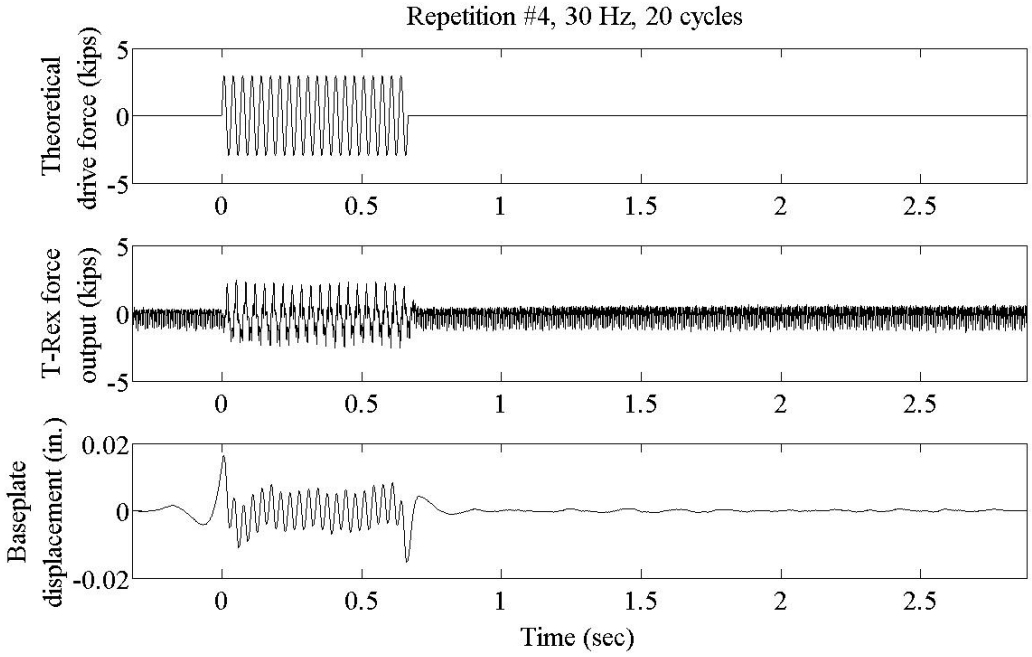

Figure 74. Theoretical drive force, T-Rex force output, and baseplate displacement for Loading Stage (Repetition) #4.

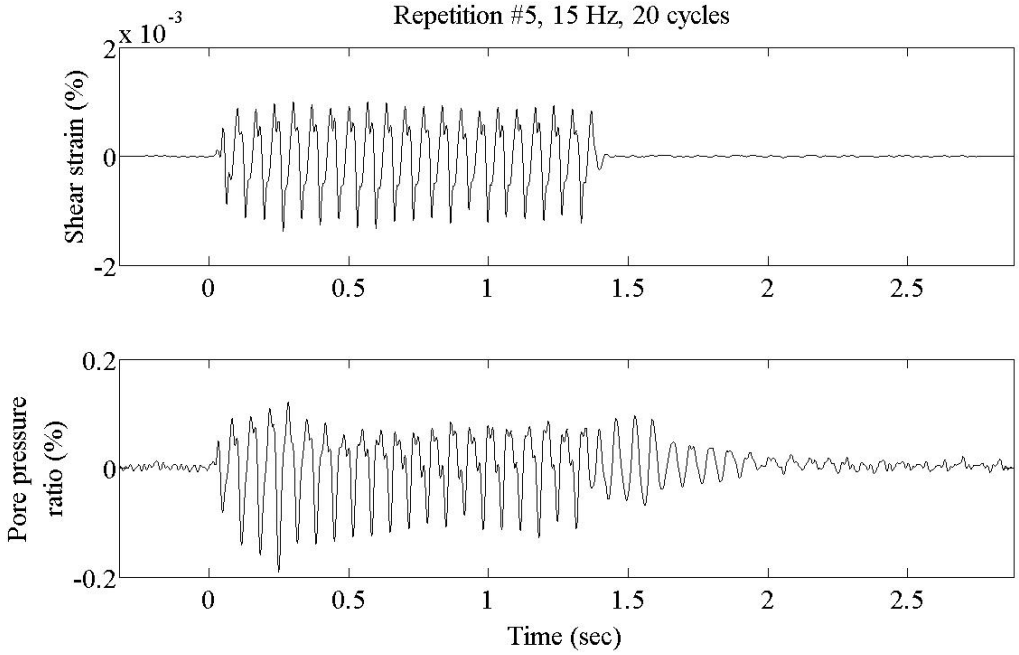

Figure 75. Shear strain and pore pressure ratio time series for Loading Stage (Repetition) #5.

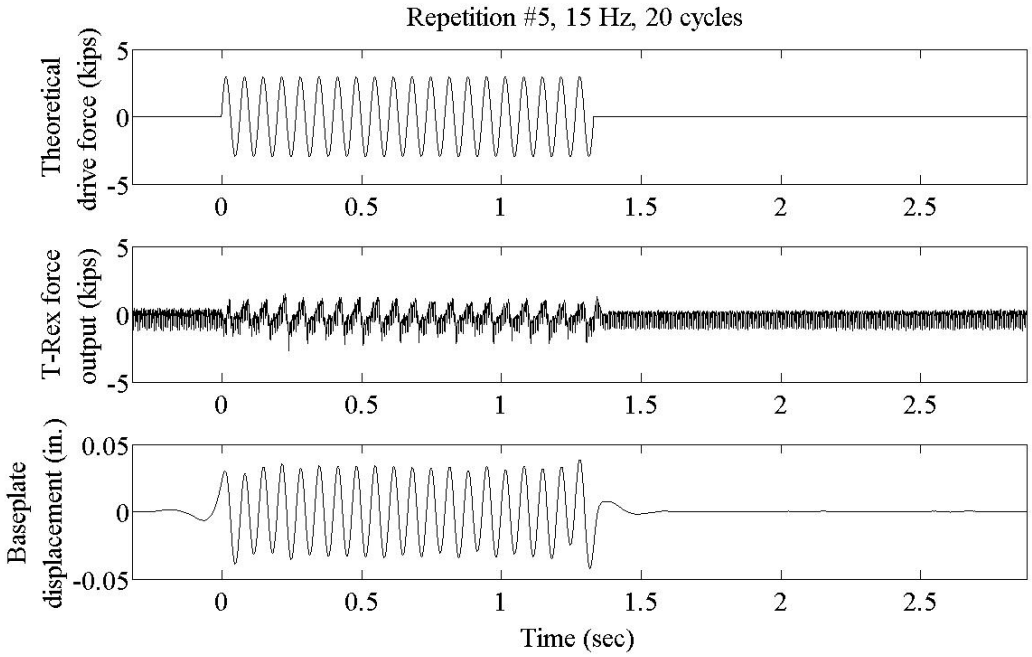

Figure 76. Theoretical drive force, T-Rex force output, and baseplate displacement for Loading Stage (Repetition) #5.

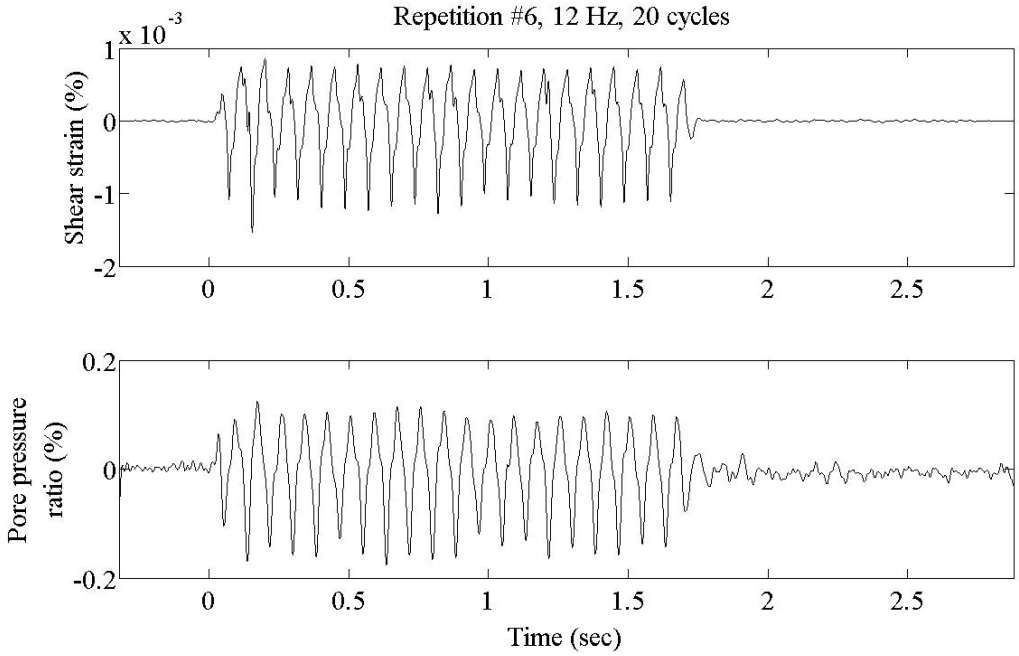

Figure 77. Shear strain and pore pressure ratio time series for Loading Stage (Repetition) #6.

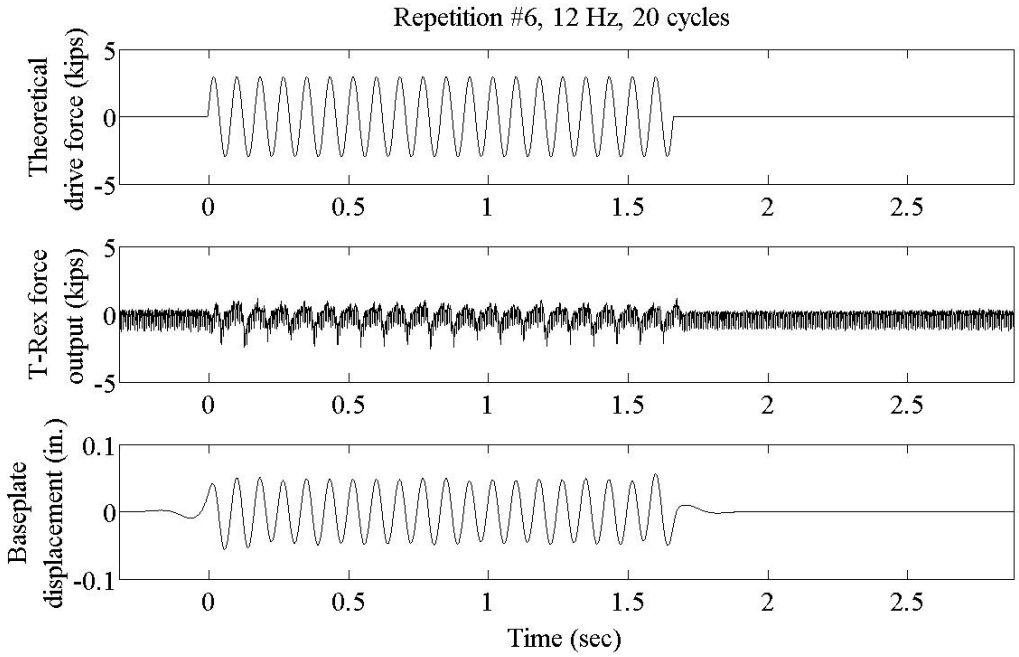

Figure 78. Theoretical drive force, T-Rex force output, and baseplate displacement for Loading Stage (Repetition) #6.

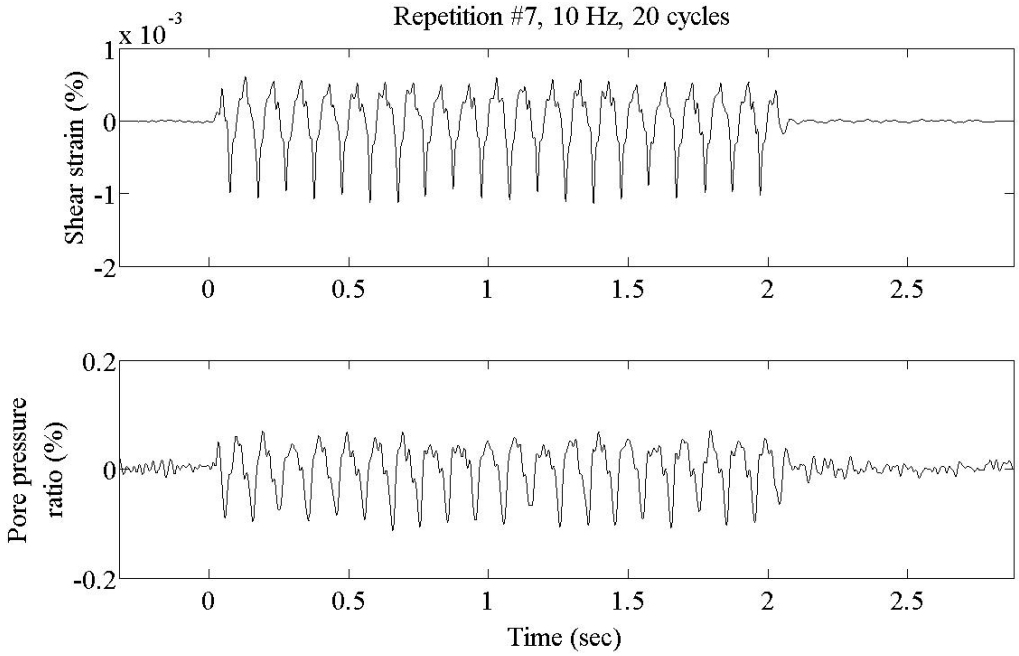

Figure 79. Shear strain and pore pressure ratio time series for Loading Stage (Repetition) #7.

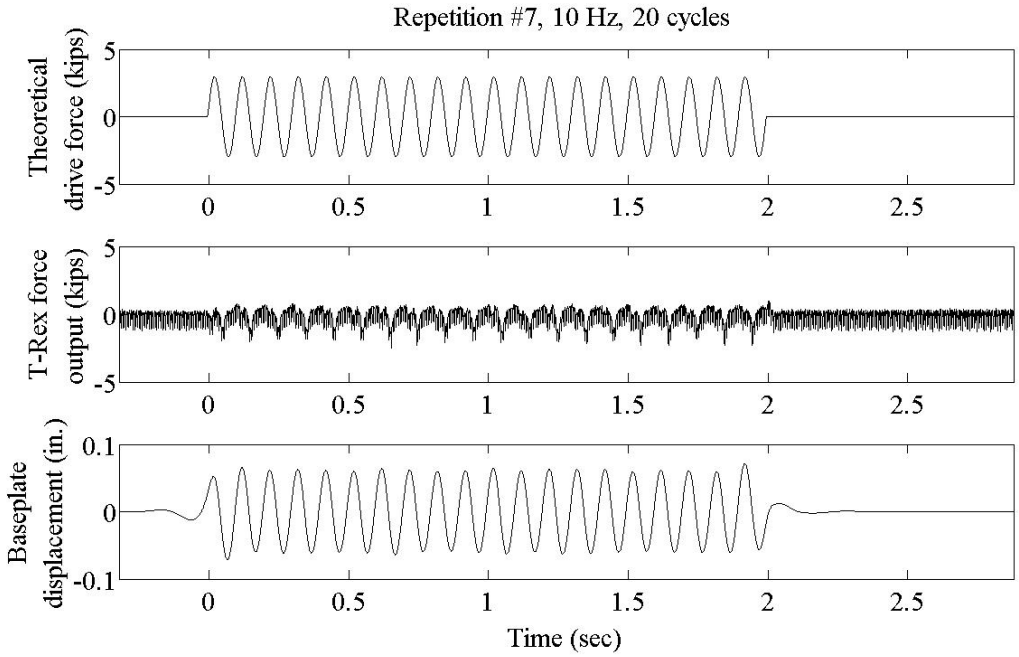

Figure 80. Theoretical drive force, T-Rex force output, and baseplate displacement for Loading Stage (Repetition) #7.

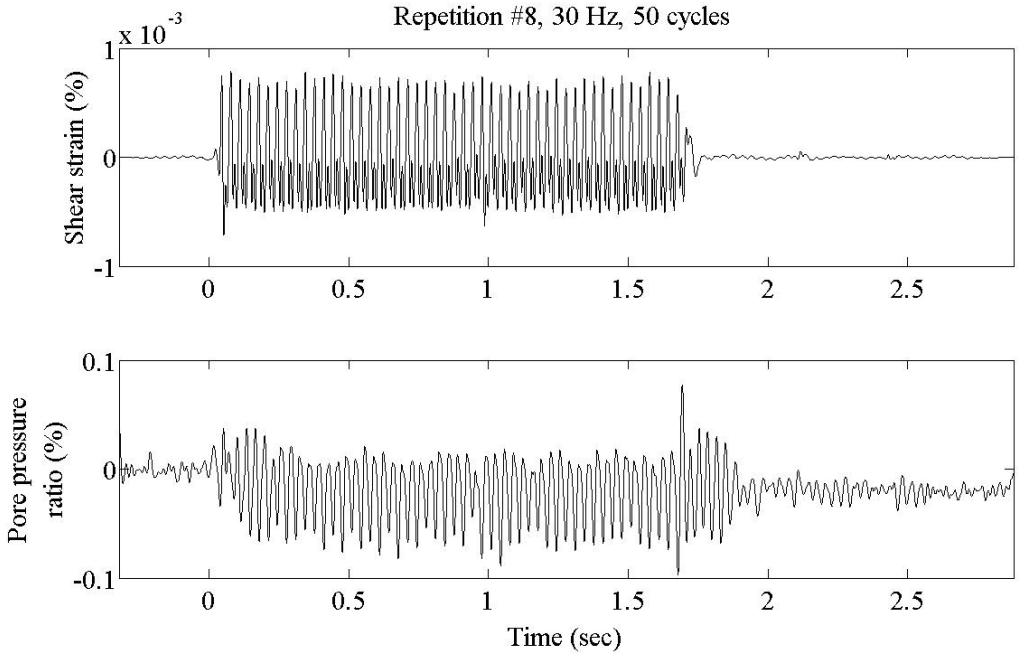

Figure 81. Shear strain and pore pressure ratio time series for Loading Stage (Repetition) #8.

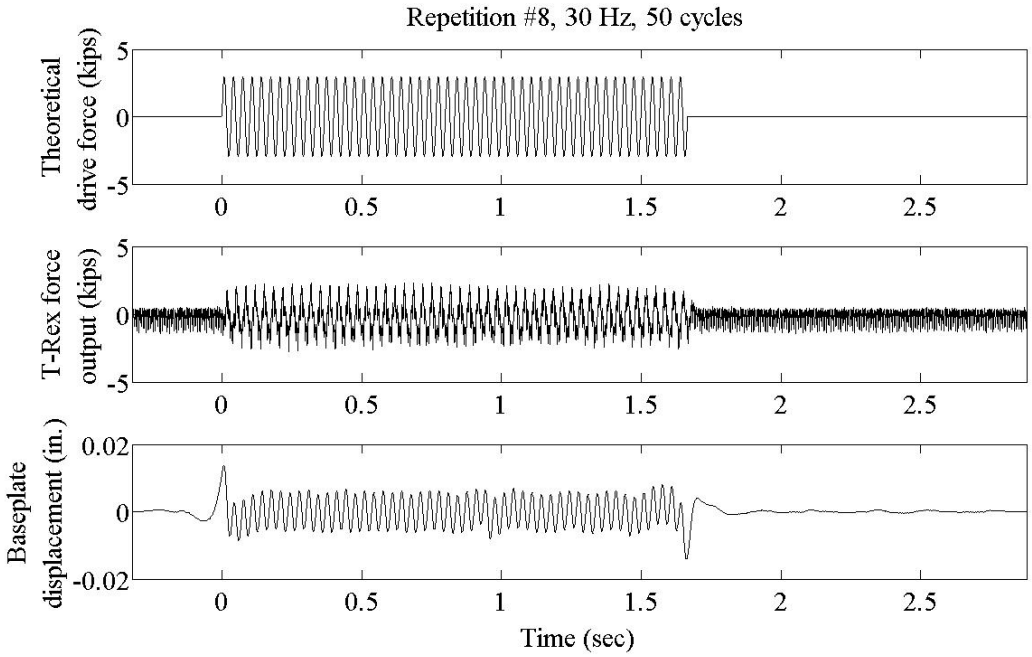

Figure 82. Theoretical drive force, T-Rex force output, and baseplate displacement for Loading Stage (Repetition) #8.

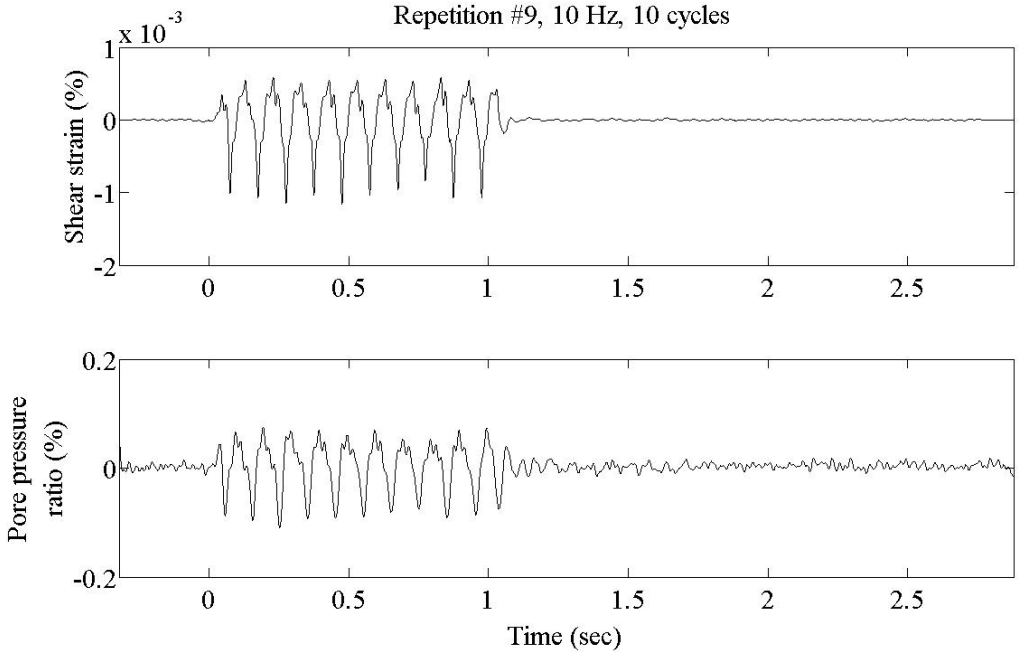

Figure 83. Shear strain and pore pressure ratio time series for Loading Stage (Repetition) #9.

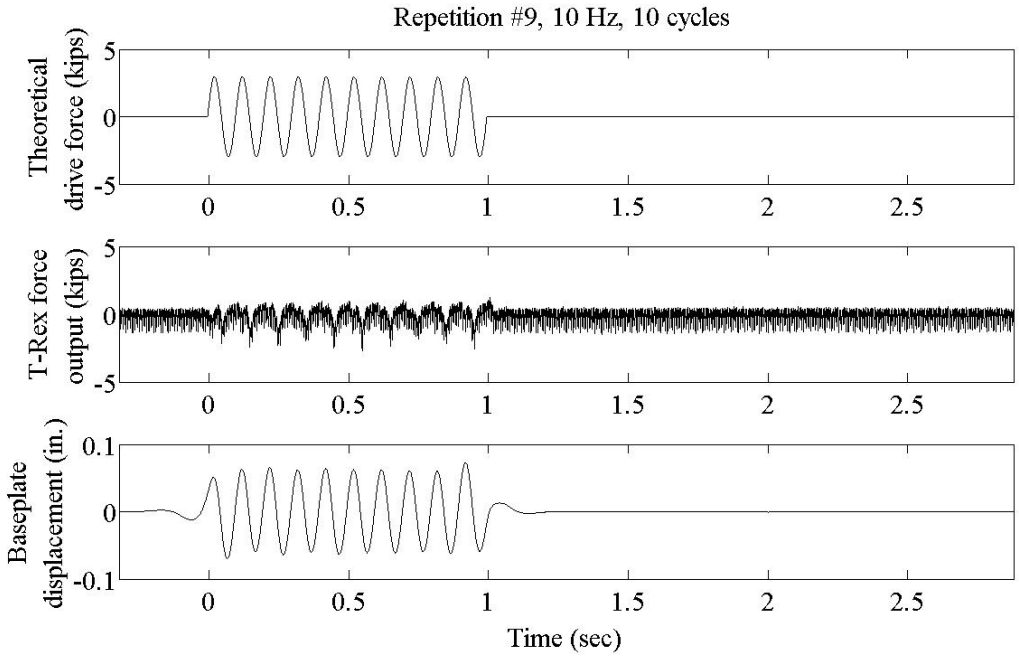

Figure 84. Theoretical drive force, T-Rex force output, and baseplate displacement for Loading Stage (Repetition) #9.

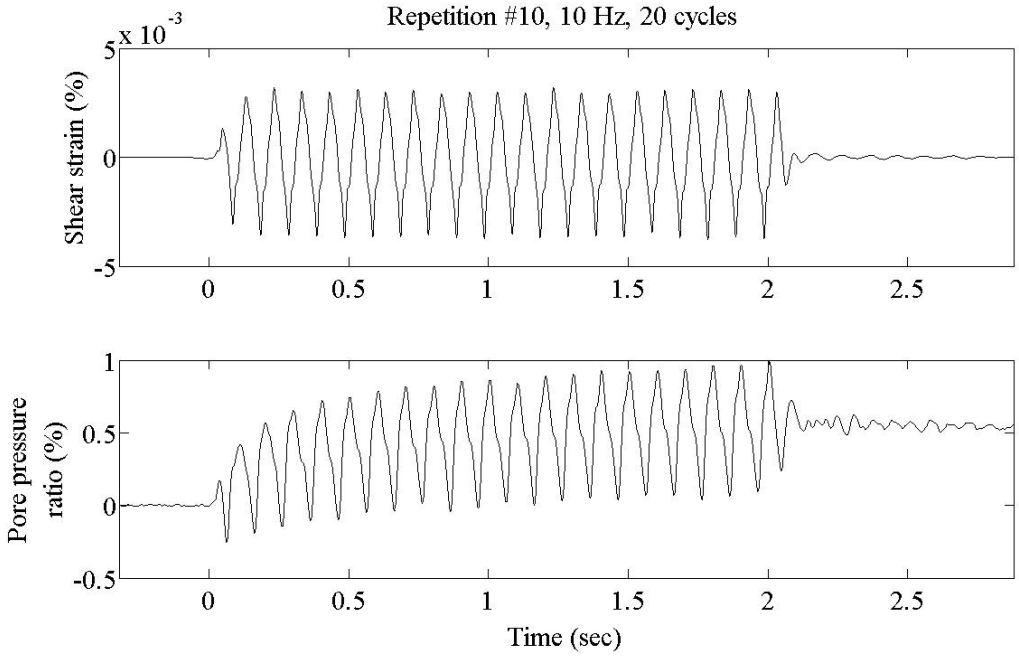

Figure 85. Shear strain and pore pressure ratio time series for Loading Stage (Repetition) #10.

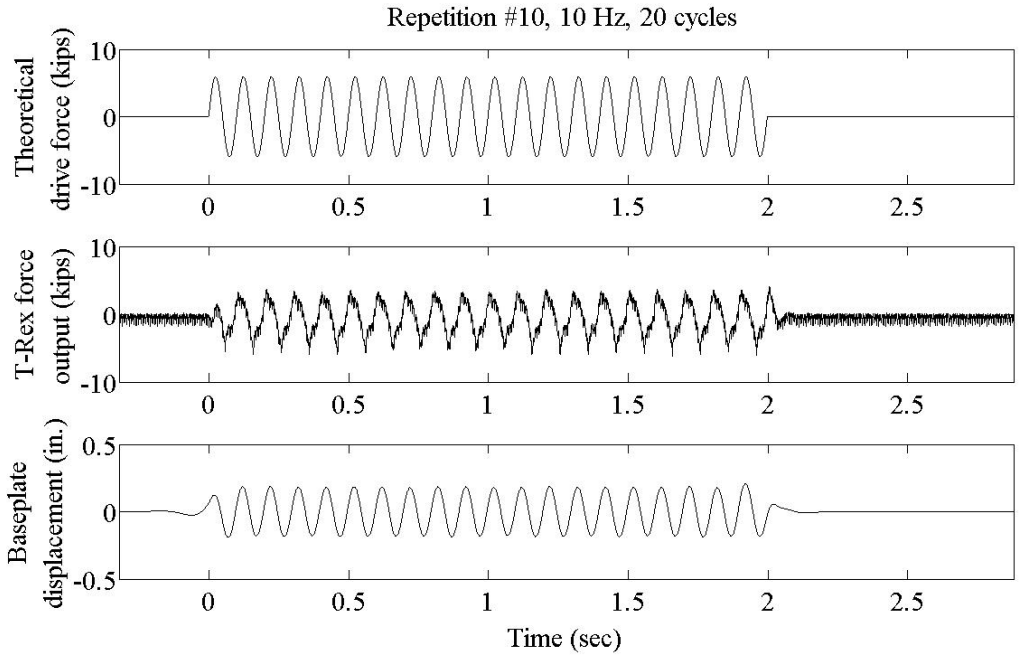

Figure 86. Theoretical drive force, T-Rex force output, and baseplate displacement for Loading Stage (Repetition) #10.

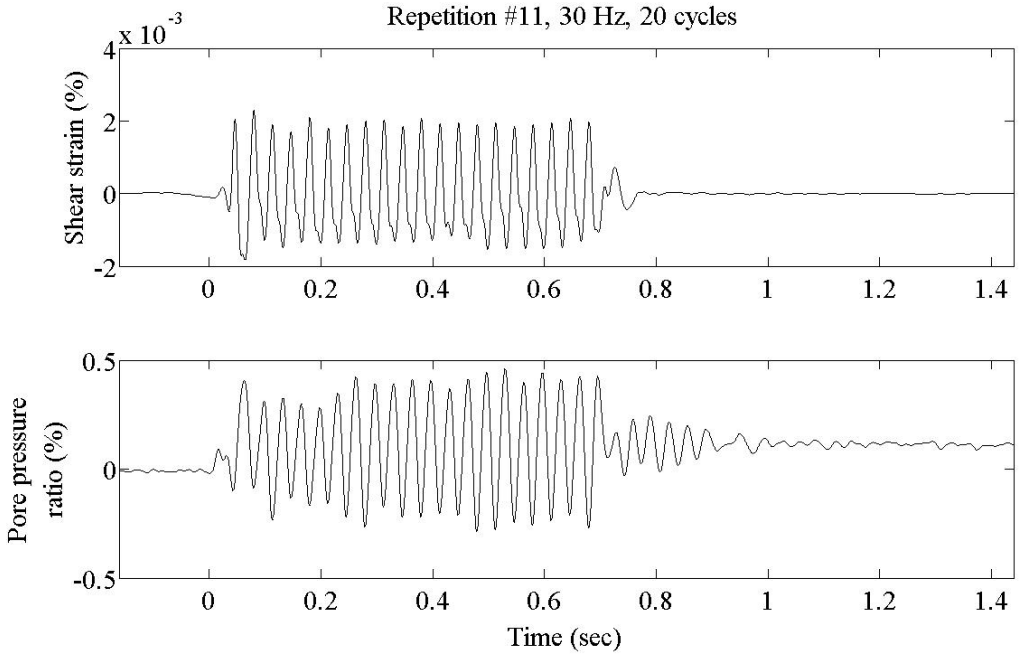

Figure 87. Shear strain and pore pressure ratio time series for Loading Stage (Repetition) #11.

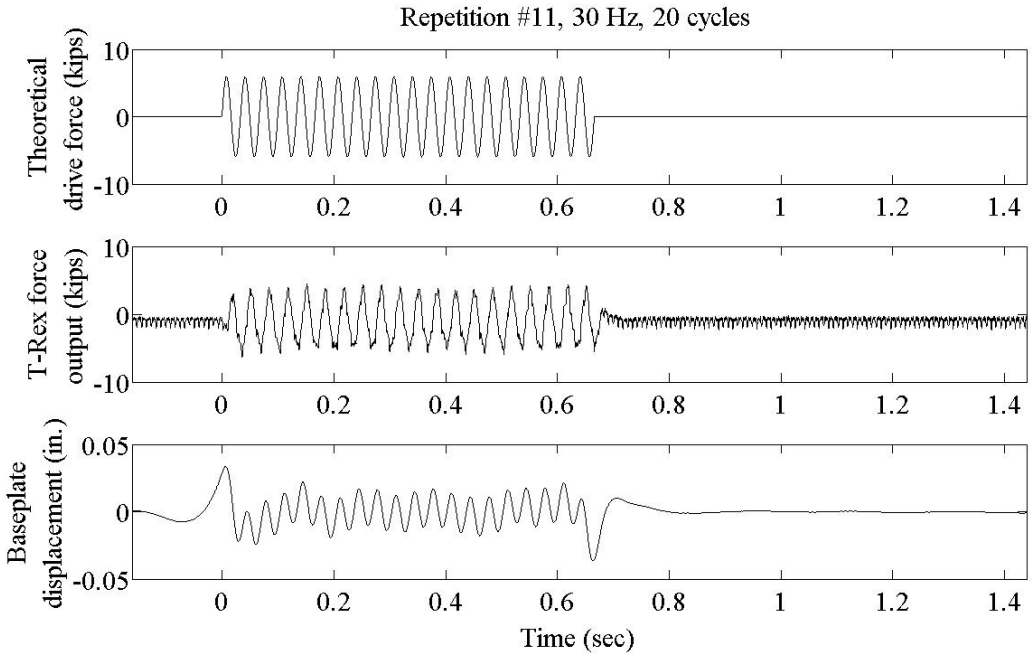

Figure 88. Theoretical drive force, T-Rex force output, and baseplate displacement for Loading Stage (Repetition) #11.

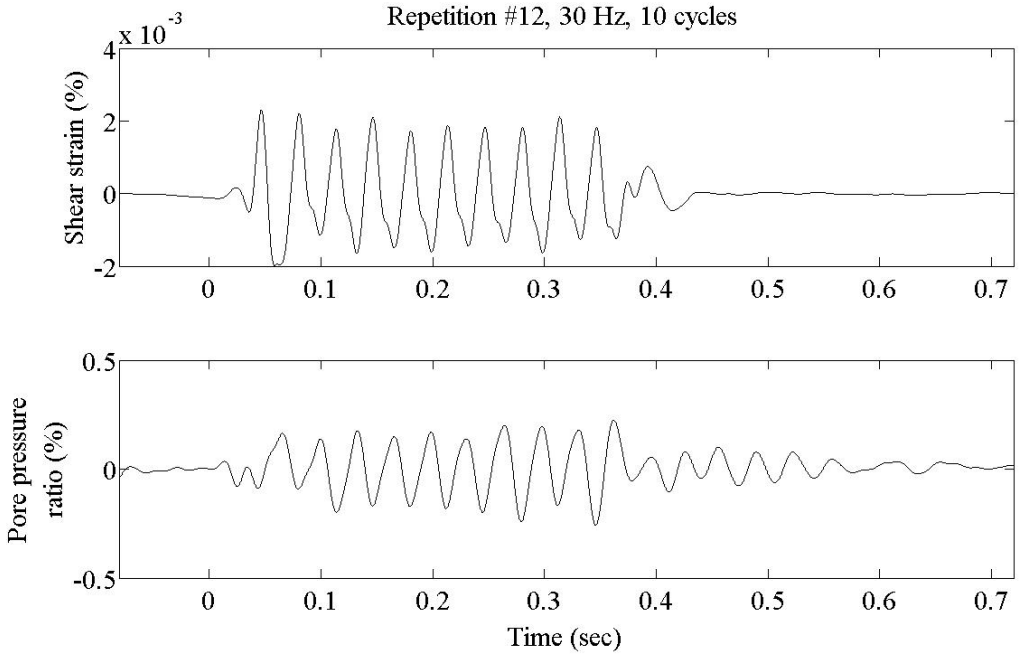

Figure 89. Shear strain and pore pressure ratio time series for Loading Stage (Repetition) #12.

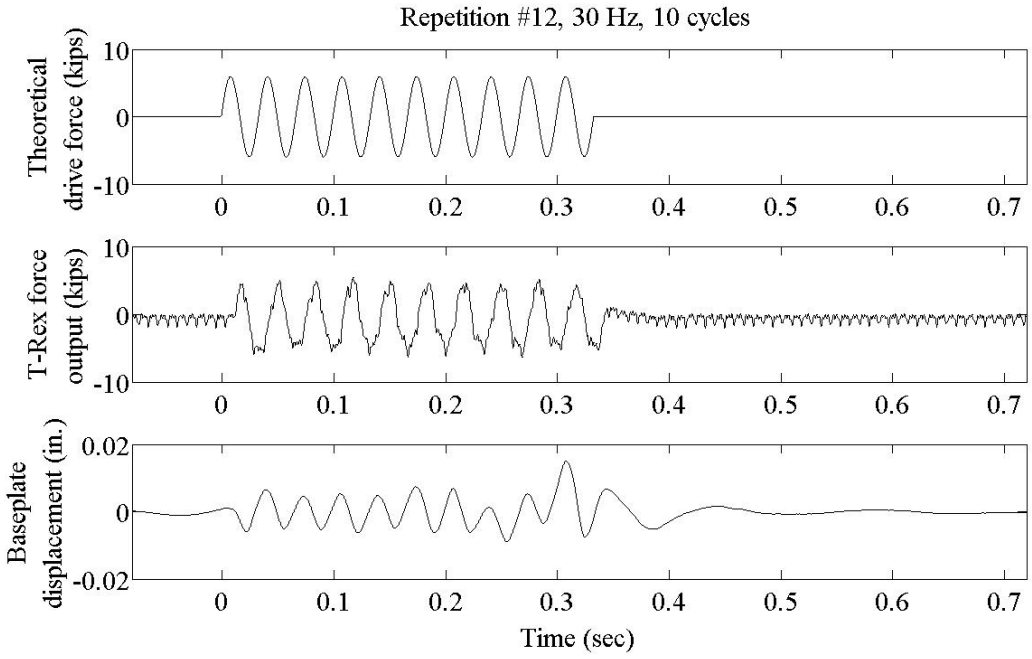

Figure 90. Theoretical drive force, T-Rex force output, and baseplate displacement for Loading Stage (Repetition) #12.

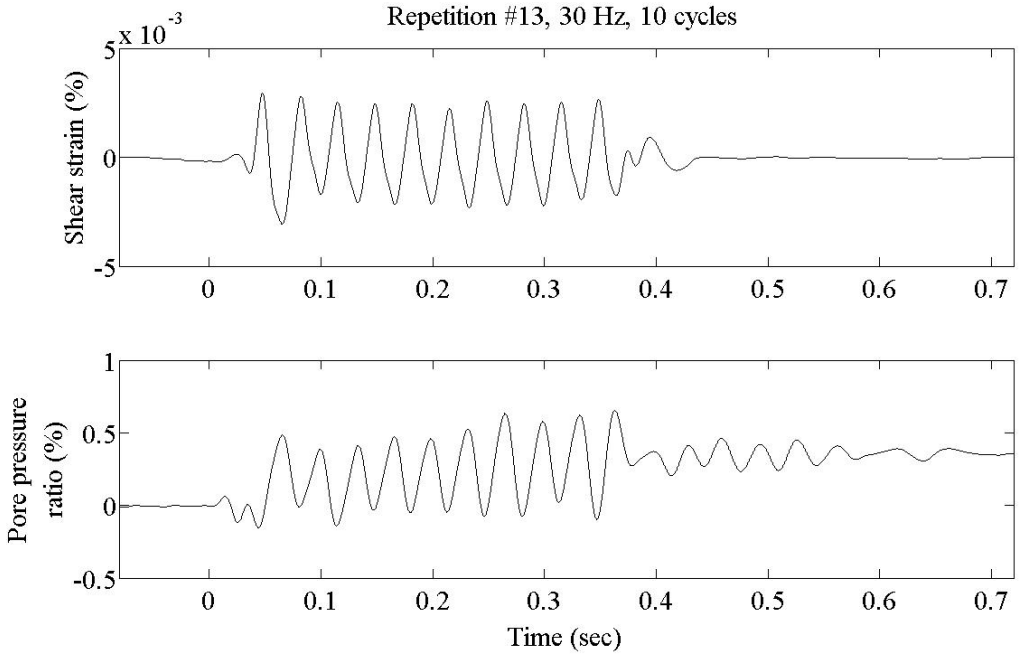

Figure 91. Shear strain and pore pressure ratio time series for Loading Stage (Repetition) #13.

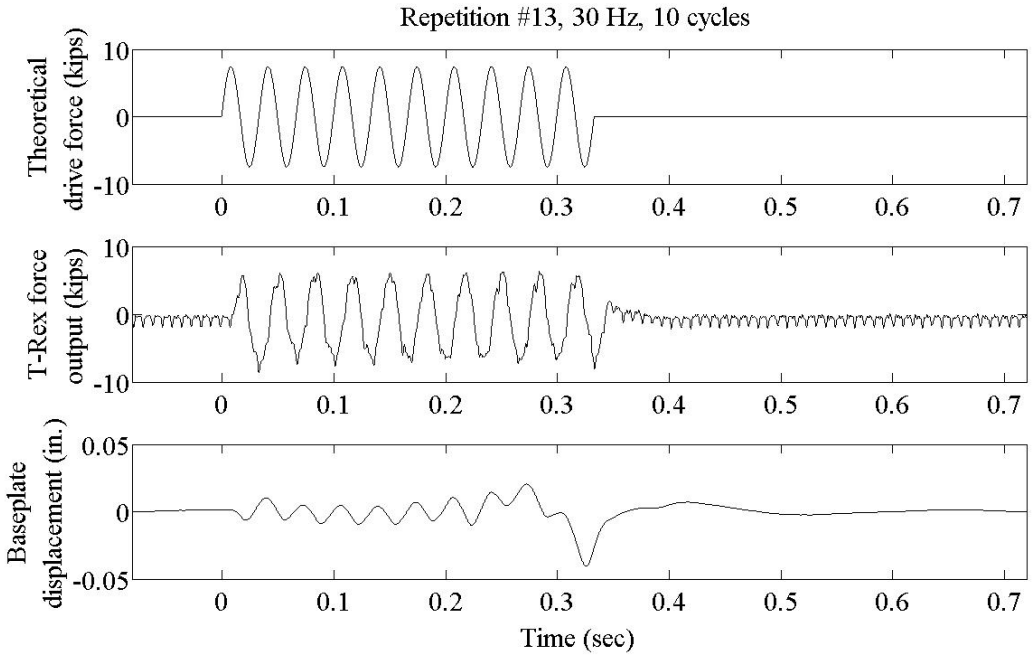

Figure 92. Theoretical drive force, T-Rex force output, and baseplate displacement for Loading Stage (Repetition) #13.

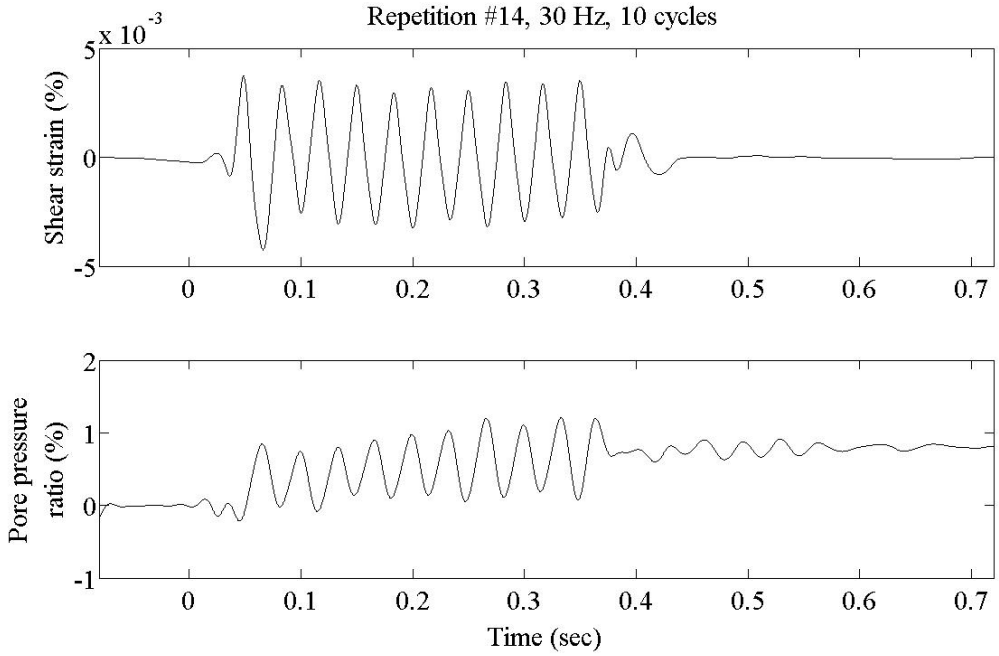

Figure 93. Shear strain and pore pressure ratio time series for Loading Stage (Repetition) #14.

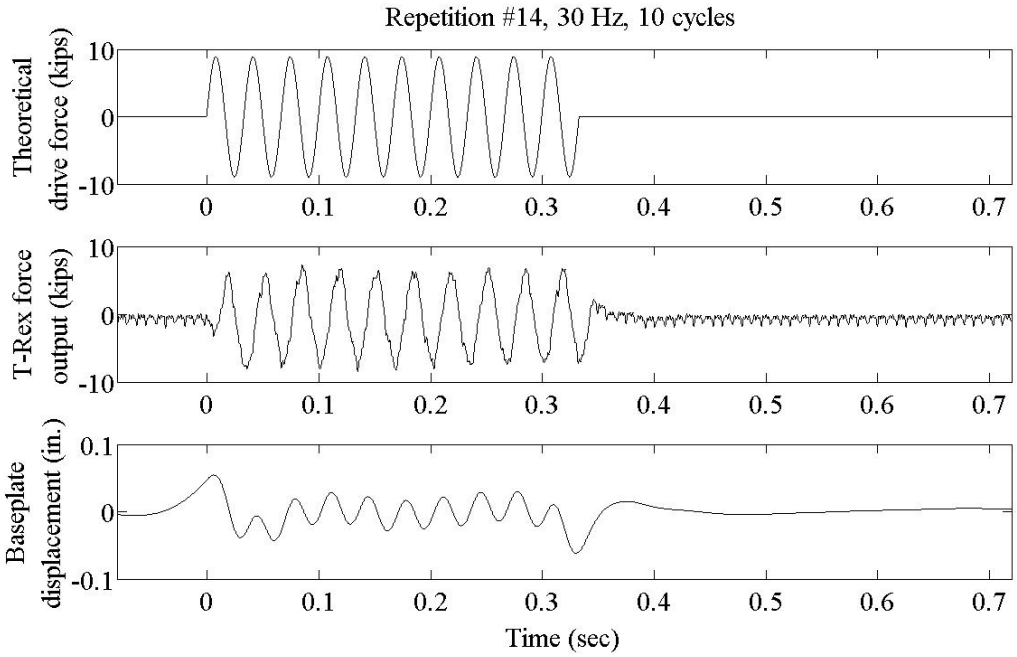

Figure 94. Theoretical drive force, T-Rex force output, and baseplate displacement for Loading Stage (Repetition) #14.

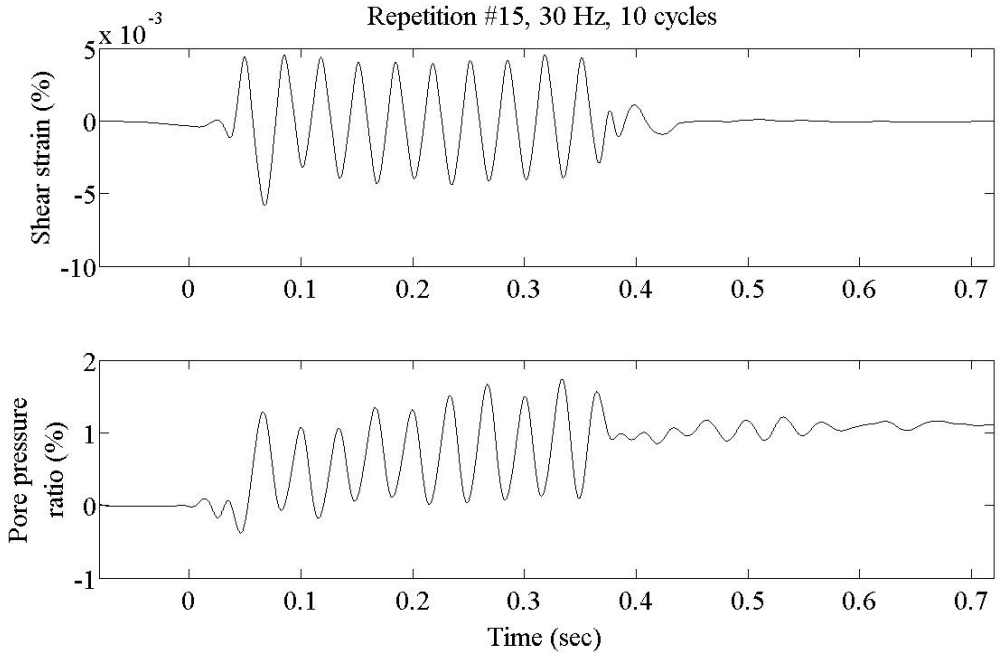

Figure 95. Shear strain and pore pressure ratio time series for Loading Stage (Repetition) #15.

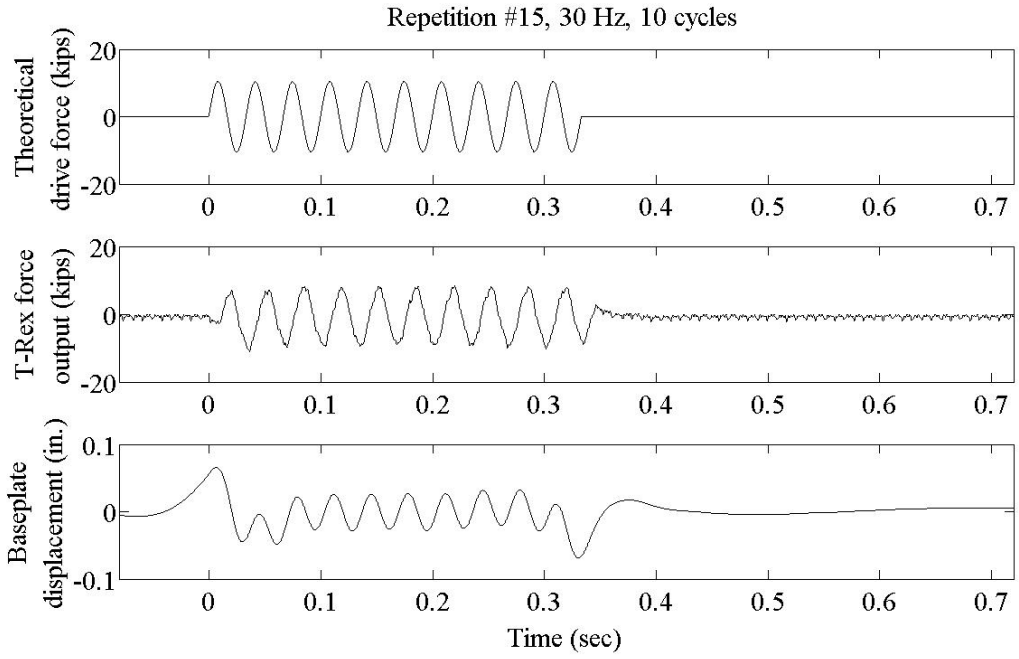

Figure 96. Theoretical drive force, T-Rex force output, and baseplate displacement for Loading Stage (Repetition) #15.

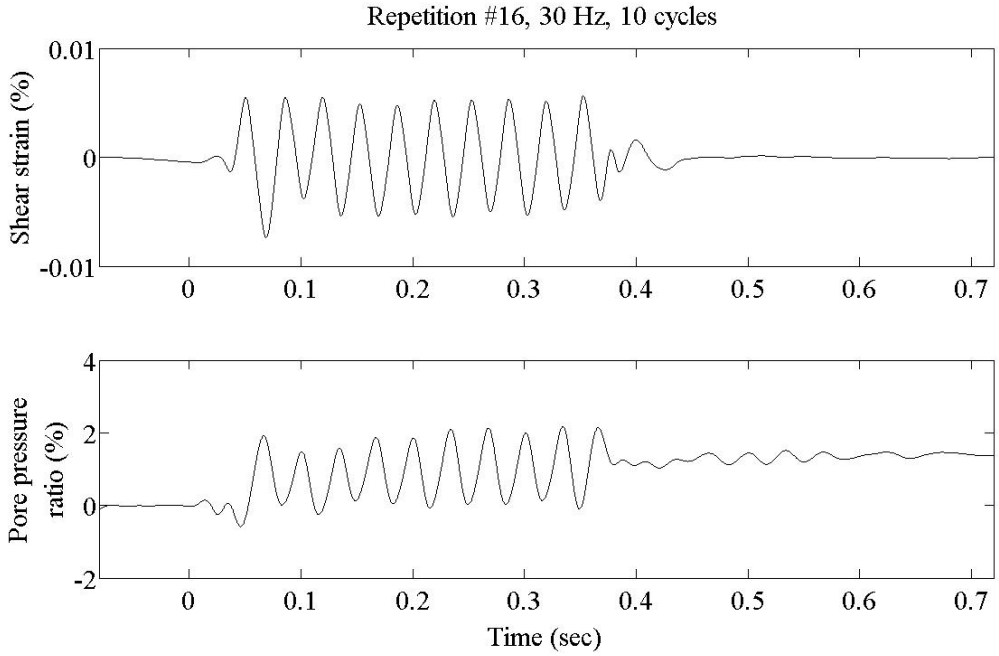

Figure 97. Shear strain and pore pressure ratio time series for Loading Stage (Repetition) #16.

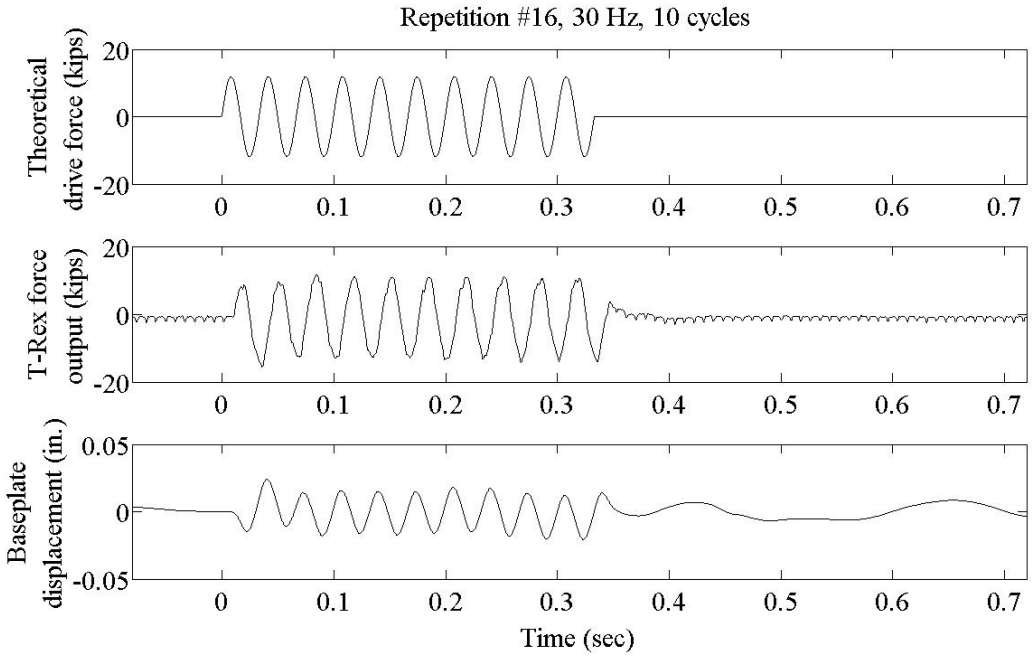

Figure 98. Theoretical drive force, T-Rex force output, and baseplate displacement for Loading Stage (Repetition) #16.

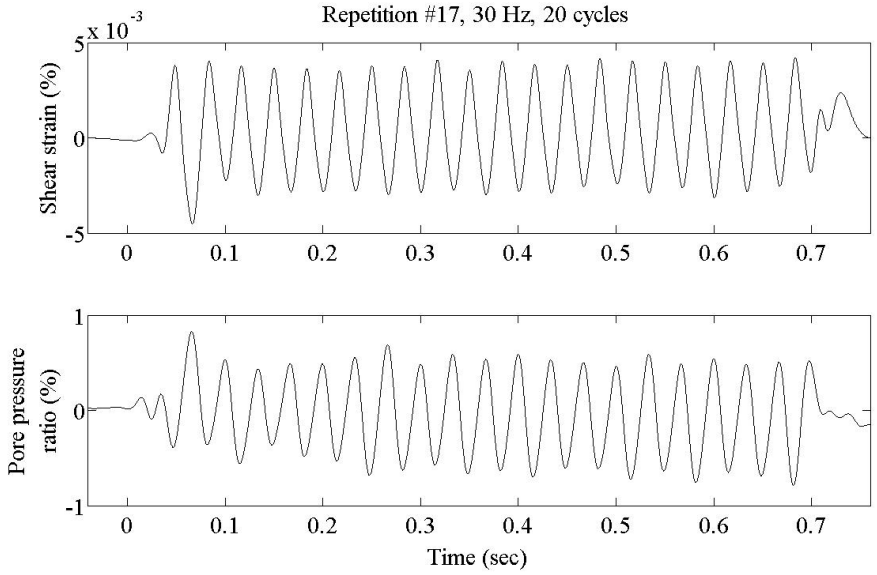

Figure 99. Shear strain and pore pressure ratio time series for Loading Stage (Repetition) #17.

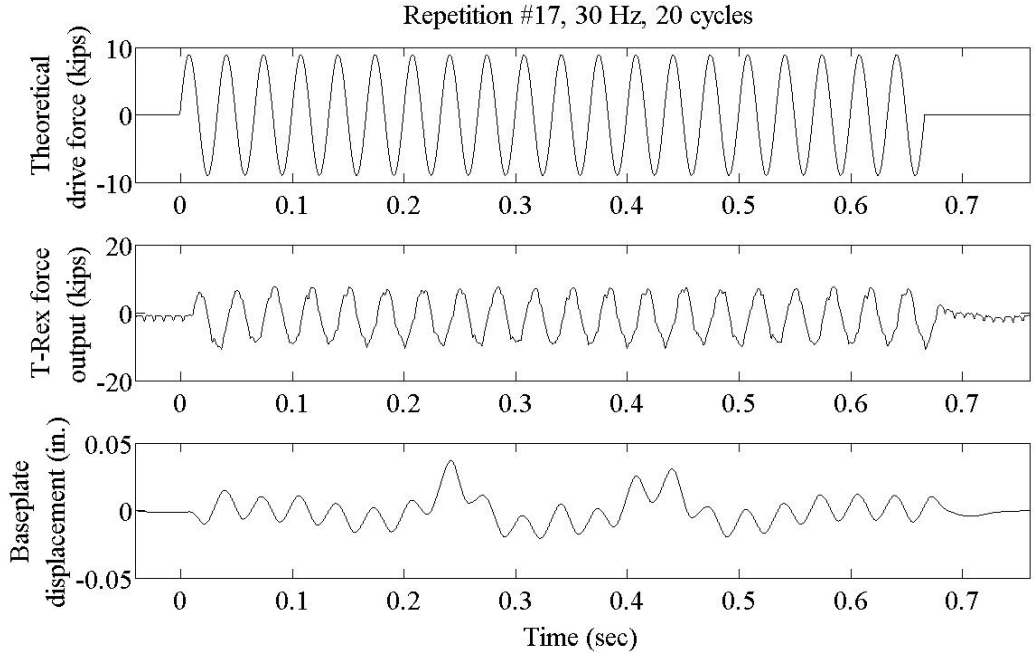

Figure 100. Theoretical drive force, T-Rex force output, and baseplate displacement for Loading Stage (Repetition) #17.

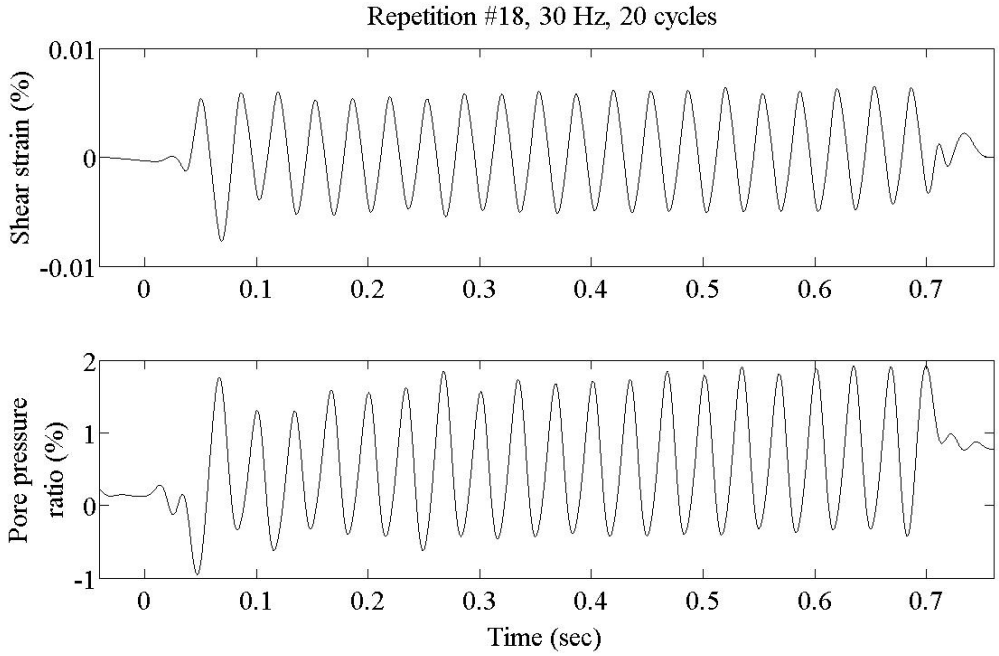

Figure 101. Shear strain and pore pressure ratio time series for Loading Stage (Repetition) #18.

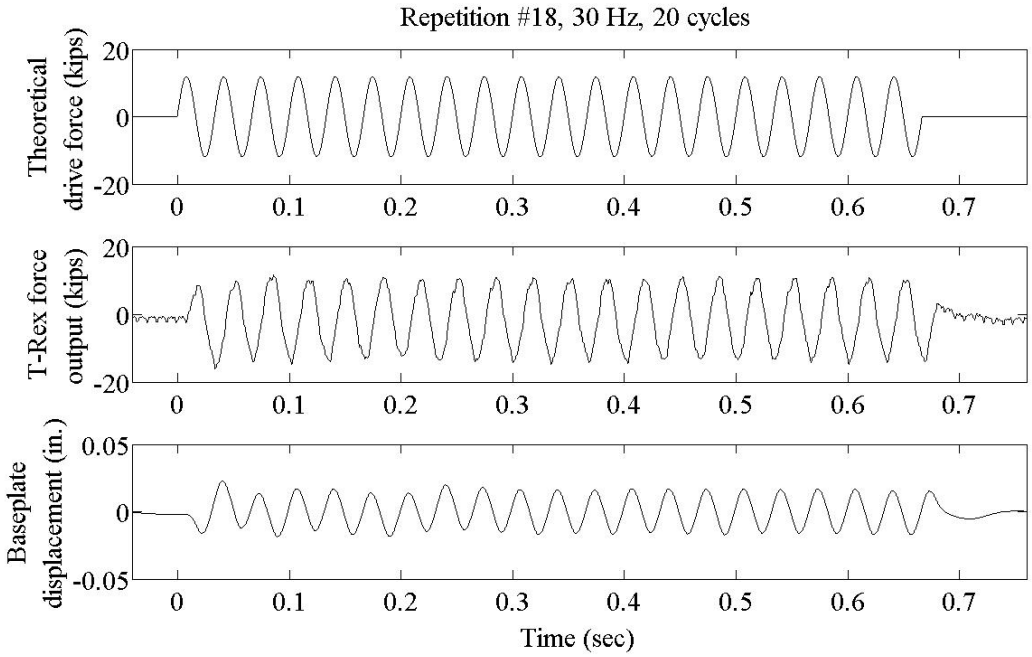

Figure 102. Theoretical drive force, T-Rex force output, and baseplate displacement for Loading Stage (Repetition) #18.

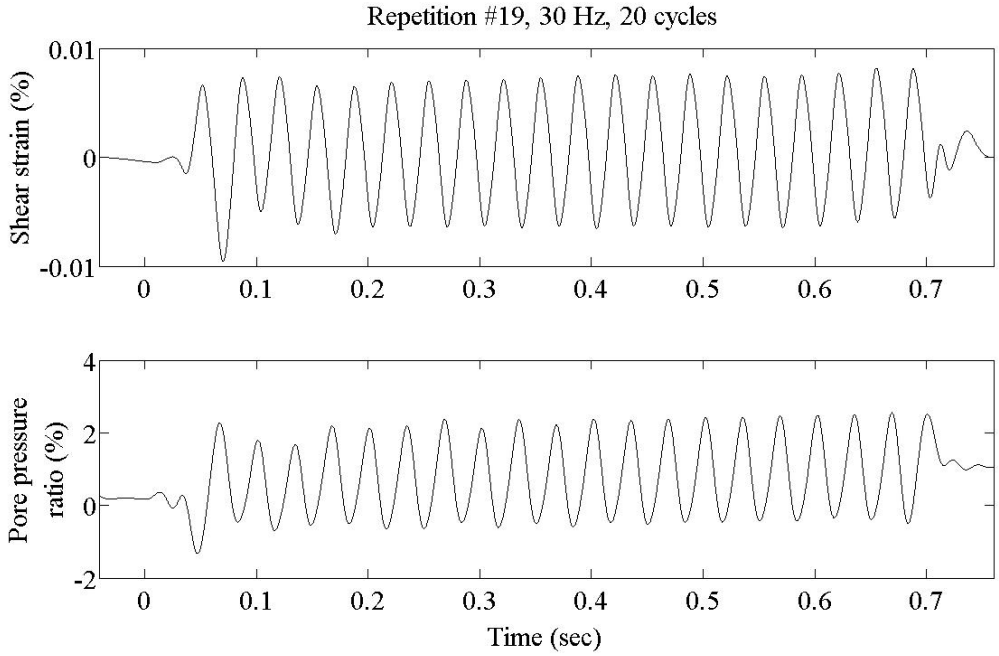

Figure 103. Shear strain and pore pressure ratio time series for Loading Stage (Repetition) #19.

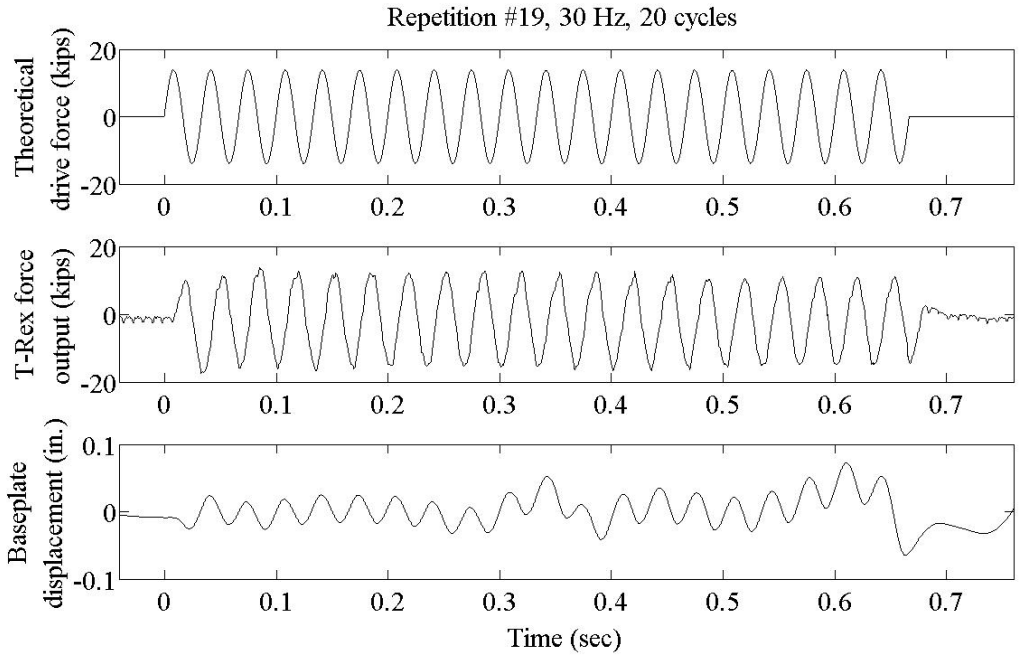

Figure 104. Theoretical drive force, T-Rex force output, and baseplate displacement for Loading Stage (Repetition) #19.

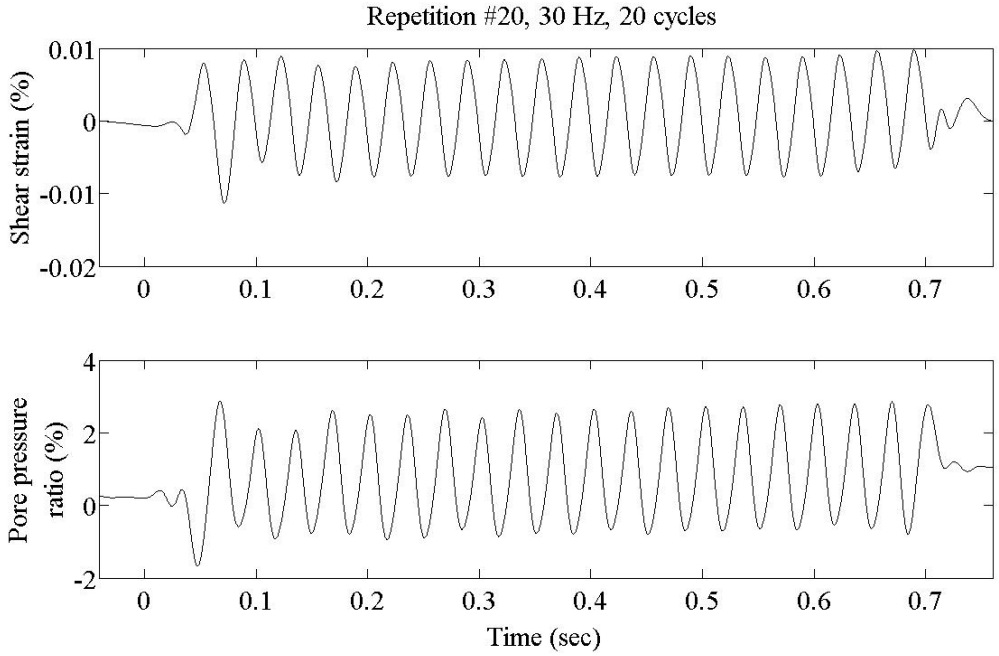

Figure 105. Shear strain and pore pressure ratio time series for Loading Stage (Repetition) #20.

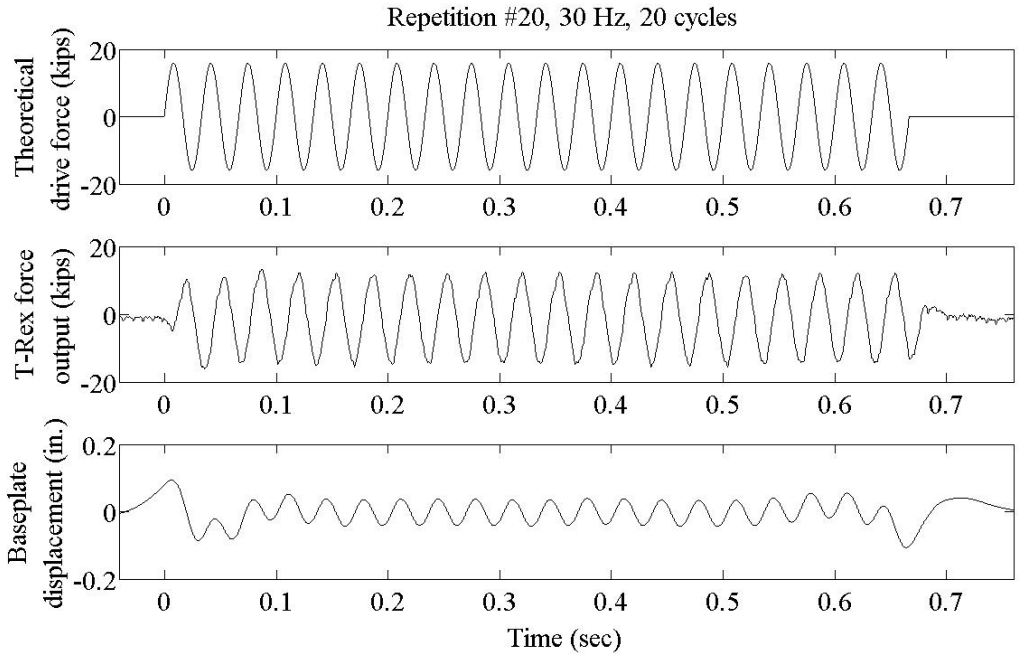

Figure 106. Theoretical drive force, T-Rex force output, and baseplate displacement for Loading Stage (Repetition) #20.

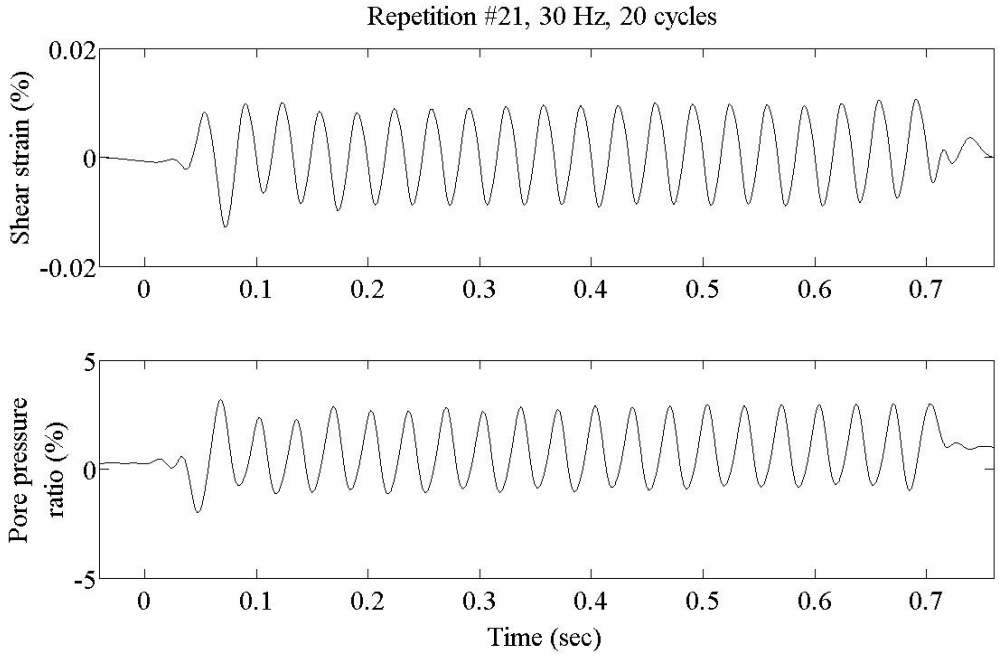

Figure 107. Shear strain and pore pressure ratio time series for Loading Stage (Repetition) #21.

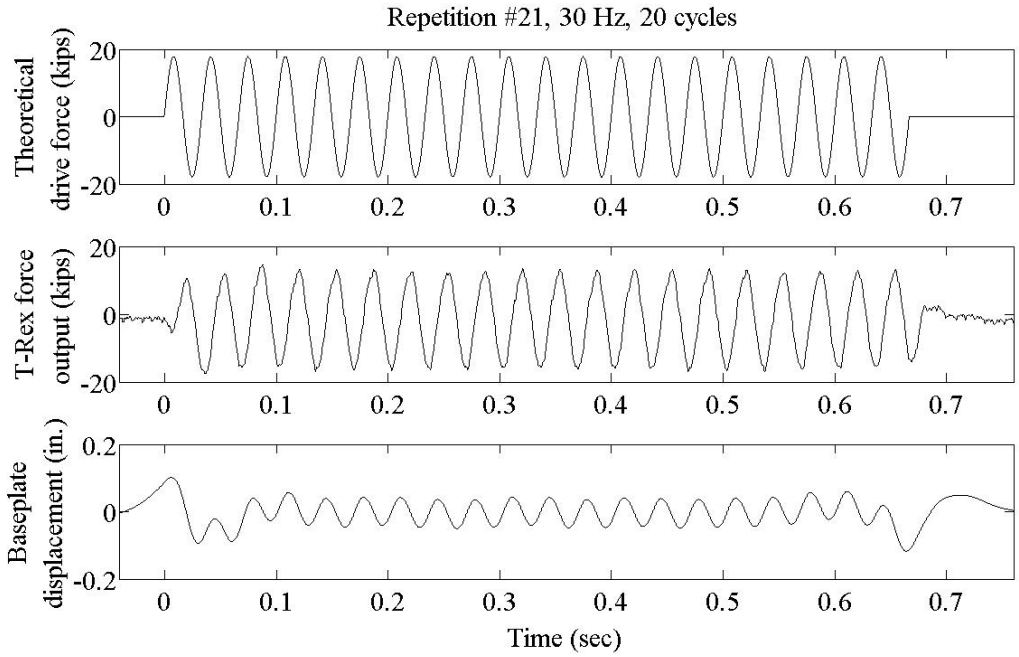

Figure 108. Theoretical drive force, T-Rex force output, and baseplate displacement for Loading Stage (Repetition) #21.

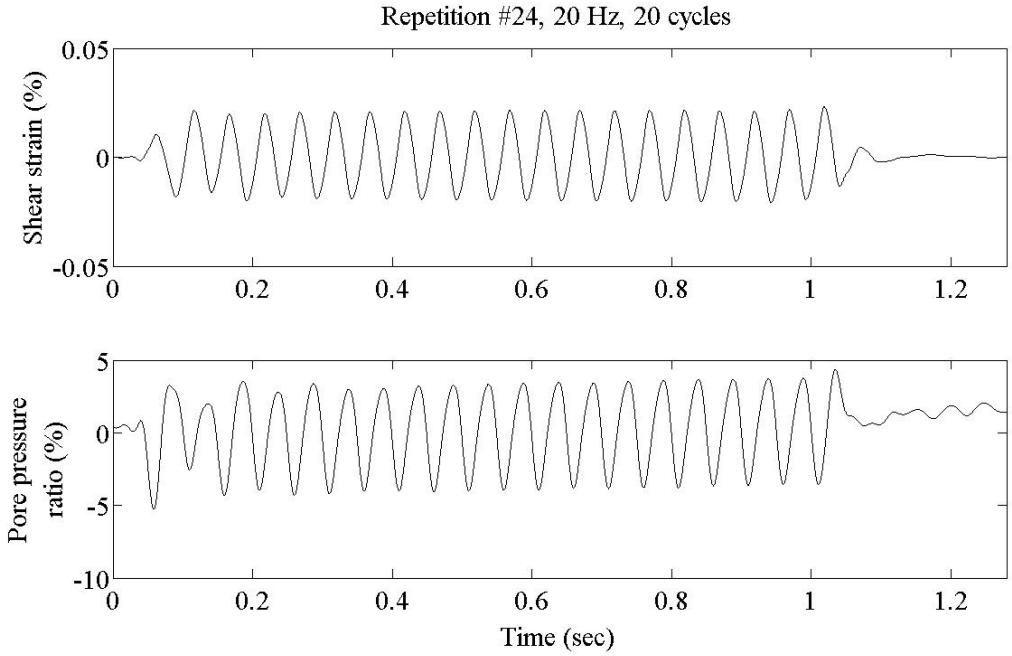

Figure 109. Shear strain and pore pressure ratio time series for Loading Stage (Repetition) #24.

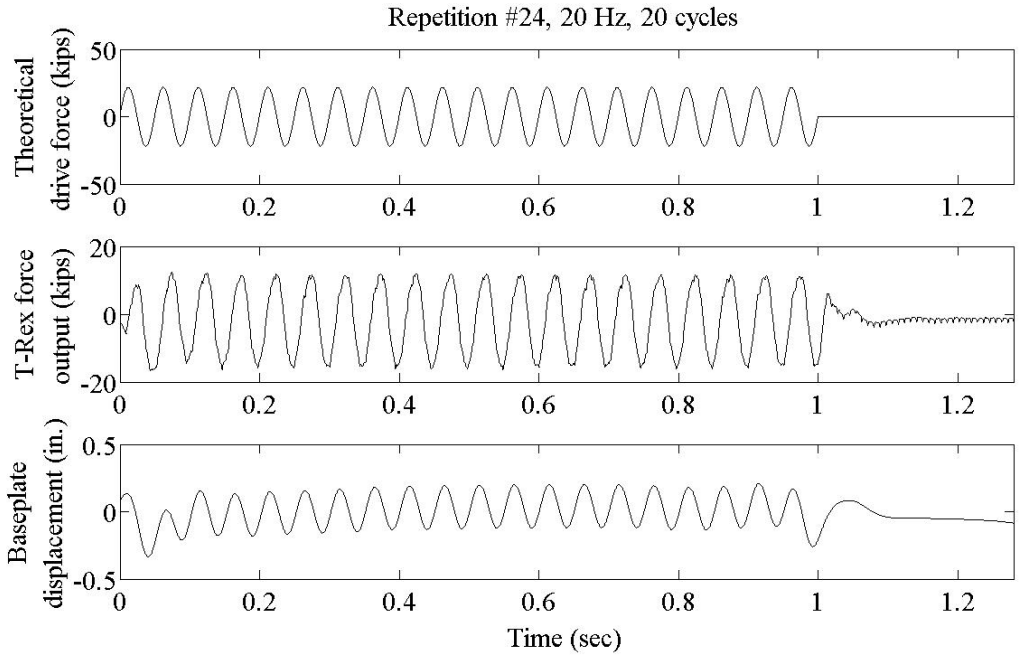

Figure 110. Theoretical drive force, T-Rex force output, and baseplate displacement for Loading Stage (Repetition) #24.

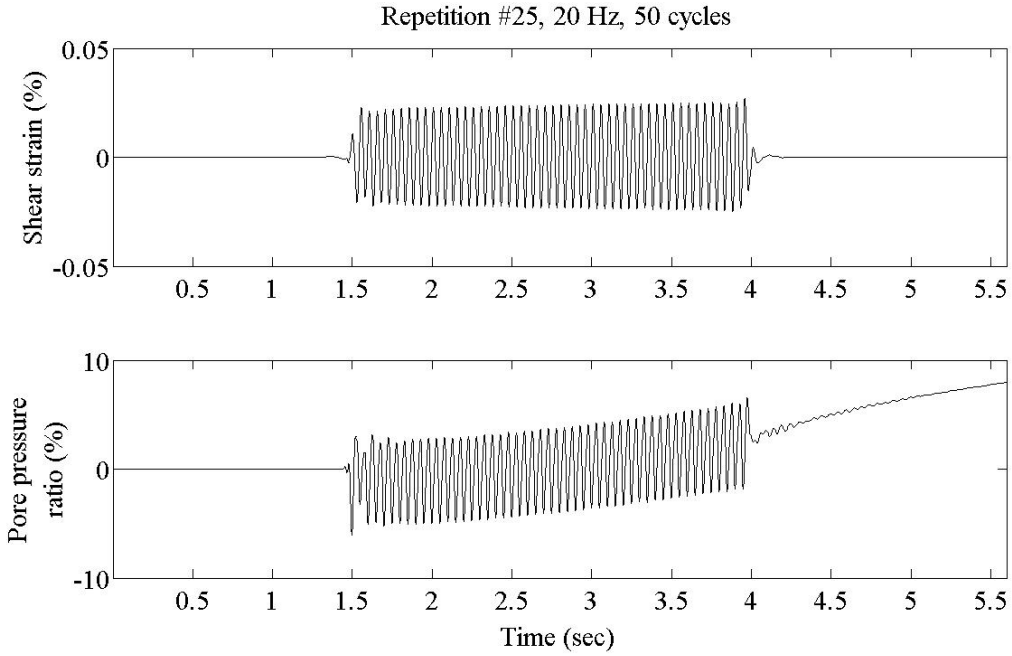

Figure 111. Shear strain and pore pressure ratio time series for Loading Stage (Repetition) #25.

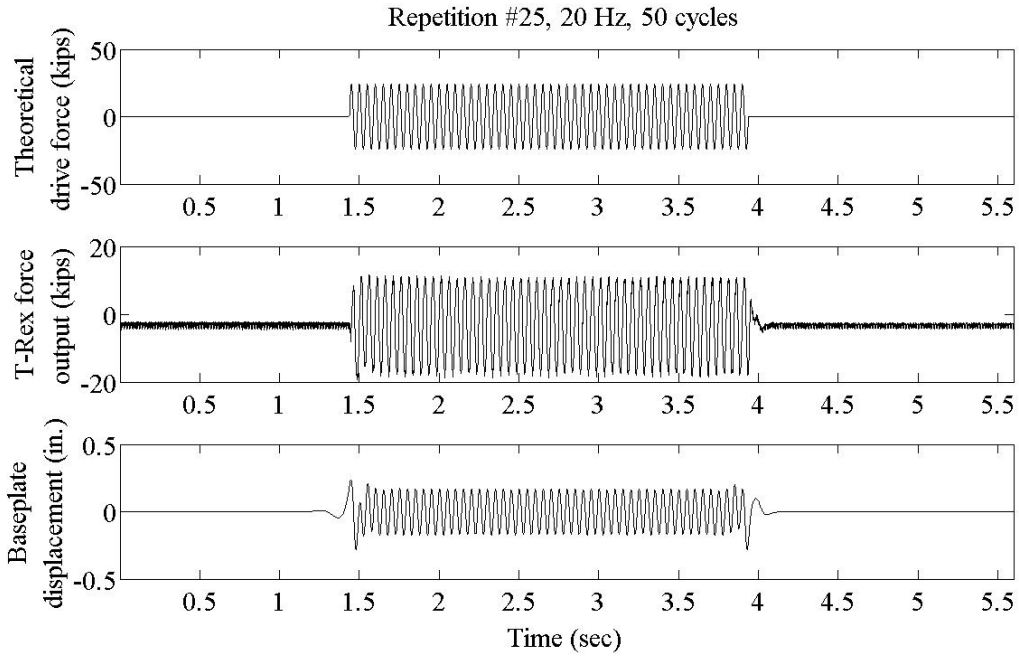

Figure 112. Theoretical drive force, T-Rex force output, and baseplate displacement for Loading Stage (Repetition) #25.

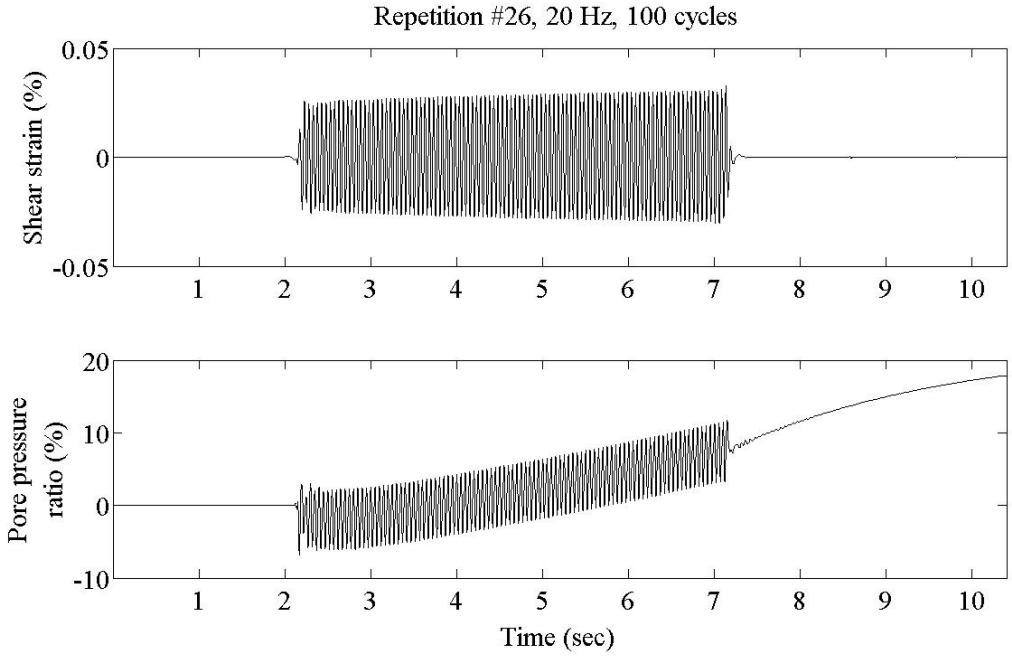

Figure 113. Shear strain and pore pressure ratio time series for Loading Stage (Repetition) #26.

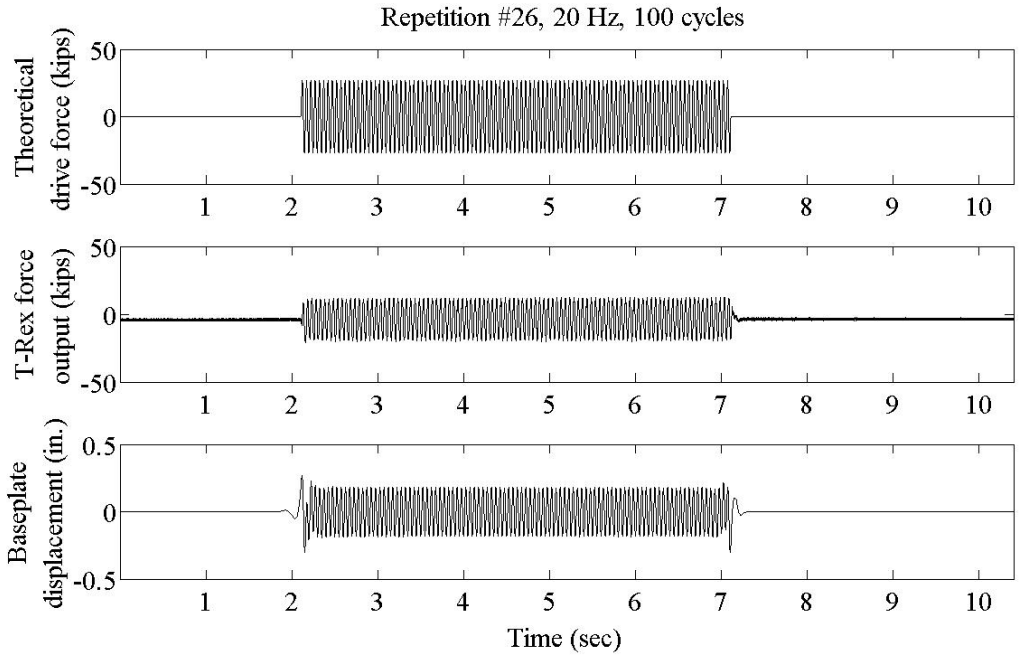

Figure 114. Theoretical drive force, T-Rex force output, and baseplate displacement for Loading Stage (Repetition) #26.

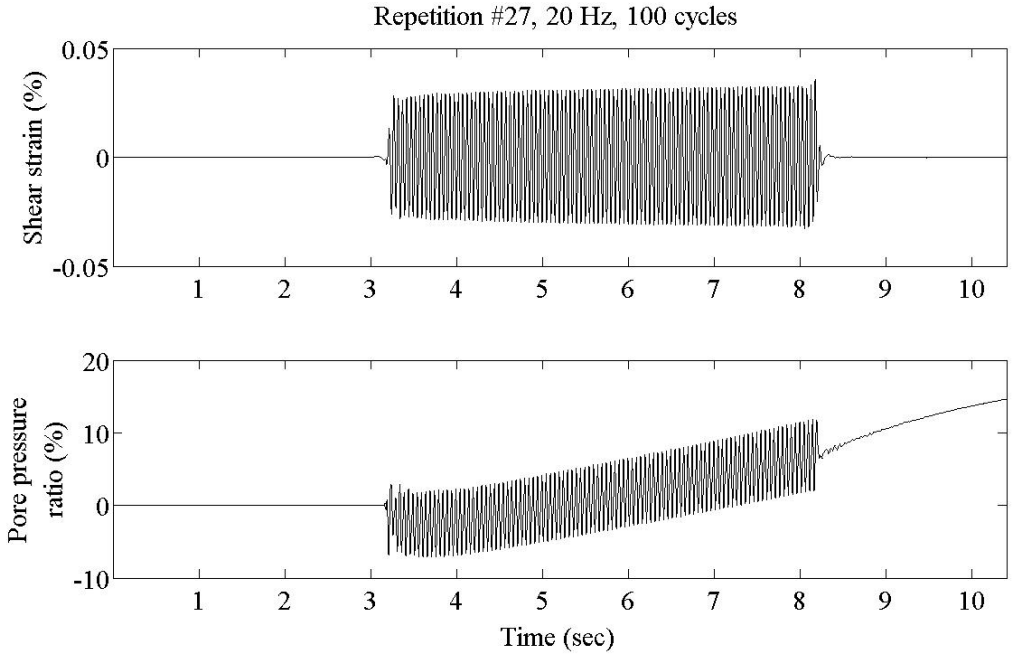

Figure 115. Shear strain and pore pressure ratio time series for Loading Stage (Repetition) #27.

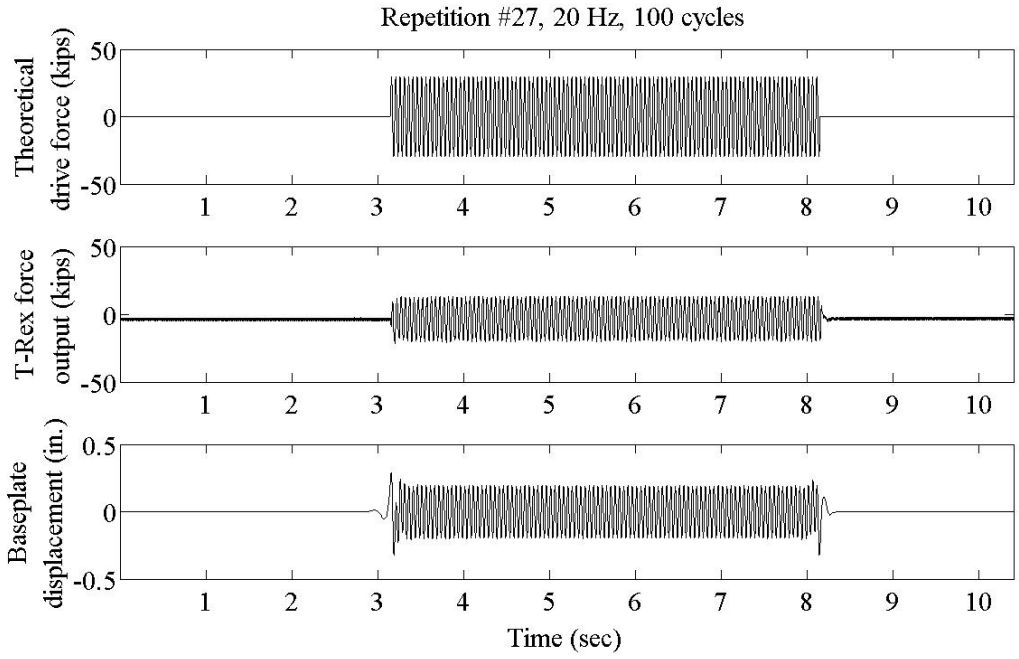

Figure 116. Theoretical drive force, T-Rex force output, and baseplate displacement for Loading Stage (Repetition) #27.

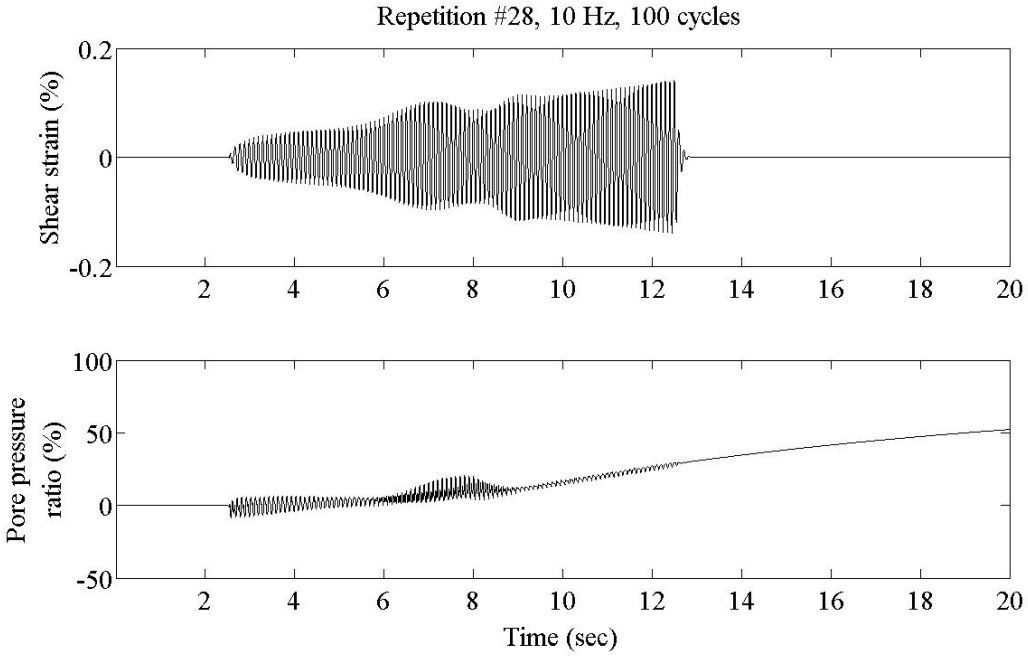

Figure 117. Shear strain and pore pressure ratio time series for Loading Stage (Repetition) #28.

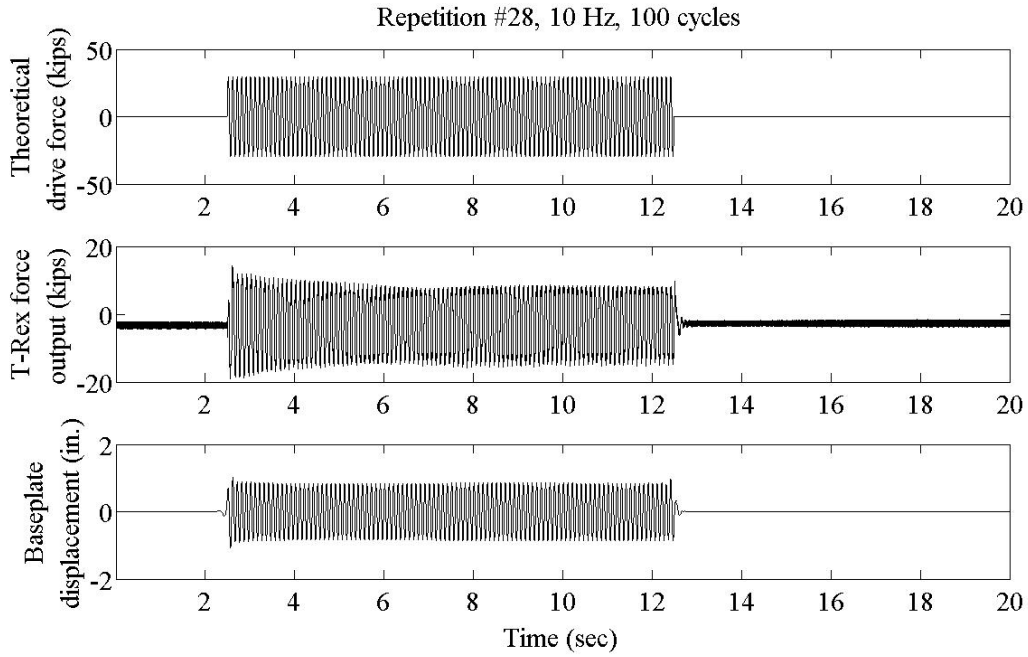

Figure 118. Theoretical drive force, T-Rex force output, and baseplate displacement for Loading Stage (Repetition) #1.

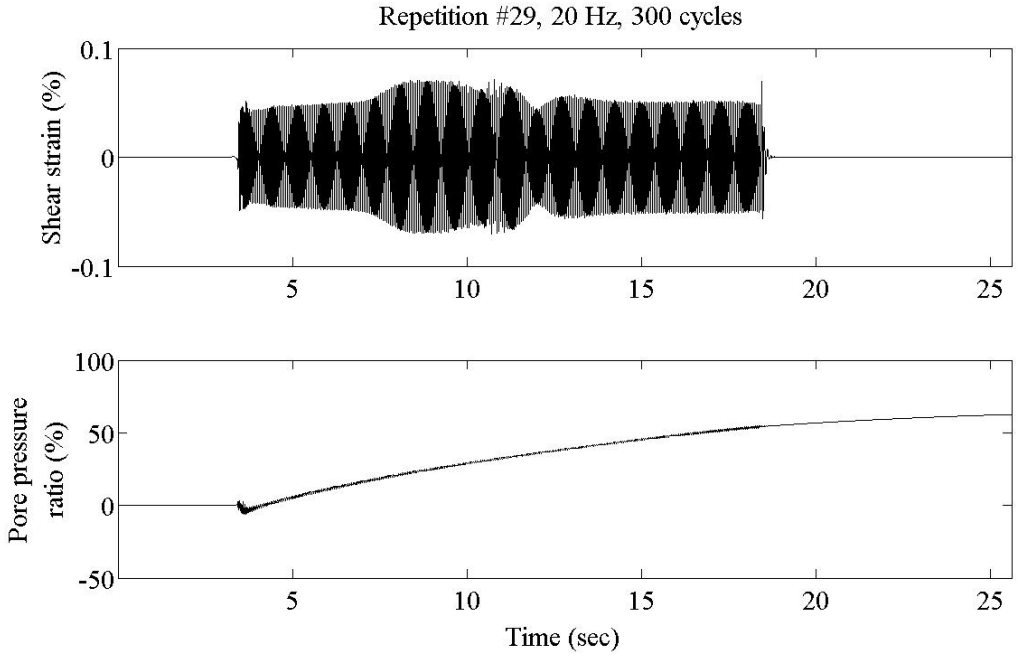

Figure 119. Shear strain and pore pressure ratio time series for Loading Stage (Repetition) #29.

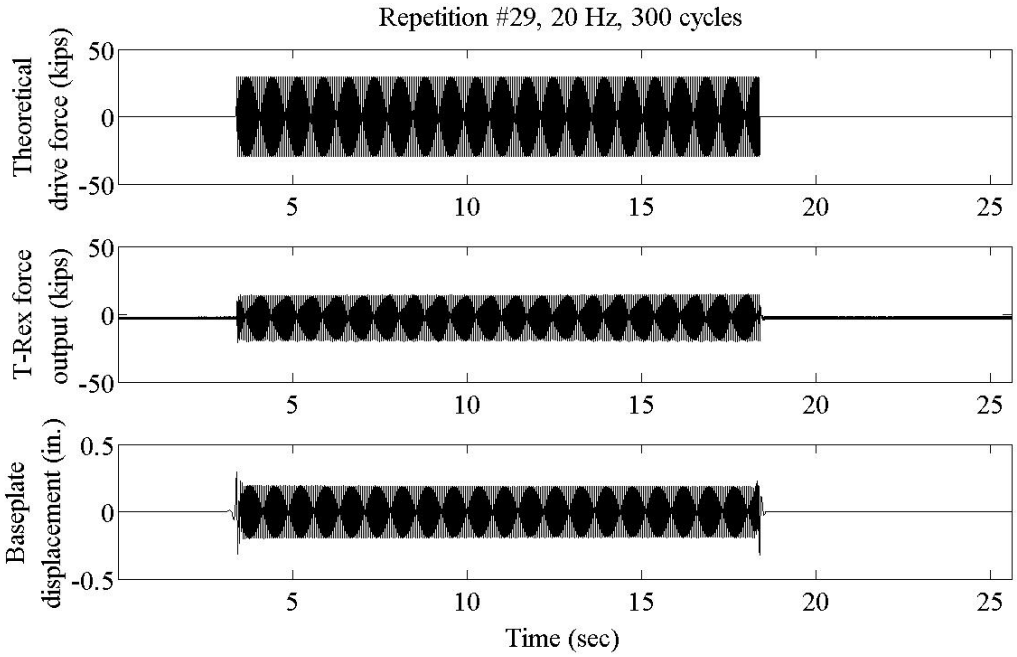

Figure 120. Theoretical drive force, T-Rex force output, and baseplate displacement for Loading Stage (Repetition) #29.

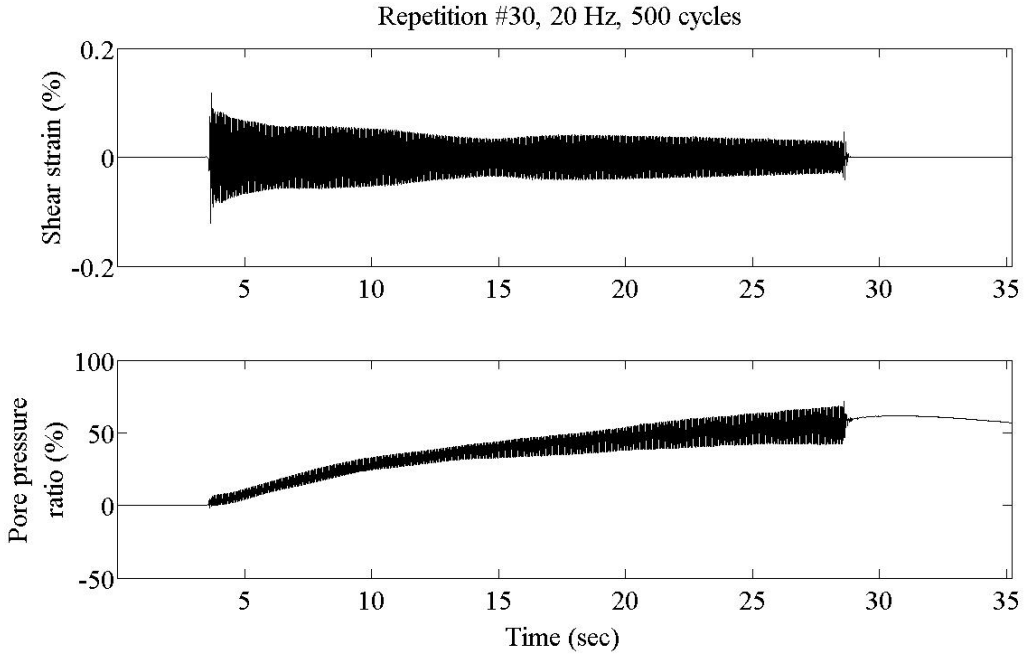

Figure 121. Shear strain and pore pressure ratio time series for Loading Stage (Repetition) #30.

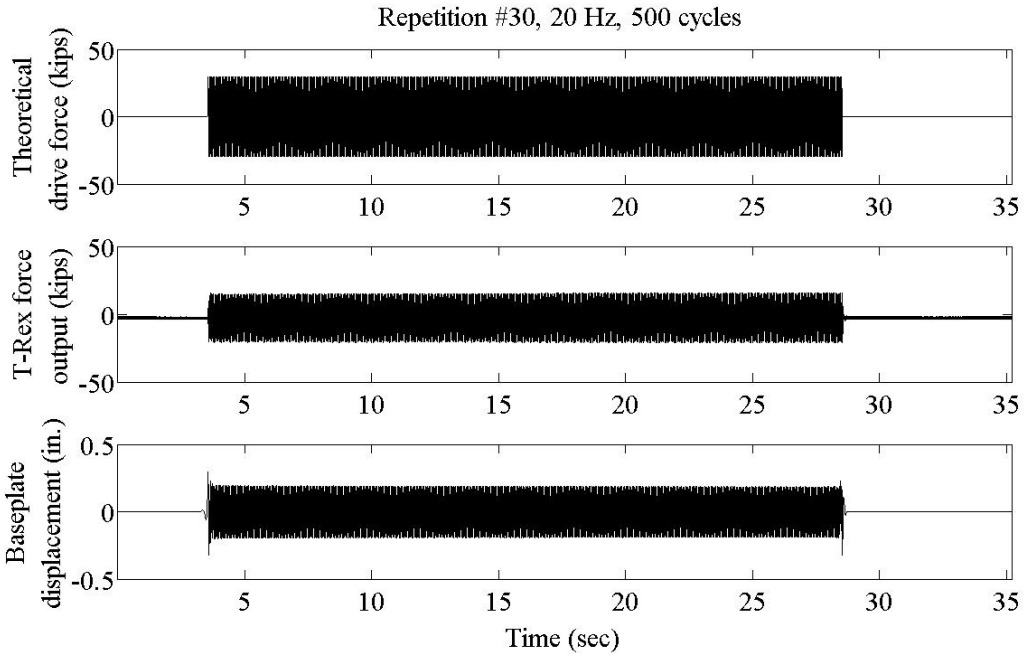

Figure 122. Theoretical drive force, T-Rex force output, and baseplate displacement for Loading Stage (Repetition) #30.

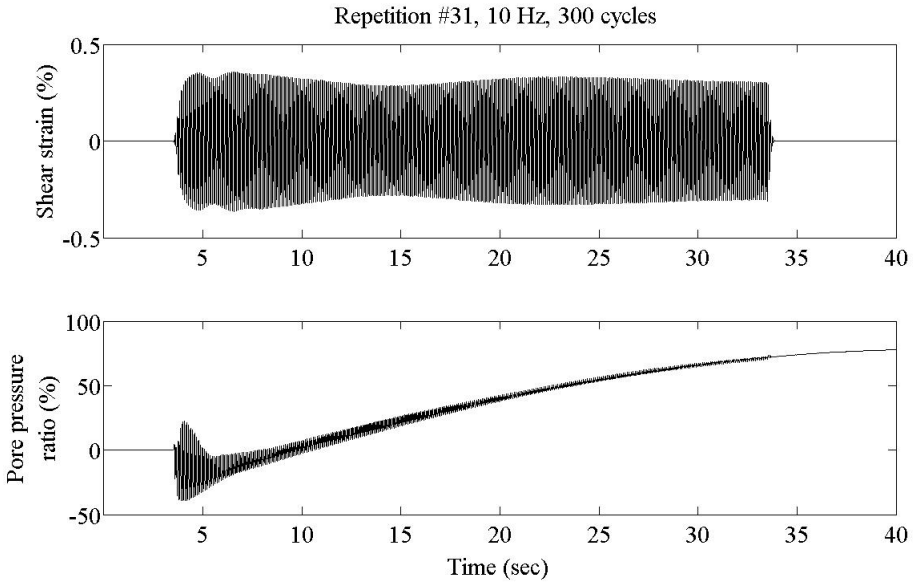

Figure 123. Shear strain and pore pressure ratio time series for Loading Stage (Repetition) #31.

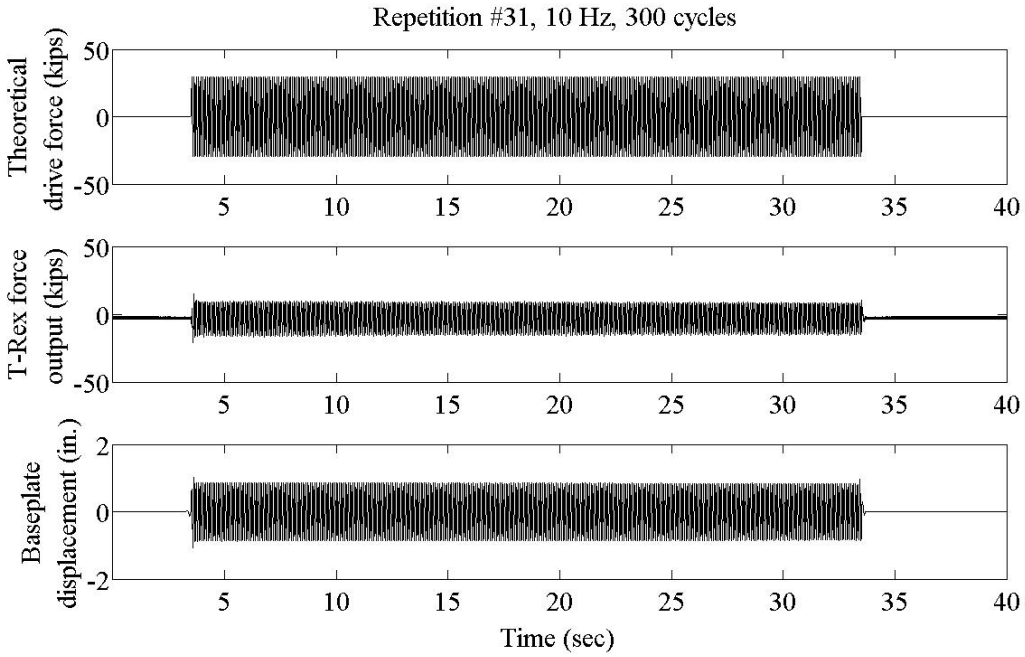

Figure 124. Theoretical drive force, T-Rex force output, and baseplate displacement for Loading Stage (Repetition) #31.

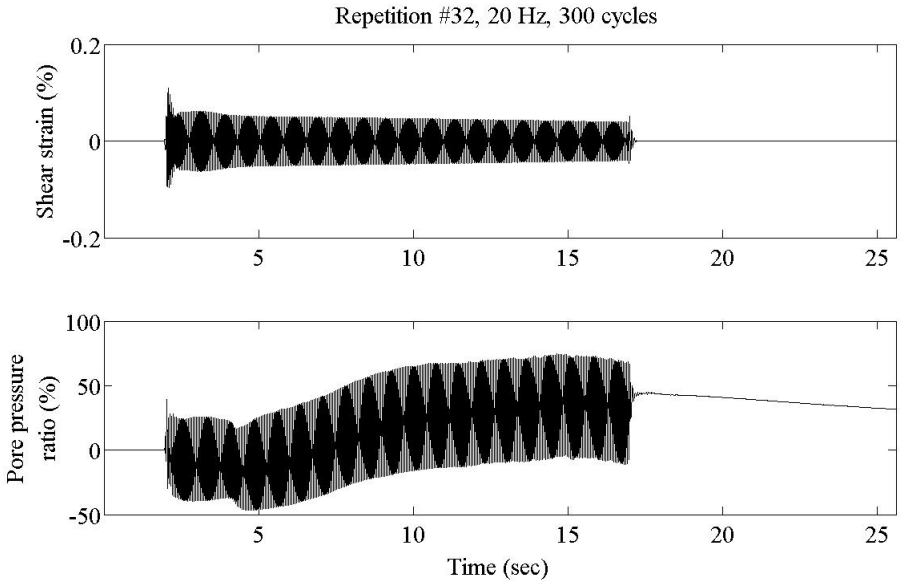

Figure 125. Shear strain and pore pressure ratio time series for Loading Stage (Repetition) #32.

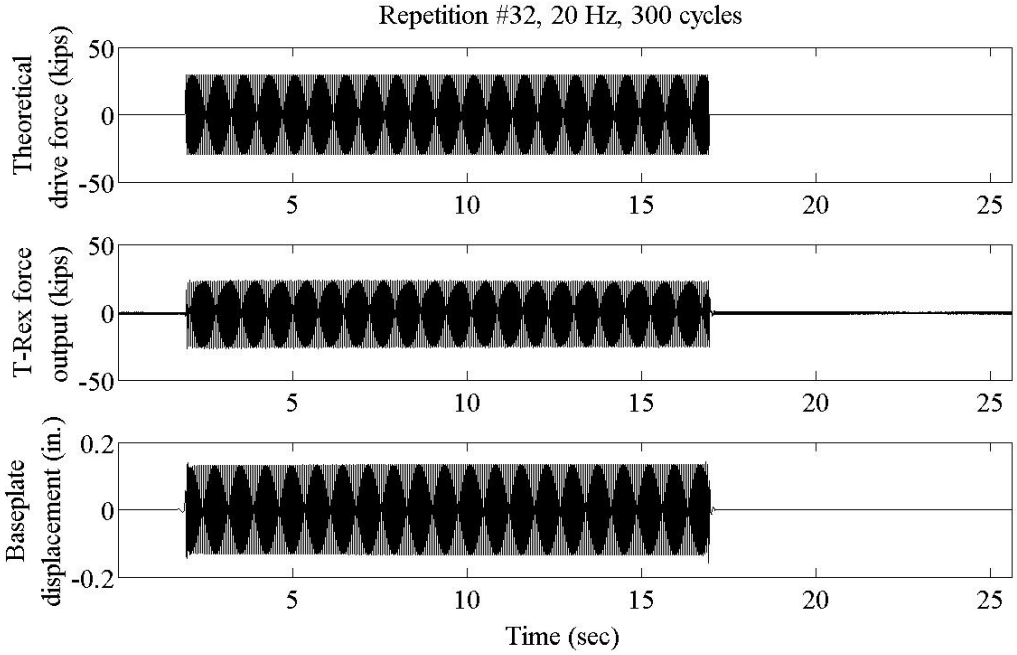

Figure 126. Theoretical drive force, T-Rex force output, and baseplate displacement for Loading Stage (Repetition) #32.

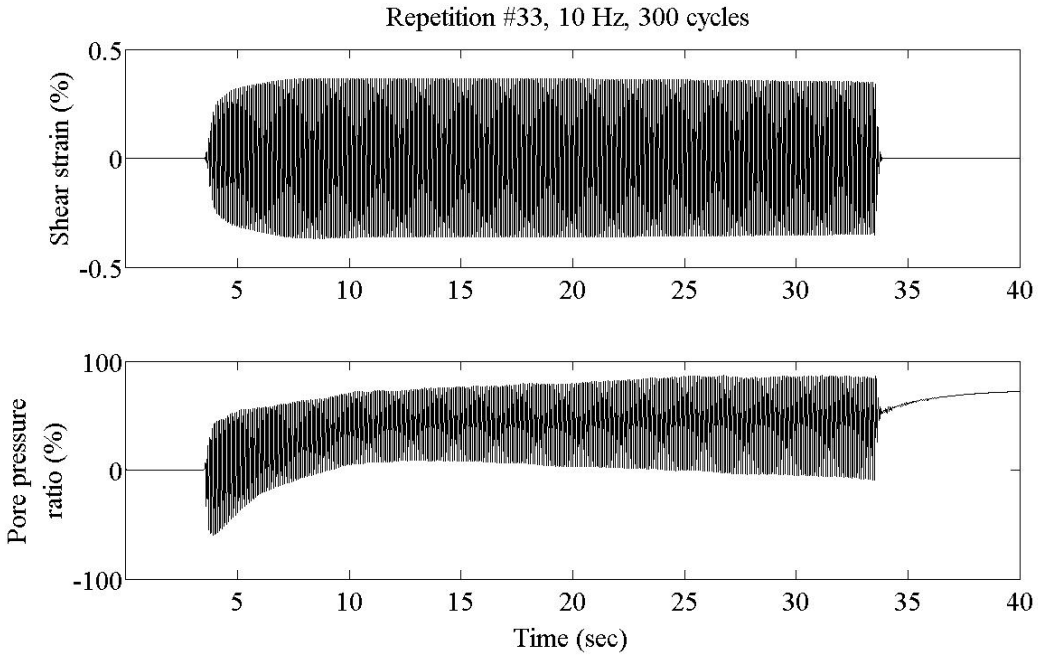

Figure 127. Shear strain and pore pressure ratio time series for Loading Stage (Repetition) #33.

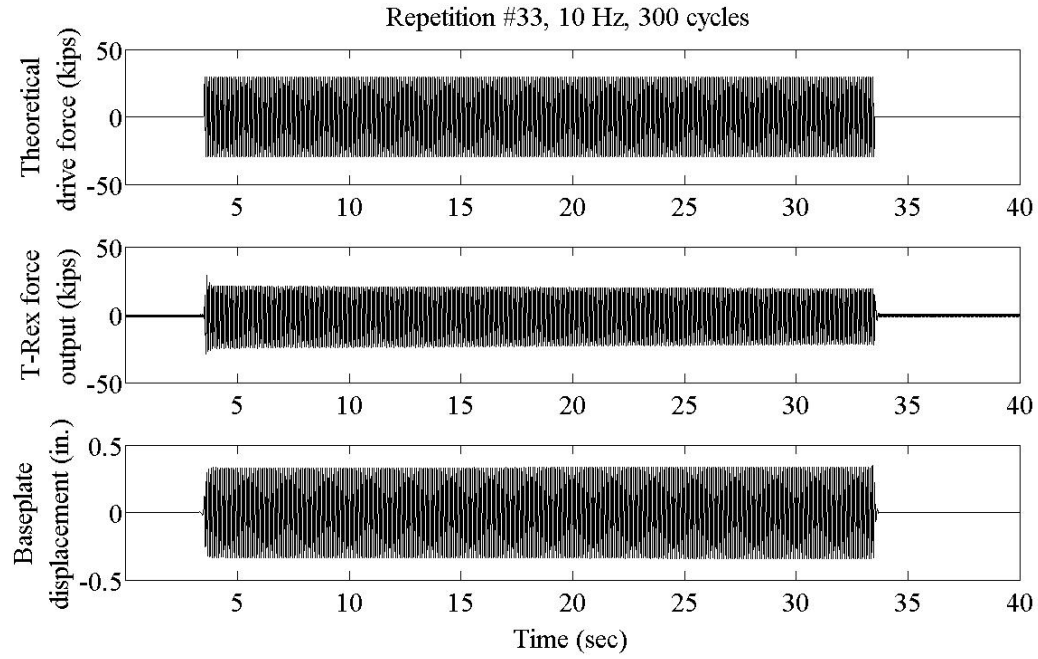

Figure 128. Theoretical drive force, T-Rex force output, and baseplate displacement for Loading Stage (Repetition) #33.

Bibliography

Andrus, R. D., and Stokoe, K. H., II. "Liquefaction resistance of soils from shear-wave velocity." Journal of Geotechnical and Geoenvironmental Engineering (ASCE) 126(11) (2000): 1015-1025.

Bennet, M.J., McLaughlin, P.V., Sarmiento, J.S., and Youd, T.L. Geotechnical Investigation of Liquefaction Sites, Imperial Valley, California. Open File Report 84-252, Menlo Park, California: Department of the Interior, 1984.

Bierschwale, J.G. and Stokoe, K.H., II. "Analytical Evaluation of Liquefaction Potential of Sands Subjected to the 1981 Westmorland Earthquake." Geotechnical Engineering Report GR 84-15, The University of Texas at Austin, Austin, 1984.

Chang, Wen-Jong. Development of an In Situ Dynamic Liquefaction Test. Dissertation, The University of Texas at Austin, Austin, TX: The University of Texas at Austin, 2002.

Cox, Brady. Development of a Direct Test Method for Dynamically Assessing the Liquefaction Resistance of Soils In Situ. Dissertation, The University of Texas at Austin, Austin: The University of Texas at Austin, 2006.

Dobry, R., Ladd, R. S., Yokel, F. Y., Chung, R. M., and Powell, D. Prediction of Pore Water Pressure Buildup and Liquefaction of Sands During Earthquakes by the Cyclic Strain Method. Washington, D.C.: National Bureau of Standards, 1982.

Holzer, Thomas L., and Youd, T. Leslie. "Liquefaction, Ground Oscillation, and Soil Deformation at the Wildlife Array, California." Bulletin of the Seismological Society of America 97, no. 3 (June 2007): 961-976.

McSaveney, Ellen. *Historic earthquakes - The 2011 Christchurch earthquake and other recent earthquakes*. August 5, 2013. http://www.TeAra.govt.nz/en/historic-earthquakes/page-13 (accessed August 11, 2013).

Menq, F-Y, Stokoe, K.H., II, Park, K., Rosenblad, B. and Cox, B. R., (2008) "Performance of Mobile Hydraulic Shakers at nees@UTexas for Earthquake Studies," 14th World Conference of Earthquake Engineering, Beijing, China, October 12-17, 2008.

NEES@UCSB. Wildlife Liquefaction Array. February 14, 2013. www.nees.ucsb.edu/?q=facilities/wla (accessed February 14, 2013).

Rathje, Ellen M., Chang, Wen-Jong, Stokoe, Kenneth H., II, Cox, Brady R. "Evaluation of Ground Strain from In Situ Dynamic Response." 13th World Conference on Earthquake Engineering. Vancouver: WCEE, 2004.

Richart, R. E., Hall, J. R., and Woods, R. D. Vibration of Soils and Foundations. New Jersey: Prentice-Hall, Inc., 1970.

Robertson, P. K., and Wride, C. E. "Evaluating cyclic liquefaction potential using the cone penetration test." Canadian Geotechnical Journal 35(3) (1998): 442-459.

Seed, H.B., Tokimatsu, K., Harder, L. F., and Chung, R. M. "The influence of SPT procedures in soil liquefaction resistance evaluations." Journal of Geotechnical Engineering (ASCE), 1985: 1425-1445.

USGS et al. Mineral and Water Resources of California. Special report, United States Senate, Washington, D.C.: U.S. Government Printing Office, 1966.

Valle-Molina, Celestino. Measurements of V_p and V_s in Dry, Unsaturated and Saturated Sand Specimens with Peizoelectric Transducers. Austin: The University of Texas at Austin, 2006.

Vucetic, M. and Dobry, R. “Pore Pressure Build Up and Liquefaction at Level Sandy Sites During Earthquakes,” *Research Report*, Department of Civil Engineering, Rensselaer Polytechnic Institute, Troy, New York, 1986.

Woods, R. D. "Screening of surface waves in soils." Journal of the Soil Mechanics and Foundations Division (ASCE) 94(SM4) (1968): 951-979.

Youd et al. “Lessons learned and need for instrumented liquefaction sites.” Soil Dynamics and Earthquake Engineering 24, no. 9 (2004): 639-646.

Youd, T. L., and Noble, S. K. "Magnitude scaling factors." NCEER Workshop on Evaluation of Liquefaction Resistance of Soils. Buffalo: Nat. Ctr. for Earthquake Engrg. Res., State Univ. of New York at Buffalo, 1997. 149-165.

Youd, T.L., Idriss, I.M., Andrus, R.D., Arango, I., Castro, G., Christian, J.T., Dobry, R., Finn, W.D.L., Harder, F.L., Jr., Hynes, M.E., Ishihara, K., Koester, J.P., Liao, S.S.C., Marcuson, W.F., III, Martin, G.R., Mitchell, J.K., Moriwaki, Y., Power, M.S., Robertson, P.K., Seed, R.B., and Stokoe, K.H., II. "Liquefaction Resistance of Soils: Summary Report from the 1996 NCEER and 1998 NCEER/NSF Workshops on Evaluation of Liquefaction Resistance of Soils." Journal of Geotechnical and Geoenvironmental Engineering (ASCE) 127, no. 10 (2001): 817-833.